



HAL
open science

Spectroscopic properties of environmental relevant systems : 2',3-dihydroxyflavone-ion complexes and polycyclic aromatic hydrocarbons : a joint experimental and theoretical study

Luc Labarrière

► To cite this version:

Luc Labarrière. Spectroscopic properties of environmental relevant systems : 2',3-dihydroxyflavone-ion complexes and polycyclic aromatic hydrocarbons : a joint experimental and theoretical study. Analytical chemistry. Université de Lille, 2022. English. NNT : 2022ULILR069 . tel-04486531

HAL Id: tel-04486531

<https://theses.hal.science/tel-04486531v1>

Submitted on 2 Mar 2024

HAL is a multi-disciplinary open access archive for the deposit and dissemination of scientific research documents, whether they are published or not. The documents may come from teaching and research institutions in France or abroad, or from public or private research centers.

L'archive ouverte pluridisciplinaire **HAL**, est destinée au dépôt et à la diffusion de documents scientifiques de niveau recherche, publiés ou non, émanant des établissements d'enseignement et de recherche français ou étrangers, des laboratoires publics ou privés.

THÈSE

Préparée et soutenue publiquement le 5 décembre 2022 à

L'Université de Lille

École Doctorale Sciences de la Matière, du Rayonnement et de l'Environnement
Pour obtenir le titre de **DOCTEUR**, mention : Chimie théorique, physique, analytique

Présentée par

Luc LABARRIÈRE

Laboratoire Avancé de Spectroscopie pour les Interactions, la Réactivité et l'Environnement
LASIRE (CNRS UMR8516)

**Spectroscopic properties of environmental relevant systems:
2',3-dihydroxyflavone-ion complexes and polycyclic aromatic
hydrocarbons. A joint experimental and theoretical study**

**Propriétés spectroscopiques de systèmes liés à l'environnement :
complexes ioniques de la 2',3-dihydroxyflavone et hydrocarbures
aromatiques polycycliques. Une étude expérimentale et théorique**

Composition du jury :

Céline TOUBIN	PR	Université de Lille	Présidente du jury
Carine CLAVAGUÉRA	DR	Université Paris-Saclay	Rapporteuse
Vincent TOGNETTI	MCF	Université de Rouen	Rapporteur
Erwan ANDRÉ	MCF	Université de Lorraine	Examineur
Xavier MERCIER	DR	Université de Lille	Invité
Jean-Paul CORNARD	PR	Université de Lille	Directeur de thèse
Aurélien MONCOMBLE	MCF	Université de Lille	Co-encadrant

Acknowledgements

Cette thèse s'est déroulée au Laboratoire Avancé de Spectroscopie pour les Interactions, la Réactivité et l'Environnement (LASIRE) et je souhaite remercier le Directeur, M. Hervé Vezin, ainsi que tout le personnel, et plus particulièrement l'équipe Physicochimie de l'environnement dans laquelle j'ai si bien été accueilli. Merci également au LabeX CaPPA d'avoir financé ce projet et de m'avoir permis de présenter mes travaux lors de congrès où j'ai pu avoir de captivantes conversations avec des chercheurs de domaines similaires au miens.

Mme Carine Clavaguéra et M. Vincent Tognetti ont accepté d'être rapporteurs de ce manuscrit et pour cela, je leur exprime ma profonde gratitude. Je remercie également Mme Céline Toubin et M. Erwan André qui ont accepté d'en être examinateurs.

Les résultats présentés dans la partie II de cette thèse ont été réalisés en collaboration avec M. Xavier Mercier, également membre du jury en qualité d'invité, et sa doctorante Mme Jessy Elias. Je les remercie tout particulièrement, notamment pour m'avoir guidé dans la sélection des systèmes moléculaires et avoir contribué à ma compréhension du sujet lors de réunions passionnantes.

Avant de commencer ma thèse, mes amis m'avaient prévenu qu'un des critères principaux pour passer trois années de thèse dans les meilleures conditions était d'être bien encadré. Pour cela, je n'aurais pas pu mieux tomber puisque mon Directeur de thèse, M. Jean-Paul Cornard, m'a accompagné du Master jusqu'à aujourd'hui. Il a su me faire confiance, et a toujours été disponible pour répondre à mes questions et me préparer aux diverses épreuves que j'ai pu rencontrer. De la même manière, j'ai rencontré mon co-encadrant, M. Aurélien Moncomble, lors de ma préparation au concours de l'agrégation de chimie. Il m'a d'ailleurs fait découvrir la chimie quantique et m'a appris tout ce que je sais sur le sujet, en ayant pris le temps de répondre à mes nombreuses questions. Tous deux, vous avez contribué à rendre ces trois années de thèses aussi agréables qu'elles auraient pu être et avez contribué à mes réussites. Je vous en serai toujours reconnaissant.

Je dois remercier tout particulièrement ma prédécesseuse, Mme Diksha Jani Thaviligadu. En effet, elle a trouvé le temps de me guider et m'accompagner lors de

mon arrivée au laboratoire alors qu'elle était en pleine rédaction du manuscrit. Je connais désormais la difficulté que cela représente. De même M. Jérémy Gaillard tient une place particulière dans ces remerciements. Il m'a transmis une partie de ses très nombreuses connaissances expérimentales, mais pas uniquement, et a répliqué les expériences dont les résultats ont été présentés dans cette thèse. Je le remercie et lui souhaite le meilleur pour la suite. Je voudrais également remercier M. François-Alexandre Miannay et Mme Yevheniia Smortsova pour leur collaboration sur le projet et pour m'avoir formé à la fluorescence résolue en temps. Merci pour votre patience et votre accueil.

Durant ces trois années de thèse, j'ai pu réaliser mon rêve et accomplir des missions d'enseignement. Pour cela je remercie Mme Annaïg Le Person et M. Alain Moissette qui m'ont offert la possibilité d'enseigner la spectroscopie en Master de chimie ainsi que la chimie générale en première année de Licence adaptée. Je garderai ces expériences extraordinaires en mémoire toute ma vie. J'ai également eu le plaisir d'encadrer Léa Havret, étudiante en troisième année de Licence de chimie, pour un stage. Merci pour ta bonne humeur qui a rendu notre collaboration très agréable, et pour la qualité de ton travail.

J'ai rencontré des gens formidables, notamment, Ákos, Lucas, Pedro, Ana Lícia, Xin, Quentin, Jérémy et Mikel ; merci d'avoir partagé mes bureaux et d'y avoir apporté votre bonne humeur. Je vous souhaite le meilleur pour la suite.

Rien n'aurait été possible sans leur soutien inconditionnel : mes remerciements vont à mes parents, à mes frères et à ma sœur. Merci de m'avoir encouragé dans tous les choix que j'ai pu faire.

Enfin, nous nous sommes rencontrés pendant nos études. Merci Angéline, mon amour, d'être présente et de croire en moi depuis le début de cette aventure. Je te remercie également de m'avoir fait rencontrer ma merveilleuse belle-famille, ainsi que Muyu ma lapine adoptive.

Table of contents

ACKNOWLEDGEMENTS	5
TABLE OF CONTENTS	9
GENERAL INTRODUCTION	15
PART I. STRUCTURAL AND OPTICAL PROPERTIES OF 2',3-DIHYDROXYFLAVONE AND ITS METAL COMPLEXES	19
CHAPTER 1. INTRODUCTION ON FLAVONOIDS AND METHODS	21
1. From organic matter to its building blocks	23
1.1. Organic matter	23
1.2. The flavonoid family	25
2. The studied metals	33
2.1. The choice of metal cations	33
2.2. Zinc, manganese and calcium	33
3. Computational methods	35
3.1. Density Functional Theory (DFT)	35
3.2. Time-Dependent Density Functional Theory (TD-DFT)	39
3.3. Polarizable Continuum Model (PCM)	40
3.4. Molecular dynamics (MD)	41
4. Experimental methods	43
4.1. Electronic spectroscopies	43
4.2. Data treatment	43
5. Technical details	45
5.1. Details of Chapter 2	45
5.2. Details of Chapter 3	46
5.3. Details of Chapter 4	50
CHAPTER 2. THE STRUCTURE AND ELECTRONIC PROPERTIES OF 2',3-DIHYDROXYFLAVONE	55
1. State of the art	57
2. Ground-state	59
2.1. The neutral form	59
2.2. Acid-base properties	64
2.3. Electronic excitation energies	67
3. Excited-state	71
3.1. Fluorescence emission in acidic medium	71
3.2. Neutral excited-state geometries	74
3.3. Fluorescence emission in basic medium	77
3.4. Hypotheses on the 517 nm emission band	79

4.	Conclusion	83
CHAPTER 3. SOLUTE-SOLVENT INTERACTIONS AND THE HYPOTHETICAL SOLVENT-COMPLEX		85
1.	Problematic and methodologies	87
1.1.	Solvent effects on the fluorescence of 3HF	87
1.2.	Recent publications and comparison with 2'3HF	88
1.3.	Objectives of the study	90
2.	Experimental observations	92
2.1.	The nature of the solvent	92
2.2.	Effect of water percentage	97
2.3.	Discussion and conclusions on the experiments	103
3.	Simulation of the solvent	105
3.1.	State of the art	105
3.2.	General shape of the spectrum	106
3.3.	Origin of the red tail	109
3.4.	Differences between A and B	111
3.5.	Performances of the PCM	113
3.6.	Conclusion on the calculation results	116
CHAPTER 4. METAL COMPLEXES OF 2',3-DIHYDROXYFLAVONE		119
1.	Introduction	121
2.	Acidic medium	125
3.	Acid-base dependency	129
4.	Binding site hypotheses	133
4.1.	The "acidic" medium complex	133
4.2.	The "basic" medium complex	139
4.3.	Thermodynamic considerations	144
5.	Conclusion	147
GENERAL CONCLUSION ON PART I.		151
PART II. THE OPTICAL PROPERTIES OF SOOT PRECURSOR SPECIES		157
CHAPTER 1. INTRODUCTION ON POLYCYCLIC AROMATIC HYDROCARBONS AND SOOT, OBJECTIVES AND METHODS		159
1.	What is soot	161
1.1.	Flame systems	161
1.2.	Environmental concerns	161
1.3.	Chemical nature	162
1.4.	Reducing soot emissions	163
2.	Polycyclic aromatic hydrocarbons	165
2.1.	General properties	165
2.2.	Their excited-states	166
3.	The inception of soot particles	174

3.1.	PAH formation	174
3.2.	Soot inception mechanisms	175
4.	Spectroscopic evidences of PAH dimerization	180
4.1.	Laser induced fluorescence (LIF)	180
4.2.	LIF signals in sooting flames	180
4.3.	Hypotheses on the origin of the broad-band	182
5.	Objectives of the study	184
6.	Methodologies	186
6.1.	Interaction in PAH dimers	186
6.2.	Excited-states of PAHs	187
6.3.	Computational details	187
CHAPTER 2. VAN DER WAALS DIMERS		191
1.	Conformers of the pyrene dimer	193
1.1.	Optimization of the structures	193
1.2.	Geometry analysis	194
2.	Electronic properties	196
2.1.	Technical details on the translation scan	196
2.2.	The identification of excited-states	199
2.3.	Comparison between the functionals	201
2.4.	Nature of the interaction	202
3.	Potential energy landscape	206
3.1.	Rotation scan	206
3.2.	Binding energies	208
4.	Electronic absorption spectra	210
4.1.	Dimerization effect on the low energy excitations	210
4.2.	Effect of the geometry	211
5.	Trimerization effect	214
5.1.	Structures	214
5.2.	Red-shift due to trimerization	215
6.	Conclusion	216
CHAPTER 3. ALIPHATICALLY-BRIDGED POLYCYCLIC AROMATIC HYDROCARBONS		219
1.	Optimization procedure	221
2.	Thermodynamics	223
3.	Geometry analysis	224
3.1.	Definition of geometrical parameters	224
3.2.	Effect of dimerization on the structure	226
4.	Electronic properties	230
4.1.	Spectral range of ABPAHs	230
4.2.	Structure – electronic properties relationship	231
4.3.	Molecular orbitals	236
5.	Conclusion	239
CHAPTER 4. PAH-BASED RADICALS		241
1.	Introduction	243

1.1.	State of the art	243
1.2.	Studied structures	244
2.	Stability of radical containing vdW dimers	247
3.	Electronic properties	249
3.1.	σ -radicals	249
3.2.	π -radicals	251
3.3.	Chemical dimer π -radicals	253
4.	Conclusion	257
GENERAL CONCLUSION ON PART II.		259
CONCLUSION		263
APPENDICES		265
TABLE OF APPENDICES		267
REFERENCES		281

General introduction

This thesis gathers the results of a PhD work that was carried out within the Physico-Chemistry of the Environment team at the Laboratoire de Spectroscopie pour les Interactions, la Réactivité et l'Environnement (LASIRE – UMR8516) in Lille, France. The team addresses several research themes among which are the study of natural environment by mean of the use of laboratory experimental and theoretical models, the speciation and the study of air, water, soil and sediment contaminants, and the assessment of water purification technics.

The Labex CaPPA (Laboratoire d'excellence – Chemical and Physical Properties of the Atmosphere) funded 50% of this PhD project. This Labex involves seven multidisciplinary laboratories working to improve knowledge on atmospheric sciences. This was completed by a 50% funding provided by the Université de Lille.

My PhD thesis focuses on two distinct and, apart from their environmental significance, unrelated topics: the complexation of metal ions by a flavonoid and the role of polycyclic aromatic hydrocarbons (PAHs) in the soot formation mechanism. It started in October 2019 and is the follow up of a Master's internship carried out in 2018 in the same team, that led to the publication of a research article on the flavonoids subject. [1] It is a well-known subject in the team, which focuses on the study of metal cation interactions with organic matter of soils and sediments by means of model molecules (building blocks of organic matter) so that the interaction complexity is reduced. The ultimate goal of this study, which is the phytoremediation of polluted soils, requires a perfect knowledge of the mechanisms of metal salt retention by surface organic matter. The complexity of the latter causes the current difficulties to determine the sites involved in the complexation of metal ions. Carboxylic functions, which are omnipresent in these compounds, are not imperative for the retention process, whereas polyphenolic functions seem to play a predominant role. The model molecules used in this work are flavonoids, secondary metabolites present in the plant kingdom that are precursors of organic matter and therefore possess chemical functions similar to that of the macromolecular structure. They are often multisite ligands for cations meaning that site competition occurs at the molecular level, which has led scientists, including our team, to try to elucidate the

reactivity of these molecules. The elucidation procedure has been proven for many years within the team and involves the combination of electronic spectroscopies and quantum chemical calculations. This joint use of two methods allows the structure of the complexes to be determined, and the affinity of functional groups for a variety of cations to be ranked. During her work as a former PhD student in the team, Dr Jani Thaviligadu showed that morin, a penta-hydroxyflavone, has singular acid-base and complexing properties compared to analogous molecules. It was therefore decided that my PhD work would focus on 2',3-dihydroxyflavone (2'3HF), a simpler flavonoid with only two hydroxyl groups occupying "strategic" positions.

Error! Reference source not found. of this thesis is dedicated to this subject. Chapter 1 is an introduction on organic matter, flavonoids, and the metal cations studied in this work. It is also in this chapter that the methods used throughout the thesis are introduced. Before studying the complexation, it is crucial to perfectly master the structural and spectroscopic aspects of the free ligand. Thus, a study on these aspects of 2'3HF was performed and published in *RSC. Advances* in 2020. The results are presented in Chapter 2. An outcoming result of the study is that 2'3HF spectroscopic properties are peculiar and highly dependent on solvation. Two approaches were considered to explain this trait. An experimental work was carried out to unravel the dependence of UV-visible and fluorescence spectra of 2'3HF on the solvent, and to investigate the effect of water impurities. In parallel, a purely theoretical approach was considered, using molecular dynamics followed by electronic transition calculations to get insights on the effect of specific solute-solvent interactions. The results of both studies are given in Chapter 3. As an outcome of the previous chapters, the 2'3HF ligand is well understood and its metal complexes can be studied. This is finally done in Chapter 4, which allows to revisit results on the morin-cation systems.

The second research subject is entirely new to the team and is the outcome of a collaboration with Xavier Mercier's team from the PhysicoChimie des Processus de Combustion et de l'Atmosphère laboratory (PC2A – UMR8522, Université de Lille), another Labex CaPPa laboratory. It is a hot topic in flame chemistry: the elucidation of the soot inception process. Indeed, soot is a solid material formed from the incomplete combustion of fuels through complex and still debated mechanisms. It is known that polycyclic aromatic hydrocarbons (PAHs) play a key role in the process, but the transition from such gaseous molecules to a graphite-like solid is still an

unelucidated topic. Among the experimental tools available in laboratories to unravel the mechanism of soot nucleation is the Laser-Induced Fluorescence technic (LIF). Interestingly, when probing the soot inception zone of laboratory flames, LIF measurements show unidentified signals that are thought to be due to intermediate species before soot formation. The collaboration started with the suggestion from Xavier Mercier's team of PAH-based structures to explain the origin of the signals. The study was performed exclusively using quantum chemical calculations to study molecular structures and compute their electronic spectra. While there is an abundance of literature concerning the association of PAHs as an initial process of soot formation, quantum chemical methods have mostly been used to calculate thermodynamic and kinetic quantities. To our knowledge, this is the first time that they are used to attempt to reproduce spectral observations in flames and the originality of this work lies in this aspect.

Part II of the manuscript presents the results of our theoretical approach. Chapter 1 gives an overview of soot, and introduces the complex spectroscopic properties of PAHs. In this chapter, the different hypotheses proposed for the formation of soot and the spectral observations made in flames are also presented. One of the oldest hypotheses to explain soot formation is the physical stacking of PAHs to form bigger clusters until apparition of a primary soot particle. To explore this hypothesis, physical dimers and trimers of small PAHs were studied. The results are presented in Chapter 2 and discussed in terms of the implications of such physical systems to explain LIF measurements. Because the physical oligomers appear unstable due to the large entropic disadvantage of dimerization, covalent dimers were also investigated and the results are presented in Chapter 3. Neither physical nor chemical oligomers were found to account for the experimental LIF data meaning that a third hypothesis had to be explored. To this aim, a promising hypothesis of radical PAH-based species was studied and is presented in Chapter 4.

PART I.

Structural and optical properties of
2',3-dihydroxyflavone and its metal
complexes

CHAPTER 1.

Introduction on flavonoids and methods

This chapter is dedicated to introducing the chapters of Part I by giving the context and general definitions on organic matter, flavonoids and the studied cations. It also contains introductions on the computational and experimental methods used throughout Part I.

The description of the methods is followed by a listing of technical details on the technics used in the following chapters. Also, additional introductions and more advanced literature reviews are given in each chapter, depending on the subject.

1. From organic matter to its building blocks

1.1. Organic matter

1.1.1. General knowledge

Interest in the chemistry of organic substances in soils, sediments and natural water is not new but has grown in recent years with major advances in methodology and knowledge of the role of organic substances in many environmental processes. Humic substances (HS) are ubiquitous in the natural environment and are found wherever organic matter, that refers to carbon-based materials, is being decomposed. HS are heterogeneous mixtures and often ill-defined but the scientific community working on these substances has come up with a classification into three fractions according to their aqueous solubility. [2, 3] Fulvic acids, the smallest size members of the HS family, are soluble under all conditions of pH. On the other hand, humic acids consist of the fraction of HS that is precipitated from aqueous solution when the pH is decreased below 2. Finally, humins, the most coal-like HS family members, are insoluble in water at any pH. This classification is arbitrary because HS solubilities depend on their molecular weight, their state of aggregation, and their metal and mineral interactions. Moreover, it is important to mention that these fractions do not represent pure compounds but each of them consists of a complicated and heterogeneous mixture of organic substances, which furthermore, evolve over time.

Although their structural definition is not clear, humic acids are considered less hydrophilic and bigger than fulvic acids. Overall, both contain functional groups such as phenols, carboxylic acids, quinones, and catechols. [4] A hypothetical structure of a part of humic acid was constructed by assembling, totally randomly, recurrent fragments which are experimentally observed in HS. The structure, presented on Figure I. 1, shows the variety of functional groups that can be found in these macromolecules.

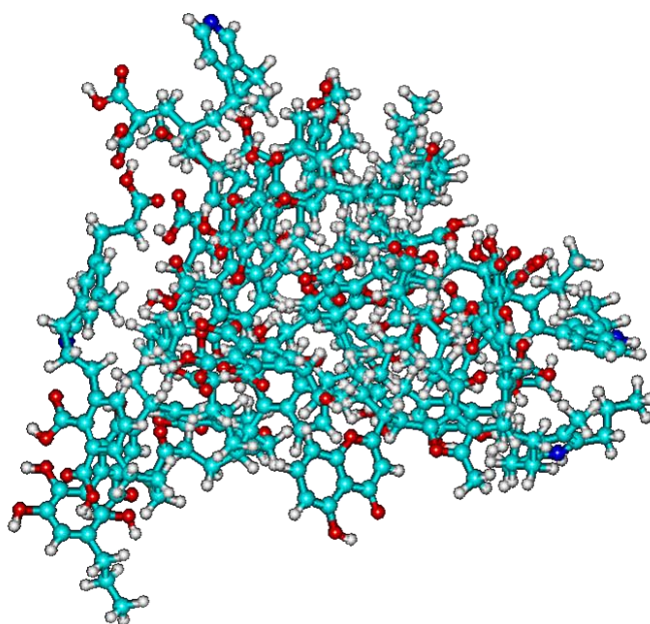


Figure I. 1: Typical structure of a humic acid

1.1.2. Importance for the present study

HS have numerous interesting properties which explains their extensive study from the environmental science community, [4] among which are anti-inflammatory, [5] antiviral, [6] antibacterial, [7] pollution remediation properties.

This latter property is particularly interesting in the context of this thesis and partially related to Part II. Indeed, HS have shown their ability to contribute to the removal of toxic chemicals such as polycyclic aromatic hydrocarbons (PAHs) from the environment. The operating mode of HS for PAH decontamination appears to be the increase of their solubility in water by weak interaction with aliphatic chains of HS. [8] This was evidenced for PAHs such as methylated naphthalenes, [9] fluorene, [10] and phenanthrene, [11] and it was observed that dissolved organic matter increased the biodegradation of pyrene and phenanthrene. [12] More interesting for Part I of this thesis are their heavy metal pollution remediation properties. It was shown that HS could bind metal cations. Their carboxylic and phenolic functional groups are thought to be responsible for this complexing power. [13] This property has been studied extensively regarding the ability of HS to remove heavy metals from soil and water. [14, 15] Also, their ability to bind Ca(II), Zn(II) and Mn(II) cations (among others) increases their bioavailability and help plants absorb them as nutrients. [16]

The study of the complexing properties of HS would aim

- To determine the nature of the complexation or chelation sites involved in the retention of metals
- To compare the complexing powers of these sites with respect to different metals
- To observe the influence of physicochemical conditions on the complexation processes
- Finally, to obtain a better understanding of the interactions at the microscopic level between the various sites in competition within the HS and the different metal cations in the natural environment.

Such study is a real challenge in view of the complexity of this macromolecular system. Thus, it is conceivable to limit the study to small fragments that have similar chemical functions. This way, the study of the complexation processes becomes possible both from an experimental and theoretical point of view and gives results that become exploitable. However, extrapolation of the results obtained from model molecules to HS requires a judicious choice of the fragments. Thus, a good compromise would be the use of HS precursors, ubiquitous in the plant kingdom.

Polyphenols are a large group of naturally occurring molecules commonly found in plants. They have been extensively studied for several decades due to their large spectrum of beneficial effects on health. More than 10,000 polyphenols have been identified in nature. [17] There is a great diversity in the chemical structure of polyphenols but their common characteristic is the presence of phenolic hydroxyl group. Polyphenols are subdivided into several families of which the two most important are the phenolic and cinnamic acids and flavonoids.

1.2. The flavonoid family

1.2.1. Biological properties

Flavonoids are widely found in plants as secondary metabolites, mostly in the form of glycosides that enhances their hydrophilicity. [18–20] Among them are famous compounds such as:

- Quercetin: found in vegetables, fruits, etc.
- Rutin: found in green tea, apples, berries, peaches, etc.
- Hesperidin: found in oranges, lemons, etc.
- Apigenin: found in chocolate
- Luteolin: found in artichoke, basil, celery and parsley. [21]

Their effect on human health is the largest field of research on their subject as they have numerous biological applications due to their properties, among which are neuroprotective, [22] anticarcinogenic, [23–25] antimicrobial, [26, 27] antiviral, [28] antioxidant, [29] and hepatoprotective. [30] Promising effects against Alzheimer's disease have been evidenced. [29, 31, 32] Also, flavonoids have been thought to be responsible for the “French paradox” as consumption of red-wine was found to be negatively correlated with cardiovascular diseases, although it is a controversy belief. [33–36]

1.2.2. Optical properties

Another important topic on their subject is their optical properties and, in particular, their ability to absorb UV radiation. Indeed, the UV-B radiations (280 – 315 nm) induce a large variety of responses in plants, and can inflict DNA damage. [37, 38] Fortunately, plants have the ability to synthesise UV-absorbing pigments to protect them from UV-B. It was for example found that the ability to synthesise kaempferol was a requirement for a proper protection of Arabidopsis plants against UV-B exposure. [39] Also, the exposition of Brassica napus to UV-B radiations has been shown to increase concentrations of kaempferol and quercetin glycosides by 150% compared to control plants. [40] Overall it is systematically observed that mutant plants with reduced protective pigments are more subject to DNA damage. [37] This is still a hot topic in the literature because UV radiance is expected to increase in the future due to climate change. [41]

1.2.3. Classification into sub-groups

Flavonoids are all composed of the A and C phenyl rings, as well as the B ring that can freely rotate. They are classified into sub-groups among which are anthocyanins,

flavanones, flavones, and isoflavonoids, of basic carbon skeleton shown on Figure I.

2

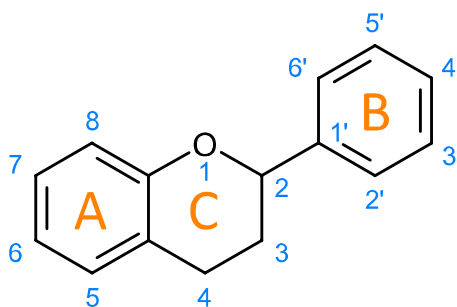


Figure I. 2: The basic carbon skeleton of flavonoids and atomic numbering (IUPAC nomenclature)

In this thesis, a focus is put on flavones, whose basic structure is depicted on Figure I. 3. Flavones have an α,β -unsaturated ketone on positions 4, 3 and 2 and are composed of a chromone moiety (*i.e.* the A and C rings) and a phenyl ring (the B ring). Substituting the flavone molecule on position 3 by a hydroxyl group yields the 3-hydroxyflavone (3HF), which is the basic structure of the flavonols sub-group. Some 3HF derivatives include the extensively studied quercetin, kaempferol and morin, whereas the removal of hydroxyl group 3 on quercetin and kaempferol yields luteolin and apigenin, respectively.

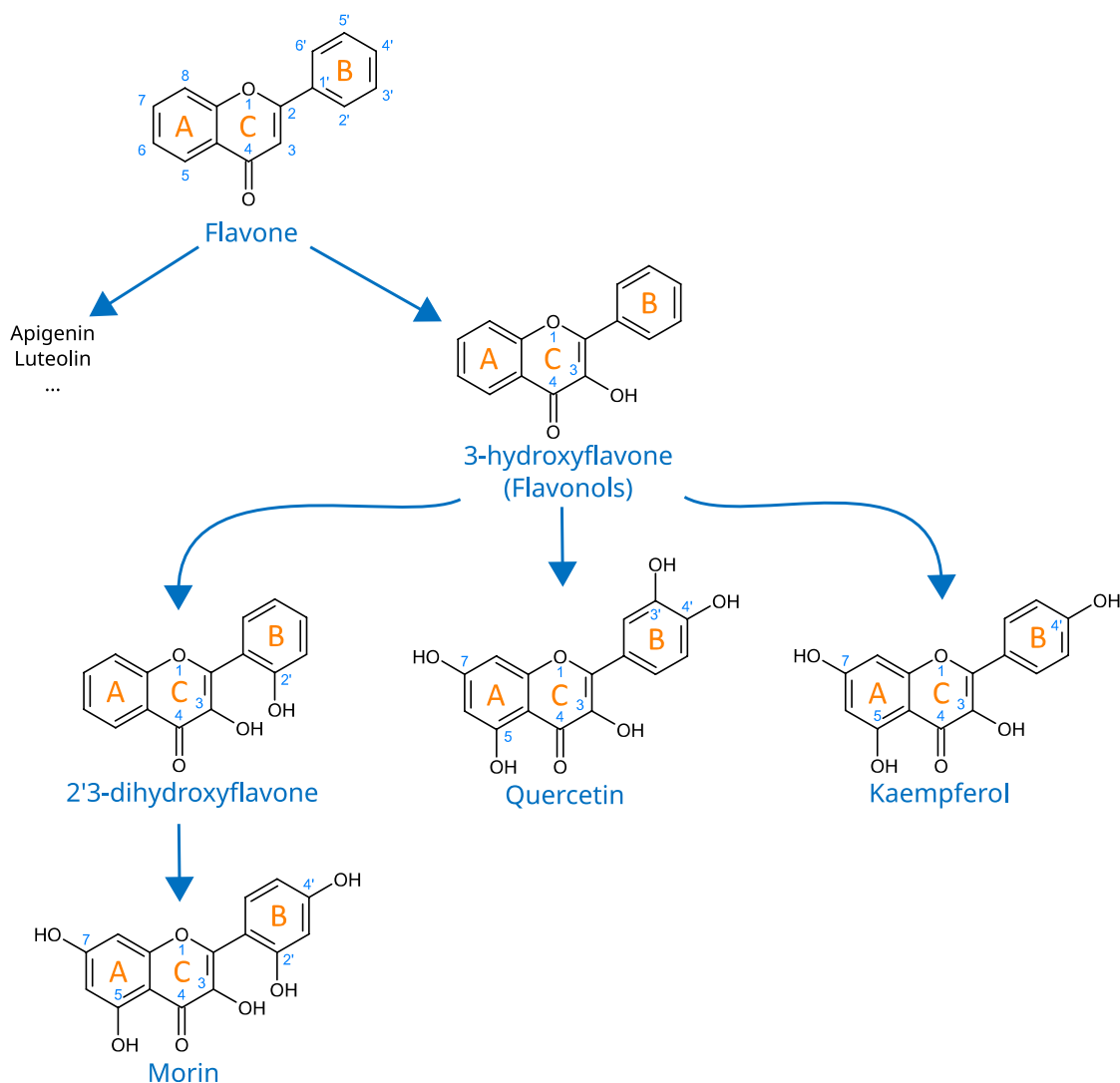


Figure I. 3: The flavones sub-group of flavonoids. The atom and ring labelling is that of IUPAC

1.2.4. 3-hydroxyflavone

3HF has been and is still being extensively studied in many fields of research despite being the simplest flavonol. Its colour depends on pH, as it is yellow in basic medium, but absorbs only UV light at a lower pH. It exhibits a dual fluorescence that was first accurately explained by Kasha and Sengupta, [42] who attributed the violet fluorescence to the normal species, and the green one to a proton-transferred (PT) tautomer, depicted on Figure I. 4.

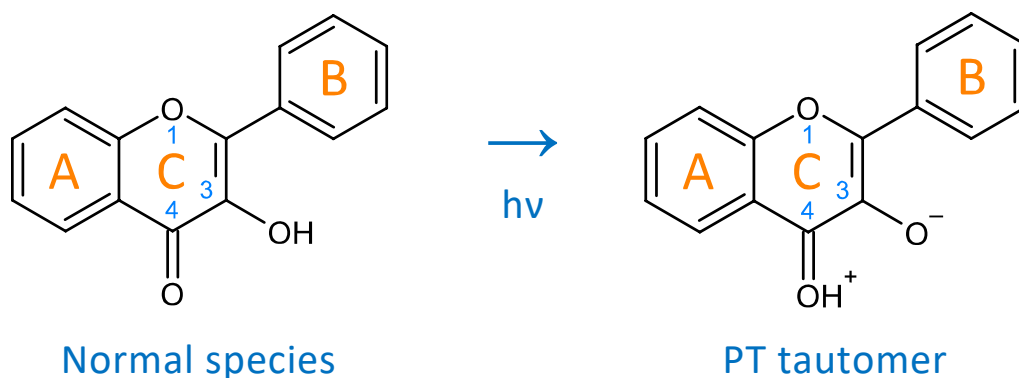


Figure I. 4: Representation of the PT tautomer obtained upon excitation of 3HF

This was confirmed later on, and the mechanism of the excited-state intramolecular PT (ESIPT) has been extensively studied ever since. [43–45]

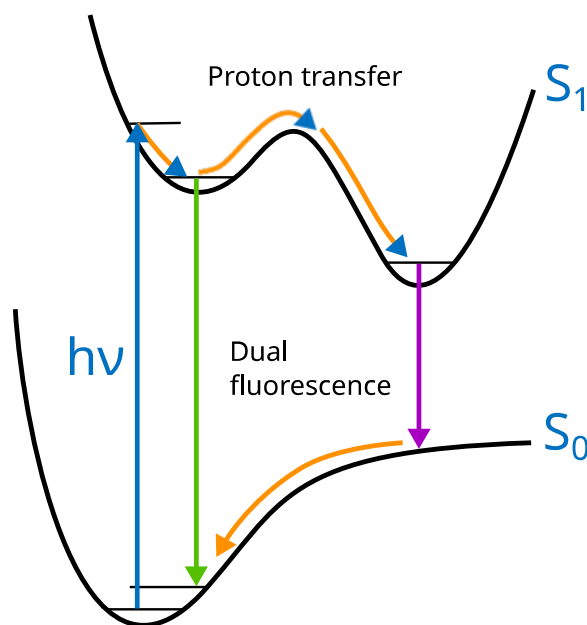


Figure I. 5: The potential energy scheme of an ESIPT

The energy profile of a typical ESIPT mechanism is represented on Figure I. 5. The process is usually considered adiabatic although other excited-states (ES) can be implied in the mechanism. It is an ultra-fast phenomenon occurring at a sub-picosecond timescale, associated with low energy barriers. The mechanism roots in the enhanced basic character of the carbonyl upon photo-absorption, which induces an intramolecular acid-base reaction. [46] In the ground-state (GS), the PT tautomer might be unstable (as depicted on the scheme), in which case the back PT would happen as soon as deexcitation happens.

The ESIPT processes usually involve electronic rearrangements, which tends to be associated with large Stokes shifts observed on the electronic spectra. They are also usually highly dependent on the hydrogen-bond (HB) donating and accepting capabilities of the solvent. [47] For example, it was found that adding stoichiometric quantities of HB donating solvents to 3HF containing solid argon-matrices inhibited the PT process and enhanced the normal form fluorescence. [48]

The interesting photophysics of 3HF and its derivatives are valuable and are exploited as fluorescent probes in a wide variety of fields such as materials chemistry [49, 50], the quantitation of biomolecules, [51, 52] and bioimaging, [53, 54] their operating mode being the high dependence of their fluorescence spectrum on their physicochemical environment.

1.2.5. Complexation properties

The α -hydroxyketone functional group (Figure I. 6) not only has interesting photophysics, but is also a powerful bidentate site for the chelation of metal cations. It has been shown that the chelation of metal cations often improved their antioxidant properties. [55, 56] So, research groups have put emphasis on elucidating the structure of metal-flavonoid complexes.

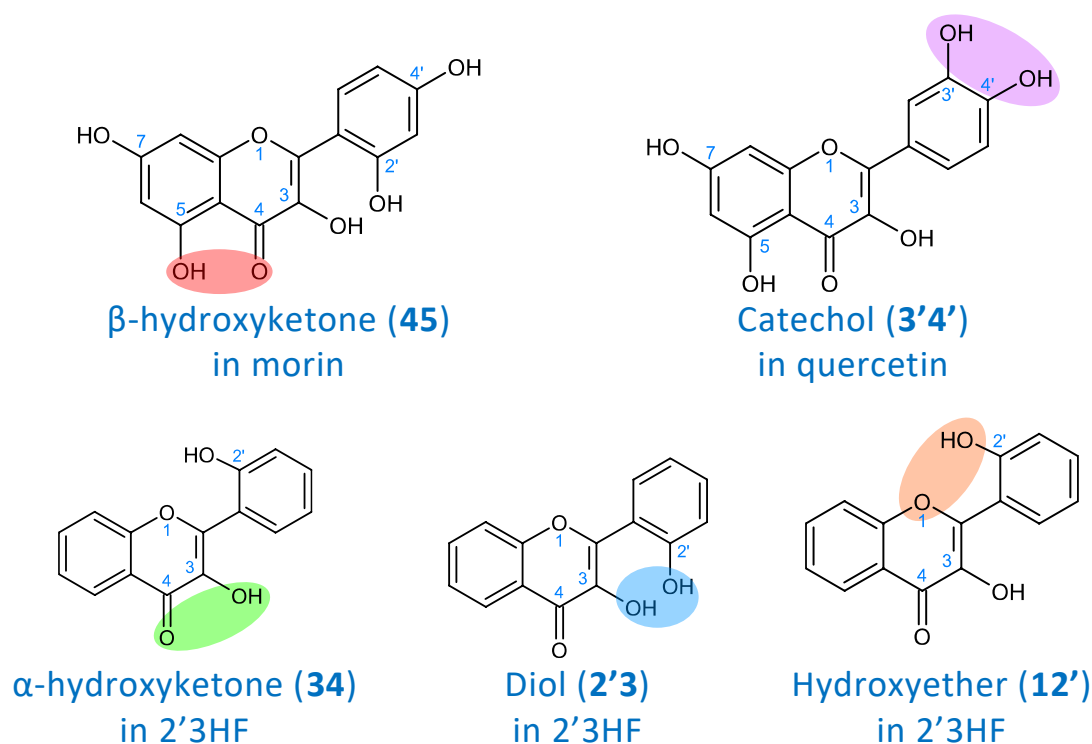


Figure I. 6: Some of the most important binding sites in flavonoids

Some of the most common binding sites for cations are shown on Figure I. 6. The binding in a monodentate mode is generally not favoured, so the study presented herein focuses only on the bidentate sites. Most flavonoids have several sites available and, for example, morin can bind cations on the β -hydroxyketone (**45**), α -hydroxyketone (**34**), diol (**2'3**), and hydroxyether (**12'**) sites, as shown on Figure I. 6, where the fixation sites are termed according to their atom numbers.

On top of the cation position, the protonation state of hydroxyl groups also matters as the cation often competes with protons to bind on the site.

Finally, the stoichiometry of the complex must be considered as it is common to observe the binding of two cations on a single ligand or, on the contrary, the binding of multiple ligands to a single cation. For example, 3HF has only one binding site (**34**) but it can form **1:2** complexes with Al(III), whereas quercetin can bind two Al(III) simultaneously on **34** and the catechol (**3'4'**) to obtain **2:1** complexes (with the stoichiometry given by the **metal:flavonoid** notation used throughout this thesis), as shown on Figure I. 7. [57, 58]

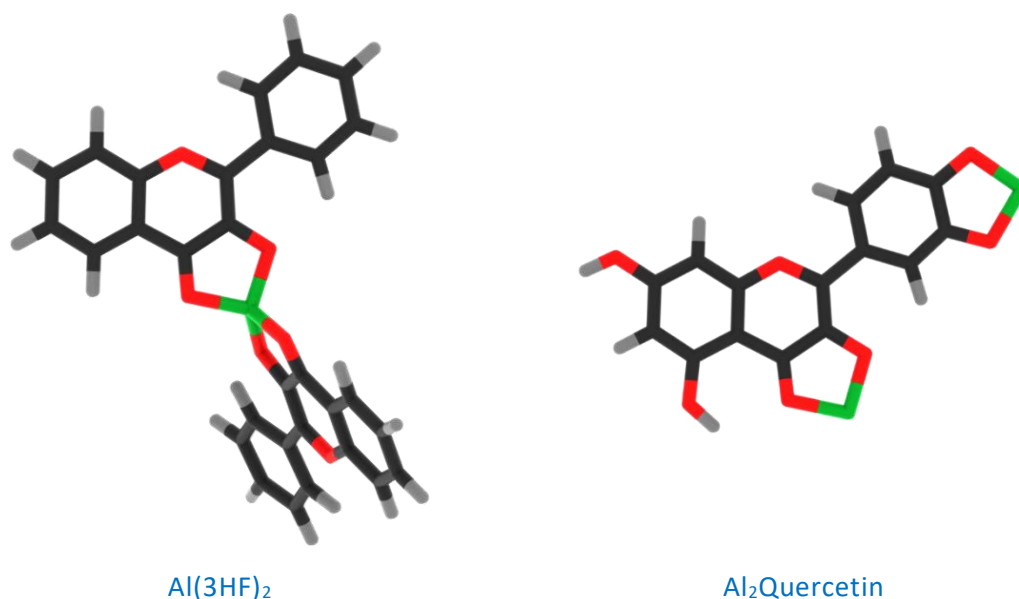


Figure I. 7: Depiction of **1:2** and **2:1** complexes that Al(III) can form with 3HF (left) and quercetin (right) according to references [57] and [58], respectively

The determination of the preferential fixation site of a metal cation within a multisite ligand, as well as the comparison of complexing powers towards different metal cations is an important research axis within our team. It is in this perspective that we have highlighted the unexpectedly large complexing power of morin due, in particular, to the simultaneous presence of hydroxyl groups in positions 2' and 3. [1,

59, 60] To better understand the influence of this structural feature, we focused our attention in this thesis on a simpler molecule bearing only the aforementioned hydroxyl groups: 2',3-dihydroxyflavone (2'3HF).

The literature of metal-flavonoid complexes will be detailed in the Chapter 4 of this part which is entirely dedicated to the study of 2'3HF complexes. However, a small introduction on the studied metal cations is presented hereafter.

2. The studied metals

2.1. The choice of metal cations

The vast majority of research groups found that polyvalent cations bonded flavonoids in a bidentate fashion rather than monodentate. [19, 20] This is corroborated by experimental observations (often backed-up by computational evidences) using X-ray crystallography, [61, 62] NMR, [63, 64] and infrared, Raman and UV-visible spectroscopies. [1, 57, 58, 65–70] Thus, it was chosen to study only divalent cations and to focus our attention on bidentate chelating modes. As a follow up of the previous thesis work on morin, [60] the three period four species that were chosen are Ca(II), Zn(II), and Mn(II). This allowed to assess the effect of the differences in electron configurations since Ca^{2+} has no $3d$ electrons, whereas the $3d$ subshells of Zn^{2+} and Mn^{2+} are full and half-full, respectively.

On top of the interesting electron configuration range that the chosen encompass, they also play important roles in natural media, some of which are reported hereafter.

2.2. Zinc, manganese and calcium

Although zinc is an essential nutrient, its inadequate supply can have a negative impact on human health and its presence in natural media and food must be monitored carefully. [71] In environmental sciences, zinc is considered a “heavy metal” and is one of the most important pollutants in water, alongside lead and mercury. [72, 73] Amongst possible health issues associated with heavy metal exposure such as zinc are carcinogenicity [74] and the inducing of cognitive deficiencies and cardiovascular diseases. [75–78]

Manganese is also a nutrient, [79] but can become a pollutant in case of excessive anthropogenic rejections. This is the case for marine wildlife, [80] but also for human health and it was for example observed to be a risk factor for Parkinson’s disease. [81, 82]

Both (Zn(II) and Mn(II)) pollutants can be found in water industrial discharges, [83–85] or more common wastes, [86] but also in the air in the form of aerosols, [87] and

soil. [78, 88, 89] Unfortunately, heavy metal exposures are expected to increase in the near future due to climate change. Indeed, extreme weather conditions tend to mobilize pollutions contained in sediments, as during the flood of the Seine in 2016. [90, 91]

Calcium is an alkaline earth metal and one of the most abundant elements in the Earth crust. Its presence in soil supports the growth of plants which can absorb it via the xylem as Ca^{2+} or in a chelated form. [92]

Thus, it is found in the human diet and is the most common metal in the human body. It plays a central role in skeletal mineralization, [93] as well as in other bio-chemical mechanisms such as calcium signalling, [94] and, for example, deficiencies in the mitochondrial handling of Ca^{2+} is thought to play a major role in neurodegenerative diseases such as the Alzheimer's disease. [95]

3. Computational methods

3.1. Density Functional Theory (DFT)

3.1.1. General knowledge

DFT is nowadays considered indispensable considering its high performance over cost ratio. It is in practice applicable to “large” systems and has been extensively used throughout this thesis. The use of DFT for the calculation of any molecular system first requires the choice of a density functional approximation (DFA). A brief introduction on Kohn-Sham-DFT (KS-DFT) is given herein, in order to better explain the choices that were made. [96]

In the context of DFT, the electronic energy is written as a functional of the electron density ρ

$$E[\rho] = T[\rho] + V_{ee}[\rho] + V_{\text{ext}}[\rho] \quad (1)$$

With $T[\rho]$ the kinetic energy of the electrons, $V_{ee}[\rho]$ the electron-electron interaction, and $V_{\text{ext}}[\rho]$ the external potential due to the nuclei.

Unfortunately, $T[\rho]$ and $V_{ee}[\rho]$ are unknown. In 1964, Kohn and Sham reintroduced the use of non-interacting electron orbitals to obtain an approximation of the kinetic and electron-electron interaction energies, and formulated the main equation of KS-DFT

$$\left(-\frac{1}{2}\nabla^2 + v_{\text{KS}}(\mathbf{r})\right)\phi_i(\mathbf{r}) = \epsilon_i\phi_i(\mathbf{r}) \quad (2)$$

$$\left(-\frac{1}{2}\nabla^2 + v_{\text{ext}}(\mathbf{r}) + \int \frac{\rho(\mathbf{r}')}{|\mathbf{r}-\mathbf{r}'|} d\mathbf{r}' + v_{\text{xc}}(\mathbf{r})\right)\phi_i(\mathbf{r}) = \epsilon_i\phi_i(\mathbf{r}) \quad (3)$$

in which $v_{\text{ext}}(\mathbf{r})$ is the external potential, $-\frac{1}{2}\nabla^2$ the kinetic energy operator, $\int \frac{\rho(\mathbf{r}')}{|\mathbf{r}-\mathbf{r}'|} d\mathbf{r}'$ the Hartree potential describing the electron-electron Coulomb repulsion and $v_{\text{xc}}(\mathbf{r})$ the exchange-correlation potential. The equation is an eigenvalue equation associated with the Kohn-Sham orbitals $\phi_i(\mathbf{r})$ and their energies ϵ_i . The KS orbitals

are those of non-interacting electrons of a fictitious system in the field $v_{xc}(\mathbf{r})$ defined so that

$$\rho(\mathbf{r}) = \sum_i^N |\phi_i(\mathbf{r})|^2 \quad (4)$$

With $\rho(\mathbf{r})$, the electron density of the real system.

The kinetic energy of the real system $T[\rho]$ is obtained by correcting the kinetic energy of the fictitious system $T_s[\rho]$ by a term contained in $v_{xc}(\mathbf{r})$ (written $T_{(xc)}[\rho]$ hereafter) so that

$$T[\rho] = T_s[\rho] + T_{(xc)}[\rho] \quad (5)$$

$$T[\rho] = -\frac{1}{2} \sum_i^N \int \phi_i^*(\mathbf{r}) \nabla^2 \phi_i(\mathbf{r}) d\mathbf{r} + T_{(xc)}[\rho] \quad (6)$$

And similarly, the electron-electron interaction of the real system $V_{ee}[\rho]$ is obtained by correcting the classical interaction energy $V_H[\rho]$ by a term contained in $v_{xc}(\mathbf{r})$ (written $V_{(xc)}[\rho]$ hereafter) so that

$$V_{ee}[\rho] = V_H[\rho] + V_{(xc)}[\rho] \quad (7)$$

$$V_{ee}[\rho] = \frac{1}{2} \int \frac{\rho(\mathbf{r}_1)\rho(\mathbf{r}_2)}{|\mathbf{r}_1 - \mathbf{r}_2|} d\mathbf{r}_1 d\mathbf{r}_2 + V_{(xc)}[\rho] \quad (8)$$

Ultimately, the energy of a molecular system can be written as

$$E[\rho] = T_s[\rho] + V_{\text{ext}}[\rho] + V_H[\rho] + E_{xc}[\rho] \quad (9)$$

With $E_{xc}[\rho]$, the exchange-correlation functional defined as

$$E_{xc}[\rho] = T_{(xc)}[\rho] + V_{(xc)}[\rho] \quad (10)$$

The $E_{xc}[\rho]$ term is the only unknown for the determination of the total energy and one has to choose an approximation, the DFA. The DFA must correct the classical electron-electron interaction by exchange and correlation terms, as well as the kinetic-energy.

The DFAs that have been developed over the years can be classified according to their complexity and some common approximations, including the ones used in this work, are introduced hereafter.

3.1.2. Local Density Approximation (LDA)

In the LDA scheme, the $E_{xc}^{LDA}[\rho]$ term is taken to be the analytic forms of $E_x^{HEG}[\rho]$ and $E_c^{HEG}[\rho]$ found for the homogeneous electron gas (HEG), but applied to density $\rho(\mathbf{r}) \neq \rho_{HEG}(\mathbf{r})$.

$$E_{xc}^{HEG}[\rho] = E_x^{HEG}[\rho] + E_c^{HEG}[\rho] = \int \rho_{HEG}(\mathbf{r}) \epsilon_{xc}^{HEG}(\rho_{HEG}(\mathbf{r})) d\mathbf{r} \quad (11)$$

so that

$$E_{xc}^{LDA}[\rho] \approx \int \rho(\mathbf{r}) \epsilon_{xc}^{HEG}(\rho(\mathbf{r})) d\mathbf{r} \quad (12)$$

LDA is the first DFA that was suggested and it met a considerable enthusiasm from the scientific community. Its success results from its exactness in the limit of slowly varying or high-density systems which resulted in its widespread application, especially in solid-state physics. [97]

3.1.3. Generalized Gradient Approximation (GGA)

In the GGA scheme, a dependence of the functional on the gradient of the density is introduced to verify some exact properties so that [98]

$$E_{xc}^{GGA}[\rho] \approx \int \rho(\mathbf{r}) \epsilon_{xc}(\rho(\mathbf{r}), \nabla\rho(\mathbf{r})) d\mathbf{r} \quad (13)$$

The mathematical forms of GGAs are more complicated but they usually outperform the LDA scheme. Some examples of GGAs are the exchange and correlation functionals B88 and LYP, respectively, [99, 100], as well as PBE which has an exchange and a correlation term. [101, 102]

3.1.4. Global Hybrid (GH)

Hartree-Fock theory allowing the exact computation of the exchange energy of a system, it has quickly been suggested to use it in the DFAs. The first suggested idea was to use a functional of the form

$$E_{xc}[\rho] = E_X[\rho] + E_C[\rho] \quad (14)$$

With $E_X[\rho]$ being the exact exchange energy of a Kohn-Sham Slater determinant and $E_C[\rho]$ being everything else not included. However, the modification does not systematically improve the results. The reason is that the $E_{xc}[\rho]$ term cannot truly be split into two pure exchange and correlation terms (the name XC is misleading), and only the XC correction as a whole has a physical meaning. [103]

Using the adiabatic connection formula, A. D. Becke suggested a less drastic correction to GGAs by some proportion of $E_X[\rho]$ using [104]

$$E_{xc}[\rho] = (1 - c_X)E_{xc}^{GGA}[\rho] + c_X E_X[\rho] \quad (15)$$

With the c_X parameter referred to as the exact exchange proportion included (or the Hartree-Fock exchange although it is not strictly equal to the true Hartree-Fock exchange), usually close to 25%. [105]

Some common GHs include B3LYP [99, 100, 106] and PBE0, [101, 102, 107] the latter being used throughout this thesis.

3.1.5. Range-Separated Hybrid (RSH)

GH functionals have deficiencies, especially in TD-DFT, such as when describing Rydberg states or charge-transfer excitations. The errors originate from not reaching a r^{-1} asymptote for the exchange potential as expected. “Long-range Corrected” and “Range-Separated” hybrids (named RSHs in this thesis regardless of their LC or RSH mathematical implementation) have been suggested to correct this behaviour. [108, 109] The idea is to split the exchange potential into short- and long-range parts, the long-range part having more exact exchange than the short-range part (100% exact exchange in the case of the LC scheme). Thus, the two parts are linked by the means of an error function. Two RSHs used in this thesis include CAM-B3LYP [108] and LC- ω PBE. [110, 111]

3.1.6. Double Hybrid (DH)

The DH scheme extends the GH logic to the correlation energy and applies a second-order Møller-Plesset (MP2) correlation correction to it. [112] This is done very simply by using

$$E_{xc}[\rho] = (1 - c_C)E_C^{GGA}[\rho] + c_C E_C^{PT2}[\rho] + (1 - c_X)E_X^{GGA}[\rho] + c_X E_X[\rho] \quad (16)$$

with c_C and c_X , the parameters that control the amounts of perturbative correlation and exact exchange, respectively. In the equation PT2 stands for perturbative second-order correlation. An example of DH functional used in this work is B2PLYP with $c_C = 27\%$ and $c_X = 53\%$. [112]

3.2. Time-Dependent Density Functional Theory (TD-DFT)

By introducing a small time-dependent perturbation at time t_0 to a system in its GS, it is possible to remain in the linear-response regime. This is the approach to TD-DFT that was used throughout this thesis and is presented here. [96]

When applying a small time-dependent perturbation, the external potential becomes

$$v_{\text{ext}}(\mathbf{r}, t) = v_{\text{ext}}^{(0)}(\mathbf{r}) + v_{\text{ext}}^{(1)}(\mathbf{r}, t) \quad (17)$$

we obtain the time-dependent Kohn-Sham equation

$$\left(-\frac{1}{2}\nabla^2 + v_{\text{KS}}(\mathbf{r}, t) \right) \phi_i(\mathbf{r}, t) = i \frac{\partial}{\partial t} \phi_i(\mathbf{r}, t) \quad (18)$$

$$\left(-\frac{1}{2}\nabla^2 + v_{\text{ext}}(\mathbf{r}, t) + \int \frac{\rho(\mathbf{r}', t)}{|\mathbf{r} - \mathbf{r}'|} d\mathbf{r}' + v_{xc}(\mathbf{r}, t) \right) \phi_i(\mathbf{r}, t) = i \frac{\partial}{\partial t} \phi_i(\mathbf{r}, t) \quad (19)$$

The many-body system will react and the density will be a Taylor series that can be approximated to its first order such that

$$\rho(\mathbf{r}, t) = \rho^{(0)}(\mathbf{r}) + \rho^{(1)}(\mathbf{r}, t) \quad (20)$$

With $\rho^{(1)}(\mathbf{r}, t)$, the linear response of the electron density on the time-dependent potential. The term $\rho^{(1)}(\mathbf{r}, t)$ is related to the perturbation through the density-density response function $\chi(\mathbf{r}, t; \mathbf{r}', t')$ such that

$$\rho^{(1)}(\mathbf{r}, t) = \int \int \chi(\mathbf{r}, t; \mathbf{r}', t') v_{\text{ext}}^{(1)}(\mathbf{r}', t') d\mathbf{r}' dt' \quad (21)$$

Which is a result that is obtained for the fully interacting system. By construction, the Kohn-Sham system has the same density, and thus we have

$$\rho^{(1)}(\mathbf{r}, t) = \int \int \chi_{\text{KS}}(\mathbf{r}, t, \mathbf{r}', t') v_{\text{KS}}^{(1)}(\mathbf{r}', t') d\mathbf{r}' dt' \quad (22)$$

Where the Kohn-Sham density-density response function was introduced. In frequency space, it is given by Green function theory as

$$\chi_{\text{KS}}(\mathbf{r}, \mathbf{r}', \omega) = \sum_{j,k} (f_k - f_j) \frac{\phi_j(\mathbf{r})\phi_k^*(\mathbf{r})\phi_j^*(\mathbf{r}')\phi_k(\mathbf{r}')}{\omega - (\epsilon_j - \epsilon_k) + i\eta} \quad (23)$$

The response function involves a sum over all unperturbed (no time-dependence) occupied and unoccupied Kohn-Sham orbitals, their occupation numbers f_k and f_j , as well as their energies ϵ_k and ϵ_j . If k and j are both occupied or both unoccupied, the contribution is zero, and if the difference in energy between the orbitals matches the frequency of the perturbation, the response goes to infinity (it is a pole), which represents a resonance with the incoming perturbation.

3.3. Polarizable Continuum Model (PCM)

In order to simulate a solvated system, it is necessary to take into account the interactions of the solute with the closest solvent molecules, as well as the bulk background. To this end, these approaches can be considered:

- The including of explicit solvent molecules in the quantum-mechanical (QM) calculation
- The adoption of a quantum-mechanics-mechanical-mechanics (QMMM) approach, in which many solvent molecules are included, but only the solute is treated quantum mechanically as well as some close solvent molecules
- The use of a continuum model such as PCM

The PCM is based on classical electrostatics. The solute is put into a cavity of surface $\sigma(\mathbf{s})$ and its charge distribution represented by $\rho_{\text{M}}(\mathbf{r})$. This way, it is possible to describe the electrostatic potential as that of the solute and the apparent surface charge

$$V(\mathbf{r}) = V_{\text{M}}(\mathbf{r}) + V_{\sigma}(\mathbf{r}) \quad (24)$$

In this thesis, the IEFPCM implementation in the Gaussian 16 software is used, in which the solvent reaction field is made self-consistent with the potential of the solute (SCRF). [113]

For the ES calculations, the solvent response to the change of electronic state by the solute must be taken into account. It can be decomposed into two fast and slow components. The electron distribution response is a fast process that can occur during the time-scale of an electronic excitation, whereas the nuclei re-orient in much longer timescales. In this thesis, vertical electronic excitations were computed in the “non-equilibrium” regime in which the fast component of the solvent response is equilibrated with the ES density using a linear response formalism, whereas the slow component is kept equilibrated with the GS conformation. On the contrary, the “equilibrium” regime was used whenever vertical electronic emissions were described, which corresponds to the equilibration of both components with the ES.

In Chapter 3, the performances of a full QM approach using sampling from molecular dynamics are compared to the PCM.

3.4. Molecular dynamics (MD)

MD denotes a commonly used method in which a molecular system in an initial state is allowed to evolve according to the numerically solved Newtonian equations of motions. Most commonly, the forces applying on the nuclei are calculated using a “force field”. This approach, used once in this thesis, has the advantage of being computationally cheap so that large systems can routinely be simulated for nanoseconds. However, it has the major drawbacks of not being able to describe chemical reactivity (except when using reactive force-fields [114]), being highly parametrized, and to not include electronic polarization effects.

It is thus natural that *ab initio* MD (AIMD) technics were developed, hoping to solve such deficiencies, at the cost of much longer computation times. In AIMD, the forces are computed at each timestep from electronic structure calculations, for which it is assumed that the Born-Oppenheimer approximation is valid and that the nuclei can be treated classically. This way, the nuclei dynamics are given by the equation of motion [115]

$$M_i \ddot{\mathbf{R}}_i = -\nabla_i E_0(\mathbf{R}) \quad (25)$$

in which M_i is the mass of nuclei i , and $E_0(\mathbf{R})$ is the GS energy at the nuclear conformation \mathbf{R} . The energy $E_0(\mathbf{R})$ can be obtained by any computational method, and most commonly, by DFT. More precisely, the calculations performed in this work are Born-Oppenheimer molecular dynamics (BOMD), meaning that the energy is obtained by minimization at each timestep, similarly to static calculations.

As stated above, AIMD is much more computationally demanding than classical MD, and it is common to use simple GGAs such as PBE or BLYP with small basis-sets to simulate few hundreds of picoseconds of the dynamics of hundreds of atoms.

4. Experimental methods

4.1. Electronic spectroscopies

Amongst molecular spectroscopic techniques, UV-visible absorption and fluorescence emission spectroscopies are particularly well suited to the monitoring of metal cation complexation by ligands in solution. Indeed, the complexometric dosage requires the addition of a metal salt to a ligand solution which leads to an equilibrium between the free and complexed ligands. If the complexing power of the solute is low, the metal ion concentration can become large and precipitate, usually in the form of hydroxides, and perturb the measurements. While experimenting in acidic media largely limits the issue, it is often interesting to study the acid-base properties of the formed complexes, which requires an increase in pH. For this reason, in order to avoid premature precipitation, it is essential to work with the lowest possible species concentrations.

In this respect, electronic spectroscopies are the method of choice as they are very sensitive compared to other spectroscopic techniques. Unfortunately, they have the drawback of displaying limited spectral information. Indeed, when used alone, these spectroscopies provide no structural information that could shed light on the complexing site involved during metal fixation (as opposed to vibrational or NMR spectroscopies). However, as will be shown later, their coupling with quantum chemical techniques such as TD-DFT allows to make structural predictions by comparing absorption and emission wavelengths and oscillator strengths to the measured spectra.

4.2. Data treatment

A python package as well as scripts were developed to perform most experimental (and computational) data treatment. In the case of the complexometric dosages, the data were preliminarily treated by Singular Value Decomposition (SVD) and Evolving Factor Analysis (EFA).

SVD (sometimes referred to factor analysis FA) is a linear algebra technic that factorizes a data matrix \mathbf{M} into three matrices according to

$$\mathbf{M} = \mathbf{U}\mathbf{\Sigma}\mathbf{V}^* \quad (26)$$

with the diagonal of $\mathbf{\Sigma}$ containing the square-roots of the singular values of \mathbf{M} , and \mathbf{U} and \mathbf{V} containing the left- and right-singular vectors of the corresponding singular values. When used on a set of UV-visible absorption spectra obtained from a complexometric dosage, the SVD analysis yields as many eigenvalues (the rank of $\mathbf{\Sigma}$) as there are coloured species implied in the dosage. On the other hand, EFA is simply an extension of SVD, that decomposes \mathbf{M} into submatrices so that a time-dependent analysis of the rank of $\mathbf{\Sigma}$ can be performed. [116]

The ReactLabTM chemometrics software was used for the titration data fitting of Chapter 4. It offers implementations of the SVD and EFA methods through a graphics user interface. The SVD and EFA methods are model free tools and ReactLabTM then permits to suggest chemical reactions to model the experiments, which are fitted by minimizing the residuals matrix \mathbf{R} in the following equation

$$\mathbf{M} = \mathbf{CA} + \mathbf{R} \quad (27)$$

with \mathbf{M} being the data matrix, \mathbf{C} the concentration matrix, \mathbf{A} the molar absorptivities matrix. In turn, it allows to extract conditional equilibrium constants and the spectra of pure species from the experiment.

5. Technical details

5.1. Details of Chapter 2

5.1.1. Experimental details

2'3HF was purchased from Alfa Aesar. It is sparingly soluble in water and all the experiments were carried out in methanol solutions (ultrapure, spectrophotometric grade, 99.8%), also purchased from Alfa Aesar. 2'3HF concentrations were of 10^{-5} mol L⁻¹ (4×10^{-5} mol L⁻¹ for the titration experiment), with small additions of acid (HCl, from Fluka) and base (NaOH, white pellets, from Fischer Scientific) solutions. Water was obtained by a Millipore water purification system at 18 MΩ cm⁻¹.

A Hanna pH meter was used for apparent pH measurements. UV-visible spectra were recorded with a double beam Cary 100 (Varian) spectrometer with a spectral resolution of 1 nm. The excitation and emission fluorescence spectra were recorded with a Fluorolog (Horiba) spectrofluorimeter with a resolution of 2 nm.

5.1.2. Computational details

The Gaussian 16 software [117] was used to perform the DFT and TD-DFT calculations using the PBE0 hybrid functional along with Pople's 6-311+G(d,p) basis-set [118–121] and the PCM to simulate the solvent. The optimized geometries were confirmed as minima on the potential energy surface by analytically calculating the Hessian and verifying that no imaginary frequencies were obtained.

A relaxed energy scan was performed in the GS by fixing the inter-ring dihedral angle using a 5° step, and optimising all the other coordinates. This computation has been performed using 6-311++G(d,p) basis-set. The effect of adding a diffuse function to the basis-set was also tested on several other calculations, the differences (geometrical parameters and energies) were small enough to stick to the lower level of theory for most computations.

The location of transition structures was performed using, depending on the case, either the default Berny algorithm [122, 123] implemented in Gaussian 16, or the

STQN method. [124] This was systematically followed by an IRC calculation, [125] verifying that the two obtained structures corresponded to the expected minima.

The electronic absorption spectra were reproduced by computing the required number of ESs using TD-DFT to fully describe the UV-visible domain experimentally studied. The solvent was once again described using PCM in a linear response non-equilibrium approach. The fluorescence emission energies were obtained by optimizing the first singlet ES, and computing the first transition energy, with the solvent equilibrated in the first ES.

Finally, several natural bond orbital (NBO) analyses [126, 127] were performed on the wave functions. Those analyses provided Wiberg bond indices [128] corresponding to neighbouring pairs of atoms.

5.2. Details of Chapter 3

5.2.1. Experimental details

The fluoromax (Horiba) spectrofluorimeter with a resolution of 3 nm was used for the fluorescence measurements. The UV-visible experiments were performed using the double-beam Agilent Cary 3500 spectrometer. The temperature was set and maintained at 20°C using either the functionality provided by the Cary 3500 or using an external peltier element for the fluorescence measurements.

In addition to methanol, spectrophotometric grade acetone (Sigma-Aldrich), dichloromethane (Sigma-Aldrich), DMSO (Merck Millipore), acetonitrile (Fluka) and ethanol (Alfa Aesar) solvents were used.

The water addition measurements were done by adding successive amounts of water directly into the cuvette and stirring the solution with a vortex mixer. Traces of 37% hydrochloric acid were added to the cuvette (except for dichloromethane) to avoid the observation of the anion fluorescence.

5.2.2. Computational details

The MD runs were performed using 117 MeOH molecules surrounding the solute (731 atoms in total) to match the density of a methanol-filled 20 Å periodic cubic box. The simulations were performed in the NVT ensemble.

Initial geometries

The initial geometries for the AIMD runs were generated by a 5 ns classical trajectory performed with a timestep of 2 fs. This was done using Amber 16 and the second generation General Amber Force Field (GAFF2), [129] at a temperature of 330 K that was set by a Berendsen thermostat. [130] This allowed to explore the potential energy surface of 2'3HF and its surrounding solvent molecules from which starting geometries could be extracted for the subsequent AIMD runs. Because several ring rotations were observed, eight AIMD trajectories were ran in parallel, with half of them performed on one rotamer (**A** according to the notation introduced in Chapter 2) and the other half on the other rotamer (**B**). This was necessary because leaving the potential energy well of one of the conformations was unlikely within the timespan of an AIMD run. The initial geometries were selected by looking at frames separated by 100 ps each and randomly sampling 4 **A** and 4 **B** conformations in the last 2 ns of the run.

AIMD runs

The AIMD runs were performed using the electronic structure module Quickstep [131] in CP2K. [132] As a basis set, the double- ζ polarized basis-set optimized for molecular systems was chosen with short-range diffuse functions (DZVP-MOLOPT-SR), in the Gaussian and Plane-Wave (GPW) scheme, [133] with the Goedecker-Teter-Hutter pseudopotential. [134] The 5 levels of the multi-grid were parametrized by a plane-wave cut-off of 800 Ryd, and relative cut-off of 50 Ryd. Those parameters were chosen so that both the energies and forces were converged properly. The PBE functional was chosen along with the D3 (15 Å cut-off) empirical dispersion correction. The SCF convergence criterium was set to 1×10^{-5} au. The trajectories were performed with a 0.5 fs time step in the NVT ensemble using a Nosé-Hoover chains thermostat [135] with a 1000 s^{-1} time constant. All 8 trajectories were first thermalized with a stronger thermostat.

It is known that over-structuration of the solvent can occur using GGAs such as PBE when studying systems with water as solvent. [136, 137] In this work, a methanol solution was studied meaning that the problem might also occur, which is why the temperature was set to 330 K.

Unfortunately, one of the trajectories failed to thermalize and could not be used, it has been removed from the set of trajectories. In the end, 100 ps of production data were obtained to be analysed.

Static calculations

In order to perform the static TD-DFT calculations, 500 **A** and 500 **B** conformations (according the notation introduced in Chapter 2) were randomly sampled from the ~ 200000 steps. Simulating the spectrum of 1000 geometries with 731 atoms cannot be done at a reasonable timescale with a descent theoretical framework. Thus, to lower the computational cost, only solvent molecules in the vicinity of the solute were kept, which is a selection that required the definition of 3 solvation shells:

- First shell: the methanol molecules directly interacting with 2'3HF. They were included by keeping the molecules in which the O nuclei were within 2.8 Å of any nucleus of 2'3HF (distance criterium only).
- Second shell: further away solvent molecules, whose O nuclei were within 3.6 Å of any nucleus of 2'3HF
- Third shell: methanol molecules directly interacting with the first shell. They were included by keeping the molecules whose O nuclei were within 2.8 Å of any nucleus in the first shell.

This way, the solvation cage consisted of around 13-14 solvent molecules in the vicinity of the solute. This set of conformations will be labelled as “solute and solvent” (**SAS**) in Chapter 3 and an example is shown on Figure I. 8.

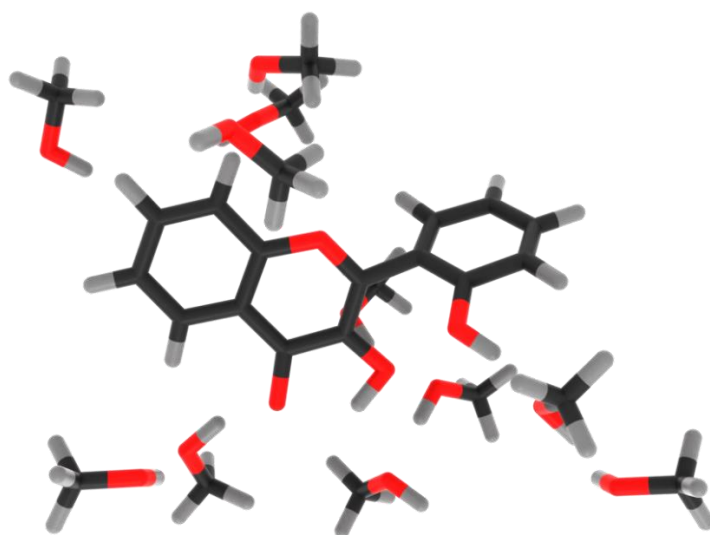


Figure I. 8: One of the selected 1000 conformations with the solvent shells

The PBE0 GH could not be chosen for the TD-DFT calculations in this chapter. Indeed, it is well-known that GHs tend to over-stabilize charge transfer ESs (due to their incorrect asymptotic behaviour), which generates artificial solute-solvent charge-transfer states in the visible part of the spectrum. As a consequence, the first ESs are physically unrealistic (often called “ghost-states”) and it is necessary to include extra ESs in the calculation, which increases the cost. [138] While the rather standard CAM-B3LYP (RSH) functional significantly improves the situation, preliminary tests showed that ghost-states still appeared at higher energies. Instead, LC- ω PBE was chosen, which completely removed the problem. Ultimately, 8 ESs of the 1000 conformations were computed which was sufficient to observe the beginning of the second absorption band of 2’3HF, in the UV range. A common drawback for the choosing of RSHs is the systematic blue-shift of electronic transitions relative to the experimental absorption maximum. Thankfully, this effect is partially neglected here. Indeed, if a set of conformations is chosen around the minimum of energy, such as using a Wigner geometry distribution or, as is the case here, an ensemble from an MD trajectory, part of the deficiency is recovered. [139] That means that LC- ω PBE will perform better in this scenario than with the more standard approach of comparing vertical transitions from the optimized geometry to the experimental spectra.

The calculations on **SAS** were done using LC- ω PBE/6-31+G(d) without PCM. Bigger basis-sets were also tested but the cost was too large compared to the improvement they offered. Also, the Tamm-Dancoff approximation was tested but degraded the results too much compared to the computational time saving.

In parallel, the same calculations were performed on a solute only ensemble without (**SO**) and with PCM (**SO-PCM**). The spectra displayed in Chapter 3 are formed from the sum of vertical electronic transitions convolved by a gaussian function of $\Gamma = 0.07$ eV width, using the following equation:

$$S_{(E)} = N \sum_n^{N_c} \sum_i^{N_{es}} f_{n,i} e^{-\frac{(E-E_{n,i})^2}{\Gamma^2}} \quad (28)$$

Where N is a normalization factor that was set in order to normalize the spectrum to 1 at the absorption maximum of the long wavelength band (band **I**), N_c the conformation count (1000 or 500 depending on the case), N_{es} the ES count, $f_{n,i}$ the oscillator strength of the electronic transition i in the corresponding geometry, E the energy and $E_{n,i}$ the resonance energy.

5.3. Details of Chapter 4

The methodology used for the study reported in this chapter is identical to that used within the team for several years concerning the complexation of metal ions by model molecules of organic matter, [1, 59, 60, 68, 140–144] with the addition of an automatic titrator.

5.3.1. Experimental details

Manganese (II) chloride tetrahydrate (Acros Organics), anhydrous zinc (II) chloride (Alfa Aesar) and calcium chloride hexahydrate (Acros Organics) were used as sources of cations in the experiments. The experimental setup consisted of a flow of the solution from the reactor, to an Agilent Cary Eclipse spectrofluorometer for fluorescence measurements at 335 and 395 nm excitation wavelengths (5 nm spectral resolution), followed by an Agilent Cary 3500 UV-visible spectrometer (2 nm spectral resolution) for absorption measurements back to the reactor. The whole setup was controlled by a Metrohm Titrande titrator as automate controller. This allowed to measure the absorption and emission spectra simultaneously during the 24-hour long titration experiments. A more in-depth description of the Metrohm Titrande system, the experimental setup and the programs used for the automate, are given in Appendix 4.

Variation of the M/L ratio

A 250 mL 2'3HF–methanol solution at $4 \times 10^{-5} \text{ mol L}^{-1}$ was maintained at a fixed pH of 4.0 while adding successive amounts of Ca^{2+} , Zn^{2+} or Mn^{2+} in methanol solutions at a $2 \times 10^{-2} \text{ mol L}^{-1}$ concentration. The electronic spectra were recorded one hour after the cation addition to ensure that the mixture reached equilibrium, as well as to allow the pH to stabilize. The Metrohm Titrand system performed automatic additions of 0.1 mol L^{-1} NaOH and HCl solutions to control the pH. This procedure allowed to follow the evolution of the electronic spectra with increasing $R_{M/L}$ Metal/Ligand molar ratio.

Variation of the pH at fixed M/L ratio

The pH of a 250 mL solution of 2'3HF in methanol with a fixed Metal/Ligand molar ratio of $R_{M/L} = 2.0$ is varied from around pH = 2.0 to pH = 10. Using the automate, the pH is varied using 0.1 mol L^{-1} aqueous solutions of NaOH (and HCl if a lowering of pH is required). The electronic spectra are recorded every 30 minutes to allow the automate to settle the pH as well as to attain chemical equilibrium.

5.3.2. Computational details

A methanol PCM was used in all of the calculations of this chapter. However, our group showed that the inclusion of explicit solvent molecules in the solvation sphere of the cation significantly improved the flavonoid-metal electronic spectra reproduction with TD-DFT. [140] The performances of the model were assessed for the present work on 2'3HF and its complexes, and a pure implicit model was tested. However, the inclusion of at least 2 solvent molecules in the coordination sphere of the cation not only simplified the optimization procedure, but also improved the reproduction of electronic spectra, as expected. For these reasons, three solvation models were used, *i.e.*, 2, 3 or 4 water molecules solvating the cation, surrounded by a PCM. Explicit water molecules were used instead of methanol to reduce the computational cost with a limited impact on the accuracy of the model. [140] As for the morin – Ca(II) system, no cation on the **12'** binding site did hold during optimization so this hypothesis was finally excluded from the study. Overall, 10 complex types were optimized for each of the three cations and three coordination spheres, giving 90 final geometries. This was done using the PBE0/6-311+G(d,p) theoretical framework. For the Mn(II) complexes, the spin multiplicity had to be taken into account. All complexes were optimized with either 2 or 6 spin

multiplicities and it was found that the higher spin was more stable in each case. This was expected due to the binding mode of 2'3HF through oxygen atoms that apply a weak field on the cation.

The electronic spectra were calculated using TD-DFT with the same functional and basis-set as for the optimization.

When needed, and to better reproduce experimental data, deprotonated complexes were optimized and their spectra computed. Finally, the most promising structures were optimised in their ES to compare the computed transition energies to the experimental fluorescence spectra.

CHAPTER 2.

The structure and electronic properties of 2',3-dihydroxyflavone

The detailed study of morin that our team recently performed highlighted its peculiar acid strength and singular ability to form complexes, even with Ca(II). [1] At the origin of such behaviour appears to be the formation of a HB network that facilitates the departure of the first proton. [59] In particular, the vicinity of hydroxyl groups 2' and 3 appear to play an important role. This led us to investigate in further detail the 2'-3 hydroxyl interaction to understand to what extent the properties of morin derive from this structural feature.

The work presented in this chapter led to a publication in *RSC Advances* in 2020. [145] It is a joint experimental and computational study on the structural, acid-base, and spectral properties of 2'3HF.

1. State of the art

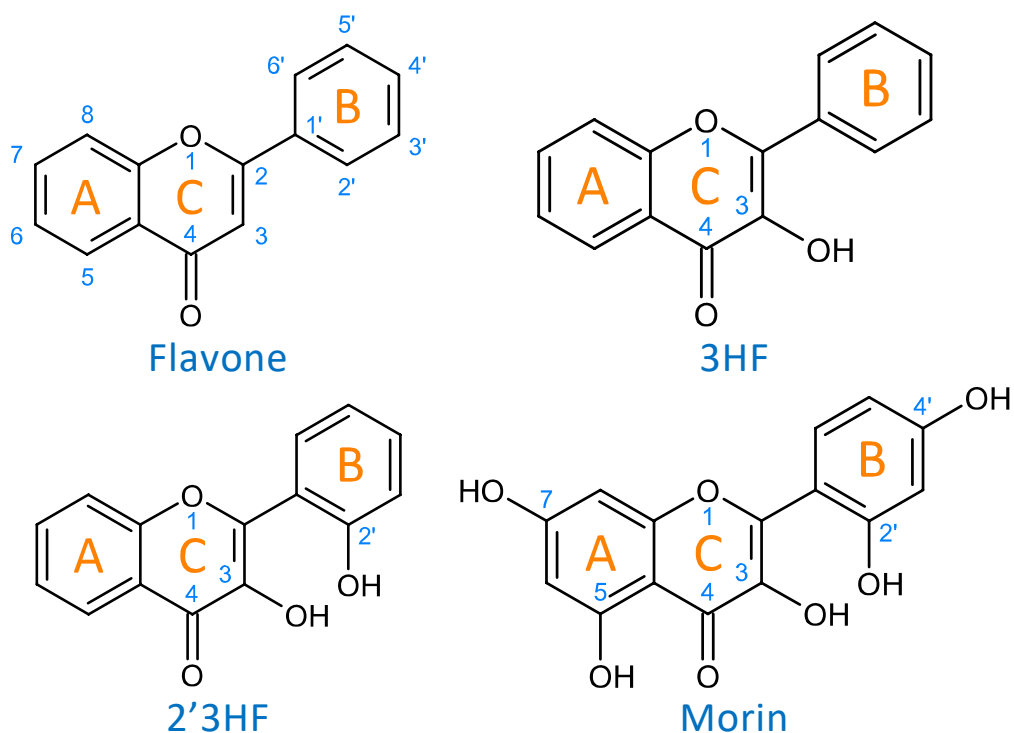


Figure I. 9: The structures of flavone, 3-hydroxyflavone (3HF), 2',3-dihydroxyflavone (2'3HF) and morin

2'3HF, of structure shown on Figure I. 9, is a molecule about which little is known. It has shown potent antiviral properties in vitro and in vivo against influenza A virus, [146] and it is an inhibitor of HIV-1 proteinase. [147] It protects cells against oxidative damage, [148, 149] and is currently studied for its ability to improve the preparation and isolation of stem cells for regenerative medicine applications. [150–152] Its crystal structure has been characterized, using X-rays, [153] and its mass spectrum recorded. [154]

It is a good candidate of study, as it is a simple 3HF derivative, but has shown to behave quite differently from other flavonols. Indeed, while studying the complexation of a variety of flavonols in 1970, Porter and Markham observed no bathochromic shift of the long wavelength UV-visible absorption band (band I) upon Al(III) salt addition. To explain this observation, they suggested the formation of a 2'3HF anion at unusually low pH. Indeed, the anion should have an already red-shifted band I compared to the neutral species, possibly close to the chelate absorption band. The reason suggested for the unexpected anion formation was the

interaction of hydroxyl groups 2' and 3, not present in most flavonols. [67] Also, 2'3HF showed high unusual electrophoretic mobility and the same reason was evoked to explain this behaviour. [155] More recently, Burns *et. al.* recorded the 1H and ¹³C NMR spectra of multi-hydroxylated flavones, [156] and established a method to predict ¹³C NMR shieldings using the spectrum of the flavone molecule (of structure depicted on Figure I. 9). They showed that the chemical shifts of molecules having hydroxyl groups interacting with one another were not predicted accurately. 2'3HF was one of the molecules that showed this symptomatic behaviour.

This chapter aims at performing a comprehensive structural analysis of 2'3HF conformers, both in the GS and the lowest energy singlet ES. For this purpose, throughout this thesis, 2'3HF will often be compared to 3HF, but also to morin (Figure I. 9), the most studied 2'-hydroxylated flavonol. This structural study is followed by a thorough analysis of 2'3HF optical properties: the UV-visible absorption and fluorescence emission properties have been studied and are presented alongside.

2. Ground-state

2.1. The neutral form

Compared to 3HF, 2'3HF exhibits an additional hydroxyl group at position 2'. This allows the formation of an intramolecular HB between O3 and H2' giving a 7-membered ring. This is in addition to the O4H3 HB present in all flavonols. If the B phenyl ring is rotated around the C1'C2 single bond, an additional HB is obtained between O1 and H2' giving a 6-membered ring. Both rotamers, noted **A** and **B**, are depicted on Figure I. 10.

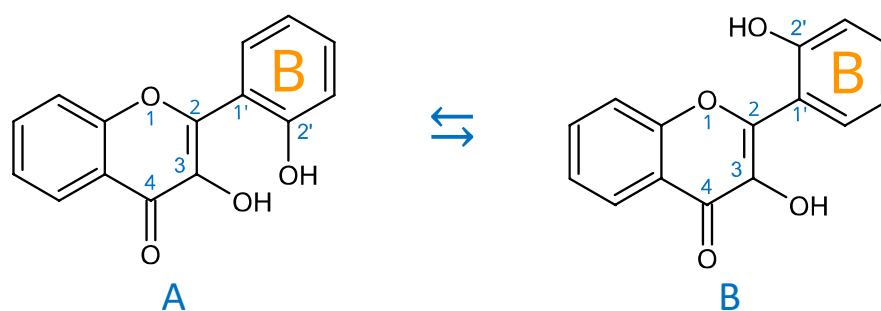


Figure I. 10: Equilibrium between the two conformers of 2'3HF: **A** (left) and **B** (right)

The **A** and **B** geometries were optimized with DFT in the gas phase and in methanol. The calculated standard reaction energies referring to the chemical equation $A \rightleftharpoons B$ are reported in Table I. 1. The differences in energy are higher in the gas phase than in methanol. This is not surprising as one would expect the intramolecular HBs to be stronger in the gas phase.

	$\Delta_r E^0$	$\Delta_r G^0$
Gas	2.38	1.97
Methanol	1.88	1.59

Table I. 1: Computed standard reaction energies in kcal mol⁻¹ for equation $A \rightleftharpoons B$, in the gas phase and in methanol

In order to estimate the strength of the OXH2' HBs (with X = 1 or 3), conformers with the O2'H2' bond in the opposite direction were optimized in methanol. Their energies were compared to the ones of their corresponding most stable conformers according to the chemical equations $A \rightleftharpoons A'$ and $B \rightleftharpoons B'$, shown on Figure I. 11. The energy results are listed in Table I. 2.

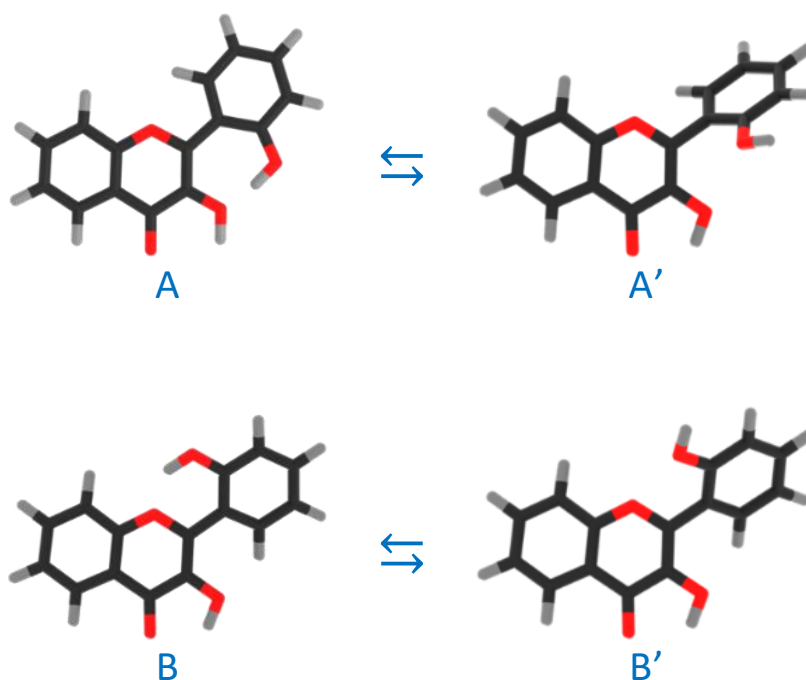


Figure I. 11: Optimized **A**, **A'**, **B**, and **B'** conformers.

	$\Delta_r E^\circ$	$\Delta_r G^\circ$
A \rightleftharpoons A'	3.30	2.50
B \rightleftharpoons B'	1.27	0.47

Table I. 2: Computed standard reaction energies in kcal mol⁻¹, for the removal of the OXH2' HB in **A** and **B**

These values must be interpreted with caution, as they do not exactly correspond to the energies of the HBs since the other internal coordinates were allowed to relax the structure and reduce the potential energy. Although both HBs are weak the one in **B** is the weakest. This is also suggested by analysing the structure. Indeed, the HB lengths are of 1.710 Å and 1.879 Å in **A** and **B**, although they display 7- and 6-membered ring, respectively. Taking into account the entropic term in the energy, the structures get even closer in energy. It is satisfactory to observe that both $\Delta_r E^\circ$ and $\Delta_r G^\circ$ are almost identical to those obtained for the same rotamer of morin (3.4 and 2.6 kcal mol⁻¹, respectively). [59]

The energy barrier of rotation around the inter-ring bond C2C1' has been evaluated in methanol, by the mean of a relaxed scan. The results are shown on Figure I. 12.

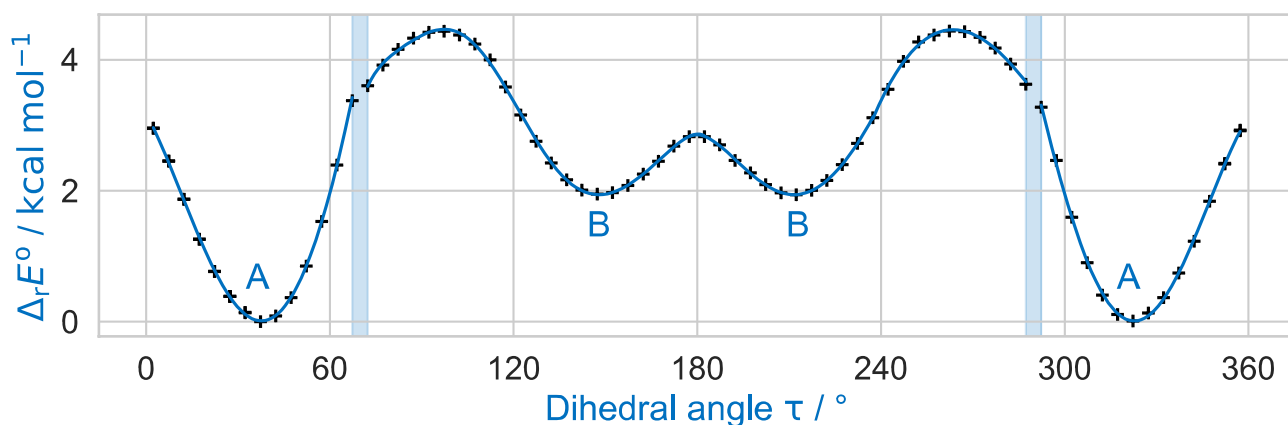


Figure I. 12: Evolution of the molecular energy with the variation of the C3C2C1'C2' dihedral angle (τ)

The energy profile shows discontinuities as artefacts generated during the relaxed scan corresponding mostly to energy jumps during the breaking of the O3H2' HB. [157] The activation energy required to rotate the B ring to convert **A** into **B** is $4.4 \text{ kcal mol}^{-1}$. The value is consistent with those found by Aparicio, that showed that flavonols had higher torsional energy barriers than regular flavones. [158] It is due to the position 3 hydroxyl group that induces an inter-ring attractive interaction with position 2' which increases rotation energy barriers. As a final observation, the potential energy minima appear at τ angles of 37.4° (**A**), 148.6° (**B**), 212.1° (**B**), and 322.9° (**A**) meaning that the molecule is not planar.

The thermodynamical results cannot single out any species, as the energy difference between **A** and **B** is too small to be conclusive, but the lowest energy conformer (**A**) is the one observed in the crystal phase. [153] Moreover, as will be seen later, its computed electronic transitions are closest from the experimental UV-visible absorption bands, so the structural analysis will focus on this particular conformer.

Some structural data are gathered in Table I. 3. The geometry does not change much when performing the calculation in methanol instead of in the gas phase, but observations can still be made. Indeed, in methanol, the τ angle and the O4H3 HB length increase, indicating a weaker conjugation effect between the B-ring and the chromone part, and thus a weaker HB.

The analysis of the X-ray data from the literature [153] shows that 2'3HF forms dimers in the crystal phase. The O4 and H3 of one 2'3HF molecule, bond themselves to the H3 and O4 of another 2'3HF, respectively. The dimer is highly sterically

constrained around positions 3, 4 and 2', explaining why the τ and C3O3H3 angles are larger than in solution.

For comparison purposes, the structural parameters of 3HF, calculated at the same level of theory in methanol solution, and morin, taken from the previous computations carried out in the team, [59] are also reported in the table. 3HF is almost completely planar, as opposed to 2'3HF and morin; and the O4H3 HB length is shorter in 3HF. This length difference can be explained by the presence of the O2'H2' hydroxyl group in the two other flavonols where the formation of the O3H2' intramolecular HB increases the charge on O3. The O3H2' HB length is shorter than the O4H3 one in both 2'3HF and morin, and it is well known that the length of the bond is one of the important parameters in assessing the strength of a HB, so the H2' appears more bonded to its HB-acceptor than H3. [159] This structural feature, along with the fact that O3H3 and O2'H2' distances are similar in all structures, would indicate that H3 is the most acidic proton of the two. This aspect is interesting on a mechanistic point of view, but the conjugated base formed through deprotonation is the same in both cases after relaxation.

	2'3HF						2'3HF				
	Solid	Gas	MeOH	Morin	3HF		Solid	Gas	MeOH	Morin	3HF
	Distances						Angles				
C2C3	1.361	1.359	1.360	1.361	1.366	C2C3C4	122.2	123.2	123.0	122.2	122.0
C3C4	1.439	1.447	1.445	1.437	1.450	C3C4C10	115.4	115.2	115.2	116.1	116.0
C5C6	1.369	1.378	1.378	1.382	1.377	C4C10C9	119.3	118.5	118.6	119.4	118.3
C6C7	1.397	1.402	1.403	1.401	1.404	C4C10C5	122.0	122.4	122.5	121.9	122.7
C7C8	1.369	1.380	1.381	1.392	1.380	C10C5C6	120.3	120.2	120.2	119.9	120.2
C8C9	1.397	1.395	1.395	1.384	1.396	C5C6C7	120.1	119.9	119.9	119.5	119.9
C5C10	1.405	1.402	1.404	1.417	1.404	C6C7C8	121.0	121.0	120.9	122.0	120.9
C4C10	1.453	1.451	1.450	1.428	1.447	C7C8C9	118.7	118.9	118.8	117.8	118.8
C9C10	1.390	1.397	1.398	1.402	1.397	C8C9C10	121.3	121.0	121.2	122.1	121.2
C2C1'	1.475	1.463	1.464	1.459	1.464	C8C9O1	116.8	116.7	116.6	117.3	116.8
C1'C2'	1.397	1.412	1.411	1.415	1.404	C9O1C2	120.4	121.7	121.6	122.3	122.3
C2'C3'	1.395	1.398	1.397	1.392	1.389	O1C2C3	120.8	119.2	119.5	119.4	119.4
C3'C4'	1.372	1.381	1.383	1.387	1.391	O1C2C1'	111.4	112.2	112.3	112.2	112.3
C4'C5'	1.382	1.394	1.395	1.398	1.392	C3C2C1'	127.8	128.6	128.2	128.4	128.4
C1'C6'	1.404	1.406	1.406	1.406	1.404	C2C1'C2'	123.9	123.8	123.8	124.4	122.1
C5'C6'	1.386	1.380	1.382	1.379	1.387	C1'C2'O2'	124.0	124.7	124.3	124.2	
C2O1	1.366	1.360	1.355	1.359	1.357	C2'O2'H2'	108.7	110.8	110.5	110.6	
C9O1	1.363	1.352	1.353	1.353	1.349	C3'C2'O2'	116.5	116.1	116.3	115.8	
C3O3	1.360	1.355	1.356	1.359	1.345	C1'C2'C3'	119.4	119.2	119.4	119.9	120.3
C4O4	1.243	1.232	1.237	1.254	1.238	C2'C3'C4'	121.1	121.2	121.1	120.9	120.7
C2'O2'	1.359	1.344	1.350	1.348		C3'C4'C5'	120.2	120.2	120.1	120.1	119.5
O3H2'	1.810	1.715	1.710	1.700		C4'C5'C6'	119.7	119.2	119.3	118.9	120.4
O2'H2'	0.892	0.973	0.975	0.976		C5'C6'C1'	120.9	121.9	121.8	122.5	120.7
O3H3	0.832	0.979	0.977	0.975	0.977	C6'C1'C2	117.4	117.7	117.7	118.0	119.4
O4H3	2.408	1.965	2.016	2.060	1.968	C10C4O4	123.0	126.2	126.0	124.6	125.6
						C3C4O4	121.7	118.6	118.8	119.3	118.4
						C4C3O3	119.1	114.0	115.0	115.7	114.3
						C2C3O3	118.7	122.8	122.0	122.1	123.7
						C3O3H3	113.7	103.7	104.8	105.6	103.8
						O4H3O3	106.0	119.7	117.7	116.5	119.8
						O2'H2'O3	155.8	157.4	156.5	157.3	
						C3C2C1'C2' (τ)	42.8	36.2	37.4	35.8	1.1

Table I. 3: Main structural parameters of the 2'3HF in crystal (from the literature [153]), gas and methanol phases (A conformer). The structural parameters are also given for morin (from a previous publication [59]), and 3HF, computed at the same level of theory (in methanol). Bond lengths are given in Å, and valence and dihedral angles are given in °

Another key structural parameter to understand the properties of flavonols is the length of the inter-ring bond C2C1'. However, the lengths are similar in the studied structures although it could have been expected to correlate with the τ angle. Thus, while 2'3HF and morin have relatively similar structures, they differ from 3HF mainly in the inter-ring angle value, which shows the important structural impact of the presence of a hydroxyl group on position 2' of flavonols.

2.2. Acid-base properties

Höfener *et. al.* suggested, using a similar computational method to ours, a first deprotonation of morin at position 7. [160] It is surprising that they did not consider deprotonations at positions 3 and 2' since studies in our group suggested the 2' hydroxyl group to be responsible for the higher acidity of morin compared to other flavonols, yielding an easy removal of a proton of the 2'/3 diol. [59] 2'3HF has only two hydroxyl groups, which greatly simplifies the problem compared to the pentahydroxyflavone, morin. Its study should therefore make it possible to confirm or refute our hypothesis.

The first pK_a of 2'3HF was measured carrying out a titration against sodium hydroxide in methanol. Figure I. 13 shows the evolution of the UV-visible absorption spectrum during the titration. Along with the increase in apparent pH, the band **I** (located at 333 nm in acidic medium) is red shifted to 387 nm, and several isosbestic points are simultaneously observed, indicating an equilibrium between two species. The overall spectrum shape is consistent with its description by Porter and Markham. [67] On the same figure, the absorbance at 387 nm is plotted against pH, the curve being obtained by fitting the monoprotic acid-base sigmoid function, of equation

$$A(\text{pH}) = \epsilon_A C_0 + \frac{C_0(\epsilon_{\text{AH}} - \epsilon_A)}{1 + 10^{(\text{pH} - \text{p}K_a)}} \quad (29)$$

using the least squares method. ϵ_{AH} and ϵ_A are the molar extinction coefficients of the acid and base species, respectively, and C_0 is the total concentration of 2'3HF. The model yields an unusually strong acidity with a pK_a of 6.7. Indeed, a value of 9.6 was found for 3HF in water, [161] and 10.0 in methanol (by our group, using the same methodology). The pK_a value of 2'3HF is thus very low and almost the same as of morin (6.3). [59]

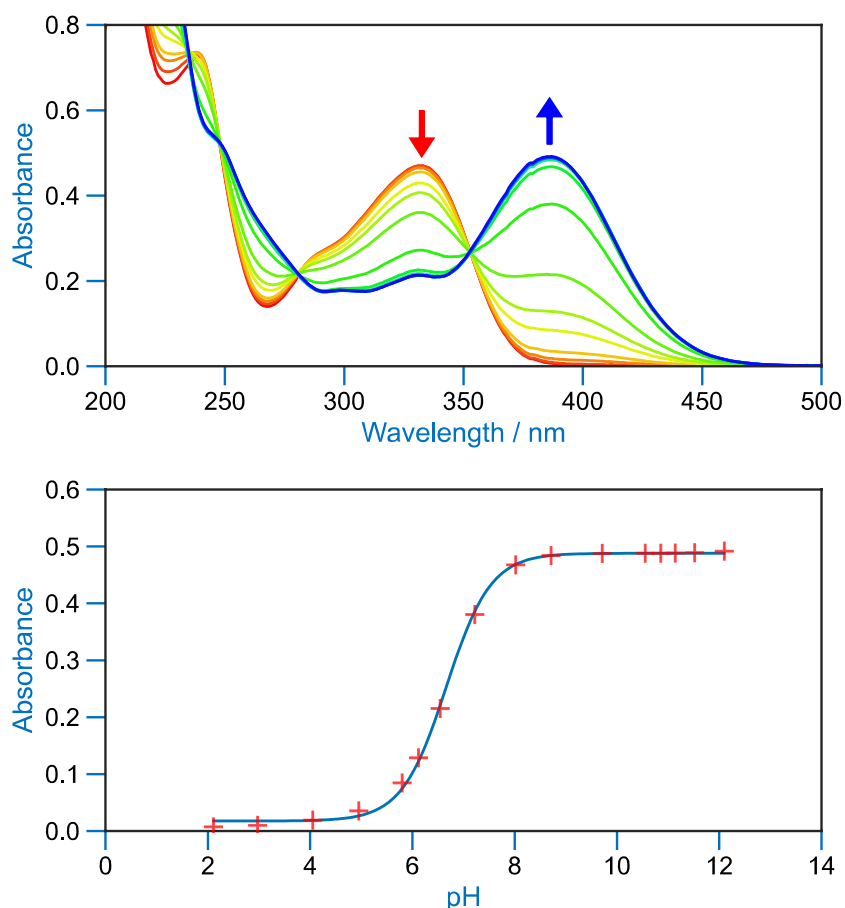


Figure I. 13: Evolution of the UV-visible absorption spectrum (top), along with the increase in apparent pH, starting from 2 to 12, in methanol. Evolution of the absorbance at $\lambda_{\text{abs}} = 387$ nm, plotted against apparent pH (bottom). The red points are experimental values whereas the blue line is the model.

In order to determine the geometry of the anion, several geometry optimizations were performed with initial structures built from the **A** and **B** conformers by removing a proton on a hydroxyl group, with the remaining proton lying between O3 and O4, O2' and O3, or O1 and O2' (positions O3O4, O2'O3 and O1O2', respectively). The optimized structures possible forms are represented on Figure I. 14.

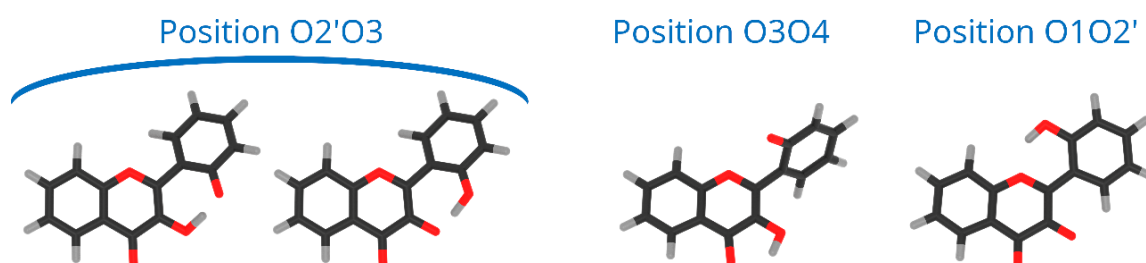


Figure I. 14: Optimized geometries depicting the possible positions for the remaining proton, after the removal of one of the two

Both positions O3O4 and O1O2' yield energies at least 11 kcal mol^{-1} higher than position O2'O3. Two distinct minima are found for a geometry with the remaining

proton lying between O2' and O3. Indeed, one of the geometries has proton H2' closer to O3 (noted **dep2'**) whereas it is closer to O2' in the other one (noted **dep3**). According to the chemical equation $\text{dep3} \rightleftharpoons \text{dep2}'$, there is a small energy difference between the two structures of only $\Delta_r E^0 = -0.09 \text{ kcal mol}^{-1}$. In order to check the existence of two individual species, the transition state (TS) between the two isomers was calculated. The results give an activation energy required to move the proton from O3 (**dep2'**), to O2' (**dep3**) of $\Delta E^\ddagger = +0.13 \text{ kcal mol}^{-1}$. The careful analysis of the imaginary frequency shows that it corresponds to the movement of H2' from O3 to O2', as expected. It must be pointed out that **dep2'** and **dep3** appear very similar, both in energies and geometries. The prediction of the existence of two distinct species must be interpreted with caution as even the smallest adjustments in the theoretical model could shift the equilibrium in one direction or the other. However, we decided to describe both species as they display quite interesting differences in optical properties.

The main structural parameters of **dep2'**, **dep3** and the TS are displayed in Table I. 4. The changes upon deprotonation appear mostly around the C3 and C2' atoms as expected.

The τ angle between the B ring and the chromone part is around 30° , a 7° lower value than in the neutral form **A**, which is expected as the 3-2' inter-ring attractive interaction is higher in these forms. However, the inter-ring bond C2C1' is only slightly shortened.

In **dep2'** and **dep3**, the HB lengths are 1.328 and 1.305 Å, respectively. Those distances are very low, and the O2'H2'O3 angle values ($\sim 170^\circ$), correspond to a quasi-alignment of the three atoms. Thus, a very strong bonding of the proton is predicted as well as a high second pK_a value, explaining no second deprotonation was observed during titration.

	dep2'	dep3	TS
C2C3	1.379	1.386	1.383
C2C1'	1.463	1.465	1.464
C1'C2'	1.432	1.422	1.425
C3O3	1.330	1.305	1.315
C4O4	1.236	1.236	1.236
C2'O2'	1.302	1.328	1.317
O3H2'	1.082	1.305	1.205
O2'H2'	1.328	1.095	1.171
C1'C2'C3'	117.1	118.7	118.1
C2C3C4	120.5	118.9	119.5
C3O3H2'	106.0	105.3	105.7
C2'O2'H2'	106.0	106.8	106.6
O2'H2'O3	170.1	170.7	171.4
C3C2C1'C2' (τ)	30.4	30.2	29.5

Table I. 4: Main structural parameters of **dep2'**, **dep3** and of the TS between the two, in methanol. Bond lengths are given in Å, and valence and dihedral angles are given in °

To conclude on the acid-base properties of 2'3HF, it can be observed that the results are consistent with similar mechanisms to other phenolic compounds. Indeed, the effect of intramolecular HBs are responsible for the lowering of the pK_a from 10.0 (in water) in the phenol molecule, to 9.5 in catechol. Thus, the effect is similar but much stronger from 3HF ($pK_a = 10.0$) to 2'3HF ($pK_a = 6.7$).

2.3. Electronic excitation energies

A comparison of the UV-visible spectra of the neutral and deprotonated species of 2'3HF with the calculated electronic transitions was made (i) to confirm the results of the structural study, and (ii) to give a complete assignment of the different spectral bands experimentally observed.

The results for the protonated species are shown on Figure I. 15. The absorption spectrum of flavonols is composed of two main bands and shoulders in the UV range. Band **I** is located at around 300–350 nm while band **II** is lower in wavelength at around 250 nm. This is what is observed for 2'3HF in methanol whose spectrum exhibits the band **I** at 333 nm with a shoulder located at 290 nm and the band **II** at 240 nm. Few descriptions of the UV-visible absorption spectrum of 2'3HF are found in the literature, [67, 162] but they are consistent with the one that we observe. The spectrum is reported to be red shifted in ethanol, with band **I** at 353 nm [163] (340 nm according to Hayashi *et. al.* [164]), with an overall shape close to the one we get. The comparison of the experimental spectrum with the calculated electronic transitions for the two conformers **A** and **B** shows that **A** reproduces the absorption

wavelengths more satisfactorily than **B**, particularly for the lowest energy transition which is calculated as more than 350 nm for the **B** conformer. It can be noticed that the shoulder is well reproduced by the calculations and corresponds to two electronic transitions: $S_0 \rightarrow S_2$ and $S_0 \rightarrow S_4$. Thus, the spectral comparison leads to the same conclusion as the thermodynamic data suggesting that the **A** conformer is the predominant species in solution.

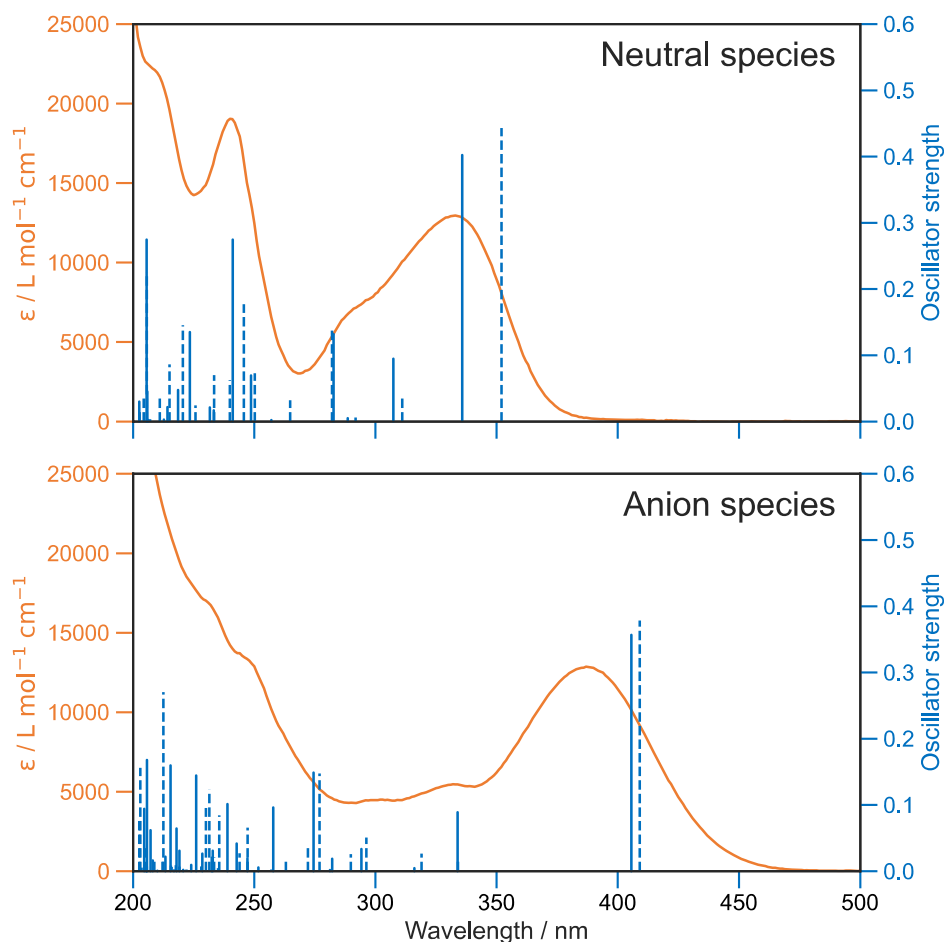


Figure I. 15: Comparison of the UV-visible absorption spectrum of 2'3HF (orange) with the computed electronic transitions (blue) for the proposed species. Top: spectrum in methanol + HCl medium and electronic transitions of **A** (solid) and **B** (dashed). Bottom: spectrum in methanol + NaOH medium and electronic transitions of **dep2'** (solid) and **dep3** (dashed)

In basic medium, the UV-visible spectrum of the mono-deprotonated form of 2'3HF shows a pronounced red-shift of band **I**, located at 387 nm. The electronic transitions computed for the deprotonated species, **dep2'** and **dep3** (Figure I. 15), show a great similitude both in energy and oscillator strength. Compared to the experiment, the computed first excitation energies of **dep2'** and **dep3** are red-shifted by 0.15 eV (19 nm) and 0.17 eV (22 nm), respectively, compared to the maximum of band **I**. These differences are below TD-DFT accuracy.

The information on the first transitions of low energy is gathered in Table I. 5 for the three species **A**, **dep2'** and **dep3**. The first transition is mainly the HOMO \rightarrow LUMO. Looking at the involved orbitals, depicted on Figure I. 16, one can see that these $\pi\pi^*$ transitions have a charge-transfer (CT) character from the phenol to the chromone moiety. This CT behaviour is the largest in **dep2'**. The analysis of this transition for **A** shows that electronic density is removed from O3 and added onto O4. This mechanism is known for allowing ESIPTs in 3HF derivatives, [45] as the acidity of H3 and the basicity of O4 are increased. It represents a first indication that an ESIPT could occur in 2'3HF. This possibility is discussed with more details in the next section.

The second transition is mainly a HOMO $- 1 \rightarrow$ LUMO one in all cases, with low probability of transition. However, **dep3** behaves somewhat differently. Indeed, although it has the same transition energy as **dep2'**, the transition in **dep3** has a 40% contribution coming from the HOMO $- 2 \rightarrow$ LUMO. This contribution has a strong $n\pi^*$ character, resulting in an even lower oscillator strength due to the selection rules and, thus, in a large change on the absorption spectrum. To understand this difference, one must notice that the energy levels corresponding to HOMO $- 3$ and HOMO $- 2$ are swapped between the two species.

	$\lambda / \text{nm (eV)}$	f	Nature
A	336 (3.69)	0.402	H \rightarrow L (95%)
	307 (4.03)	0.095	H $- 1 \rightarrow$ L (93%)
	283 (4.39)	0.132	H $- 2 \rightarrow$ L (83%)
dep2'	405 (3.06)	0.357	H \rightarrow L (98%)
	334 (3.71)	0.089	H $- 1 \rightarrow$ L (96%)
dep3	409 (3.03)	0.379	H \rightarrow L (98%)
	334 (3.71)	0.014	H $- 1 \rightarrow$ L (48%) H $- 2 \rightarrow$ L (40%)

Table I. 5: Computed transition wavelengths in nm (eV) and oscillator strengths for **A** (S_0 to S_1 , S_2 and S_4), **dep2'**, and **dep3** (S_0 to S_1 and S_2). H stands for HOMO, and L for LUMO

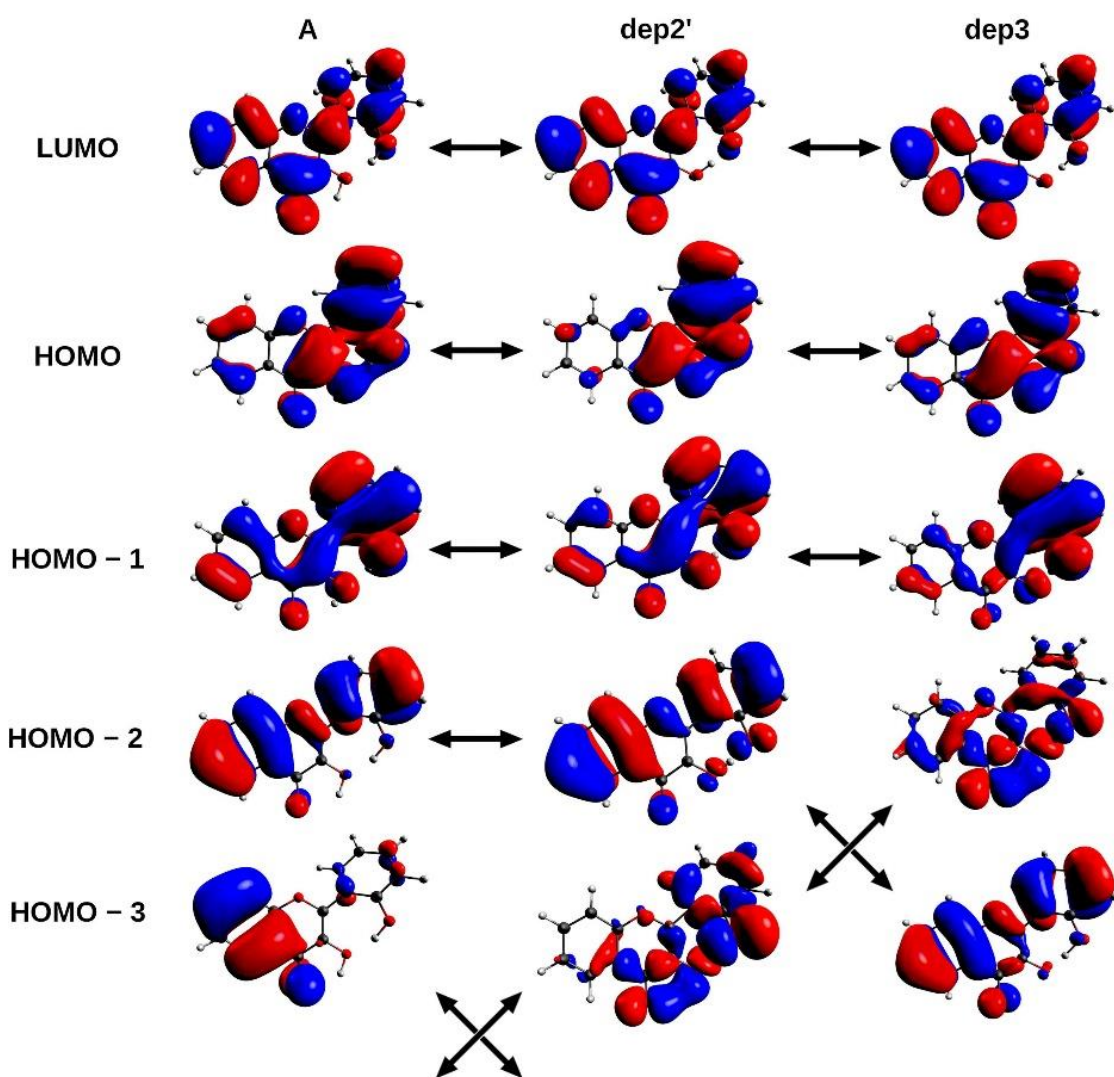


Figure I. 16: HOMO - 3, 2, 1, HOMO and LUMO of A, **dep2'**, and **dep3** species, the arrows indicate the similarities of the MOs between the different structures

3. Excited-state

3.1. Fluorescence emission in acidic medium

The fluorescence emission spectrum of 2'3HF in methanol (in acidic medium), and the fluorescence excitation spectra compared to the absorption spectrum are shown on Figure I. 17. 2'3HF exhibits a dual fluorescence. By analogy with some other 3HF derivatives, the normal form would emit at 428 nm (band **N**), and the tautomeric form at 547 nm (band **T**). This hypothesis is corroborated by the fact that the fluorescence excitation spectra corresponding to the two emission maxima are comparable. This means that the two emission bands originate from the same excited molecule. However, the excitation spectrum at 550 nm emission wavelength shows the presence of another band around 390 nm, suggesting the presence of another absorbing species. Accordingly, a third emission band located at 517 nm is evidenced using a 395 nm excitation wavelength (spectrum in orange on Figure I. 17. a). The origin of this band is discussed in section 3.4 and further more in Chapter 3. On the excitation spectrum at 430 nm emission, a sharp peak can be seen at 381 nm, along with two little humps at 404 and 410 nm. Those are due to Stokes Raman scattering from methanol, and correspond respectively to C-H stretching ($\sim 3000\text{ cm}^{-1}$), CH₃ deformation ($\sim 1500\text{ cm}^{-1}$), and C-O stretching ($\sim 1050\text{ cm}^{-1}$). [165]

The Stokes shifts for the **N** and **T** bands (with respect to absorption band **I**) are of 95 nm (6666 cm^{-1}) and 214 nm (11748 cm^{-1}), respectively. Both Stokes shifts are consequent, and the second one is typical of an ESIPT, where large geometry and electronic changes occur.

The $I_{\text{N}}/I_{\text{T}}$ band ratio was close to 1 in all experiments, but it seemed to fluctuate. This fluctuation was attributed to the solvent used which contained traces of water with an uncontrolled H₂O/MeOH ratio. Moreover, for some experiments, aqueous HCl (or NaOH) solutions were added in small amounts. These reproducibility issues are further discussed in Chapter 3.

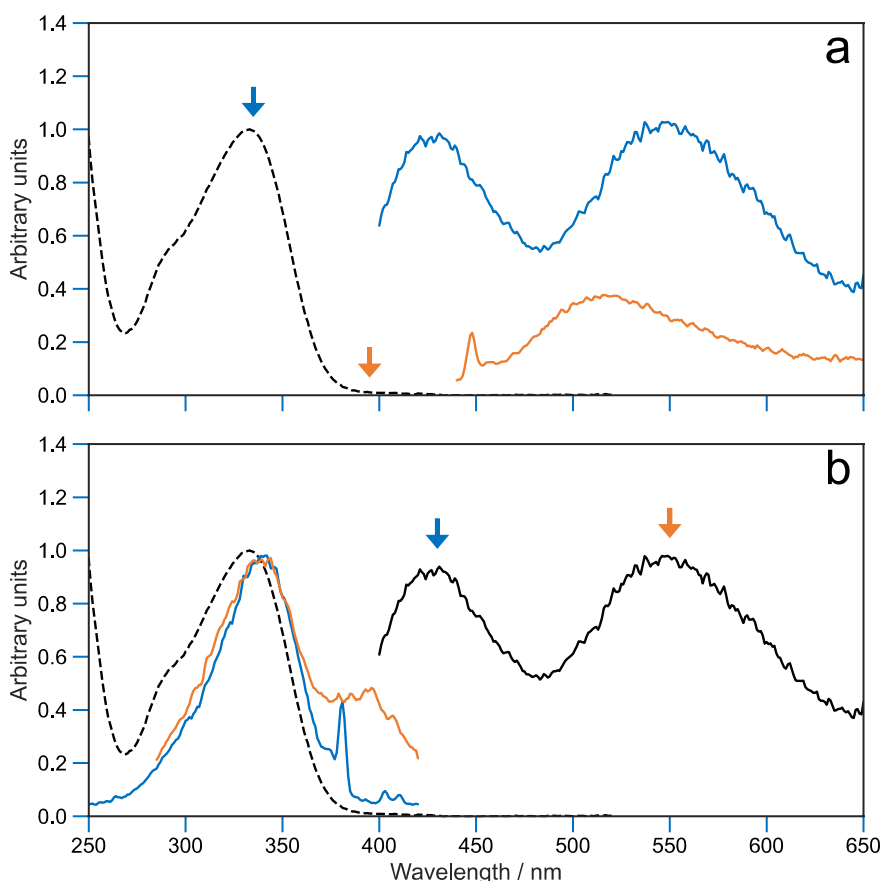


Figure I. 17: Normalized UV-visible absorption (black, dashed) spectrum compared to the fluorescence emission and excitation spectra of 2'3HF in methanol + HCl medium. Figure a: $\lambda_{\text{exc}} = 335 \text{ nm}$ (blue), $\lambda_{\text{exc}} = 395 \text{ nm}$ (orange). Figure b: $\lambda_{\text{exc}} = 335 \text{ nm}$ (black), $\lambda_{\text{em}} = 430 \text{ nm}$ (blue), $\lambda_{\text{em}} = 550 \text{ nm}$ (orange)

By optimizing the geometry of the first singlet ES, two local minima were found. They correspond to the normal form **A*** with the keto group lying at position 4, and a tautomeric form, noted **T3*** (keto group at position 3). By modifying the initial geometry, another minimum was found with the keto group at position 2', noted **T2'***. Finally, two other geometries originating from **B** were found: **B*** and **BT3*** (the latter having the keto group at position 3, and position 2' in front of position 1).

All five geometries are depicted on Figure I. 18, and the relative energies and computed emission wavelengths are gathered in Table I. 6. All tautomer geometries have lower electronic and Gibbs free energies than their normal counterpart in the S_1 state, meaning that the PT could occur if it is fast enough.

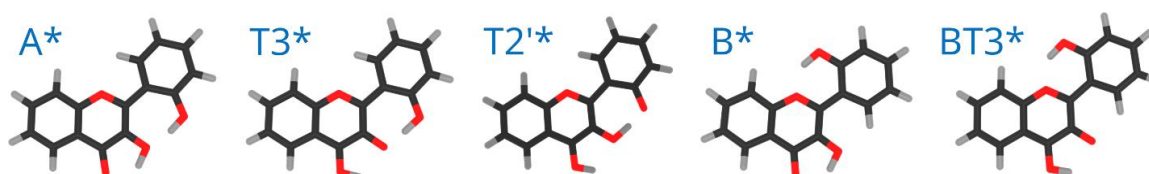


Figure I. 18: **A***, **T3***, **T2'***, **B*** and **BT3*** optimized geometries

		$\Delta_r E^0$	$\Delta_r G^0$	$\lambda_{em,theo}$ (vs. exp)
Band N	A*	14.69	14.49	430 (0.01)
	B*	14.52	14.81	431 (0.02)
Band T	T3*	0.00	0.54	556 (0.04)
	T2'*	0.35	0.00	588 (0.16)
	BT3*	7.56	8.21	563 (0.06)

Table I. 6: Computed electronic and Gibbs free energies (kcal mol⁻¹) between the five geometries in the S₁ state relative to the most stable species, and their computed emission wavelength (nm). The differences between the theoretical emissions and their corresponding experimental values (either band **N** or **T**, depending of the species) are shown in parentheses, in eV

A* and **B*** conformers have almost the same energy and emission wavelength and could be at the origin of band **N**. The electronic term of the energy (and the entropic correction that is not shown) favours **B***, whereas the vibrational correction favours **A***, reversing the result. Such small differences indicate that the **A** and **B** conformers become isoenergetic upon electronic excitation.

The three studied tautomeric forms have emission wavelengths that could correspond to the observed fluorescence band (550 nm), as even **T2'*** shows an emission energy that deviates from the experiment by only 0.16 eV, below TD-DFT accuracy. Here again, **T3*** and **T2'*** are so close in energy that **T3*** is more stable if the electronic energy is considered, whereas **T2'*** is favoured after vibrational and entropic corrections.

The theoretical study being based on the absorption and emission spectra, it will be nearly impossible to confirm or infirm the existence specific species. However, the **A** is more prominent in the GS so this work will focus on **A***, **T3*** and **T2'***.

In order to estimate if the PT is feasible within the timescale of fluorescence, the potential energy surface was explored to search for TSs. Two were located: one from **A*** to **T3*** (noted **TS:A*-T3***, $\Delta_r E^\ddagger = +0.6$ kcal mol⁻¹) and the other from **T2'*** to **T3*** (noted **TS:T2'*-T3***, $\Delta E^\ddagger = +0.1$ kcal mol⁻¹). However, attempts to find a TS between **A*** and **T2'*** yielded **TS:A*-T3*** instead. This leads to the conclusion that intra-molecular PTs to get **T3***, or even double intra-molecular PTs to get **T2'***, are very fast, with almost null energy barrier.

The calculations are consistent with experimental data that shows that 2'3HF exhibits, at least, a dual fluorescence, induced by an ESIPT. Actually, the calculations suggested a possibility for 2'3HF to show an additional fluorescence emission due to a subsequent ESIPT mechanism. It must be pointed out that only the intra-molecular PT is shown to be feasible here and the description of a solvent assisted PT, for example, would require explicit treatment of solvent molecules in high level ES molecular dynamics, far beyond the scope of this thesis.

3.2. Neutral excited-state geometries

The main structural parameters of \mathbf{A}^* are displayed in Table I. 7. Although most angles and bond lengths are kept the same, the O3H2' HB gives a 7-membered ring planar, with significantly shorter HB distances compared to \mathbf{A} , of 1.741 and 1.545 Å for O4H3 and O3H2', respectively. The angles are also highly changed, and O2'H2O3 is almost linear. Overall, the main difference between \mathbf{A} and \mathbf{A}^* is that the latter is completely planar in the ES which questions whether this change can be responsible for the large Stokes shift observed.

	A	A*	T3*	T2**
Distances (Wiberg indices)				
C2C3	1.360 (1.53)	1.397 (1.29)	1.423 (1.22)	1.395 (1.35)
C3C4	1.445 (1.11)	1.441 (1.12)	1.425 (1.18)	1.416 (1.21)
C5C6	1.378 (1.52)	1.386 (1.46)	1.382 (1.49)	1.381 (1.50)
C6C7	1.403 (1.36)	1.394 (1.41)	1.398 (1.39)	1.400 (1.38)
C7C8	1.381 (1.49)	1.398 (1.39)	1.394 (1.40)	1.390 (1.43)
C8C9	1.395 (1.34)	1.383 (1.42)	1.384 (1.41)	1.387 (1.39)
C5C10	1.404 (1.31)	1.408 (1.29)	1.414 (1.26)	1.413 (1.27)
C4C10	1.450 (1.09)	1.427 (1.14)	1.402 (1.24)	1.405 (1.23)
C9C10	1.398 (1.32)	1.409 (1.27)	1.413 (1.23)	1.412 (1.24)
C2C1'	1.464 (1.07)	1.429 (1.23)	1.430 (1.24)	1.460 (1.12)
C1'C2'	1.411 (1.31)	1.457 (1.14)	1.451 (1.16)	1.456 (1.13)
C2'C3'	1.397 (1.36)	1.402 (1.33)	1.404 (1.33)	1.421 (1.25)
C3'C4'	1.383 (1.47)	1.377 (1.48)	1.379 (1.47)	1.382 (1.46)
C4'C5'	1.395 (1.39)	1.407 (1.30)	1.404 (1.32)	1.394 (1.38)
C1'C6'	1.406 (1.34)	1.420 (1.28)	1.420 (1.28)	1.392 (1.43)
C5'C6'	1.382 (1.48)	1.378 (1.49)	1.379 (1.49)	1.402 (1.34)
C2O1	1.355 (1.00)	1.375 (0.96)	1.376 (0.96)	1.376 (0.96)
C9O1	1.353 (1.00)	1.368 (0.97)	1.355 (0.99)	1.350 (1.01)
C3O3	1.356 (1.01)	1.331 (1.07)	1.287 (1.27)	1.321 (1.12)
C4O4	1.237 (1.57)	1.269 (1.38)	1.331 (1.10)	1.335 (1.09)
C2'O2'	1.350 (1.05)	1.319 (1.16)	1.313 (1.18)	1.282 (1.32)
O2'H2'	0.975 (0.68)	0.986 (0.64)	1.043 (0.54)	1.319 (0.26)
O3H3	0.977 (0.68)	1.007 (0.60)	2.017	2.034
O4H3	2.016	1.741	0.974 (0.70)	0.971 (0.71)
O3H2'	1.710	1.545	1.371 (0.21)	1.073 (0.49)
Angles				
C3C4O4	118.8	115.7	117.7	118.8
C4C3O3	115.0	110.9	115.5	114.1
C3O3H3	104.8	101.6	84.5	84.9
O4H3O3	117.7	125.9	116.3	115.1
O2'H2'O3	156.5	166.9	173.6	172.3
C3C2C1'C2' (τ)	37.4	0.3	0.0	0.0
NPA charges				
C3	0.170	0.291	0.293	0.262
C4	0.459	0.328	0.321	0.323
C2'	0.346	0.403	0.390	0.398
O4	-0.660	-0.733	-0.644	-0.650
O3	-0.705	-0.667	-0.679	-0.705
O2'	-0.706	-0.613	-0.644	-0.650
H3	0.519	0.532	0.511	0.511
H2'	0.504	0.510	0.487	0.488

Table I. 7: Main structural parameters, Wiberg indices, and NPA charges of **A**, **A***, **T3***, and **T2**** calculated in methanol. Bond lengths are given in Å, and valence and dihedral angles are given in °

In order to assess this twisted to planar geometry change effect, one can try to substitute 3HF on position 2' with a functional group that does not modify significantly the electronic density, and to compare the Stokes shift obtained to that of 3HF. This has already been done in the past. Indeed, Strandjord *et. al.* [166]

methylated 3HF on multiple positions, including position 2', and measured the shifts. The methyl group induces a minor electron accepting effect due to hyperconjugation, while generating a strong steric hindrance. This way, comparing 3HF, 2'-Me-3HF and 4'-Me-3HF, gives insights on the effect of the steric hindrance on the Stokes shift. The results are gathered in Table I. 8.

	ν_{abs}	ν_{em}	ν_{Stokes}	τ_{GS}	τ_{ES}
3HF [166]	29150	24630	4520	1.1	0.2
2'-Me-3HF [166]	30580	24752	5828	57.3	37.7
2'3HF (this work)	30030	23364	6666	37.4	0.3
4'-Me-3HF [166]	28730	24390	4340		
4'-OMe-3HF [167]	28409	23364	5045		

Table I. 8: Absorption and emission energies and Stokes shift, in cm^{-1} , and inter-ring (τ) angles in $^\circ$ of some 3HF derivatives. The angles were obtained using the same computational methodology as for 2'3HF

The comparison of 3HF and 4'-Me-3HF shows that the methyl substitution does not change much the Stokes shift, that reduces by only 180 cm^{-1} , due to a combination of lowering both the excitation and emission energies. However, when the substitution happens on position 2', the Stokes shift increases by 1308 cm^{-1} . The substitution does not alter much the emission, but has a remarkable effect on the excitation energy. This result is corroborated by geometry optimizations of which the τ angles are given in the table. They show that, while 3HF is planar in both the GS and the ES (explaining the smaller Stokes shift), the steric hindrance in 2'-Me-3HF forces it to remain twisted in both cases, with a strong reduction of the inter-ring angle upon excitation. In the table, the energies related to the substitution by a methoxyl group on position 4' were also added. [167] The substitution by a stronger electron donor group reduces the emission energy more than the excitation energy. The Stokes shift can thus be explained by a combination of a steric hindrance between positions 2' and 3 (that generates large geometry changes upon excitation), and an electron donation effect on ring B.

The analysis of the HOMO \rightarrow LUMO transition of **A** showed that part of the electronic density was moved from O3 to O4. In order to quantify the effect of electronic density reorganisation, Natural Bond Orbital (NBO) and Natural Population (NPA) analyses were performed. The values are gathered in Table I. 7.

The NBO analysis corroborates the observation, and the Wiberg indices are, overall, negatively correlated with bond lengths, as expected. Indeed, the Wiberg index decreases from 1.57 to 1.38 for C4O4, increases from 1.087 to 1.142 for C4C10, and the natural charge on O4 decreases from -0.66 to -0.73 , going from **A** to **A***. This indicates that C4O4 becomes closer to an enolate, the whole group acting as a better base than in the ES. The opposite behaviour is observed for C3O3, and even more for C2O2. Indeed, their Wiberg indices and the charges on the oxygen atoms increase, whereas the C2C3 and C1'C2' indices decrease. On a side note, the O3H3 and O2'H2' bond orders also decrease of 0.08 and 0.04 respectively, suggesting the hydrogen atoms to be less bonded to their oxygen atoms. Finally, C2C1' is close to a single bond (1.07) which allows an easy rotation of the B ring, whereas its order increases to 1.23 in the ES. This behaviour is consistent with the molecule going from a twisted to a planar structure upon excitation.

Both tautomers are also completely planar. Their main structural parameters are gathered in Table I. 7. Along with the O2'-H2'-O3-H3-O4 network, the B and C rings are modified. The Wiberg indices confirm the positions of the keto groups that switch during **A*** to **T3*** conversion (C4O4 index evolves from 1.38 to 1.10 and C3O3 from 1.07 to 1.27) and during **T3*** to **T2'*** conversion (C3O3 index evolves from 1.27 to 1.12 and C2'O2 from 1.18 to 1.32).

3.3. Fluorescence emission in basic medium

The fluorescence emission and excitation spectra of 2'3HF in basic methanol medium are depicted on Figure I. 19, compared to the absorption spectrum. The excitation spectrum matches exactly the absorption spectrum indicating that the emission originates from an excited species formed through relaxation after exciting **dep2'** or **dep3** (noted **dep** in the remaining part of the chapter).

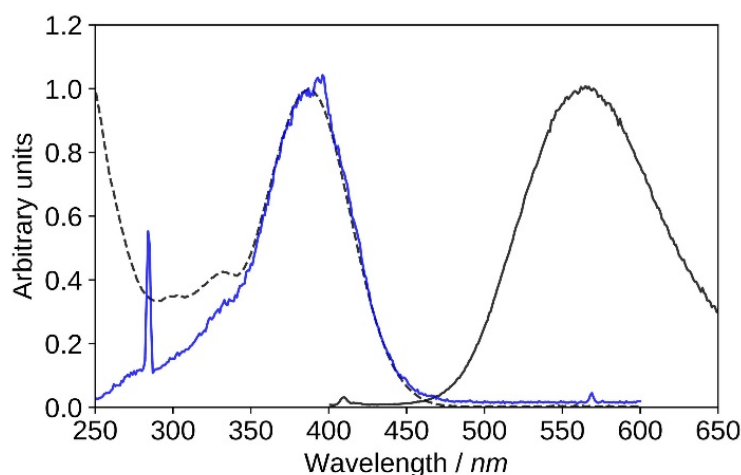


Figure I. 19: Absorption (black, dashed), excitation (blue, $\lambda_{\text{em}} = 570 \text{ nm}$), emission (black, solid, $\lambda_{\text{exc}} = 395 \text{ nm}$), spectra of 2'3HF in basic medium

The maximum of absorption of the anion is located at 387 nm, and the emission is maximum at 566 nm (noted band **D**). The sharp peak at 285 nm on the excitation spectrum is due to the second order Rayleigh scattering. Interestingly, the measured Stokes shift (8172 cm^{-1}), is larger than the one observed for the normal neutral form.

In order to determine the geometry of the ES deprotonated species, we performed optimisations in the same way as for the GS, the remaining proton being moved to the previously suggested positions. Once again, the lowest energy is found when the proton lies at position O2'O3, however this time, only one conformer could be found, with the proton lying closer to the O2' atom and a fully-planar geometry. The latter geometry will be noted **dep*** in the remaining part of the chapter. The second possible conformer is less stable by $\Delta_r G^\circ = 5.78 \text{ kcal mol}^{-1}$, and corresponds to the proton lying between O4 and O3, bonded to O3. A deprotonated tautomer with the remaining proton bonded to O4 was also optimized, but turned out to be even less stable.

The same kind of explanation as for the neutral species can be applied to interpret the large Stokes shift. However here, it is less convincing than for the neutral case since the τ angle goes from 30.4° in the GS (geometry **dep2'**), to 0° in **dep***, meaning that geometry rearrangements happen to a lesser extent than in **A** and **A***.

The calculated emission wavelength for the most stable anion is 539 nm, 0.11 eV higher than the experimental value. This is a satisfactory result, as the accurate description of an anion is far more challenging than that of a neutral species,

especially in the ES. In the end, the predicted Stokes shift is of 6099 cm^{-1} (using **dep2'** as the GS conformation).

3.4. Hypotheses on the 517 nm emission band

In the study of the neutral species ESs, the emission band of the tautomer form nm was shown to contain a contribution from another species, evidenced by exciting in the vicinity of the absorption maximum of the deprotonated form of 2'3HF (in acidic medium). The spectrum is shown on Figure I. 20. The band (noted band **X**) appears as a broad signal peaking at 517 nm when using a 395 nm excitation wavelength. Several structural hypotheses have been made to explain the origin of this emission band.

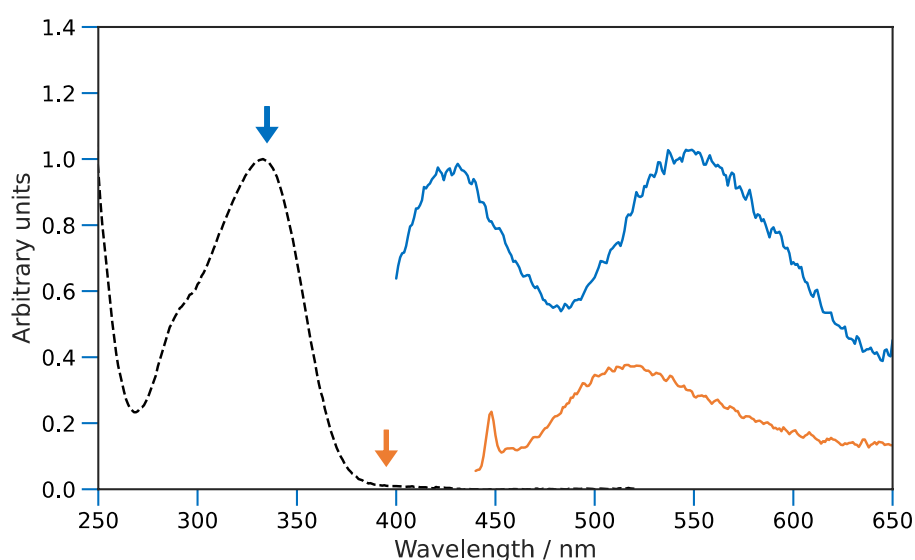


Figure I. 20: Normalized UV-visible absorption (black, dashed) spectrum compared to the fluorescence emission spectra of 2'3HF in methanol + HCl medium. $\lambda_{\text{exc}} = 335\text{ nm}$ (blue), $\lambda_{\text{exc}} = 395\text{ nm}$ (orange)

3.4.1. Hypothesis 1: emission from a cation

Protonated flavonols have not been much investigated, and one would expect the protonation to blue shift the electronic transitions with respect to the neutral form. However, it was reported that the addition of H_2SO_4 red-shifted the band **I** absorption maximum of 3HF from 344 nm to 378 nm, and its normal fluorescence from around 410 nm to 430 nm. [168] This observation was also reported for other mono-hydroxylated flavonoids [161] as, for example, 2'-hydroxyflavone shows emission at 514 nm upon protonation of its carbonyl group.

Two cation geometries were optimized, and their electronic excitation and emission energies calculated. One of them has the HB network directed towards the keto group (noted **C4**), and the other with the HB network towards the 2'-hydroxyl group (noted **C2'**) in both the GS and ESs. The results are reported in Table I. 9.

	C2'	C4
$\Delta_r G^0(S0)$	0.00	5.63
$\lambda_{\text{abs,calc}}$	373 (0.14)	422 (0.24)
$\Delta_r G^0(S1)$	65.26	63.39
$\lambda_{\text{em,calc}}$	457 (0.31)	527 (0.05)

Table I. 9: Computed relative free energies for the GS and first singlet ESs of geometries **C2'** and **C4** (in kcal mol⁻¹), and absorption and emission wavelengths (in nm). The values reported in parenthesis are the differences with the experimental values of 390 nm (approximate excitation maximum), and 517 nm (emission wavelength) in eV. The depicted geometries are the conformers in their GS

The model predicts that the most stable cation species is **C2'** in the GS, with a maximum of absorption at 373 nm, and a difference of 0.14 eV from the experimental 390 nm excitation value. In the ES, the HB network is more stable in the other direction since **C4*** is more stable than **C2'***, and **C4*** emits a 527 nm. The difference with the experimental band **X** maximum is 0.05 eV, and is thus very close.

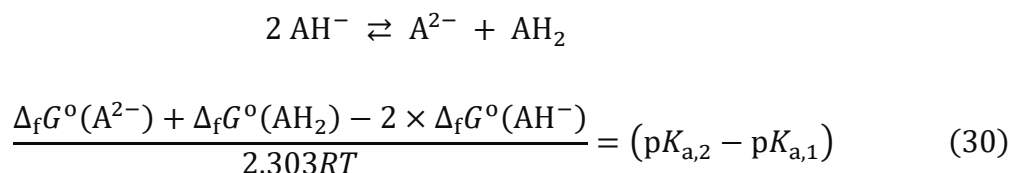
This hypothesis is promising as the calculated absorption and emission energies match the experimental values within TD-DFT accuracy. However, some experimental observations lead us to doubt this explanation. Indeed, the experimental data suggest that band **X** shows no pH dependence, or worse, a possible increase of intensity with increasing basicity. In any case, bands **N**, **T**, **X** and **D** can simultaneously be observed from the same solution, by varying the excitation wavelength, and the simultaneous observation of the cation, neutral and anion species is unlikely. In the end, the two computed species **C4** and **C2'** could probably exist in extreme pH conditions, but we doubt they are responsible for the recording of band **X**. Experimenting in those conditions and observing the effects on band **X** could help clarify its behaviour with changes in pH.

3.4.2. Hypothesis 2: deprotonation of the anion for explaining band A

The excitation spectrum of the emitting species of band **D** matches closely the absorption spectrum of the anion (**dep**). This only ensures that the excited species is **dep**, but does not provide any information on the geometry of the emitting species, apart from the fact that it is formed through relaxation from **dep**. It was also mentioned that band **X** seemed to be increasing during the titration with NaOH, even though band **D** is so wide, that this observation can also be due to its simultaneously increasing intensity.

If the intensity of band **X** truly increases with pH, before being hidden by band **D**, one explanation can be that **dep** loses its remaining proton after excitation, *i.e.*, an Excited-State “Inter”-molecular Proton Transfer (ESInterPT). Actually, the computed wavelength for **dep*** (539 nm) matches also the 517 nm maximum of band **X**, giving an even lower error of 0.10 eV, and a Stokes shift of 6497 cm⁻¹, a shift better explained by the structural analysis made on the neutral species (in section 3.2). Band **D** would thus be the emission signal of the doubly deprotonated 2’3HF (**dep2’3***) formed through an ESInterPT. The calculation of the emission wavelength of the doubly deprotonated species yields 618 nm, with an error of 0.18 eV, below TD-DFT accuracy.

No second deprotonation can be seen in the GS, meaning that for this hypothesis to be true, the second pK_a must be much lower in the ES than in the GS. Calculating pK_a values using first principle methods is challenging. However, one can compute relative values which will be more accurate due to error cancellations. Indeed, subtracting both acid base equilibria yields:



Using the calculated Gibbs free energies of **A**, **dep2’** and **dep2’3** for AH₂, AH⁻ and A⁻, respectively in the GS, and **A***, **dep***, and **dep2’3*** in the ES, the second deprotonations are predicted to happen 24 and 28 units of pH after the first ones, for the GS and first ESs, respectively. While this second deprotonation pK_a is high in the GS, which is a result that the geometry analysis predicted, it is calculated to be even

higher in the ES. This is also expected, as the molecule goes from a twisted geometry to a planar one from **dep** to **dep***, tightening the bonding of H2' to the oxygen atoms.

Based on this explanation, it appears chemically speaking doubtful that the band **D** would originate from **dep2'3***, and in the same way, band **X** from **dep***. Studies in various solvents, with various bases could help clarify this point, as a second deprotonation would be even more unlikely in hydrocarbon solvents. Until clarification of the behaviour of band **D** in such solvents, we favour the hypothesis of an emission from **dep***, meaning that another explanation has to be found for explaining band **X**.

3.4.3. Hypothesis 3: formation of a complex with the solvent

Because the first two hypotheses are very unlikely, the next chapter of this thesis is entirely dedicated to specific and non-specific 2'3HF-solvent interactions. We will show how the scientific literature has actually been suspecting the existence of a stable solvent-complex with 3HF in the GS and that the existence of the 517 nm band might originate from the same phenomenon in 2'3HF.

4. Conclusion

The barely studied 2'3HF, has been investigated using a combination of electronic spectroscopies and density functional theory methods. 2'3HF has shown to exhibit the typical spectral behaviour of some flavonols, with an absorption band at 333 nm (band **I**), and a second one (band **II**) at 240 nm. It exhibits a dual fluorescence from the normal form (428 nm) and a tautomer (547 nm), analogously to 3HF, and shows a remarkably high Stokes shift for its normal form. A thorough analysis showed that the shift was mostly due to the steric hindrance provoked by the 2'-hydroxyl group. The ES IPT was properly predicted by the calculation of the relative energies between the conformers in the ES, along with the estimation of the energy barriers. 2'3HF exhibits a very low pK_a of 6.7, a particularity shared with morin, which confirms it originates from the 2'-3 hydroxyl interaction. The band **I** is red-shifted to 387 nm upon deprotonation. The electronic excitation energies of the predicted most stable conformer of the anion reproduce well the absorption spectrum. The emission of the anion has been assigned to the 566 nm band (**D**), since the excitation spectrum matches closely the absorption spectrum. Also, thermodynamical calculations and geometry analyses on the anionic 2'3HF highlighted the particularly strong binding of the remaining proton in-between oxygen atoms 3 and 2', explaining why no second deprotonation could be observed experimentally. Finally, another emitting species was evidenced when exciting in long wavelength part of the absorption spectrum. Its emission maximum wavelength is 517 nm, and the band (**X**) is best seen in acidic medium, even though it is possible that it is still present in basic medium, but hidden by the wide band **D**. Two hypotheses on the origin of this band were discussed and ruled out. Chapter 3 of this thesis is dedicated to understanding band **X** and exploring the third hypothesis of a solvent complex.

CHAPTER 3.

Solute-solvent interactions and the hypothetical solvent-complex

At the end of Chapter 2, we showed that the two first hypotheses we suggested for the explanation of band **X** were unlikely. The third hypothesis remains: the existence of a solvent complex with 2'3HF. The idea of the existence of a fluorescent solvent – 3HF complex has existed since the eighties when, for example, McMorow and Kasha in 1983 studied the ESIPT mechanism of 3HF and noticed that adding sub-stoichiometric quantities of water to dry hydrocarbon solutions of 3HF generated a third fluorescence band, located between the **N** and **T** bands. They suggested it to be due to a “perturbed” PT tautomer, then revised the hypothesis in favour of a solvent-complexed anion emission. They even proposed the successive formation of mono and poly-solvated complexes. [169] The photophysics of 2'3HF appear similar and band **X** could originate from the same kind of species.

It is in the context of this questioning that an experimental study of the environmental effects on 2'3HF photophysics was undertaken.¹ For this, we focused the study on polar solvents and their HB accepting and donating properties, hoping to narrow down the possibilities for the explanation of band **X**. The first half of this Chapter is dedicated to presenting the results of the study. In the meantime, we explored the solvation of 2'3HF and assessed the performances of the PCM using *ab-initio* molecular dynamics. Thus, we will evaluate how the PCM is likely to describe a good proportion of solute-solvent interactions, despite its low computational cost.

¹ The study was partially performed by the third year Licence student Léa Havret during her two months internship in the team

1. Problematic and methodologies

1.1. Solvent effects on the fluorescence of 3HF

To the best of our knowledge, the first report on the dual-fluorescence of 3HF was done in 1974 by Frolov *et. al.* Their explanation was that the violet fluorescence originated from the normal molecule and the green one from an 3HF-[ROH] complex. [170] Later on, in 1979, the currently accepted interpretation of a PT was given by Sengupta and Kasha. [42] Thus, the solvent has always been assumed to be of great importance to explain the spectral properties of 3HF and its derivatives. A few years later, as stated in the introductory paragraph of this chapter, McMorrow and Kasha studied the ESIPT mechanism of 3HF in depth. [169] They highlighted that the addition of sub-stoichiometric quantities of water to dry hydrocarbon solutions of 3HF had a strong effect on the spectrum. Indeed, a third fluorescence band appeared between the **N** and **T** brands (similarly to band **X** of 2'3HF). In their preliminary communication, [171] they assumed it to be due to a “perturbed” PT tautomer, before revising their hypothesis. Their final conclusion was the formation of 3HF anion complex with the HBD solvent traces.

In 1985, Strandjord and Barbara used time-resolved fluorescence spectroscopy to study the solvent effects on the kinetics of the ESIPT in 3HF. [44] They confirmed the strong dependence of the PT on the HB donating (HBD) capability of the solvent: HBD solvents complex the carbonyl and thus, inhibit the PT. Later, in 1987, Brucker and Kelley put 3HF into a 10 K argon matrix and performed a spectroscopic study. [48] They found that in a dry matrix, only the tautomer emission could be observed showing that the PT is very fast (or that proton tunnelling occurs). However, when embedding HBD solvents such as water or methanol into the matrix, 3HF-[ROH]_n were formed and their emission signals successively appeared on the spectrum. They attributed band **N** to 3HF-[ROH]₂ complexes due to the inhibition of the PT by ROH. An emission band between **N** and **T** (similar to band **X**) was also observed which was attributed to 3HF-[ROH]₁ complexes. Thus, their hypothesis suggests that the spectral origin of band **X** is that of a perturbed PT tautomer, similarly to the original assumption by McMorrow and Kasha. However, this time, the excitation spectrum at

the maximum λ_{em} of the band could be recorded which was observed to be red-shifted relative to the normal absorption, as is the case for 2'3HF.

1.2. Recent publications and comparison with 2'3HF

From this early literature, it appears as a consensus that 3HF is triply fluorescent with the violet emission coming from a normal species solvent complex (**N**), the green one coming from the lone PT tautomer (**T**) and band **X** coming from another solvent-complex of unidentified structure. 3HF also exhibits an anion emission (band **D**) in higher pH media. [172]

Although the subject could appear as closed due to the amount of experimental data on the photophysics of 3HF, taking a look at the more recent literature shows that it is still a hot topic. In order to explain why, it is important to sum up the knowledge gathered on the subject

- Emission band **T**, visible when exciting in the neutral species absorption maximum, can unambiguously be attributed to a PT tautomer emission for 3HF (~535 nm) and 2'3HF (547 nm)
- Emission band **N**, visible when exciting in the neutral species absorption maximum, can unambiguously be attributed to the normal species emission for 3HF (~400 nm) and 2'3HF (428 nm), probably present due to solvent induced perturbations on the ESIPT mechanism
- Band **D**, visible in basic media when exciting in the anion absorption maximum (longer wavelengths), can be attributed to the emission from the anion of 3HF (~480 nm, between **N** and **T**) and 2'3HF (566 nm, with higher wavelength than band **T**)
- When exciting near the absorption maximum of the anion in acidic media, band **X**: at 517 nm for 2'3HF (between **N** and **T**), whereas it is observed at the same spectral position as band **D** for 3HF. It appears when HBD solvent impurities are present, which suggests the formation of solute-[ROH] complexes, either in perturbed PT tautomer (**PPTT**) or ion pair (**IP**) structures.

The fact that band **X** appears at the same spectral position as band **D** in 3HF often creates confusion. It vehiculates the idea that band **X** is due to 3HF anion at unusually low pH due to solvent perturbations. However, band **X** and **D** are very distinct in 2'3HF, which suggests that the emissive species have distinct electronic properties and structures. Thus, **PPTT** hypothesis is still a plausible explanation.

In 2008, Protti as a post-doc in our group performed a mixed computational and experimental study on the origin of band **X** for 3HF in DMSO. In this paper, band **X** was assimilated to band **D** and an **IP** $[3\text{HF}]^- - [\text{DMSOH}]^+$ formation was suggested to explain its observation at unusually low pH. [173] Protti continued to computationally and experimentally work on the subject with his own group always on the basis of a triple emission of 3HF: **N**, **T** and **D**. [174–177] However, in 2015, Dereka *et al.* [172] showed that the long-wavelength absorption band of 3HF observed in neutral and basic media originated from two distinct species. The first one has been confirmed by the group using infrared transient absorption as the anion of 3HF with a short lifetime of 40 ps (in methanol), pre-dominant in basic media (at the origin of band **D**). The other species has a longer lifetime of 2 ns, and is suspected to be a $3\text{HF} - [\text{ROH}]$ complex (at the origin of band **X**). Very recently in 2021, an **IP** (formed through an ESInterPT) was observed in ES one-the-fly molecular dynamics simulations. [178] However, band **X** can be selectively obtained by exciting using longer wavelengths, which suggests it has an origin in the GS.

The hypotheses are summed up on Figure I. 21.

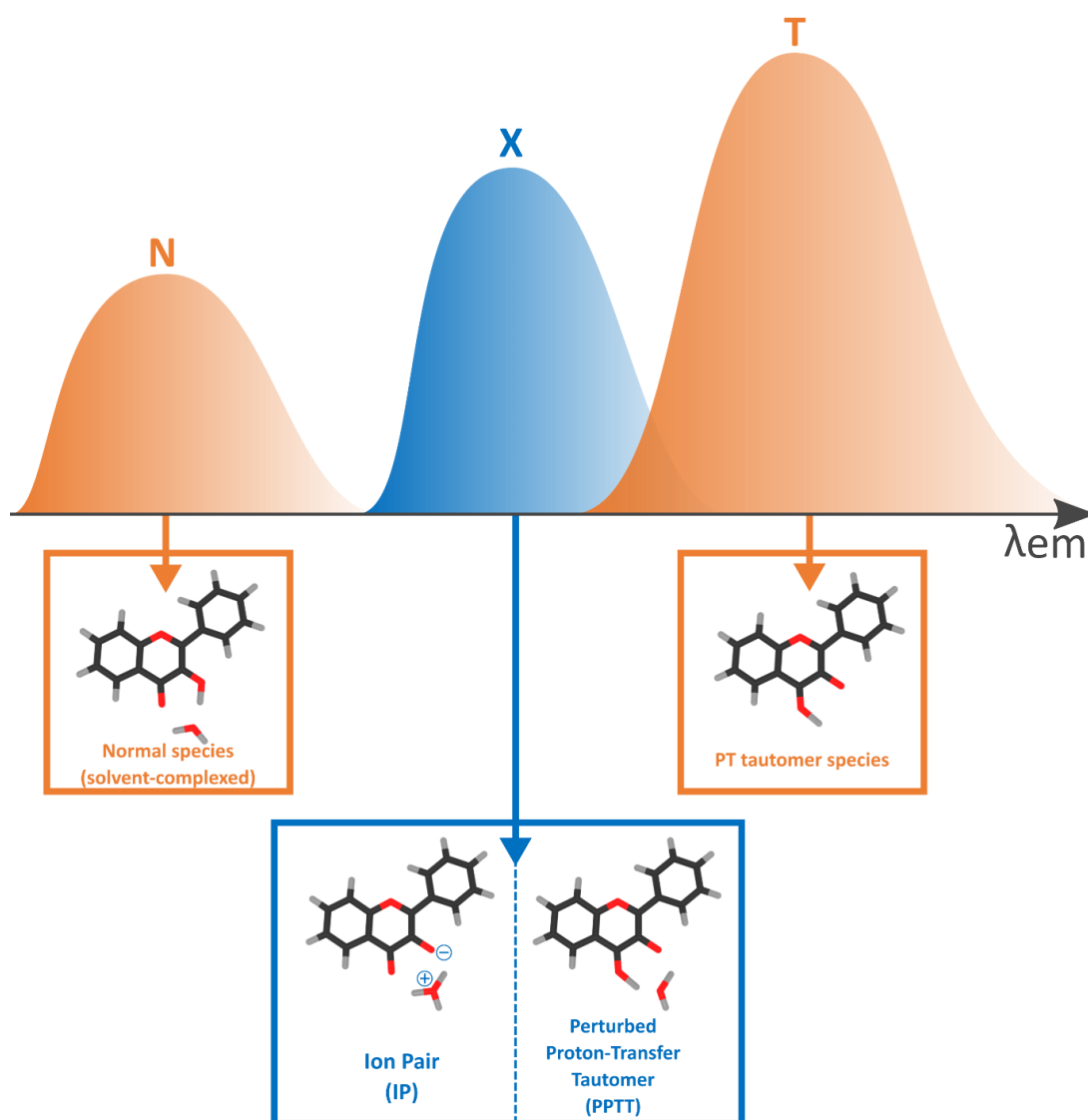


Figure I. 21: Summary of the hypotheses on the origin of emission bands in 3HF

Using steady-state and time-resolved fluorescence, our group recently showed that a similar process could be observed for morin. Indeed, morin and its mono-deprotonated forms are non-fluorescent, although a fluorescence band (similar to band **X**) was observed at 500 nm in acidic conditions. The fluorescence is thought to be due to a morin-solvent complex, but no structure of the complex was suggested at this time. [179]

1.3. Objectives of the study

We believe that the study of 2'3HF could shed light on the ES mechanisms in all 3HF derivatives because 2'3HF is non-ambiguously quadruply fluorescent with an emission of anion at higher wavelengths than the PT tautomer. In order to get better

insights on the origin of the band in 2'3HF, we studied its spectral properties in various solvents. The results are presented in the first half of this chapter (section 2).

The computational way to confirm this hypothesis requires to improve the description of the solvent. Indeed, the addition of few explicit solvent molecules in addition to the PCM has shown to improve the accuracy in several cases, including for describing metal-complexes, [140] and has been extensively used in our group. [1, 59, 68, 142] However, some attempts of adding explicit water or methanol molecules in the vicinity of O4, O3 and O2' had very little effect on the excitation and emission energies. Thus, we believe that the accurate description of 2'3HF–solvent specific interactions would require statistical considerations, with the computation of many conformations to be meaningful. For this reason, we undertook an AIMD study of 2'3HF in methanol of which the second half of this chapter is dedicated to presenting the results (section 3).

2. Experimental observations

2.1. The nature of the solvent

2.1.1. General observations

Various polar solvents were selected for studying the effect 2'3HF environment on its spectra. Their HBD and HB accepting (HBA) capabilities are important for the study, so, their α (acidity) and β (basicity) parameters are reported in Table I. 10 according to their Kamlet-Taft definition. [180, 181] Their π^* (dipolarity/polarizability parameter) were also added to the table. [182]

	α	β	π^*
Water	1.17	0.47	1.09
Methanol	0.98	0.66	0.60
Ethanol	0.86	0.75	0.54
Acetone	0.08	0.43	0.71
DMSO	0.00	0.76	1.00
Acetonitrile	0.19	0.40	0.75
Dichloromethane	0.13	0.10	0.82

Table I. 10: Kamlet-Taft α , β and π^* parameters for the studied solvents in this chapter. Taken from reference [183]

	Abs (band I) / nm	N / nm	T / nm	X / nm
Methanol	333	427	551	524
Ethanol	335	425	543	517
Acetone		410	537	521
DMSO	334	426	537	
Acetonitrile	329	410	535	529
Dichloromethane	336	420	538	537

Table I. 11: Absorption and emission maximum wavelengths of 2'3HF in various solvents, measured from the spectra on Figure I. 22. The emission maximum of band N in dichloromethane must be interpreted with caution because of its low intensity

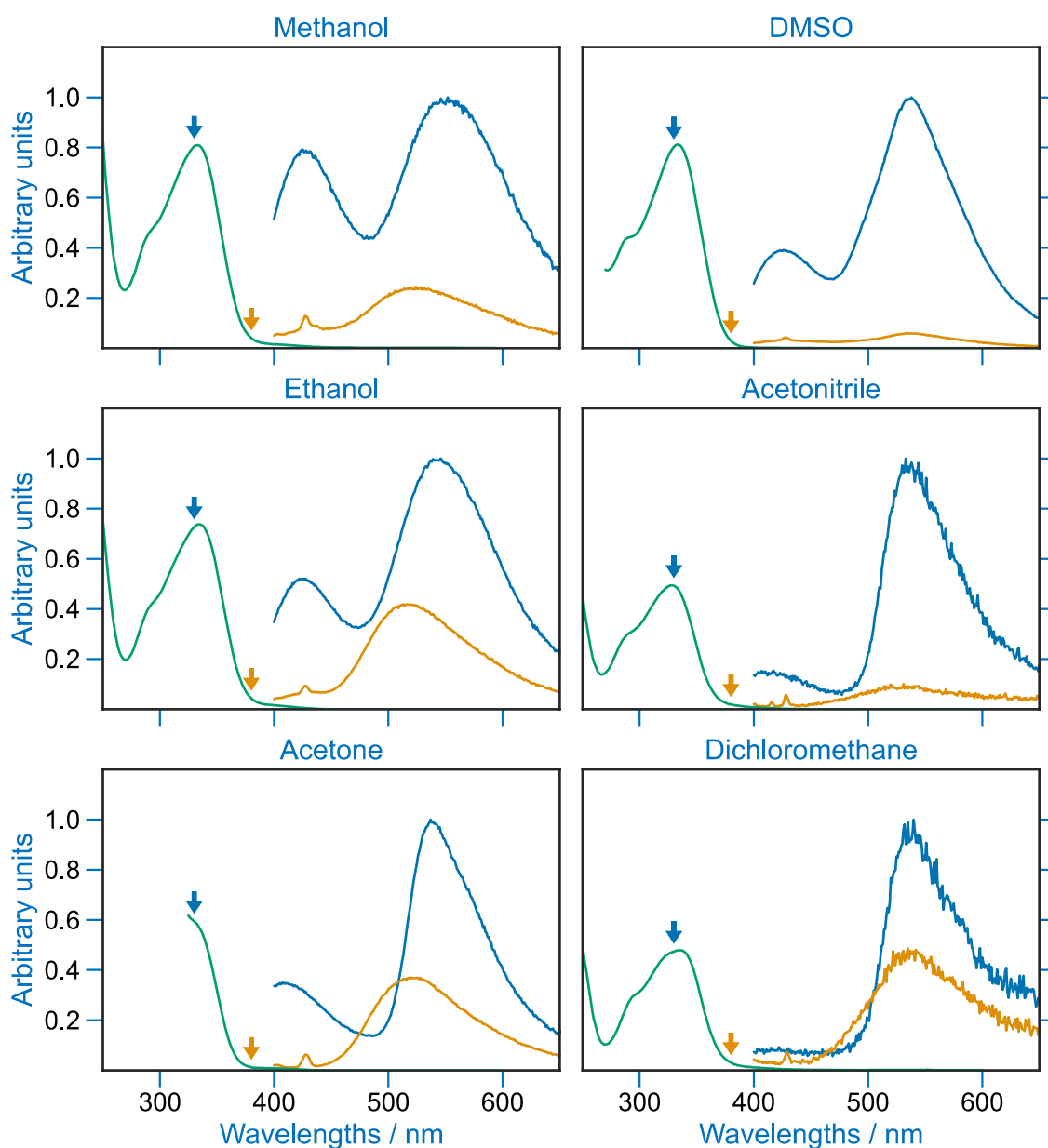


Figure I. 22: Absorption (green) and fluorescence ($\lambda_{\text{exc}} = 330$ nm, blue $\lambda_{\text{exc}} = 380$ nm, orange, as indicated by the arrows) of 2'3HF in dichloromethane, and acidified acetonitrile, acetone, methanol, DMSO and ethanol. The fluorescence intensities were multiplied by a normalization factor corresponding to the emission maximum of band T

The absorption and emission spectra of 2'3HF in the selected acidified solvents are displayed on Figure I. 22, except for water in which 2'3HF is barely soluble. For ease of reading, the appropriate absorption and emission maximum wavelengths are reported in Table I. 11.

Before commenting on the results, it must be mentioned that the weak signals at around 430 nm (~ 3000 cm^{-1}) on the emission fluorescence spectra ($\lambda_{\text{exc}} = 380$ nm) are due to the $\nu_{\text{C-H}}$ Raman signals of the corresponding solvent. Also, acetone and

DMSO absorb in the studied spectral range which is why the absorption spectra were cut.

The maximum of the absorption band **I** is located at a mean of 333 nm, and the fluorescence bands **N**, **T** and **X** are at 419, 543 and 527 nm, respectively. Overall, the effects of the solvent on band positions are rather small. Even the emission maximum wavelength of band **X** remains only slightly impacted, which is surprising if due to a solvent complex. It must be mentioned that the measured wavelengths for the methanol solutions are slightly different compared to the experiments of Chapter 2. Indeed, **N**, **T** and **X** were maximum at 428, 550 and 517 nm, respectively. The results are not completely reproducible which highlights the particular dependence of 2'3HF spectra on subtle experimental details such as water contaminations in solvents. Such high dependencies on the dryness of the solvent were also observed for 3HF by several authors, [169, 184] as discussed in the introductory section of this Chapter.

In order to better visualize the effect of the solvent on the fluorescence properties, the correlation between the α , β , and π^* parameters and the band positions were explored. The results are displayed on Figure I. 23.

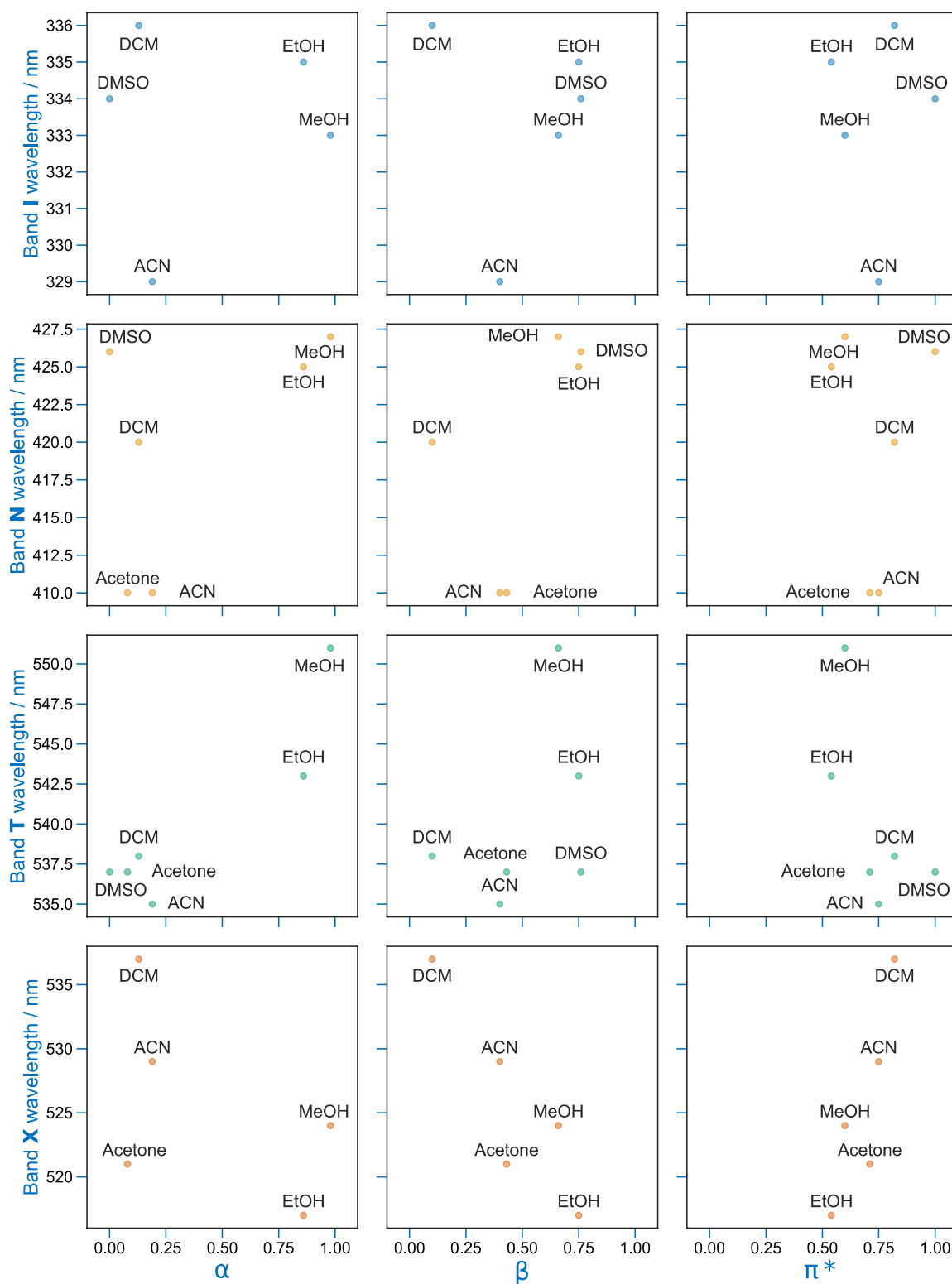


Figure I. 23: Correlation between the α , β , and π^* parameters and band I, N, T, and X positions

It is hard to obtain general conclusions from a set of only 6 solvents, however, two observations can still be made:

- The band T position seems to be dependent on the solvent nature, since it is quite different for MeOH and EtOH compared to other solvents.

- The band **X** position is dependent on the solvent basicity (β) as well as on its dipolarity/polarizability (π^*)

2.1.2. Effect on the proton transfer

The **T** band is red-shifted in acidic solvents. This is particularly striking when looking at the correlation between α and the band position, suggesting a strong impact of HBD solvents. The effect observed is a red-shifted **T** emission with increased acidity of the solvent. Also, having another look at Figure I. 22 shows that the largest changes on the spectra are on the intensities. Indeed, the I_N/I_T band ratio is significantly modified and varies from around 1 in methanol, to almost 0 in dichloromethane. In order to better assess this effect, the correlation between I_N/I_T and the parameters was investigated. The results are depicted on Figure I. 24. As for band **T** position, the I_N/I_T ratio is also positively correlated with α . This suggests that the ESIPT mechanism occurs in a single intramolecular step and is perturbed by HBD solvents, similarly to what was found for 3HF.

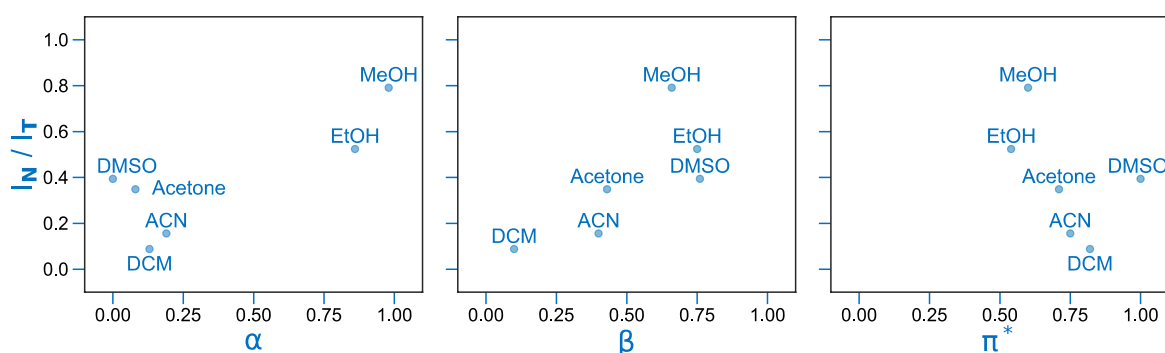


Figure I. 24: Correlation between the α , β and π^* parameters and the I_N/I_T ratio

2.1.3. Effect on band X

The correlation between the band **X** position and β is consistent with the idea of a solvent-complex that would withdraw a proton from the solute, supporting the **IP** hypothesis. However, it must be interpreted with caution since band **X** was not observed in DMSO, despite its strong basicity of $\beta = 0.76$. Actually, competing effects could take place here, since the opposite correlation is observed for π^* . The correlation on the band position is such that a basic solvent tends to blue-shift band **X**. This is once again a surprising behaviour as one would expect the emission of an **IP** to be red-shifted due to an increase of negative charge on the solute, in analogy with the position of band **D**.

2.2. Effect of water percentage

So far in this thesis, the dryness of the solvent was said to be important when studying the spectral properties of 3HF derivatives. In order to better assess the effect, acidic methanol, ethanol, acetone and DMSO solutions of 2'3HF were prepared (with unknown initial water content), and successive quantities of water were added to them.

The evolutions of the absorption spectra are displayed on the left of Figure I. 25. The most impacted spectra are those measured in methanol with a hyperchromic effect on band **I** and, more importantly, on its long-wavelength tail, corresponding to the absorptive species responsible for the emission of band **X**. The same behaviour is observed for ethanol, with a lesser effect on the red-tail. Finally, the absorption intensity of the red-tail is small in acetone and almost null in DMSO.

Band **I** in acetone appears slightly red-shifted, whereas close to no changes are observed in DMSO. A zoom on the red-tail is presented on Figure I. 25. A low absorbing species is clearly observed around 400 nm (at the origin of the emission band **X**). This is particularly true for methanol and ethanol, whereas only weak bands are seen for acetone and DMSO. This is not surprising for DMSO since no band **X** was observed. On the contrary, the emission spectrum in acetone highlighted a strong emission from band **X** although close to no absorption occurs at the studied excitation wavelength. Thus, the species responsible for band **X** in acetone must display a strong fluorescence yield.

The effect of adding water is strongest in methanol whereas changes can be observed in the other solvents but are too small to be accurately measured. Now switching to the effects on the emission spectra shown on Figure I. 26, the effects are much larger than for absorption spectroscopy and large spectral shape modifications are observed.

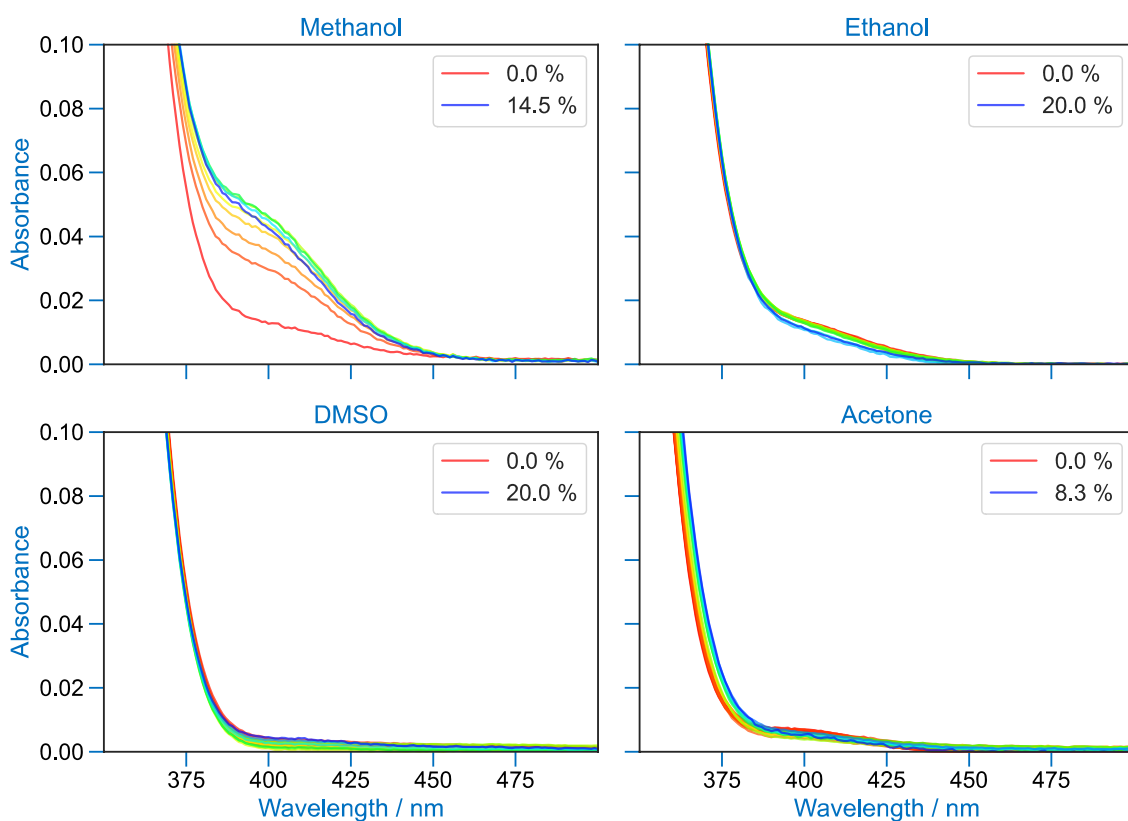
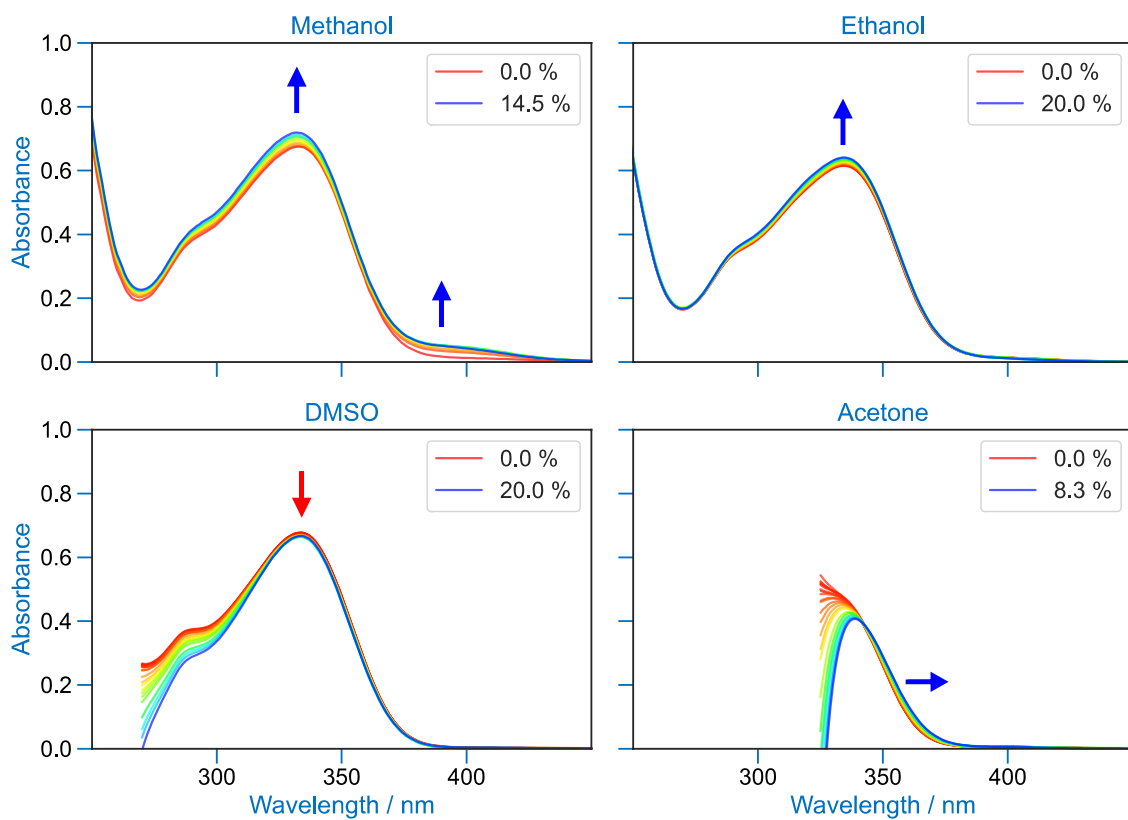


Figure I. 25: Evolution of the absorption spectrum of 2'3HF in various solvents with progressive addition of water volumes. The indicated water percentages are given as volume percentages. At the bottom is shown a zoom on the red tail of band **I**

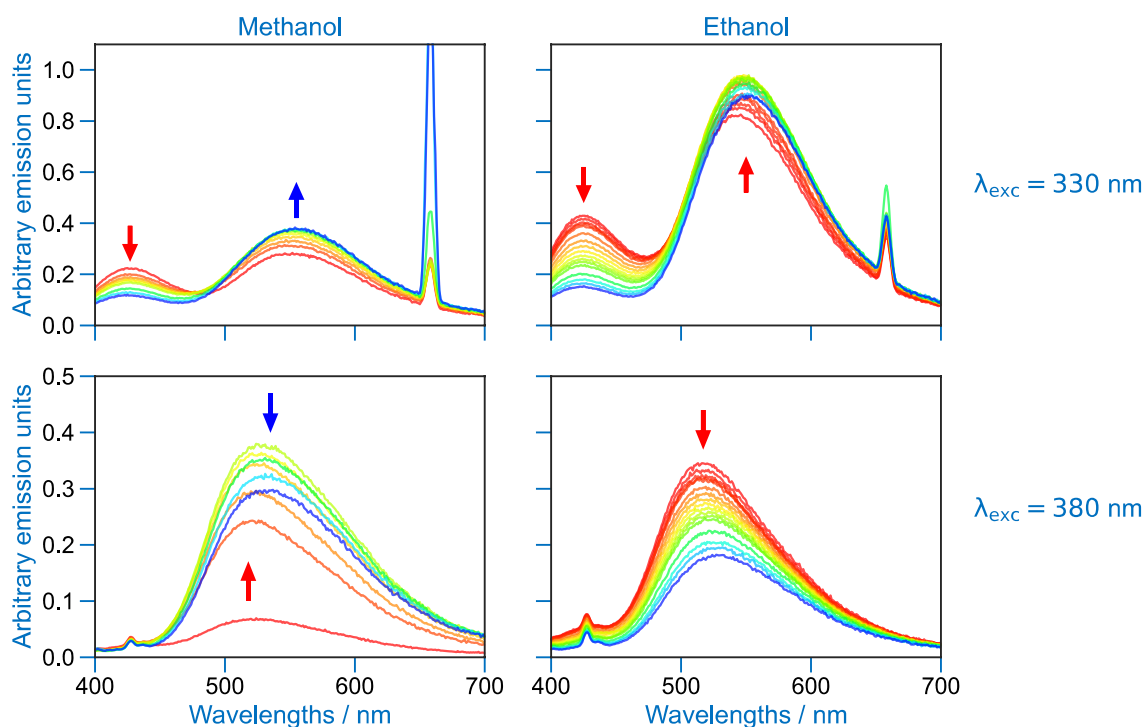


Figure I. 26: Evolution of the emission spectrum of 2'3HF in methanol and ethanol with progressive addition of water volume. The excitation wavelengths are indicated on the right of the figure.

First of all, the I_N/I_T ratio comes close to 0 upon water addition. This is an opposite behaviour as the one highlighted in the previous section. Indeed, strong HBD solvents were assumed to bind to the carbonyl of 2'3HF and inhibit the PT. Here, water actually exhibits the opposite behaviour, despite its large $\alpha = 1.17$. This is also as opposed to the literature findings for 3HF in which water usually inhibited the PT like any other strong HBD solvent. [169, 178]

This behaviour might actually be explained in terms of particular 2'3HF–H₂O interaction scheme. Indeed, the interaction of H₂O with 2'3HF could be a solvent-assisted PT, as schemed on Figure I. 27.

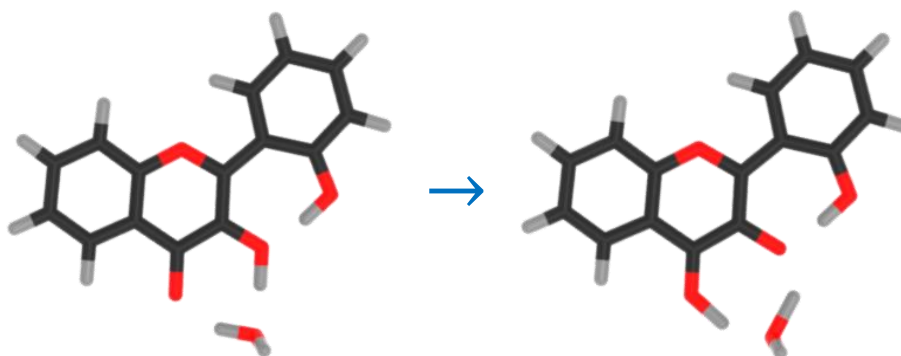


Figure I. 27: The hypothetical water-assisted ES IPT scheme

The difference between water, methanol and ethanol being the size of the substituent, *i.e.*, H-OH, Me-OH and Et-OH, the explanation for the particular behaviour could be a threshold size requirement of the substituent, although it is an unsatisfactory assumption. Here again, the results appear contradictory as band **X** is enhanced in presence of water in methanol but lessened in ethanol.

Perhaps the most striking observation that can be made on Figure I. 26 is the net increase of band **X** intensity with small water addition (from 0% to 1% water addition) which looks like stoichiometric interactions between water and 2'3HF. Experimenting in perfectly dry conditions as well as doing smaller water additions would be mandatory to confirm such hypothesis, which is planned in our team for future studies.

In order to better assess the effect of the water percentage on the spectra, the emission intensities at 540 nm (corresponding to bands **X** and **T**) were plotted against the water amounts added to methanol and ethanol solutions. The results are shown on Figure I. 28. The spectral intensities show a net increase (decrease for the emission of band **X** in ethanol) until around 5% water. The 5% water appears as a threshold value, especially for band **X** in methanol, which can be interpreted as a build-up of specific 2'3HF-H₂O interaction until the stabilization of a water cluster around the solute. Then, a slower decrease of band intensities is observed with further water addition, due to a change of bulk solvent properties. It is particularly surprising to observe that, despite their close solvation properties, methanol and ethanol have quite different effects on 2'3HF spectra.

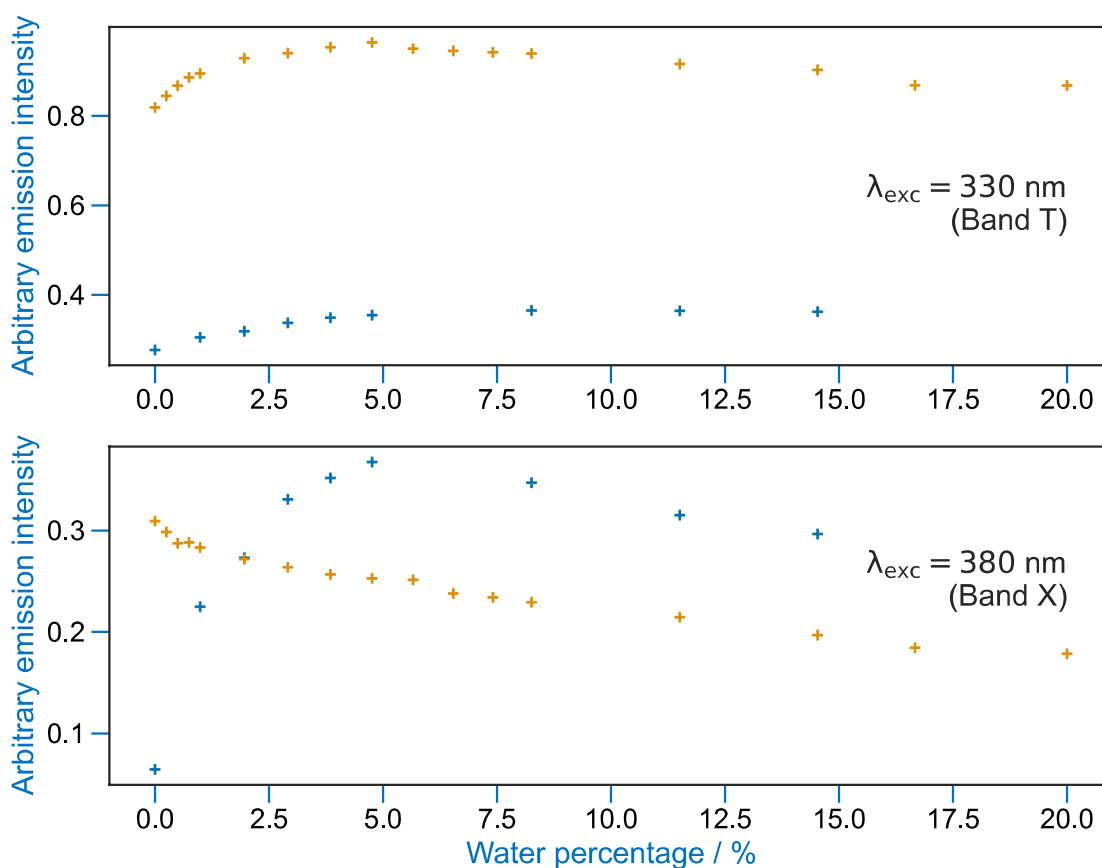


Figure I. 28: Evolution of the fluorescence intensity at 540 nm for methanol (blue) and ethanol (orange) solutions of 2'3HF upon addition of water volumes

Similar effects, although even more sudden, can be observed for DMSO and acetone for which the results are shown on Figure I. 29 and Figure I. 30. The first water addition corresponds to a 0.07% water content which has the effect of significantly decreasing all fluorescence intensities. At around 1% water, the spectrum has converged and starts to vary slowly, once again probably due to a change of the bulk solvent properties.

A striking difference compared to the methanol and ethanol experiments is that the I_N/I_T ratio remained constant upon water addition. To our current state of knowledge, this fact cannot be explained. Indeed, the solvent-assisted PT mechanism that was suggested for 2'3HF-H₂O complexes should also be valid in acetone/water and DMSO/water mixtures, since it also requires a decrease of I_N/I_T upon water addition.

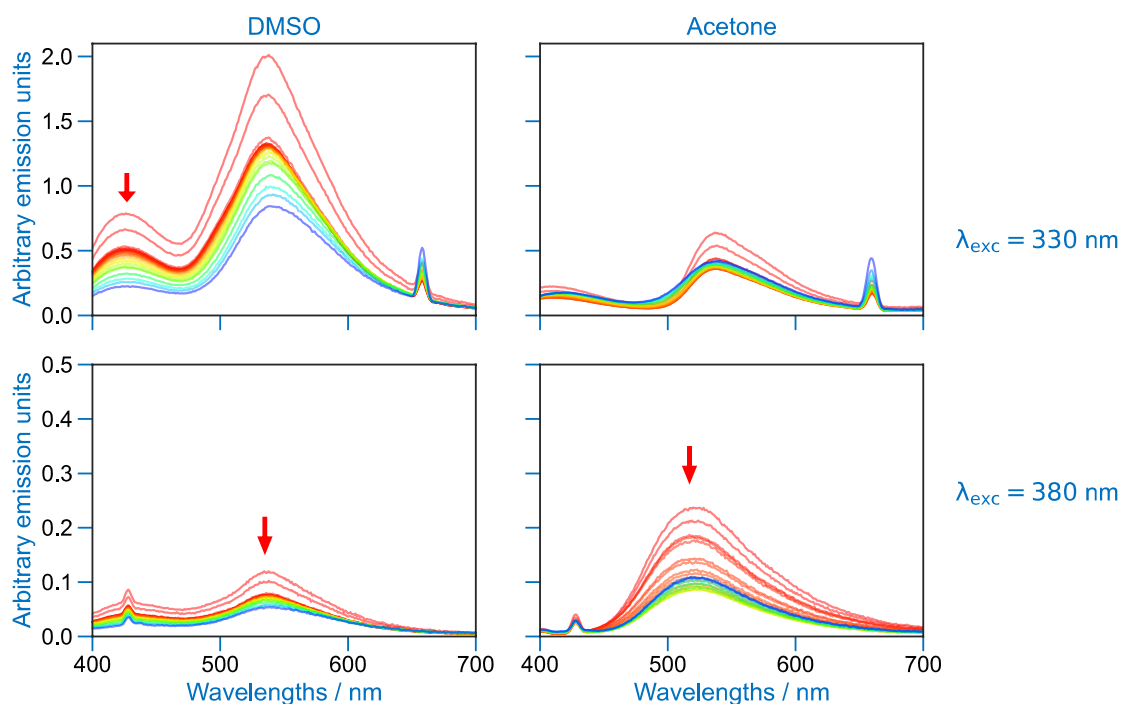


Figure I. 29: Evolution of the emission spectrum of 2'3HF in DMSO and acetone with progressive addition of water volumes. The excitation wavelengths are indicated on the right of the figure

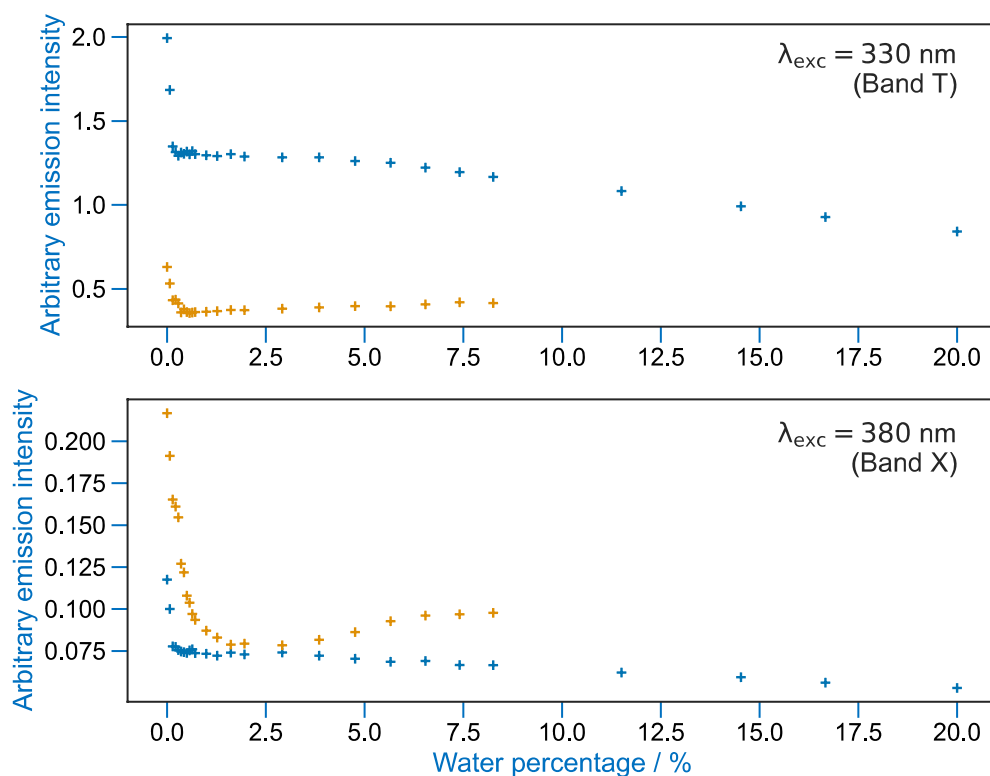


Figure I. 30: Evolution of the fluorescence intensity at 535 nm for DMSO (blue) and acetone (orange) solutions of 2'3HF upon addition of water volumes.

2.3. Discussion and conclusions on the experiments

The experimentation in a variety of polar solvents showed that 2'3HF probably undergone a similar ESIPT mechanism to that of 3HF, which is a process that would occur in a single intramolecular step. This is a reasonable assumption since HBD solvents tend to inhibit the PT so that the normal fluorescence can be observed around 430 nm.

This study once again highlights the complex interactions of 3HF derivatives with surrounding solvent molecules. Indeed, small additions of water amounts to 2'3HF solutions were shown to induce strong effects on the spectra, and in particular, to enhance the PT process. This contradicts the previous assumption. A change of PT mechanism upon water complexation in favour of a solvent-assisted mechanism was suggested to explain this contradiction. Unfortunately, the I_N/I_T was shown to remain constant upon water addition to acetone and DMSO solutions, which seriously challenges this hypothesis. The particular role that water plays on the ESIPT process of 2'3HF remains unknown in this study but it can be hypothesised that the 2' hydroxyl group plays an important role in it, since 3HF does not have this property. Experiments in dry conditions are planned in future work, to shed light on this property.

Another observation that was made through the experiments is that band **X** appears to be dependent on the HBA capabilities of the solvent. This suggests a mechanism involving **IP** formation, in accordance with the vicinity of the excitation maximum of band **X** with that of the anion. Unfortunately, the large spectral distance between bands **X** and **D** is a disturbing observation since **IP** and anion species should have similar emission spectra. Also, the fact that a basic solvent such as DMSO yields no band **X** seriously contradicts the hypothesis.

Based on the observations given above we believe that a revisiting of the **PPTT** hypothesis can be suggested. Indeed, although PT tautomers of 2'3HF (and 3HF) are unstable in the GS, it is plausible for them to be stabilized in solvent-complexed forms. Also, such a **PPTT** tautomer in the GS would have its main absorption band red-shifted relative to that of the normal species, matching the experimental observation. The formation of such a species would require HBA capabilities of the solvent to stabilize the proton on the carbonyl, as well as HBD to stabilize the

negatively charged hydroxyl group. This would perfectly explain that no band **X** was observed in DMSO since, although it is quite basic, it is also the least acidic solvent of those studied ($\alpha = 0.00$). A representation of a such a solvent-complexed PPTT is given on Figure I. 31.

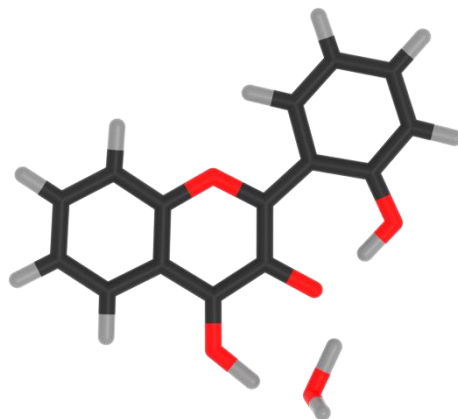


Figure I. 31: Representation of the water-complexed **PPTT**

Finally, upon excitation, the **PPTT** would yield a fluorescence similar to that of the PT tautomer. This is plausible since the **T** and **X** bands are quite close in wavelengths (means of 543 and 527 nm were obtained in this chapter), in contrary to the **IP** emission that must be compared to band **D**, found at even longer wavelengths.

3. Simulation of the solvent

3.1. State of the art

We mentioned how simply adding few hydrogen-bonded solvent molecules in static calculations to describe specific solute-solvent interactions would probably be insufficient. Actually, the accurate description of the solvent effect on electronic spectra has been studied by many groups in the past, which allows to better understand what is computationally required.

For example, our group have been using a semi-explicit solvation model for a few years to significantly improve the description of intra-ligand electronic transitions of metallic complexes. [140]

Also, among the fields of research on organic molecules that require the accurate description of solute-solvent interactions, one can mention the acid-base reactions and the accurate calculation of pK_a . Indeed, a DFT MD approach was for example suggested by Sulpizi and Sprik and applied to a series of acids and bases up to the acid-base species of the 1,4-(hydro)benzoquinone. [185] The technic required the computation of 5–20 ps trajectories of water-filled (60 water molecules with the solute) cubic boxes of around 10 Å. Using another approach and in an attempt to compute the pK_a^* (in the S_1) of coumarins, Houari. *et al.* used TD-DFT and various solvent models to compute Gibbs free energies and plug them in a Förster cycle. [186] An improvement of the calculation of pK_a^* values was observed when switching from an implicit to a semi-explicit (SE) (with 3 water molecules) solvent treatment. On the contrary in the GS, the SE description degraded the results. The authors noted that this defect was probably due to the fact that solvent interactions beyond the first solvation shell were important but not included in their calculations.

Another property that requires a good understanding of solvent effects on the molecule is the ESIPT mechanism. Indeed, in our study of the mechanism in Chapter 2, it was described using the PCM although solvent-specific interactions could have been expected to play a key role in the process. Fortunately, the experimental work detailed in the previous section showed that the band positions were not significantly

impacted by the environment, which is the property that we focused on reproducing with TD-DFT.

Finally, a more complete approach was used by Salaeh et al. for the study of the ESIPT mechanism of 3HF which required a combination of static TD-DFT and ES molecular dynamics. Their results were that the tautomer emission seen in HBD solvents was a solvent-assisted mechanism characterized by longer time constants compared to the full intramolecular mechanism in hydrocarbons. [45]

The objectives of the study were to explore the solute-solvent effects on the absorption spectrum of 2'3HF and to assess the performances of the implicit model. A secondary objective was to evidence the solute-solvent interactions that would red-shift the electronic transitions to have a better idea of what the solvent complex at the origin of band **X** could be. So, it was decided to compute AIMD trajectories from which random conformations of the solute and its solvent cage were sampled. Then, the absorption spectra of the obtained systems could be calculated and compared to the one computed with the implicit model. The technical details on how the AIMD and spectra calculations were performed are given in section 5.2.2 of Chapter 1.

3.2. General shape of the spectrum

Three spectra were computed using three solvent models: Solute-Only (**SO**), Solute-Only-with-PCM (**SO-PCM**), Solute-And-Solvent (**SAS**), and are displayed on Figure I. 32.

On the figure, a 0.068 Boltzmann factor (calculated with PBE0/6-311+G(d,p)) was applied to the **B** spectrum to introduce its lower thermodynamic stability. Also, a gaussian broadening of $\Gamma = 0.07$ eV was used for the transitions.

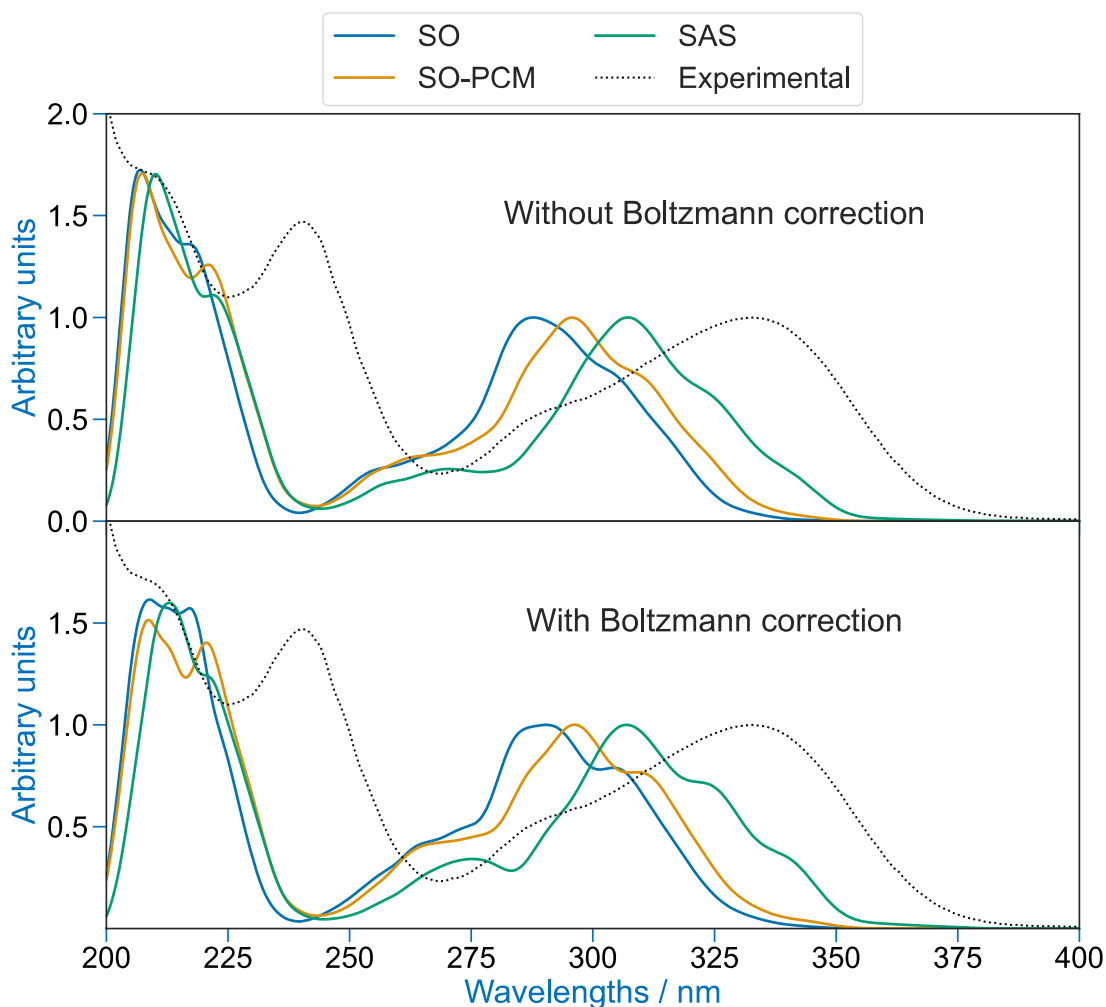


Figure I. 32: Simulated spectra obtained from 500 **A** and 500 **B** geometries with (top) and without (bottom) Boltzmann factors. The spectra were normalized on the absorption maximum of band **I**. The solid line spectra are those calculated using the Solute-Only (**SO**), Solute-Only-with-PCM (**SO-PCM**), Solute-And-Solvent (**SAS**) solvent models.

First of all, the simulated spectra appear to have an underlying structure, similar to a (vibronic structure) which is mainly due to the low sample count. Unfortunately, this problem cannot be solved. Indeed, 1000 geometries is already a rather large amount and 500 conformers are more commonly used in similar computational methodologies. [139, 187, 188]

Overall, the computed spectrum is blue-shifted compared to the experimental one. This is the result of the tendency of LC- ω PBE to blue-shift electronic transitions, as was discussed in the technical details section. Interestingly, it can be seen that the inclusion of PCM recovers part of the shift (around 7 nm) but not all of it, and that including an explicit solvent cage has a great impact on the position of band **I** (around 17 nm). The effect is less pronounced on band **II**.

Apart from the spectral shift, the biggest difference between theory and experiment lies in the red tail of band **I**. Indeed, the theoretical spectra reach 0 absorbance slowly compared to the experimental one which has a “shorter” tail. The difference is biggest for the **SAS** spectrum which suggests for long wavelength transitions to be induced by explicit solvent molecules in direct interaction with the solute. The effect is even more pronounced for the **A** geometry and it may be tempting to believe it has a physical origin. For example, methanol molecules could be thought to be more inclined to form HBs with **A** than with **B**, but caution must be taken here as this may be due to sampling artifacts. Indeed, the randomization might have selected few conformations with red-shifted transitions and large oscillator strengths (although uncommon in the whole trajectory) for the **A** geometry, but not for **B**.

In order to assess the quality of the 1000 geometry pool, it was further subdivided into 5 sets of 500 randomly selected geometries. If the spectra obtained from the 5 random rolls (shown on Figure I. 33) differ from one another, it means that sampling artifacts occur.

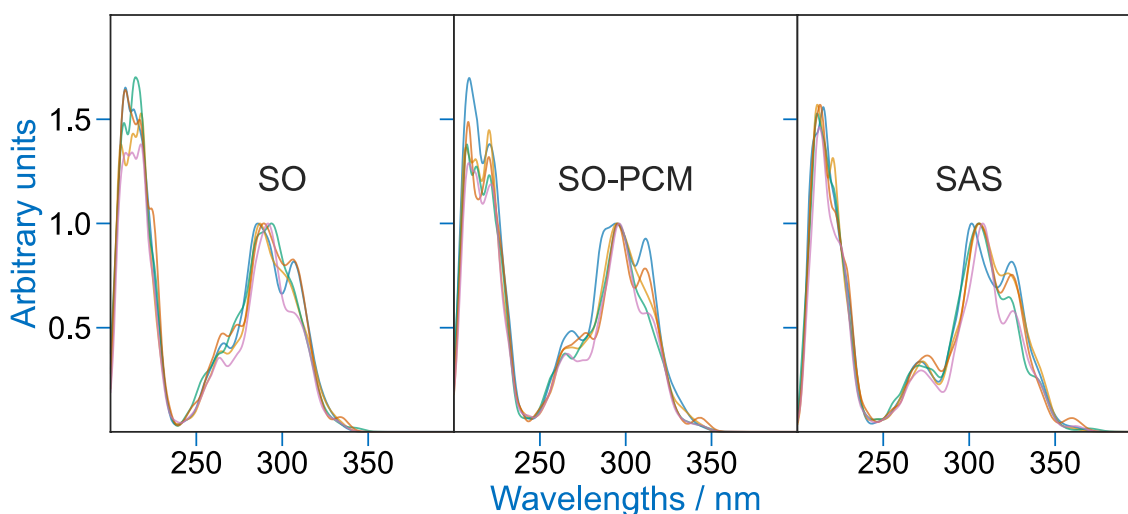


Figure I. 33: Spectra formed from 500 conformations randomly chosen from the 1000 conformations pool

Although the spectrum shape is consistent across the rolls, the long wavelength part of the spectrum is significantly impacted. This result shows that a comparison between **A** and **B** on the ease of intermolecular HB formation cannot be made from the calculations since too few molecules that have an impact on this part of the spectrum were selected during sampling.

Still, some conformations have red-shifted electronic transitions and the inclusion of them (or not) greatly modifies the shape of band **I**. Also, the sharp peak at 320 nm is

present in the **SO**, **SO-PCM** and **SAS** spectra, meaning that it is the instantaneous conformation of the solute in few geometries that is responsible for it. Whether these conformations are solely obtained from random vibration of 2'3HF or induced by neighbouring methanol molecules is unknown to the current state of knowledge. However, the hypothesis of a direct electronic interaction of a methanol molecule with 2'3HF (through charge-transfer for example) can be excluded due to the presence of the peak on the **SO** spectrum.

3.3. Origin of the red tail

In order to assess the influence of the environment of 2'3HF on its absorption spectrum, the correlations between five parameters on the computed wavelength and oscillator strength of the $S_0 \rightarrow S_1$ transition were explored. The parameters are defined as follows:

- N MeOH: The number of MeOH molecules included in the static calculation. This value differs depending on the calculation because of the way the solvation shells were defined and it is important verify that it has no effect on wavelengths and oscillator strengths.
- Dihedral angle (τ): The dihedral angle between the two moieties of the molecule
- $d(O_4 - H_{\text{MeOH}})$: The distance between the O4 (carbonyl) in 2'3HF and any proton in an MeOH molecule
- $d(O_{2'3\text{HF}} - O_{\text{MeOH}})$: The distance between any O atom in 2'3HF and any O atom in an MeOH molecule
- $d(2'3\text{HF} - \text{MeOH})$: The distance between any atom in 2'3HF and any atom in an MeOH molecule.

The results are shown on Figure I. 34.

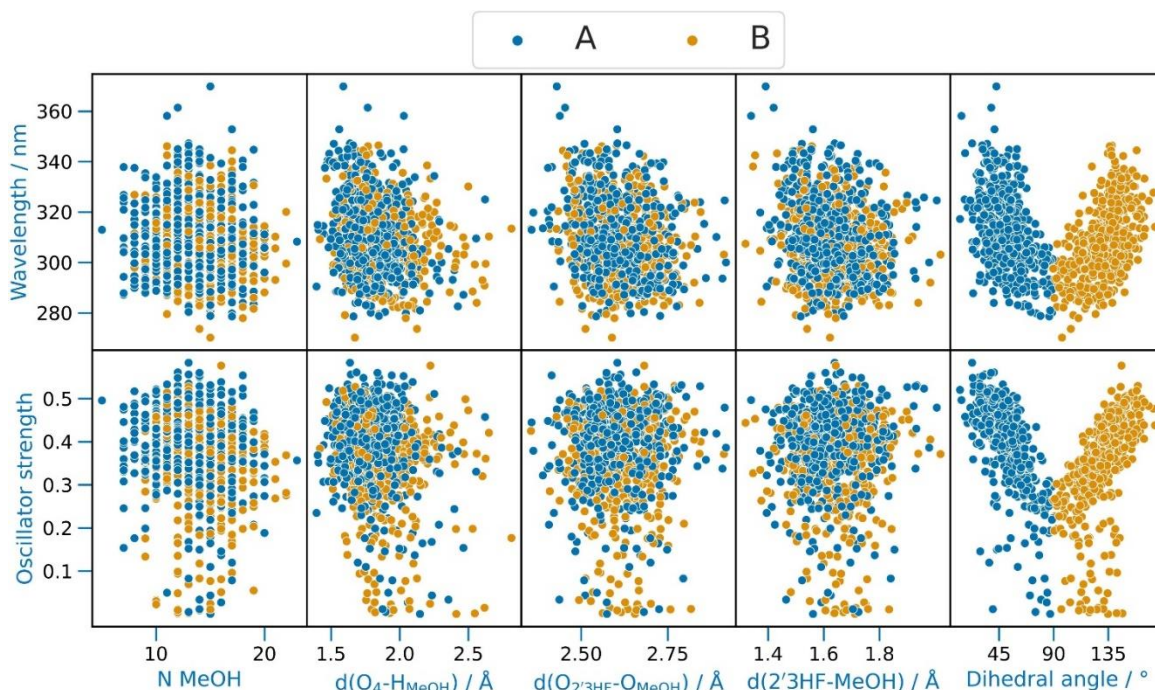


Figure I. 34: Correlation pair plots between the oscillator strength and wavelength of the $S_0 \rightarrow S_1$ transition and one of the five parameters defined in the text (using the SAS spectra). **A**: blue and **B**: orange

A striking preliminary observation is that the transitions span a spectral range of almost 100 nm and 0.6 oscillator strength values. This results from the reproduction of the spectrum using a set of geometries which allows to obtain realistic band widths. Indeed, this approach includes vibrational broadening, an information that the more traditional procedure (using a single optimized geometry) cannot provide.

The number of solvent molecules included in the calculations does not correlate with computed wavelengths and oscillator strengths, meaning that this parameter has no effect on the calculations. This is important and indicates that the solvation shells were properly defined for the use case.

The three distance parameters show structureless scatter plots. This is surprising since these parameters quantify the direct interaction of solvent molecules which could have been expected to induce strong spectral changes.

Finally, the dihedral angle is the only parameter for which significant results are obtained. Two clusters corresponding to the **A** and **B** geometries are evidenced, with a clear correlation with wavelengths and oscillator strengths. The correlation is such that the transition is blue-shifted and prohibited when approaching the 90° dihedral angle. This is expected as the delocalization of the electrons is minimum at the perpendicular geometry and increases upon approaching planarity.

It can be concluded that intermolecular HB formation has no direct effect on the spectrum. On the contrary, solvent molecules seem to have an indirect effect, by “helping” the solute approach planarity, which in turn, has the effect of red-shifting electronic transitions.

3.4. Differences between A and B

On the simulated spectrum on Figure I. 32, it could be seen that the overall shape of the spectrum resembled better that of the experimental one when applying Boltzmann factors. A convincing argument for this is that the shoulder of band **I** (corresponding to $S_0 \rightarrow S_2 + S_0 \rightarrow S_4$) is too far from the maximum of band **I**, which yields a gap on the simulated spectrum, not present on the measurements. Thus, it is worth looking at the differences between the simulated spectra for each conformation. This is done on Figure I. 35.

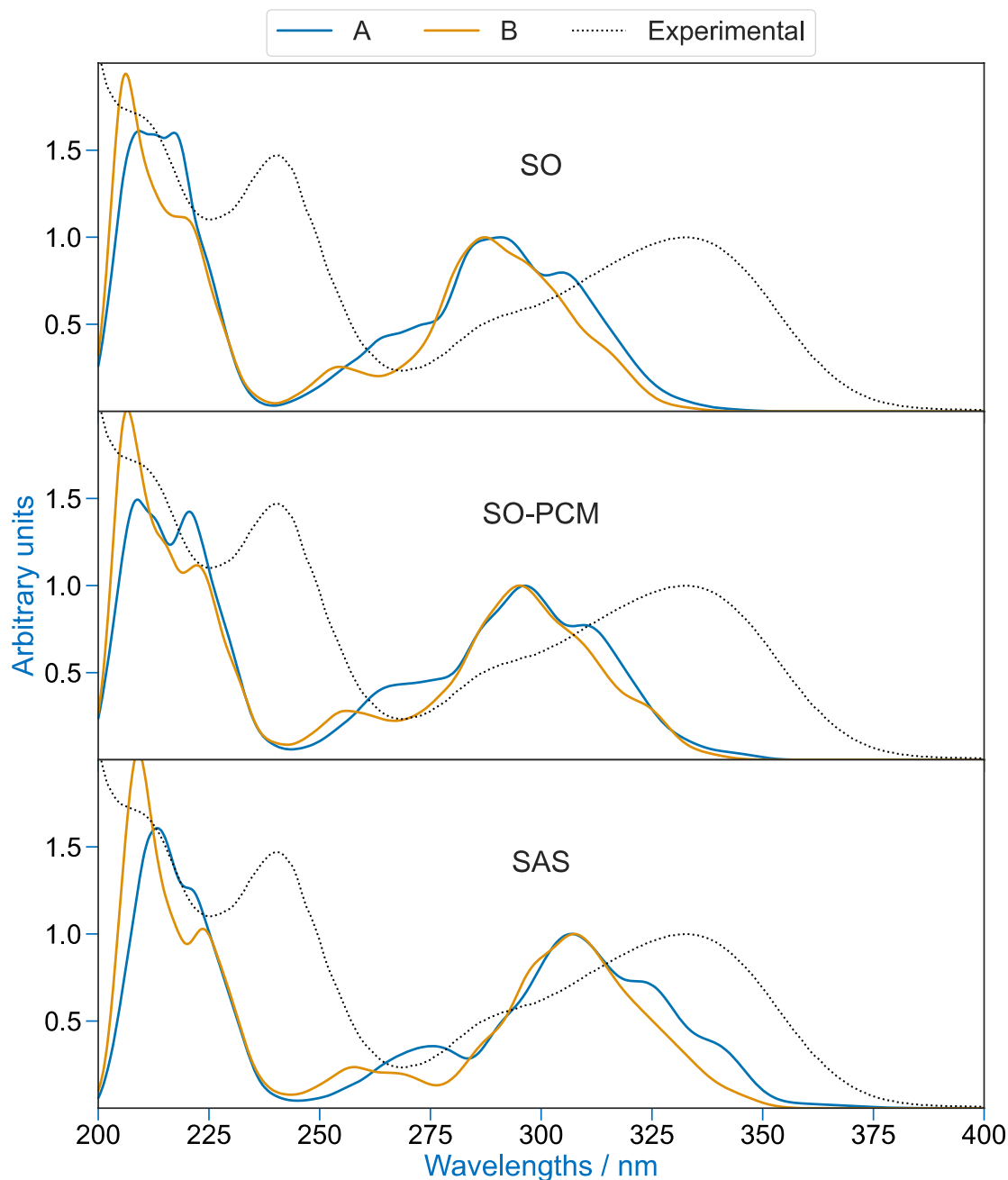


Figure I. 35: Experimental absorption spectrum (black dotted) and simulated spectra for the **A** and **B** (solid blue and orange) geometry ensembles at each level of theory **SO**, **SO-PCM**, **SAS**

Apart from the long-wavelength part of band **I**, which was shown to be due to the randomization, the energy gap between band **I** and its shoulder is shown to be better reproduced using **A** rather than **B**. This observation was also made in Chapter 2 (using PBE0/6-311+G(d,p)) and is the reason why it was chosen to focus on the study of **B**.

From Figure I. 34, it could be seen that **A** and **B** deviated from the plane from around 50° , a value that contrasts with the structural analysis performed in Chapter 2. Indeed, dihedral angles were of 37.4° for **A** and 148.6° for **B** (31.4° deviation from the plane),

whereas the actual mean dihedral angles during the MD runs are 51.2° and 131.0° (49.0°) for **A** and **B**, respectively. In order to properly comment this difference, the **A** and **B** geometries were reoptimized using PBE/6-31++G(d,p), a similar theoretical framework to the one used for the trajectory calculation. This was done with and without PCM to assess its effect and the resulting dihedral angles are given in Table I. 12, compared to the PBE0/6-311+G(d,p) level of theory used in Chapter 2.

	PBE0 Dihedral angle / °		PBE Dihedral angle / °	
	A	B	A	B
Gas	36.1	152.4 (27.6)	33.0	157.5 (22.5)
PCM	37.4	148.6 (31.4)	34.3	152.5 (27.5)

Table I. 12: Dihedral angles between the two moieties of 2'3HF in **A** and **B** optimized using PBE or PBE0 and the 6-311+G(d,p) basis-set (in parentheses are given $180 - \tau$ values to allow a better comparison between **A** and **B**). The values are to be compared with the mean values of 51.2° and 49.0° found during the MD runs for **A** and **B**, respectively

The mean dihedral angles are around 20° higher than those obtained for PBE/6-31++G(d,p) optimized geometries. This is due to the inclusion of a solvation shell in the more complete theoretical framework of AIMD. Moreover, the comparison between the PBE/6-31++G(d,p) and PBE0/6-311+G(d,p) optimized geometries shows that PBE tends to underestimate the dihedral angle in 2'3HF. This means that if any difference was obtained using PBE0 in AIMD calculations, it would be the observation of even bigger dihedral angles. This is an expected result since pure GGAs are known to over-delocalize electrons on the molecule, resulting in a stabilization of geometries that allow such delocalization. [189]

This is an important clarification since the dihedral angle was shown to have a great effect on the $S_0 \rightarrow S_1$ transition energy. Interestingly, the PCM partially recovers the increase of angle but underestimates it severely.

3.5. Performances of the PCM

On Figure I. 36 are plotted the oscillator strengths and wavelengths of the $S_0 \rightarrow S_1$ transition in each conformation with respect to the dihedral angle in each solvent model.

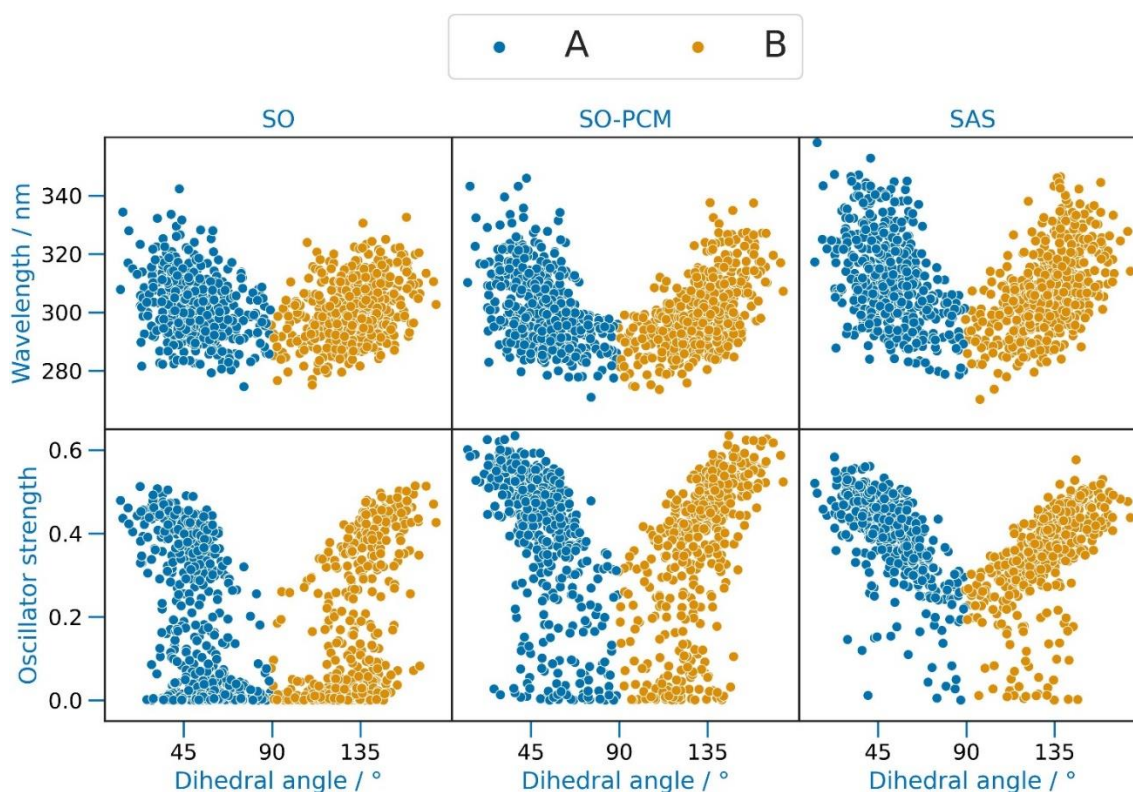


Figure I. 36: Correlation between the dihedral angle and the oscillator strength and the wavelength of the $S_0 \rightarrow S_1$ transition in each solvent model: **SO**, **SO-PCM**, and **SAS**. **A**: blue and **B**: orange

The dihedral angle has a strong effect on the spectral properties of 2'3HF as can be seen from the shape of the scatter plots, which is the result that was highlighted in the previous section. However, there are clear differences in the effects depending on the model. Indeed, the **SO** model yields a less structured scatter plot compared to **SO-PCM** and **SAS**. The inclusion of an implicit or explicit solvent in the calculations appears to be accompanied by an enhanced effect of the dihedral angle on the spectrum.

Thus, the dihedral angle is a key parameter in the description of 2'3HF spectrum which appear to originate from two effects:

- An increase in dihedral angle diminishes electron delocalization on the molecule, which in turn blue-shifts transitions
- An increase in dihedral angle allows solvent molecules to better surround 2'3HF and interact with it.

Interestingly for the latter effect, whereas many 0.00 oscillator strength transitions are observed using the **SO** model, the inclusion of explicit solvent molecules (**SAS**)

makes them acquire intensity. Also, this effect is partially recovered by the PCM (**SO-PCM**).

In summary, the PCM:

- Recovers some of the dihedral angle increase due to the solvation
- Recovers the electronic effect of solvent molecules in the vicinity of 2'3HF

which translates into the appropriate qualitative prediction of wavelength and oscillator strength changes due to solvation.

A final comment can be made on the good performances of the static approach. The electronic transitions of **A** obtained in Chapter 2 were broadened using $\Gamma = 0.25$ eV and compared to the **SAS** spectrum on Figure I. 37. Although the static calculation could be performed in less than an hour (as opposed to few months for the AIMD + 1000 TD-DFT calculations), the performances of the models are similar, if not better for the static theoretical framework. Indeed

- Band **I** and **II** positions are better reproduced. This is particularly a well-known success of PBE0 when calculating excitation wavelengths of regular organic dyes. [190, 191]
- The energy gap between band **I** and its shoulder is better reproduced

The only property that is better described by AIMD is the intensity of band **II** that appears to be underestimated in the static approach.

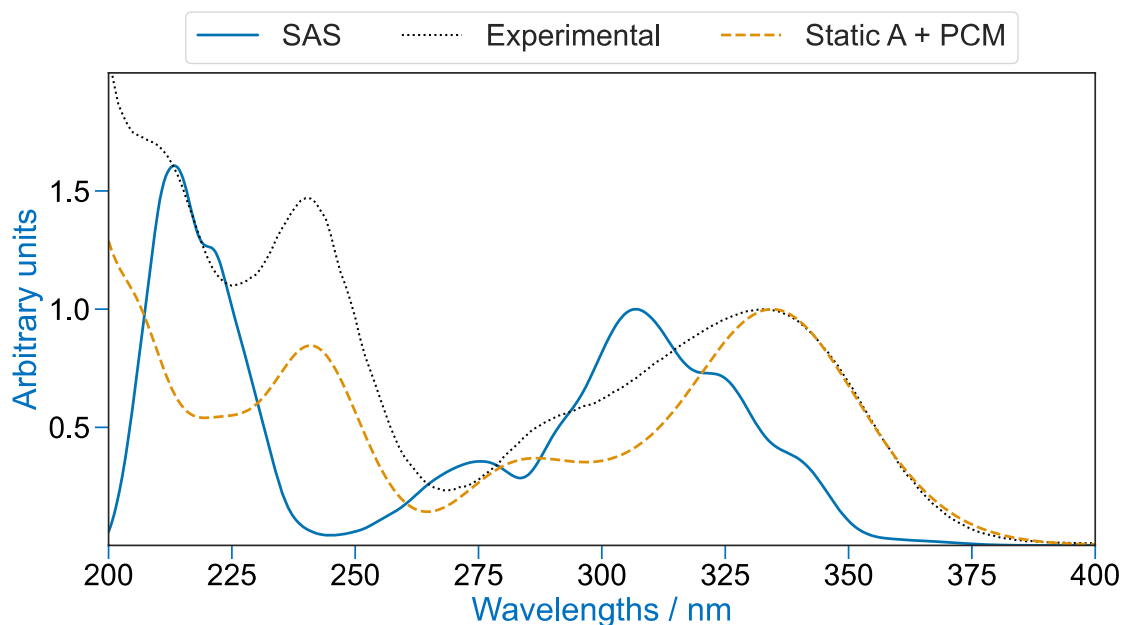


Figure I. 37: Comparison between the **SAS** and static PBE0/6-311+G(d,p) calculations and the experimental spectrum

3.6. Conclusion on the calculation results

In order to better understand the solvent effect on the absorption spectrum and assess the performances of the PCM, expensive AIMD calculations followed by 3000 TD-DFT calculations were performed. The results indicate that the small computational cost of the PCM is of great value considering its ability to recover a good proportion of the solvent interaction with the solute.

The main shortcoming of this computational work is the impossibility to identify a structure for the hypothetical solvent-complex that could be at the origin of band **X**. This is highlighted by the fact that no effect of HBs on the spectrum was evidenced. A probable explanation is that longer simulation times would be required in able to observe proton transfers (intra- or intermolecular) that would form the hypothetical species: **PPTT** and **IP**.

CHAPTER 4.

Metal complexes of 2',3-dihydroxyflavone

The two preceding chapters were dedicated to presenting the structural, acid-base and spectral properties of 2'3HF as well as its interaction with solvents.

In this chapter, we will investigate its interactions with metal cations. The objectives are to determine the fixation site of cations on 2'3HF and the complexation power of this ligand to compare the results with morin. Because our team showed that morin complexed cations on its position **34**, [1, 59, 60] 2'3HF was expected to exhibit the same behaviour.

2'3HF has less acid-base functional groups than morin, so, the deprotonation schemes of its complexes will be easier to understand, that will hopefully give further insights on other flavonol complexes acid-base properties.

The methodology adopted in the study will be the same as that used for morin, *i.e.*, the combination of electronic spectroscopic technics and quantum chemical calculations at the TD-DFT level of theory.

1. Introduction

In Chapter 1, a short introduction on metal-flavonoid complexes was given. The complexation of flavonoids with metal cations influences their properties, so, the understanding of the processes involved is of primary importance for environmental and biological applications. For example, morin can be used as a probe for the quantification of aluminium in human blood, urine, gallstone and soil samples. [192]

As a reminder, some of the most important sites available to cations to bind to flavonoids are represented on Figure I. 38.

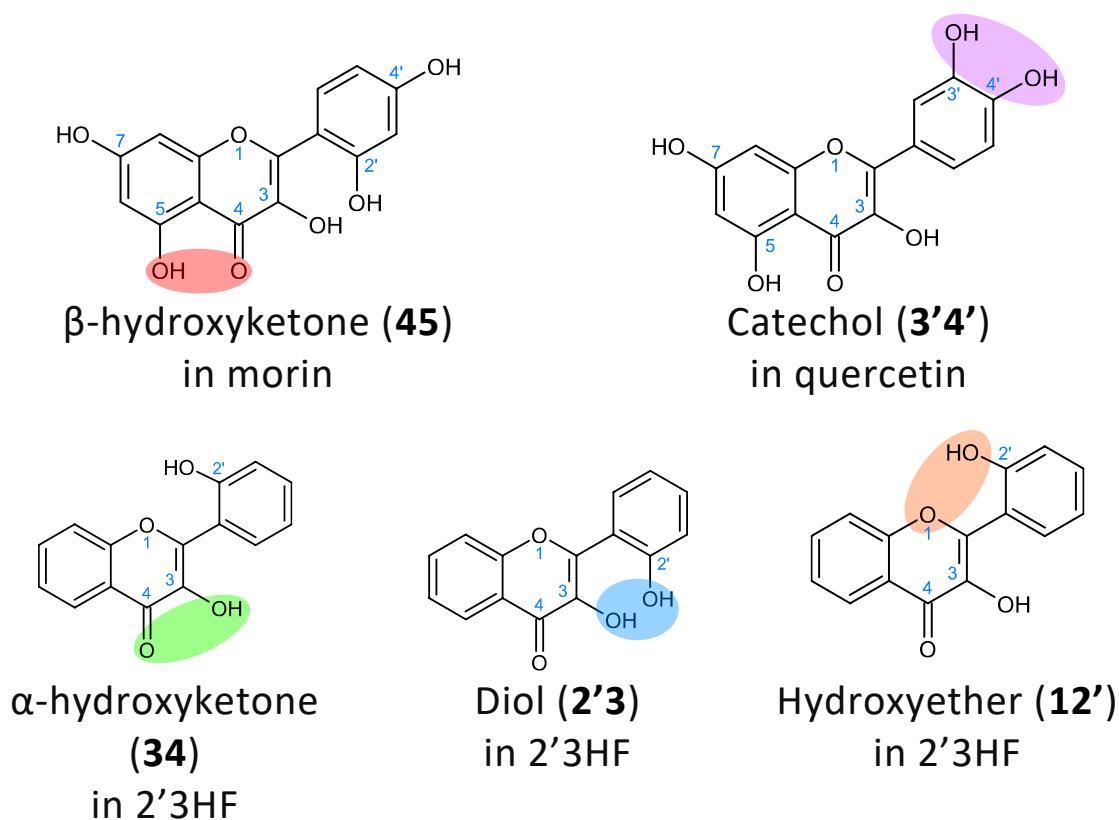


Figure I. 38: Some of the most important binding sites in flavonoids

In 1996, morin complexes of Mn(II) and Zn(II) among others were synthesized and characterized using a variety of techniques. [193] The authors suggested a binding on position **12'**, and highlighted improved anti-tumoral properties to that of morin alone. Instead in 2011, using ^1H NMR and computational techniques, two research groups found position **2'3** as the binding site of zinc. [194, 195] Then later in 2014, another group found site **12'** for the same system. [63] In 2017, using DFT, it was suggested that Cu(II) and Fe(II) bonded morin and quercetin on position **34**. [196] The authors

also showed that the complexes had better in vivo anti-diabetic effects than the ligands alone. Using a combination of experimental and theoretical technics, authors suggested for quercetin to protect DNA from oxidative damage due to copper ions. The reasons suggested are the binding of Cu(II) to quercetin which reduces its catalytic action, as well that the enhanced radical scavenging properties of the quercetin – Cu(II) complex compared to that of the free ligand. [197]

Thus, the flavonoid complexes properties are well studied, but there exist misunderstandings regarding their structure. One of the complexities in such studies relies in the necessity to study each flavonoid separately to take their differences in electronic properties into account. Also, metal cations are often in competition with protons to bind on fixation sites, and each protonation state of the functional groups have to be taken into account in the elucidation process. An example of competition scheme is represented on Figure I. 39.

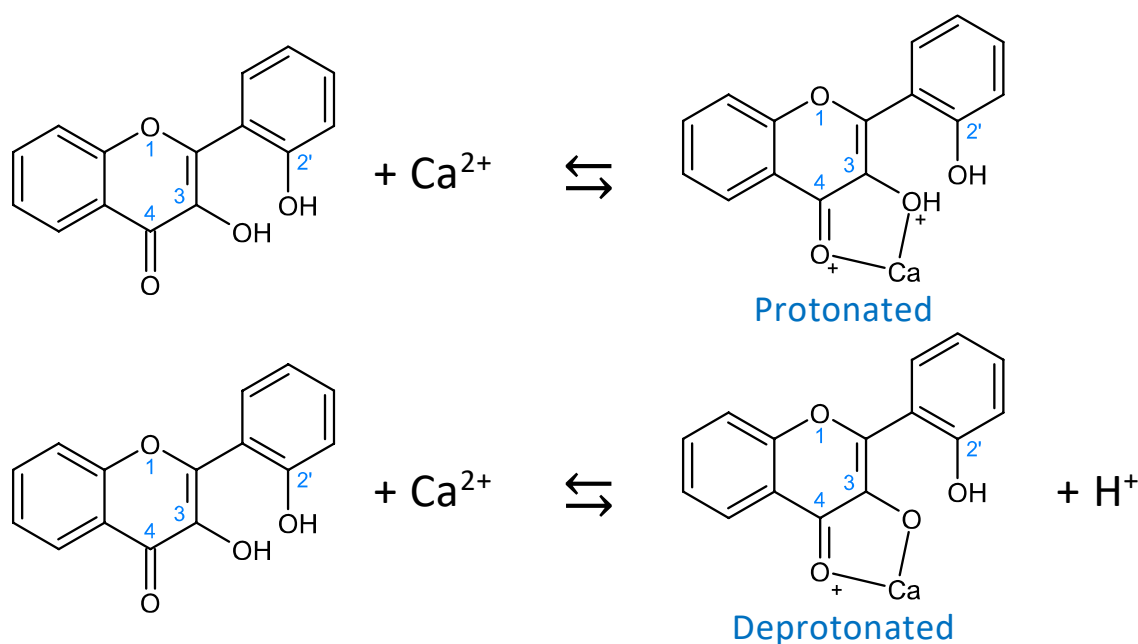


Figure I. 39: Depiction of a metal cation – proton competition in 2'3HF

For example, a research group suggested in 2020 for Cu(II) to bind to quercetin on **34**, and to morin on **45**. [198] However, the team considered the **34** site in its protonated version, overlooking the stabilizing inter-ring interaction that our group suggested the same year. [59] Recently, in an interesting work from early July 2022, a research group synthesized a morin – Zn(II) complex and embedded it in hydrophilic nano-formulations which enhanced the solubility (and thus bioavailability) of the complex for anticancer applications. [199] Using X-ray

crystallography, they found that Zn(II) bonded morin on position **34**, as described by our group.

About calcium, our group published an article in 2020 on the morin – Ca(II) complex and its protonation states. We showed that the structure of the complex was probably that of a **34** complex with deprotonated O3. Subsequent deprotonations of a solvent molecule in the coordination sphere of the metal and of O7 were found while increasing the pH. Unfortunately, on the basis of comparison between computed and measurement spectroscopic data, there was an ambiguity with the possible complexation on site **2'3** (in its fully deprotonated scheme). Thus, the differentiation between these two hypotheses required thermodynamic computations. Complexes **2'3** and **34** do not have the same chemical formula (complex **34** has one more proton), so the calculation of the energies has to include the solvation free energy of the proton (taken from ref [200]) which adds an error in the calculation. Thankfully, the computed energy differences were large enough, (*i.e.*, 32.2 kcal mol⁻¹, 38.2 kcal mol⁻¹ and 40.9 kcal mol⁻¹ for the protonated, mono-deprotonated and bi-deprotonated forms, respectively), to assign the **34** as the actual one with little doubt.

The same study was performed on Zn(II) and Mn(II) of which the results can be found in Dr. Jani-Thaviligadu's thesis. [60] In apparent pH = 4.2 medium, it was found that morin formed 1:1 complexes with Ca(II), Zn(II) and Mn(II) with conditional complexation constants of $\log\beta_{ML} = 1.50, 4.83$ and 4.40 , respectively.

The most probable complexation site is the **34** site in all cases. For Mn(II), the coexistence of the **34** and **2'3** complexes is suggested.

The finding that the inter-ring interaction in morin is at the origin of its unusual complexing power that led us to study 2'3HF. The complexing power of 2'3HF has been studied in the past and more specifically, its aluminium complexes. Porter and Markham in 1970 suggested the possibility of deprotonation of 2'3HF at unusually low pH with the remaining proton lying between oxygen atoms 2' and 3 (as confirmed by our study in Chapter 2). They assumed that this left the **34** binding site easily accessible to Al(III) for complexation. [67] However, it must be emphasized on the fact that the deprotonation of a functional group does not necessarily lead to complexation on the same position. A famous example of this is the complexation of metal cations with caffeic acid on the catechol rather than on the carboxylic acid, despite its more labile proton. [201–204]

In this chapter, the Ca(II), Zn(II) and Mn(II) complexes of 2'3HF are studied. The objectives are to verify that 2'3HF indeed exhibits similar complexing properties as morin, but also to study the deprotonations of the considered complexes. We also hope to obtain less ambiguous results on the differences between complexes **2'3** and **34**.

The ten structures optimized for the 2'3HF- Ca^{II}(H₂O)₂ complex can be seen on Figure I. 40. and the structures with other cations and solvation shells are shown on Appendix 1, Appendix 2 and Appendix 3.

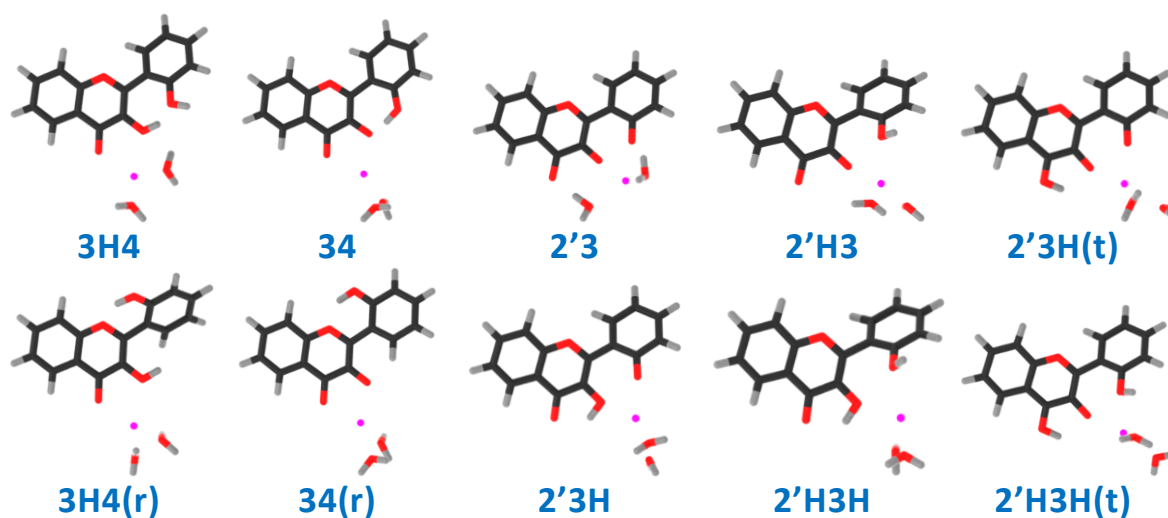


Figure I. 40: The optimized 2'3HF- Ca^{II}(H₂O)₂ structures

The nomenclature for the optimized complexes is the following:

- The binding site is identified by the oxygen atoms that chelates the cation, giving the three possible sites for 2'3HF: **12'**, **2'3** and **34'**
- If an oxygen atom is protonated, his atom number is followed by **H**: **12'H**, **2'H3**, **2'3H**, **2'H3H**, and **3H4**
- 2'3HF has two conformers (**A** and **B**, according to the nomenclature introduced in Chapter 2) where the phenyl ring is rotated around the inter-ring bond. So, complexes with ligands in their **B** geometry are indicated by **(r)**: **34(r)**, **3H4(r)**
- Tautomer geometries are also possible and indicated by **(t)**: **2'H3H(t)**, **2'3H(t)**

2. Acidic medium

The starting point of the methodology developed in our group for metal-ligand interaction studies is the recording of electronic spectra upon addition of metal salts to an acidic solution of ligand. Experimenting in acidic media is necessary to limit the anion concentration so that only the neutral ligand can be observed on the spectrum. This simplifies the identification of potential complexes that would be formed during the complexometric dosage. The evolution of the UV-visible absorption spectrum upon addition of a cation salt at fixed pH = 4 is shown on Figure I. 41. Upon addition of the salt, a bathochromic shift of around 55 nm occurs in each case and isosbestic points can be observed, indicating an equilibrium between two absorbing species.

In order to investigate the stoichiometry of the complexes, the spectrum matrices were plugged into the ReactLabTM chemometrics tool. In all three cases, the (model free) SVD and EFA analyses confirmed the presence of only two absorbing species: the ligand and the complex. Next, ReactLabTM was fed with chemical reaction models corresponding to 1:1, 1:2 and 2:1 complexes. The 1:1 stoichiometry models fitted successfully, to yield $\log \beta_{2'3HF-M}$ values that are given in Table I. 13 compared to those found for the morin-M systems.

	$\log \beta_{2'3HF-M}$		
	Ca(II)	Mn(II)	Zn(II)
2'3HF (pH = 4.0)	4.03	4.35	4.19
Morin (pH = 4.2)	1.50	4.83	4.40

Table I. 13: $\log \beta_{2'3HF-M}$ values obtained for the 1:1 complexes of 2'3HF and morin

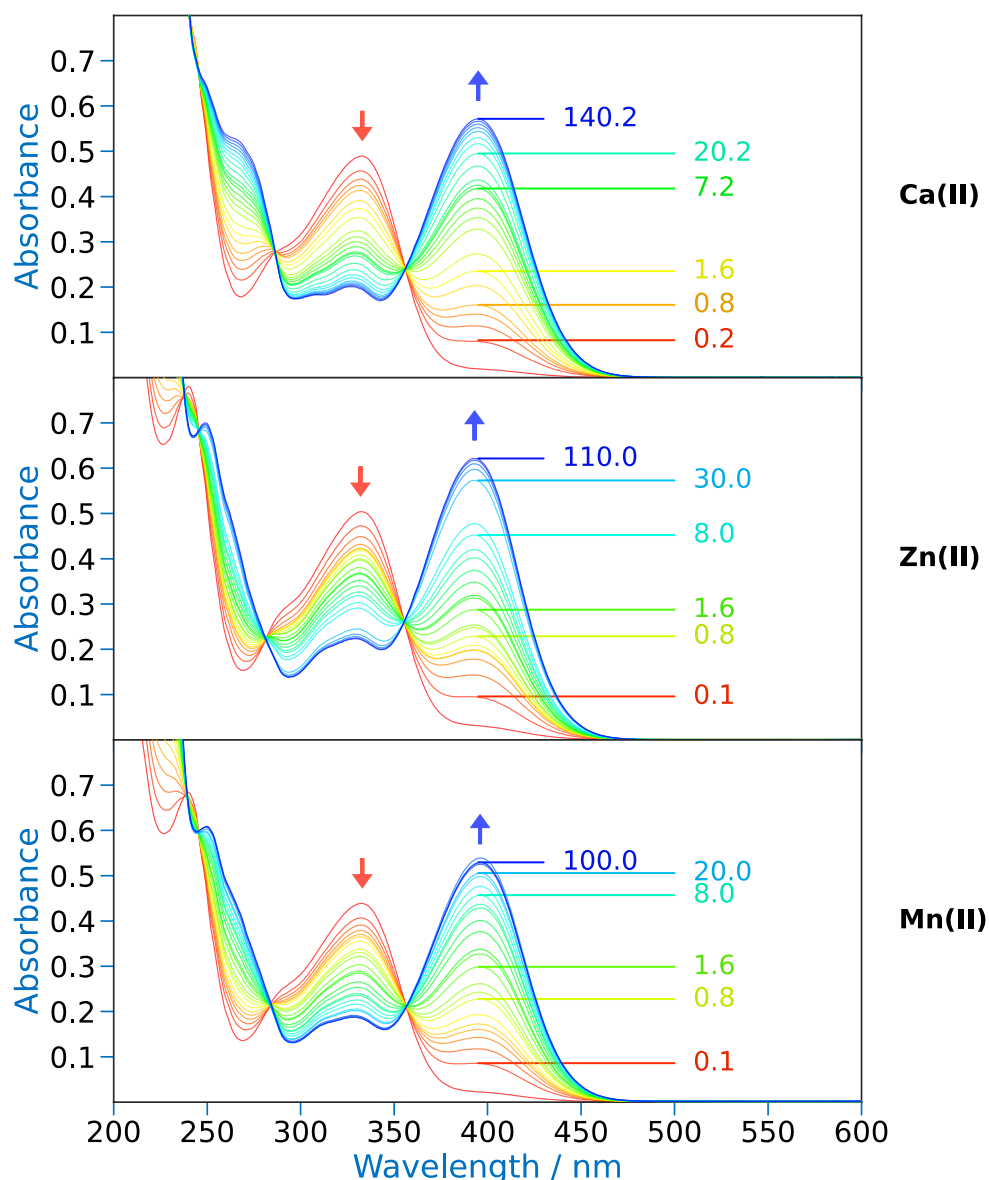
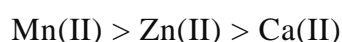


Figure I. 41: Evolution of the UV-visible absorption spectrum upon adding a Ca(II), Zn(II) or Mn(II) solution to a 2'3HF methanol solution at fixed pH = 4.0. Some of the molar ratios $R_{M/L}$ are on the figures

First of all, 2'3HF has lower affinities for Zn(II) and Mn(II) compared to morin. This difference can easily be explained by the pH conditions since more basic media tend to facilitate the metal complexation. However, morin appears to have a lower affinity for Ca(II), which is hard to explain. Indeed, all cations have a similar affinity with 2'3HF, the $\log \beta_{2'3HF-M}$ being ordered as follows



Also, we suggested for Mn(II) to be able to form two complexes with morin whereas only one appears for 2'3HF.

The chemometrics treatment allows to obtain the absorption spectrum of each complex, shown on Figure I. 42. The spectra are very similar both in the shape of the absorption bands, in wavelengths, and in molar extinction coefficients. This observation suggests that the same chelation site is involved in the binding of all three metal cations. On the same figure, the measured absorption spectrum of 2'3HF anion (**dep**) is also compared to the complexes.

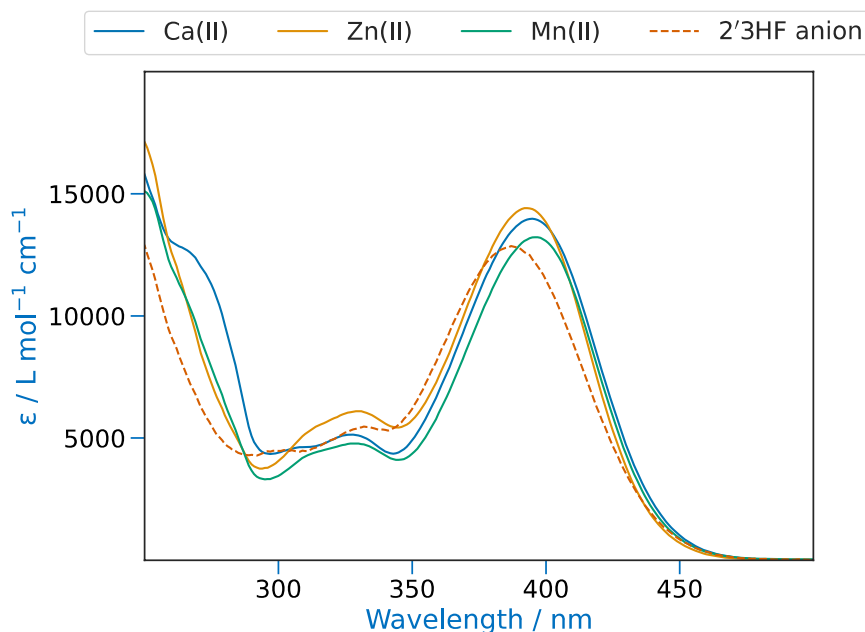


Figure I. 42: Comparison of the absorption spectra of all 2'3HF complexes as well as 2'3HF anion

This anion appears to have very similar electronic absorption properties to those measured for the complexes. The only difference that can be highlighted is a slight displacement of the band, the absorption maxima for band **I** of the four species being 387, 393, 395 and 396 nm for **dep**, 2'3HF-Zn, 2'3HF-Ca, and 2'3HF-Mn, respectively.

Simultaneously to the recording of the UV-visible absorption spectra, the emission spectra were recorded by exciting in the absorption band of the free ligand ($\lambda_{\text{exc}} = 335$ nm) and in that of the complex ($\lambda_{\text{exc}} = 395$ nm). The 2'3HF-Mn complex is non-fluorescent as opposed to 2'3HF-Ca and 2'3HF-Zn, a particularity that will have to be investigated using computational methods. The fluorescence spectra evolution during titration by Ca(II) and Zn(II) solutions is shown on Figure I. 43.

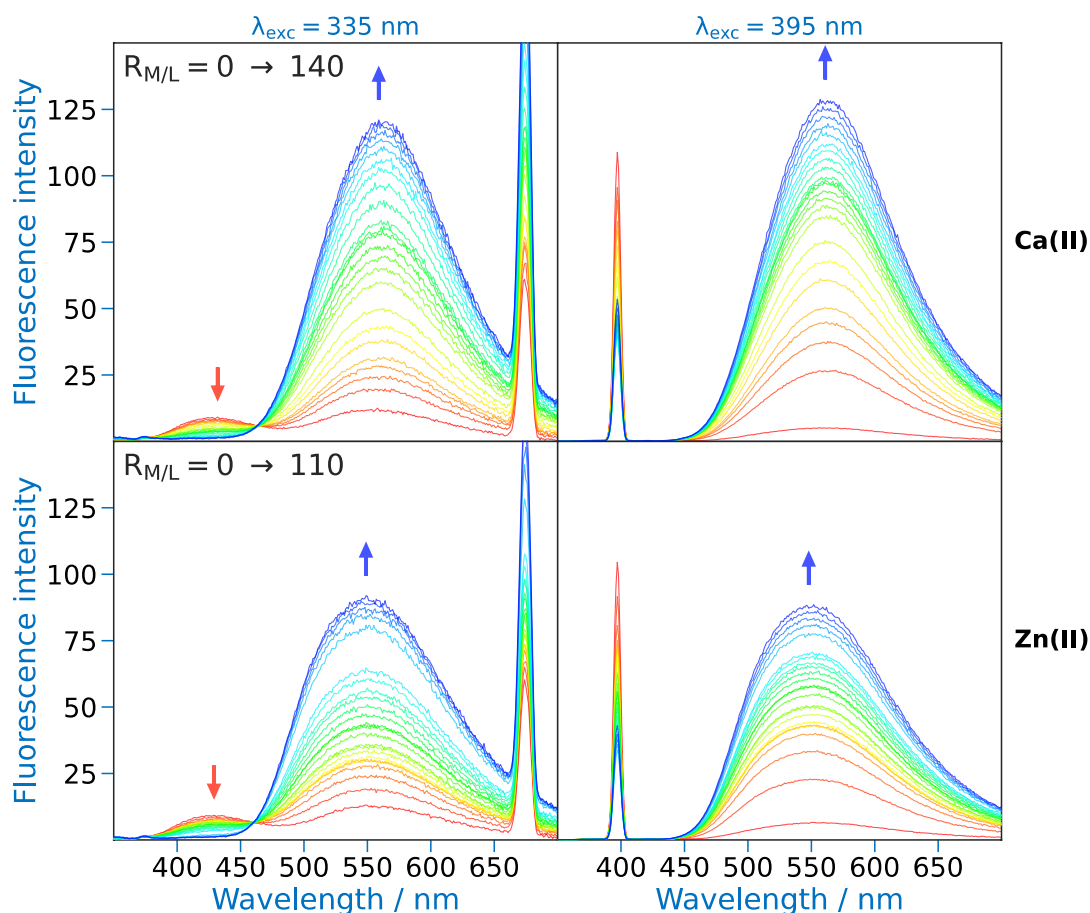


Figure I. 43: Evolution of the fluorescence emission spectrum (left: $\lambda_{\text{exc}} = 335 \text{ nm}$, right: $\lambda_{\text{exc}} = 395 \text{ nm}$) upon adding Ca(II) or Zn(II) solutions to a 2'3HF methanol solution at fixed pH = 4.0.

Prior to any cation addition, the fluorescence spectrum of the lone ligand can be seen. It consists of bands **N** and **T** (normal and PT tautomer forms) when exciting at $\lambda_{\text{exc}} = 335 \text{ nm}$, and to a mixture of bands **D** and **X** (anion and solvent-complex) when exciting at $\lambda_{\text{exc}} = 395 \text{ nm}$. Upon metal Ca(II) or Zn(II) addition, the spectrum of the ligand gives place to that of the complex, which consists in a single broad fluorescence band located at 559 and 549 nm, for calcium and zinc, respectively. As for the absorption spectra, the fluorescence spectra of the complexes are similar to that of 2'3HF anion (566 nm). In addition, it is interesting to note that a decrease in pH is observed when the metal salt is added during the titration, requiring the addition of NaOH to keep the pH constant. This observation suggests that the complex is formed with partial or total deprotonation of the ligand. Interestingly, the emission maxima of the complexes are smaller than that of the anion, although the opposite behaviour is observed in absorption spectroscopy. This leads to smaller Stokes shifts of 7428 and 7231 cm^{-1} , for Ca(II) and Zn(II), respectively, compared to the 8172 cm^{-1} for 2'3HF anion.

3. Acid-base dependency

When varying the molar ratio of a pH = 4 solution, it could be observed that a 1:1 complex was formed. In flavonols, the complexation is generally highly dependent on pH because the cation is in competition with the proton to bind the molecule on a site. The study of the pH dependence of the complexes is thus of great importance.

For this reason, the pH of $R_{M/L} = 2$ solutions were varied and the complexation reactions were monitored using UV-visible absorption and fluorescence spectroscopies. The evolutions of the absorption spectra are reported on Figure I. 44. For better visualization, the spectra sets were splitted into two pH ranges.

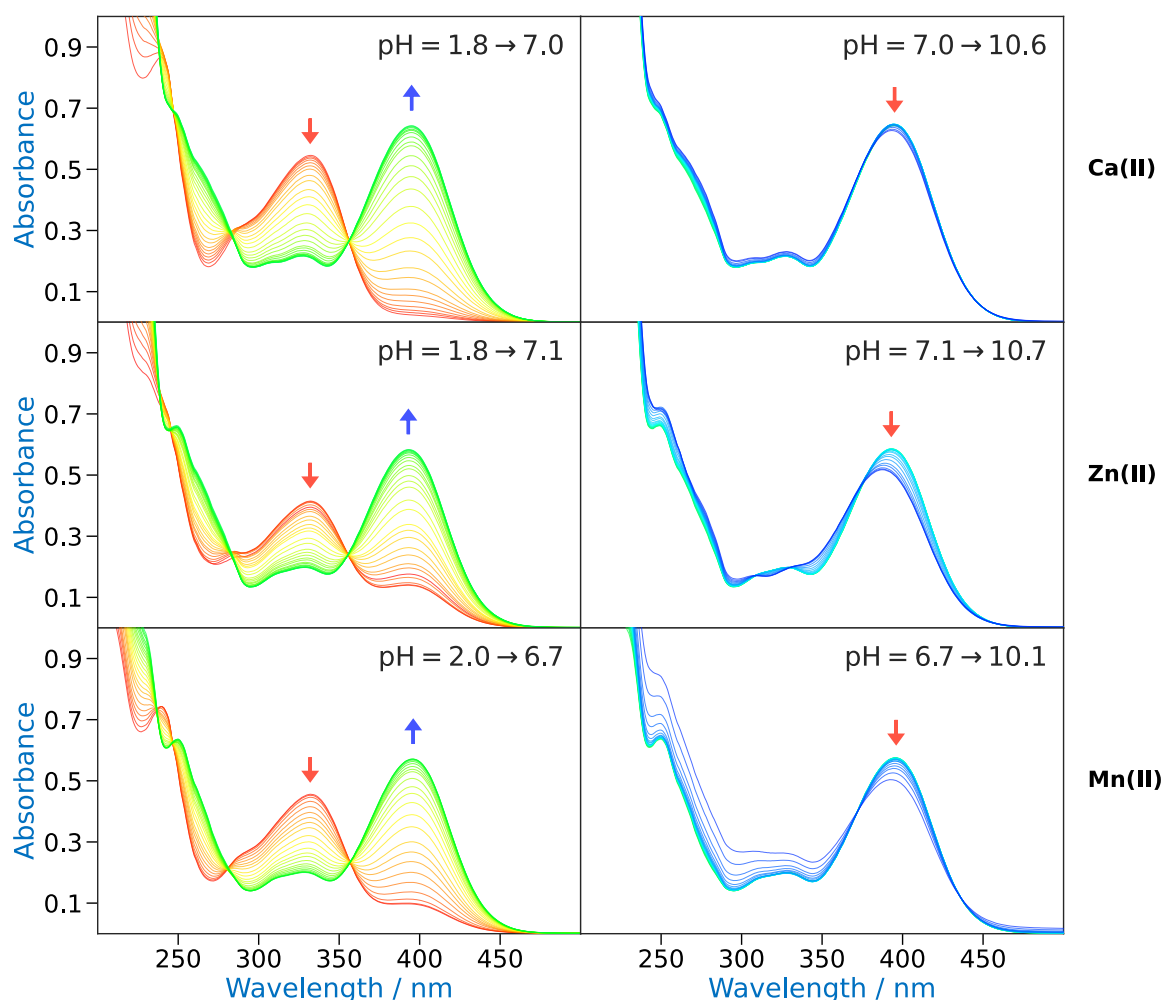


Figure I. 44: Evolution of the UV-visible absorption spectrum upon variation of the pH of a Ca(II), Zn(II) and Mn(II) and 2'3HF solution with a molar ratio $R_{M/L} = 2.0$. pH ranges are indicated at the top right of each plot

Even though a strong competition occurs at low pH values of around 2.0, small quantities of complexes are still observed (except for Ca(II) for which 2'3HF has the lowest affinity). This shows the unusual complexing power of 2'3HF, since few flavonoids are able to form complexes in such acidic media. As the pH increases, the absorption band of the complex grows as in the previous experiment, with the same absorption maxima, characteristic of the 1:1 complex. This behaviour is observed until around 7.0 pH value for which the formation of the 1:1 complex is complete.

Around pH = 9.5, a new phenomenon is observed. In all three cases, hypochromic and hypsochromic effects are observed with wavelength maxima moving to around 393, 387 and 392 nm for Ca(II), Zn(II) and Mn(II), respectively, although it can be assumed that the shift is not complete because of the impossibility to go to higher pH values using NaOH in methanol. In order to better visualize the phenomenon, the evolution of the absorbance at $\lambda_{\text{abs}} = 385$ nm with respect to pH is plotted on Figure I. 45.

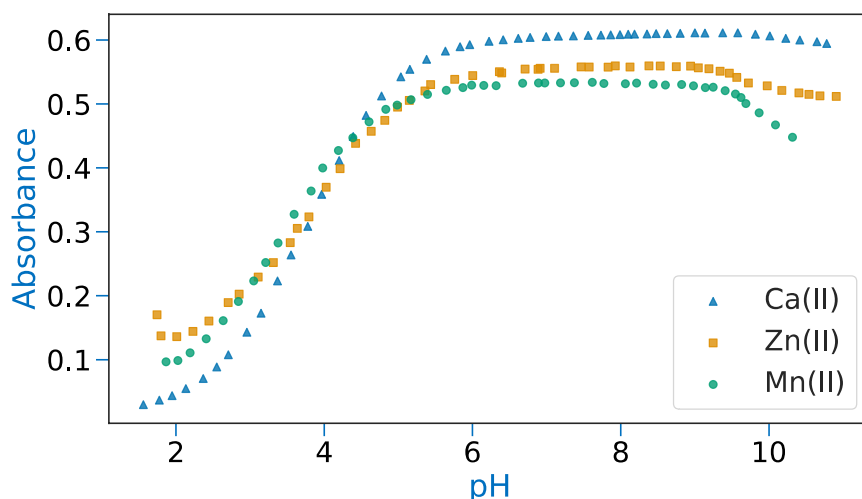


Figure I. 45: Evolution of the absorbance at $\lambda_{\text{abs}} = 385$ nm upon the increase in pH of Ca(II), Zn(II) and Mn(II) and 2'3HF solution with a molar ratio $R_{M/L} = 2.0$

Once again, the almost identical complexation properties of 2'3HF with all three cations is highlighted. On the figure, the two first measurements on the 2'3HF–Zn system are off from the others. This is due to the fact that the solution was prepared at neutral pH, then brought to acidic medium. The decomplexation having rather long kinetics, it can be assumed that the equilibrium was not attained at the recording of those spectra.

On the figure, the hypochromic effect at pH = 9.5 is better observed and three phenomena can be suggested to explain it:

- (a) The deprotonation of the ligand in the 1:1 complex
- (b) A change of site by the cation
- (c) The formation of a 2:1 complex
- (d) The deprotonation of a solvent molecule in the coordination sphere of the 1:1 complex

The hypotheses will be discussed when comparing the experimental and calculation results. Finally, a brown precipitate is observed for the Mn(II) measurements. This results in an increase of the background above 450 nm, due to Mie scattering. The stoichiometry of the 2'3HF complex is 1:1 although a molar ratio of 2.0 was used in the experiments. Thus, traces of free Mn(II) and its hydroxides and carbonates are still present in the medium, which are known to get oxidized by O₂ to form non-soluble species at around pH = 8.5 (in water). [205, 206]

The evolution of the fluorescence spectrum is shown on Figure I. 46. Once again, the (alkaline) 2'3HF–Mn(II) system is not fluorescent and the spectra are not shown. A similar behaviour to the one in absorption is observed, with the exception of the apparition of a small red-shift instead of a hypsochromic effect.

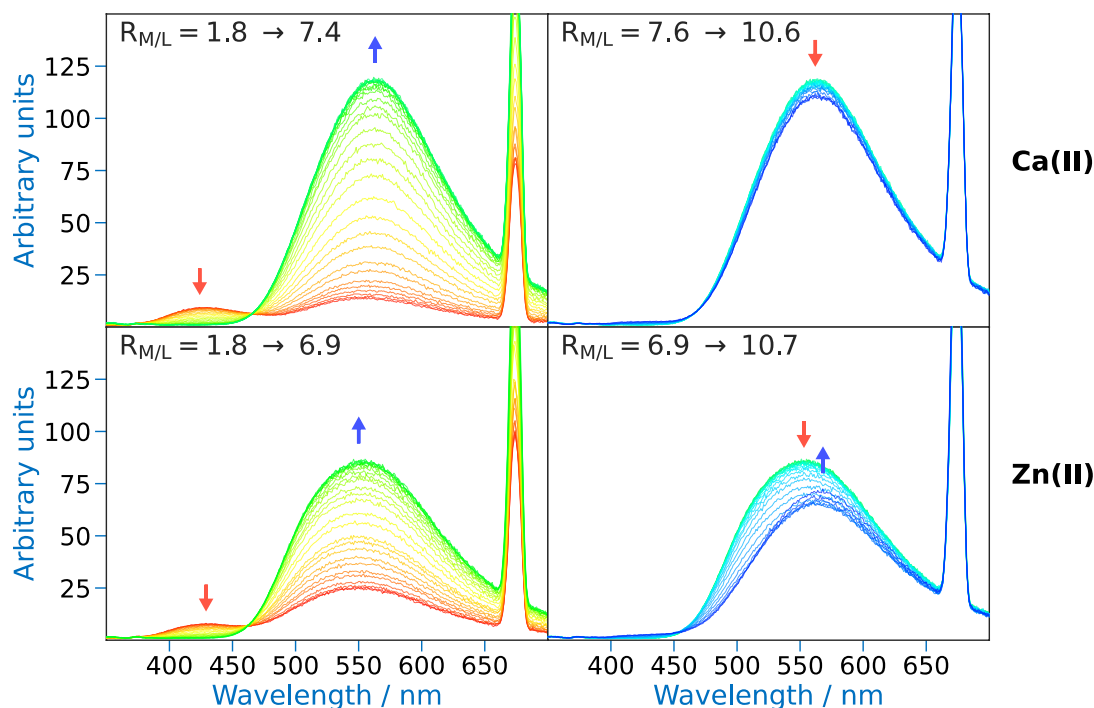


Figure I. 46: Evolution of the fluorescence emission spectrum ($\lambda_{exc} = 335$ nm) upon varying the pH of a Ca(II) or Zn(II) and 2'3HF solution with a molar ratio $R_{M/L} = 2.0$. pH ranges are indicated at the top left of each plot

The fluorescence of the complexes moves to 564 and 563 nm for Ca(II) and Zn(II), respectively, although again, the pH was not high enough to complete the phenomenon. Overall, the effect of pH on the spectra is rather small and can be summarized in Table I. 14.

	Absorption / nm (eV)	Fluorescence / nm (eV)
First species		
Ca(II)	395 (3.139)	559 (2.218)
Zn(II)	393 (3.155)	549 (2.258)
Mn(II)	396 (3.131)	
Second species		
Ca(II)	393 (3.155)	564 (2.198)
Zn(II)	387 (3.204)	563 (2.202)
Mn(II)	392 (3.163)	
Spectral shift		
Ca(II)	-2 (0.016)	5 (-0.020)
Zn(II)	-6 (0.049)	14 (-0.056)
Mn(II)	-4 (0.032)	

Table I. 14: Summary of the experimental wavelengths on the 2'3HF-M complexes

4. Binding site hypotheses

4.1. The “acidic” medium complex

4.1.1. Absorption vs. vertical transitions

As stated in the introduction of this chapter, the procedure used to elucidate the binding site of cations on flavonols is to calculate the electronic transitions of all possible bidentate complexes, and to compare them to the experimental spectra. As a reminder, the three available binding sites of cations on 2'3HF are shown on Figure I. 47. As stated in the introduction, the 12' complex geometries failed to optimize with any cation and was excluded from the study. Also, the protonation state of the oxygen atoms is important, meaning that 10 complex types can be optimized: **3H4**, **34**, **2'3**, **2'H3**, **2'3H(t)**, **3H4(r)**, **34(r)**, **2'3H**, **2'H3H**, **2'H3H(t)**.

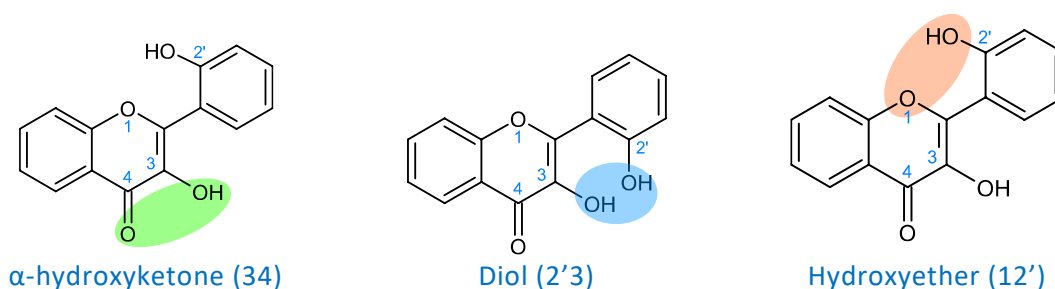


Figure I. 47: The three available binding sites on 2'3HF

Already, it can be seen from all of the transitions in Appendix 5, Appendix 6 and Appendix 7, that the number of water molecules in the coordination sphere of the cation has close to no effect on the electronic transitions. Thus, only the results for 4 water molecules will be given and discussed, unless explicitly stated.

The hypothesis of position 34

In morin, the complexation on position 34 is the most probable so it can be expected to be important in 2'3HF as well. The electronic transitions (represented by vertical lines) for the **34** and **34(r)** complexes are shown on Figure I. 48.

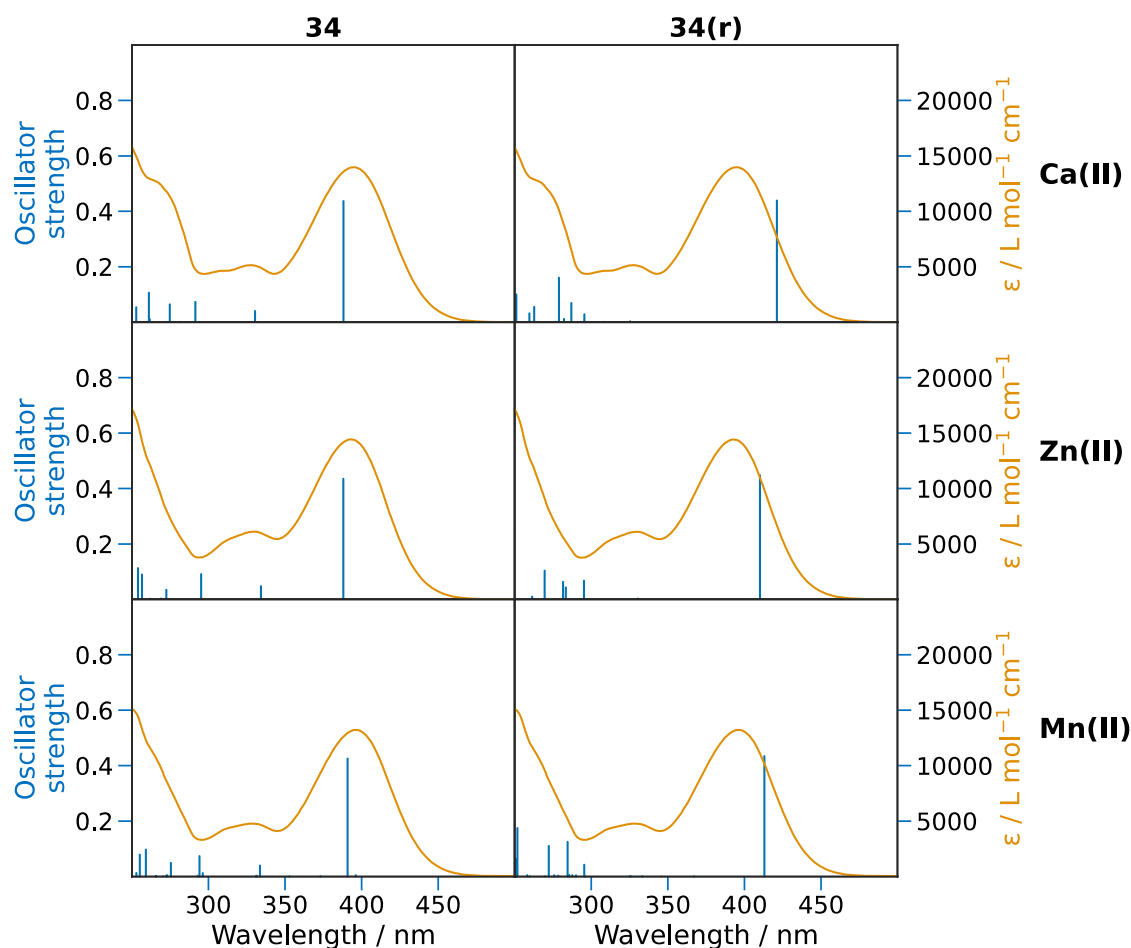


Figure I. 48: Comparison between the experimental absorption spectrum of the 2'3HF-M (Ca(II), Zn(II) or Mn(II)) complex and the computed electronic transitions of the optimized **34** and **34(r)** complexes

The results for the **3H4** and **3H4(r)** complexes are shown in appendix and were not included here because the transitions cannot reproduce the experimental spectrum. For the **34** and **34(r)** complexes, it can be seen that the transitions reproduce well spectrum, although the latter has the deficiency of not reproducing well the band at 330 nm. For 2'3HF, as for morin, it is observed that the **34** complex is promising.

The first electronic transitions of **34** are computed as 388, 388 and 391 nm (0.06, 0.04 and 0.04 eV absolute errors with respect to the experimental absorption maximum) for Ca(II), Zn(II) and Mn(II), respectively. The reproduction is better than for **34(r)** which has transitions of 421, 410 and 413 nm (0.19, 0.13 and 0.13 eV errors). However, the phenyl is free to rotate and both species can be expected to coexist in solution, similarly to the lone ligand.

The hypothesis of position 2'3

The possibility of complexation on position 2'3 is also quite interesting and may explain the unusual complexing capabilities of 2'3HF and its derivatives. According

to the figures in Appendix 5, Appendix 6 and Appendix 7, three structures yield electronic transitions that could match the experimental spectra: **2'H3**, **2'H3H(t)** and **2'3**.

Starting with the **2'3H** structure for which the electronic transitions are shown on Figure I. 49, the computed transitions for Ca(II) reproduce the spectrum quite well, but not for the other cations (0.07, 0.31 and 0.25 eV errors for Ca(II), Zn(II) and Mn(II), respectively), although experimental data suggested that all three cations bound 2'3HF on the same site. Also, the band at 330 nm is not well reproduced. Based on these results, the **2'H3** structure appears unlikely but cannot be completely ruled out.

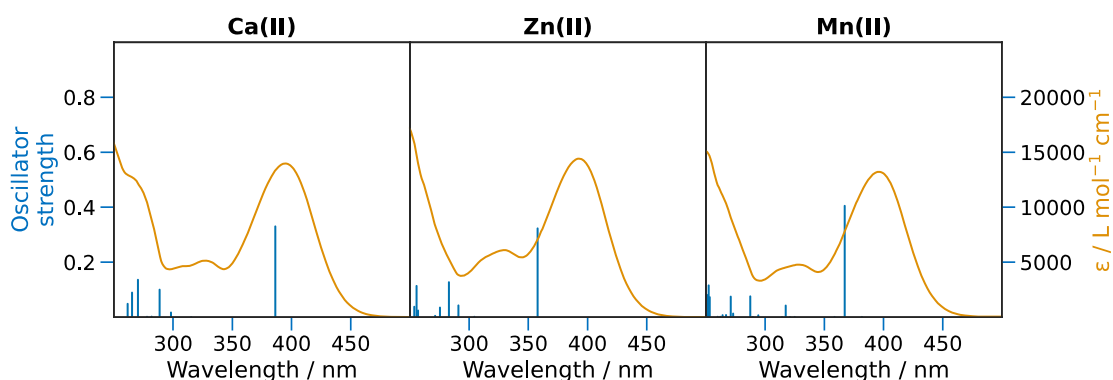


Figure I. 49: Comparison between the experimental absorption spectrum of the 2'3HF-M (Ca(II), Zn(II) or Mn(II)) complex and the computed electronic transitions of the optimized **2'H3** complexes

Another interesting protonation state for position 2'3 is the tautomer complex **2'H3H(t)** whose transitions are shown on Figure I. 50.

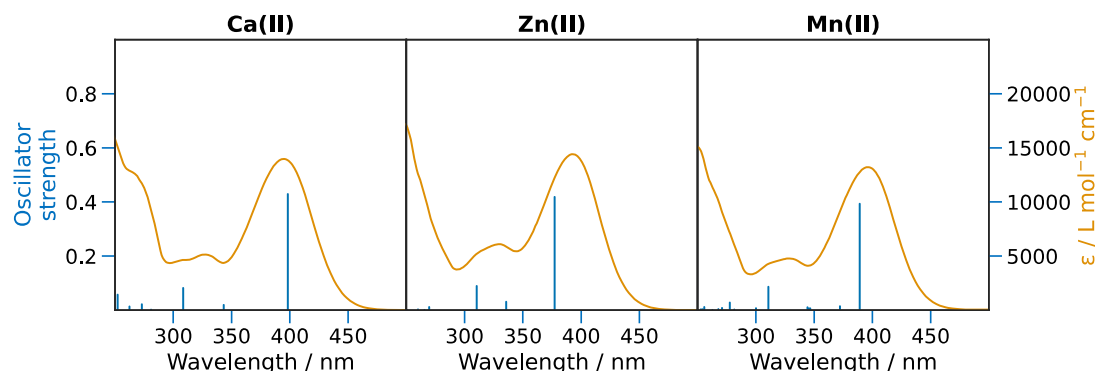


Figure I. 50: Comparison between the experimental absorption spectrum of the 2'3HF-M (Ca(II), Zn(II) or Mn(II)) complex and the computed electronic transitions of the optimized **2'H3H(t)** complexes

The transitions reproduce quite well the spectrum, and especially, they reproduce the band at 330 nm even better than the transitions of **34**. The wavelengths are of 398,

377 and 389 nm (0.02, 0.13 and 0.06 eV errors), for Ca(II), Zn(II) and Mn(II), respectively. The **2'H3H(t)** is thus a good candidate structure for the complexes of 2'3HF. However, its protonation state is unlikely. Indeed, varying the pH at a given molar ratio showed that the complexation was favoured at higher pH. Also, upon addition of a metal solution, the pH was observed to decrease which required addition of small quantities of NaOH to remain in fixed pH conditions. This suggests that the removal of at least one proton from the ligand occurs in contradiction with the **2'H3H(t)** structure.

The final potential candidate is the **2'3** structure whose electronic transitions are shown on Figure I. 51. It involves the deprotonation of both hydroxyl groups of 2'3HF. The calculations give transitions at 412, 379 and 396 nm (0.13, 0.12, 0.00 eV errors), for Ca(II), Zn(II) and Mn(II), respectively, relatively close to the experimental wavelengths. However, the band at 330 nm is not particularly well reproduced, although this argument is not enough to rule out this hypothesis.

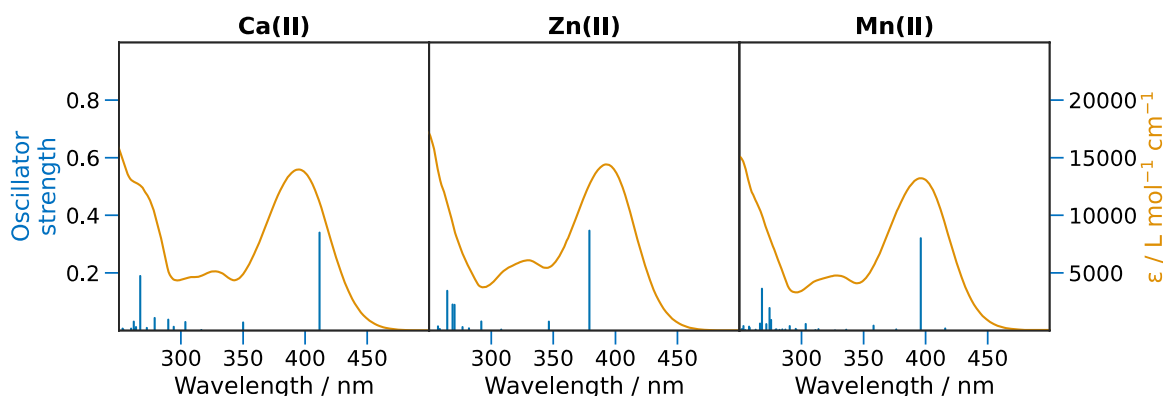


Figure I. 51: Comparison between the experimental absorption spectrum of the 2'3HF-M (Ca(II), Zn(II) or Mn(II)) complex and the computed electronic transitions of the optimized **2'3** complexes

4.1.2. Energy differences

The comparison of the electronic transitions to the experimental absorption spectrum led to the selection of five structures as candidates (represented on Figure I. 52): **34**, **34(r)**, **2'H3**, **2'H3H(t)** and **2'3**. In order to identify the structure of the complex among these geometries, a comparison of the Gibbs free energies was performed. All energies are reported in Table I. 15.

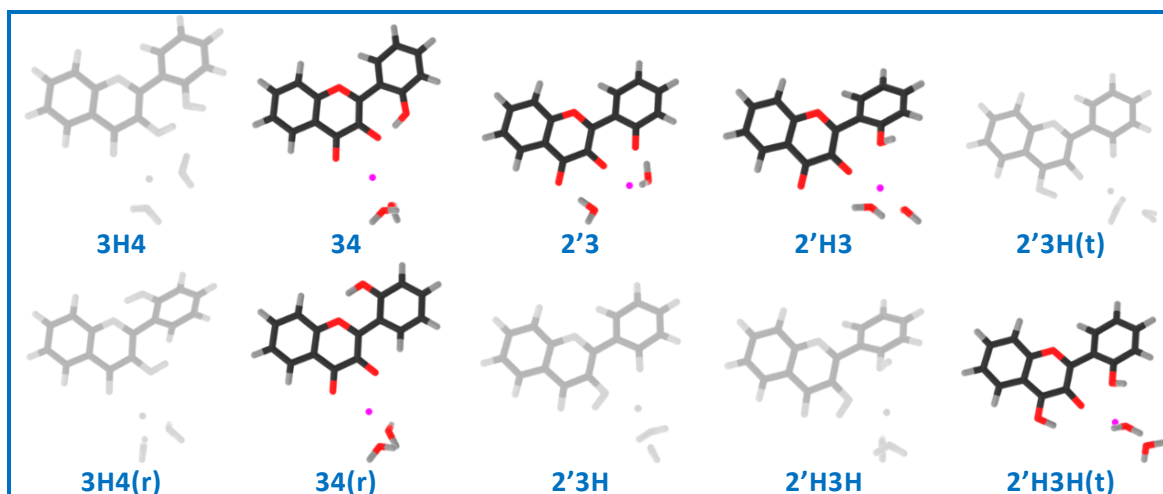


Figure I. 52: Good structure candidates for the complexes according to the analysis of the electronic transitions (in colour), and the excluded ones (in grayscale)

Complex charge	2(H ₂ O)			3(H ₂ O)			4(H ₂ O)			
	Ca	Zn	Mn	Ca	Zn	Mn	Ca	Zn	Mn	
+1	34	0.00	0.00	0.00	0.000	0.00	0.00	0.00	0.00	0.00
	2'H3	16.89	20.95	18.13	13.83	13.88	13.76	13.17	16.41	4.91
	2'3H	14.15	16.21	14.17	12.69	15.36	13.87	12.95	15.15	14.29
	2'3H(t)	15.08	14.17	12.34	16.23	13.93	12.99	16.50	14.82	14.58
	34(r)	7.337	6.89	6.18	8.56	5.58	6.94	7.64	6.36	7.23
+2	3H4	0.00	0.00	0.00	1.11	2.49	0.44	0.00	3.44	0.00
	2'H3H	10.08	14.14	12.01	4.36	10.75	5.87	5.05	8.17	6.32
	2'H3H(t)	9.46	8.42	7.84	4.57	5.55	2.43	5.17	4.59	3.59
	3H4(r)	4.84	5.90	4.17	0.00	0.00	0.00	0.41	0.00	0.74

Table I. 15: Relative Gibbs free energies (kcal mol⁻¹) of all the studied complexes, except **2'3** which is the only neutral species and cannot be compared to the other complexes. The +1 and +2 complexes must be compared separately due to the difference in particle count, and for each complex charge, the energy is given relative to the lower energy structure

In the table, the relative energies of all structures, even those excluded, were added. Also, the **2'3** structure is neutral, whereas **34**, **2'H3**, **2'3H**, **2'3H(t)** and **34(r)** are charged +1 and **3H4**, **2'H3H**, **2'H3H(t)** and **3H4(r)** are charged +2, and the comparison of energies can only be made for the same complex charge (so that they have the same particle count).

Starting with the +2 charged complexes, the **2'H3H(t)** structure is the only one that was not ruled out by the electronic transitions analysis. However, it is less stable than **3H4** and **3H4(r)**. That means that the cation would rather bind 2'3HF into these fixation schemes rather than in **2'H3H(t)** and this hypothesis can safely be ruled out.

Now comparing the energies of the +1 charged complexes, it can be observed that the **34** geometry is the most stable one for each cation and each coordination sphere. Even the **34(r)** complex is significantly less stable than **34** and is unlikely to be observed, despite the possibility for **34** to convert to **34(r)** through rotation around the inter-ring bond.

4.1.3. Experimental vs. theoretical fluorescence

At this point, only two hypotheses remain: the **2'3** and **34** geometries. The same result was found in the morin cation systems in a previous thesis work. [60] In order to identify the binding site, the **2'3** and **34** complexes were optimised in their lowest energy ESs to compare the calculation of their fluorescence emission wavelengths to the experimental spectra. The Mn(II) complex is non-fluorescent and the study was focused on the Ca(II) and Zn(II) complexes. Actually, the analysis of the electronic transitions of the Mn(II) complexes shows that a low energy transition (around 650 nm) with null oscillator strength is obtained for all Mn(II) complex geometries. The spin changes during the transition, which explains the forbiddance of the transition. Thus, an intersystem crossing in the ES might be at the origin of the fluorescence quenching by Mn(II).

The results for Ca(II) and Zn(II) are reported in Table I. 16.

		Wavelength / nm (Absolute deviation / eV)		
		34	2'3	Exp
Ca(II)	2(H ₂ O)	505 (0.24)	522 (0.16)	559
	3(H ₂ O)	506 (0.23)	518 (0.18)	
	4(H ₂ O)	508 (0.22)	524 (0.15)	
Zn(II)	2(H ₂ O)	496 (0.24)	472 (0.37)	549
	3(H ₂ O)	498 (0.23)	494 (0.25)	
	4(H ₂ O)	498 (0.23)	495 (0.25)	

Table I. 16: Computed emission wavelengths for each structure of **34** and **2'3** complexes in nm with deviations relative to the experimental emission maximum (in eV) in parentheses

The calculated emission wavelengths are rather far from experimental data with mean absolute deviations of 0.23 and 0.24 eV for **34** and **2'3**, respectively. Both remain below TD-DFT accuracy for emission wavelengths. Interestingly, whatever the structure and number of water molecules around the metal, the calculated wavelengths are higher for Ca(II) systems than for Zn(II) ones, which is consistent

with experimental observations. The reproduction of the experimental wavelength with **2'3** is better than with **34**, although the difference is too small to be conclusive.

4.2. The “basic” medium complex

Neither **34** or **2'3** could be ruled out. The identification of the complex present in basic conditions could help identify the one in acidic condition. In section 3, hypsochromic and hypochromic effects on the absorption bands were observed during the increase in pH. The hypotheses that were suggested were the following:

- (a) The deprotonation of the ligand in the 1:1 complex
- (b) A change of site by the cation
- (c) The formation of a 2:1 complex
- (d) The deprotonation of a solvent molecule in the coordination sphere of the 1:1 complex

(a) Deprotonation of the ligand

The deprotonation the ligand is only compatible with **34** yielding **34dep**, because **2'3** already has both labile protons removed. The **34dep** structure was optimized with Zn(II) and two water molecules and is shown on Figure I. 53. Only two water molecules were tested in the calculations to reduce the computational cost. Also, the Mn(II) and Ca(II) complexes could not be optimized because the 2' hydroxyl group would always deprotonate one molecule in the coordination sphere of the cation.

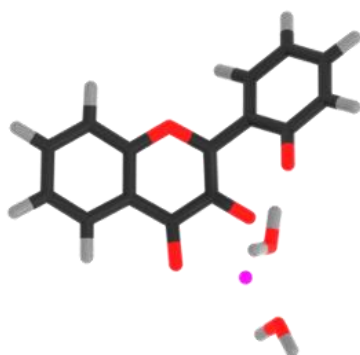


Figure I. 53: The **34dep** complex, with 2(H₂O) and the Zn(II)

The **34dep** structure looks unstable because the inter-ring interaction (between O3 and O2') is removed. Thus, the rotation of the phenyl ring is easier and the

optimization algorithm converged to a structure stabilized by a O2' – H2O interaction. The electronic transitions of the **34dep** with Zn(II) and two water molecules are shown on Figure I. 54 compared to the experimental spectrum.

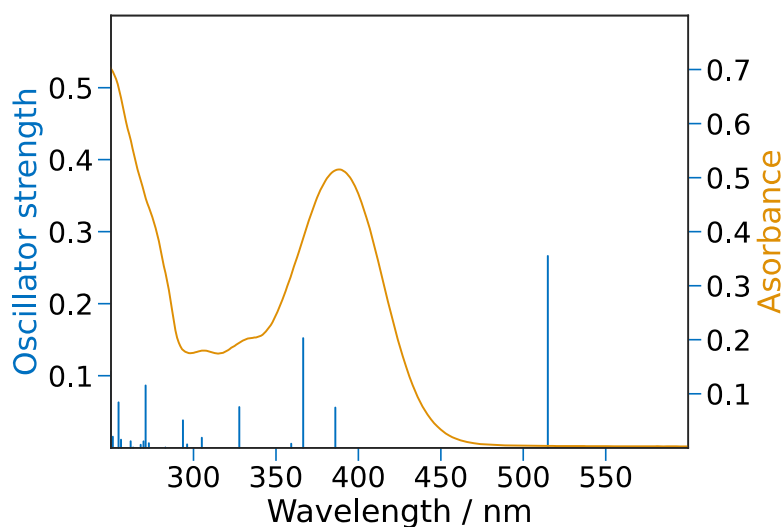


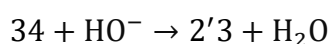
Figure I. 54: Computed electronic transitions of **34dep** with Zn(II) and two water molecules in the coordination sphere, compared to the absorption spectrum of the basic medium complex

It is clear from the spectrum that the **34dep** complex cannot explain the experimental observations because of the two low electronic transition energy, so hypothesis (a) is unlikely.

Because the **34dep** and **2'3** structures have the same chemical formula, it is possible to compare their energies. It was found that **34dep** is 10.15 kcal mol⁻¹ less stable than **2'3** meaning that the cation would rather switch to site **2'3** upon second deprotonation than staying on position **34**. This completely rules out hypothesis (a) in favour of the change of site by a cation (b).

(b) A change of site by the cation

A possible explanation for the experimental observations is for the cation to change site in alkaline media. According to the results so far, this would imply the formation of **34** in acid conditions, followed by its deprotonation according to the following chemical equation



Actually, the comparison of the electronic transitions of **2'3** to that of the basic medium complex shown on Figure I. 55 yields absolute errors of 0.15, 0.07, and 0.03

eV (Ca(II), Zn(II) or Mn(II), respectively) relative to the absorption maximum. This is below TD-DFT accuracy, meaning that this hypothesis is indeed plausible.

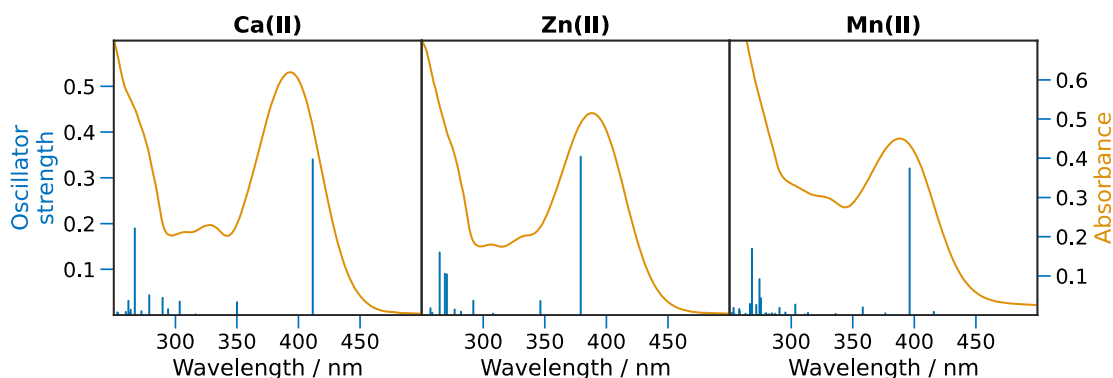


Figure I. 55: Computed electronic transitions of **2'3** with four water molecules in the coordination sphere compared the absorption spectrum of the basic medium complex

It is also possible to compare the experimental fluorescence emission of the basic medium complex to the computed emission of **2'3** as done in Table I. 17.

	Wavelength / nm (error / eV)	
	Ca	Zn
2(H ₂ O)	522 (0.18)	472 (0.43)
3(H ₂ O)	518 (0.20)	494 (0.31)
4(H ₂ O)	524 (0.17)	495 (0.30)
Experimental	564	563

Table I. 17: Comparison between the experimental emission of the basic medium complex and the computed emission wavelength for complex **2'3**. The values in parentheses are the errors relative to the experimental emission maximum in eV

It is shown that the description could match the experiments for Ca(II), however the results for Zn(II) are rather bad. The error is still within acceptable range, so this hypothesis cannot completely be ruled out, especially for the Ca(II) system.

(c) The formation of a 2:1 complex

The switching of the cation from position **34** to position **2'3** was shown to be feasible, however, the binding of an additional cation on **2'3HF** to form a 2:1 complex is also a possibility. The $2'3HF - Zn_2 - (H_2O)_4$ complex was optimized in its GS and its electronic transitions computed. The comparison with the experiment is shown on Figure I. 56.

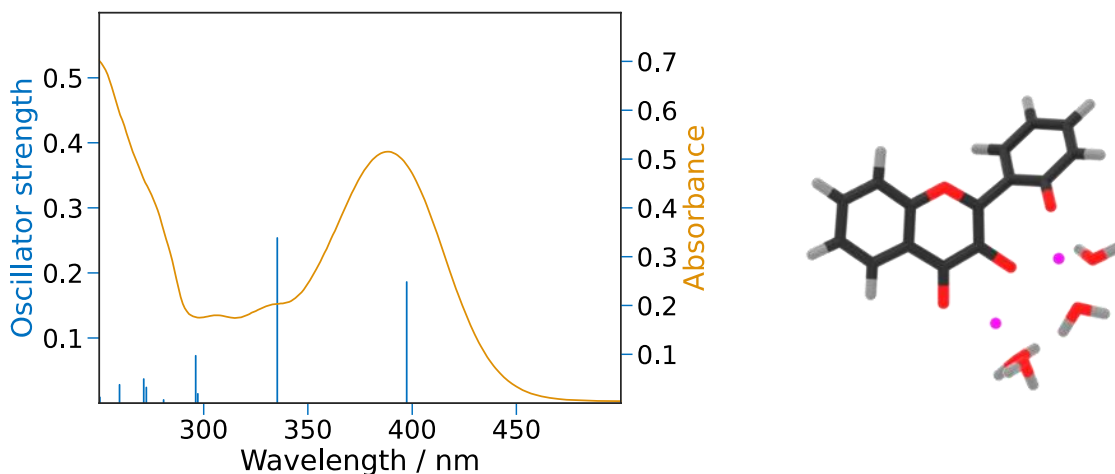


Figure I. 56: Computed electronic transitions of the $2'3\text{HF} - \text{Zn}_2 - (\text{H}_2\text{O})_4$ complex compared the absorption spectrum of the basic medium complex. The structure of the complex is also shown on the right of the figure

The hypothesis can be ruled out with little doubt because of the wrong predicted shape of the absorption spectrum.

(d) Deprotonation of the solvent

The deprotonation of a solvent molecule in the coordination sphere of the cation is a probable explanation for the basic medium complex because of the small spectral changes that occur. Two systems are possible: $34(\text{OH})$ and $2'3(\text{OH})$. The complexes were optimised with one water molecule and one hydroxide in the coordination sphere and their electronic transitions were computed. The results are shown on Figure I. 57.

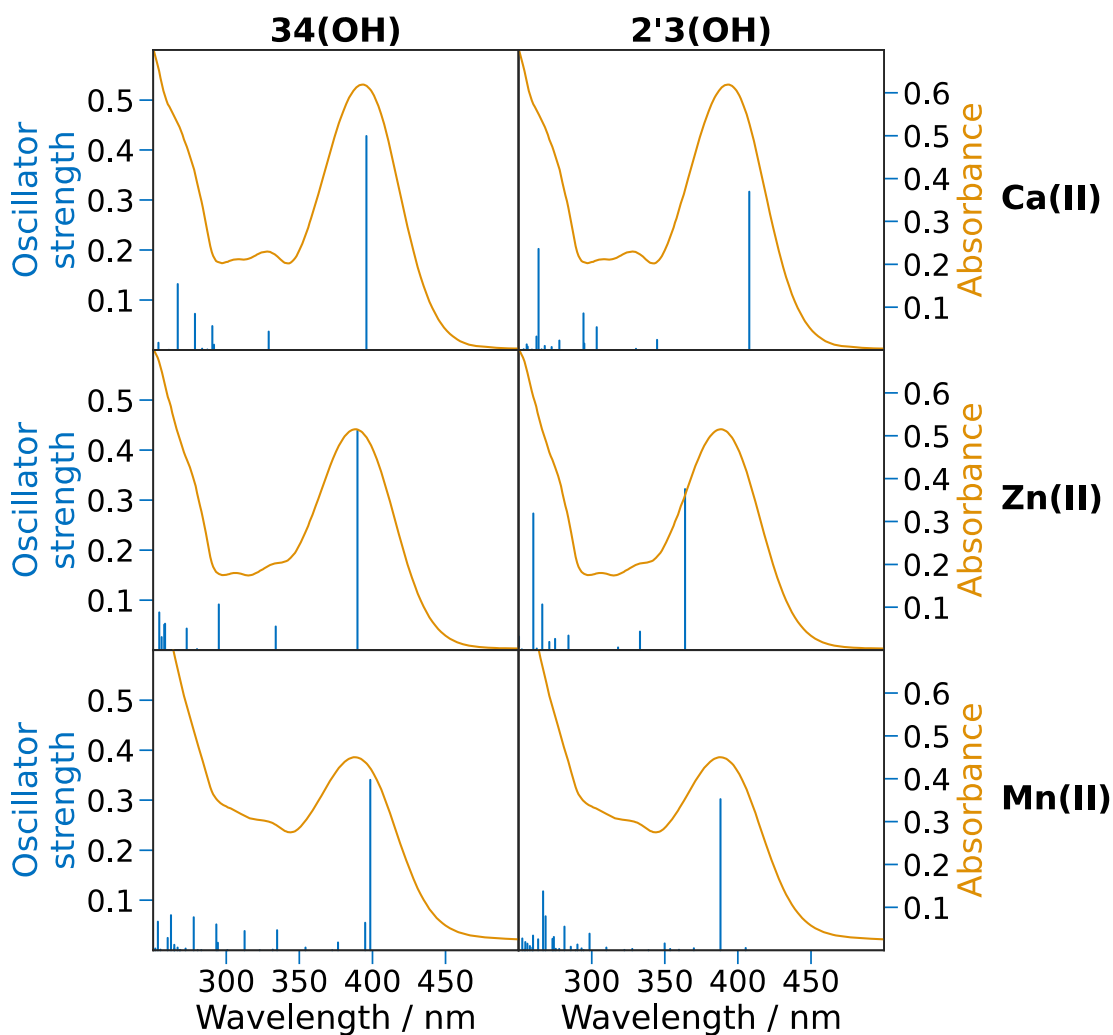


Figure I. 57: Computed electronic transitions of **34(OH)** and **2'3(OH)** with two water molecules compared to the absorption spectrum of the basic medium complex

Overall, the spectra are well reproduced by the computed transitions for all cations. This hypothesis is very probable and is the hypothesis that was retained for the first deprotonation of the morin – Ca(II) system. [1]

The structures were optimised in their first ES and the computed emission wavelengths are gathered in Table I. 18.

	Wavelength / nm (absolute error / eV)		
	34(OH)	2'3(OH)	Experiment
Ca(II)	510 (0.23)	524 (0.17)	564
Zn(II)	503 (0.26)	491 (0.32)	563

Table I. 18: Computed emission wavelengths for the 34(OH) and 2'3(OH) complexes compared to the experimental data. The values in parentheses are the absolute errors in eV

The emission wavelength is somewhat from the experimental value for Zn(II) in the 2'3(OH) structure, but below TD-DFT accuracy. Also, the computed values for the other systems could match the experimental observations. Thus, the calculation of the electronic transitions does not yield an unequivocal answer and the deprotonation of a solvent molecule in the coordination sphere of the cation in either the **34** or **2'3** structures is a plausible hypothesis.

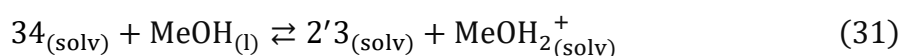
4.3. Thermodynamic considerations

To sum up, the study in alkaline solutions ruled out few hypotheses on the acidic medium complex but could not yield an unequivocal answer. Three reaction schemes resist:

- Hypothesis **34** → **2'3**: Formation of **34** followed by the deprotonation of hydroxyl 2' and the switching of binding site to form **2'3**.
- Hypothesis **34** → **34(OH)**: Formation of **34** followed by the deprotonation of a solvent molecule in the coordination sphere to form **34(OH)**.
- Hypothesis **2'3** → **2'3(OH)**: Formation of **2'3** followed by the deprotonation of a solvent molecule in the coordination sphere to form **2'3(OH)**.

However, further arguments, can be made to favour one hypothesis or the others, and are presented hereafter.

Indeed, complexes **34** and **2'3** are linked through the following acid-base equilibrium



meaning that a pK_a value can be calculated using the following Gibbs free energy [200]

$$\Delta_r G^0_{34 \rightarrow 2'3} = \Delta_f G^0(2'3) + \Delta_{solv} G^0(H^+) - \Delta_f G^0(34) \quad (32)$$

with $\Delta_{solv} G^0(H^+) = -257 \text{ kcal mol}^{-1}$ the solvation free energy of the proton (in methanol, taken from reference [207]), and $\Delta_f G^0(2'3)$ and $\Delta_f G^0(34)$ the formation Gibbs free energies of **2'3** and **34**, respectively. Doing so yields the pK_a values reported in Table I. 19.

	2(H ₂ O)	3(H ₂ O)	4(H ₂ O)
Ca(II)	22.8	23.4	24.1
Zn(II)	21.7	19.7	22.5
Mn(II)	22.0	20.9	22.2

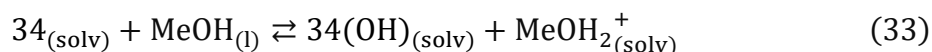
Table I. 19: Computed pK_a values of the **34** \rightarrow **2'3** acid-base equilibrium

This computational procedure to compute pK_a values is highly sensitive on the level of theory meaning that the results should be interpreted carefully.

First of all, the results suggest that **34** is more stable than **2'3** below pH values around 22. This allows to safely rule out hypothesis **2'3** \rightarrow **2'3(OH)**, since it would require for **2'3** to present in acidic conditions. Thus, only hypotheses **34** \rightarrow **34(OH)** and **34** \rightarrow **2'3** remain meaning that the structure of the complex in acidic medium can safely be attributed to **34**.

The change of site hypothesis (**34** \rightarrow **2'3**) involves the deprotonation of **34** starting at around pH = 9.5 to yield **2'3**. However, the calculation of the pK_a values suggest for **34** and **2'3** to be found at the same concentrations at pH = 22. Thus, the pK_a values appear slightly too large to explain the experimental observations, which is a strong argument in favour of the **34** \rightarrow **34(OH)** hypothesis.

The same analysis can be made for the **34** \rightleftharpoons **34(OH)** acid base equilibrium using the following chemical equation



yielding the pK_a values reported in Table I. 20.

	2(H ₂ O)	4(H ₂ O)
Ca(II)	23.7	22.3
Zn(II)	13.0	9.3
Mn(II)	16.2	13.8

Table I. 20: Computed pK_a values of the **34** \rightleftharpoons **34(OH)** acid-base equilibrium

The obtained pK_a values for the Zn(II) and Mn(II) systems are around 14 and 11 for two and four water molecules, respectively, which is a much better match to the experimental observations than the change of site hypothesis. However, the pK_a values are still too high for Ca(II) and around the same as those found for the

34 → **2'3** hypothesis. Thus, some ambiguity remains in the case of the 2'3HF–Ca complex deprotonation.

5. Conclusion

Using a combination of steady-state electronic spectroscopies and DFT and TD-DFT, it was possible to investigate the complexation of 2'3HF with three cations: Ca(II), Zn(II) or Mn(II).

This work was undertaken to better understand the complexing properties of morin that were evidenced in a previous thesis work. Indeed, it was suggested that morin formed a **34** complex with all three cations, with the suspicion of the existence of a **2'3** complex for Mn(II) on top of the regular **34** complex. More specifically for Ca(II), it was suggested that the **34** complex would undergo the deprotonation of a solvent molecule in its coordination sphere at around pH = 8.0, followed by the deprotonation of hydroxyl 7 (not present in 2'3HF) at around pH = 9.8.

In the present work, it is shown that 2'3HF forms complexes of a **34** structure with all cations. Also, the study in high pH conditions showed the formation of a second complex at around pH = 9.5. Four hypotheses were suggested to explain the experimental observations, two of them being more plausible:

- A change of site by the cation to yield a **2'3** structure (**34** → **2'3** hypothesis)
- The deprotonation of a solvent molecule in the coordination sphere of the cation to yield a **34(OH)** structure (**34** → **34(OH)** hypothesis)

In the case of the Zn(II) and Mn(II) systems, DFT and TD-DFT calculations allowed to attribute the second complex to the **34(OH)** structure with little doubt, which has a blue shifted main absorption band compared to the first complex.

Some ambiguities remain for the Ca(II) case. Indeed, the reproduction of electronic spectra as well as thermodynamic considerations could not single out one hypothesis from the other. Actually, the formation of the second complex can be observed experimentally at such high pH values that the information is incomplete so that both complexes could coexist.

The two reaction schemes are represented on Figure I. 58.

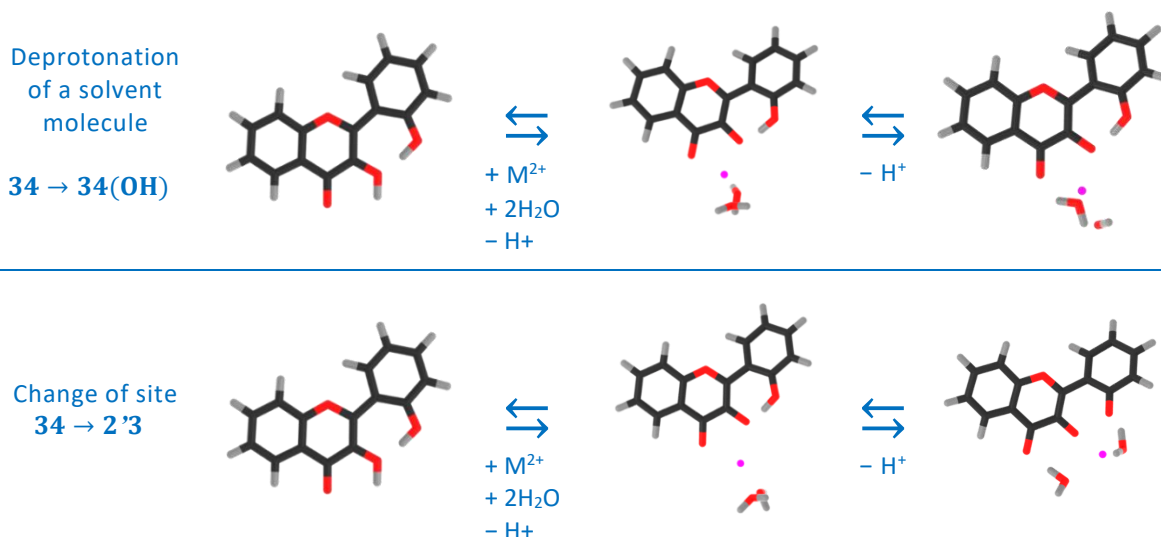


Figure I. 58: Reaction schemes suggested for the 2'3HF complexes with Ca(II), Zn(II) or Mn(II). The top example is that of Zn(II) whereas the bottom one is that of Ca(II), both with two water molecules

The behaviour of 2'3HF is shown to be very similar to that of morin, although no traces of a 2'3 complex with Mn(II) were evidenced in this study.

Also, in light of the experimental work performed in this thesis the results on morin – Ca(II) can be revisited. Indeed, the first deprotonation in the morin – Ca(II) system occurs at around $\text{pH} = 8.0$, followed by another deprotonation at around $\text{pH} = 9.8$. Only one deprotonation occurring at $\text{pH} = 9.5$ is observed in the case of 2'3HF. So, it can be suggested that the first deprotonation in the morin – Ca(II) complex occurs from the hydroxyl group 7 (absent in 2'3HF), followed by the deprotonation of a solvent molecule, at the same pH as the 2'3HF – Ca.

General conclusion on Part I.

This thesis work was originally undertaken to better understand the properties of morin and to confirm the importance of the 2' – 3 hydroxyl group interaction in enhancing the acid-base and complexation properties of flavonols. Thus, it was chosen to study 2'3HF, a flavonol bearing this diol functional group.

The study started by a thorough investigation of 2'3HF physicochemical properties. In particular, it was shown in Chapter 2 that it displayed a pK_a of around 6.7 in methanol, similarly to morin. The structural analysis showed that the remaining proton in the anion lied on the diol, tightly bound to oxygen atoms 2' and 3, suggesting for the 2' – 3 inter-ring interaction to be responsible for the enhanced acidity of the α -hydroxyketone in flavonols. A depiction of the acid-base equilibria in 3HF and 2'3HF (in methanol) is shown on Figure I. 59.

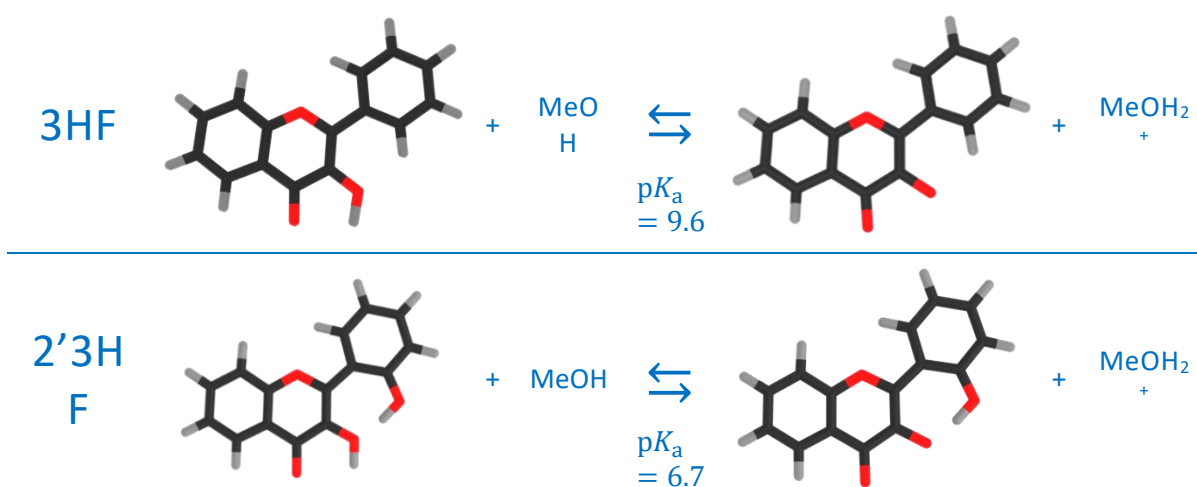


Figure I. 59: Acid-base equilibria of 3HF and 2'3HF in methanol

Then, the electronic spectra of 2'3HF were studied. In the GS it was shown that 2'3HF absorbed at 333 nm (band I) and 240 nm (band II). Upon deprotonation, the band I is red-shifted to 387 nm. In the ES, the neutral 2'3HF can undergo an ESIPT to emit a dual fluorescence due to the normal species (428 nm) and the PT tautomer (547 nm), whereas an increase in pH allows to see the broad fluorescence emitted from the anion (566 nm).

Finally, a fourth fluorescence at 517 nm was observed when exciting at around 395 nm in acidic media. Several hypotheses were suggested to explain this emission,

and the hypothesis of a solvent-complex of 2'3HF was shown to be the most promising.

In Chapter 3, two solvent-complex hypotheses were explored: the formation of an ion-pair of 2'3HF (**IP**) and a solvent molecule, or a “perturbed” PT tautomer species (**PPTT**) stabilized by interaction with the solvent. In order to elucidate the nature of the solvent-complex, absorption and fluorescence spectra of 2'3HF in six solvents were recorded. Also, the effect of water addition on the spectra was studied. According to the results of this experimental work, it can be suggested for the **PPTT** hypothesis to be the most plausible one.

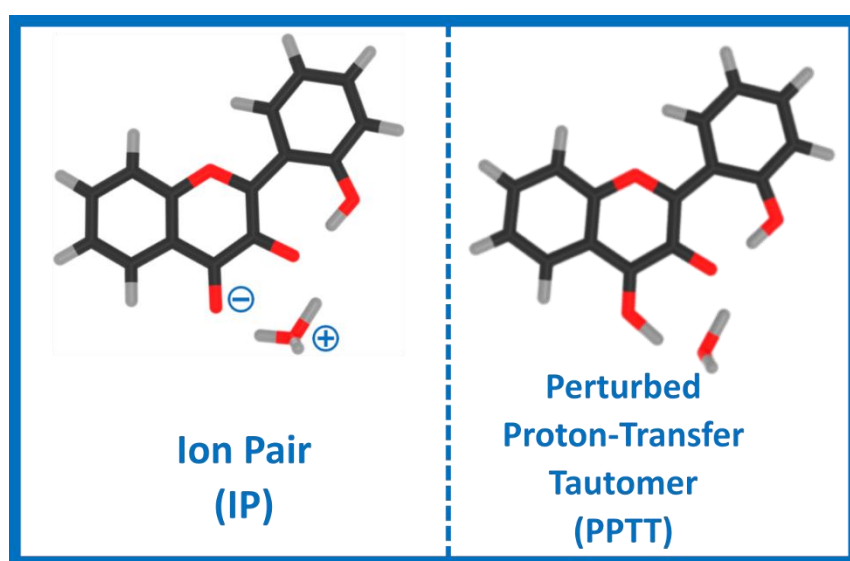


Figure I. 60: The two solvent-complex hypotheses

In the same chapter, the performances of the PCM solvation model was investigated by mean of AIMD calculations followed by 1000 TD-DFT calculations on randomly selected conformations with 3 different solvation models (3000 calculations in total). It was shown that the commonly used approach for computing electronic spectra of solvated organic dyes, *i.e.*, the optimization of the solute followed by the calculations of its vertical electronic transitions with the inclusion of a PCM, yielded similar results to the full QM approach, despite its much lower computational costs, as shown on Figure I. 61. This is particularly interesting since 2'3HF bears functional groups that can be expected to form hydrogen bonds with solvent molecules. However, those interactions were shown to have close to no impact on the spectrum. Unfortunately, no insight on the solvent-complex was obtained from the calculations, which is probably due to the too small simulation time.

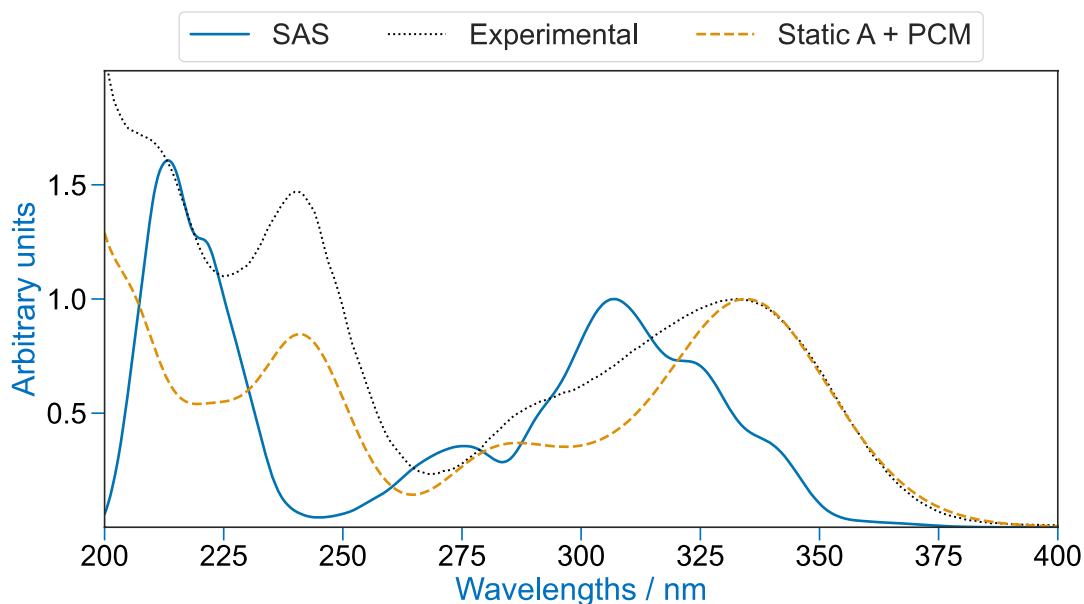


Figure I. 61: Absorption spectrum of 2'3HF simulated using a full QM approach (SAS), or the more standard approach of optimization followed by the calculation of vertical transitions (Static A + PCM). The experimental spectrum is also shown

At this point, since the physicochemical properties of 2'3HF were better understood, its Ca(II), Zn(II) and Mn(II) complexes could be studied. This was done by performing titrations using an automate coupled to a pH-meter, a pump and the UV-visible absorption and fluorescence spectrometers. The interpretation of the experimental spectra was given by DFT and TD-DFT calculations and the results are given in Chapter 4. In low pH conditions, it was shown that 2'3HF easily formed complexes with all three cations. The structure of the complexes was determined to be a “**34**” structure, corresponding to the binding of the cation on the α -hydroxyketone with hydroxyl group 3 deprotonated. Upon addition of NaOH to the solution, the complexes undergo a deprotonation at around pH = 9.5 that could unambiguously be attributed to that of a solvent molecule in the coordination sphere of the cation (hypothesis **34** \rightarrow **34(OH)**) for the Zn(II) and Mn(II) systems. In the case of Ca(II), the situation is more complicated and the deprotonation could occur either from a solvent molecule, or from hydroxyl group 2', followed by a change of site of the cation to the diol fixation site (hypothesis **34** \rightarrow **2'3**). Also, there is also a possibility for both complexes to coexist. A representation of the results and the structures of the complexes is shown on Figure I. 62.

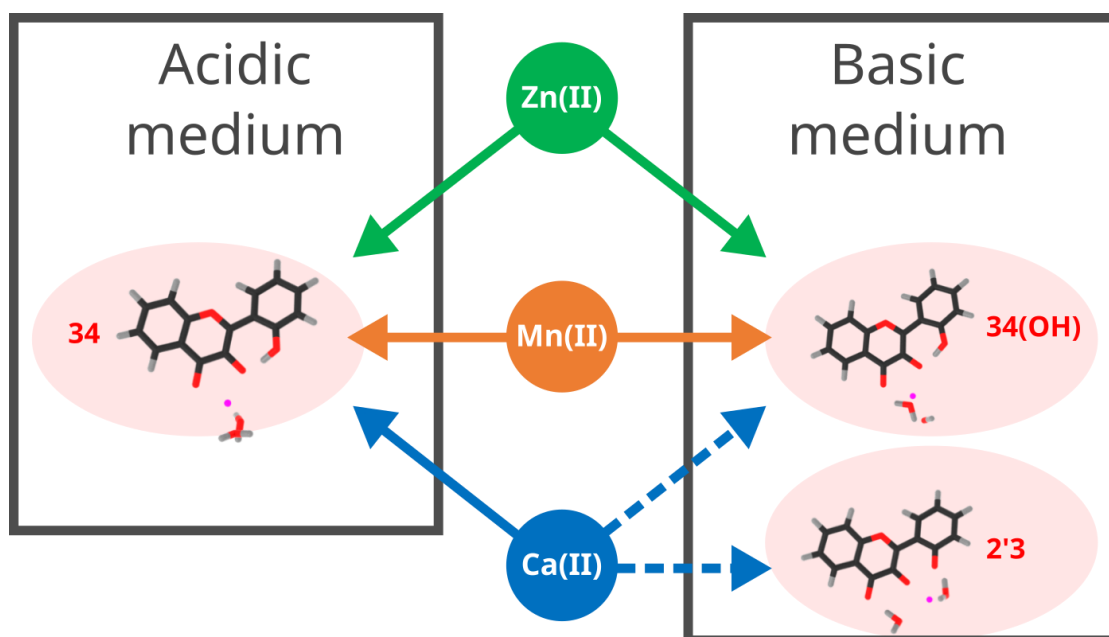


Figure I. 62: Scheme showing the structures of the Ca(II), Zn(II) and Mn(II) complexes of 2'3HF

This study brought additional insights onto the 2' – 3 inter-ring interaction, which confirmed its strong impact on the properties of the molecule. Actually, it was shown that the chemical reactivity of the α -hydroxyketo group was so different when interacting with the 2'3 diol, that it can be argued that it should be considered as a functional group as whole, similarly to carboxylic acids and catechols, rather than as separate keto and hydroxyl groups.

PART II.

The optical properties of soot
precursor species

CHAPTER 1.

Introduction on polycyclic aromatic hydrocarbons and soot, objectives and methods

This chapter serves the purpose of introduction on soot and polycyclic aromatic hydrocarbons (PAHs) and their ESs. Some vibronic spectra of PAHs were calculated and are compared to the experimental spectra herein to illustrate computational difficulties that can lead to erroneous interpretations of experimental data.

Then, some of the most promising soot inception mechanisms are presented and discussed. This study is performed in collaboration with Xavier Mercier's team from the PC2A (PhysicoChimie des Processus de Combustion et de l'Atmosphère) who perform Laser-Induced Fluorescence of sooting flames, and some of their spectra are used as experimental control to the quantum chemical calculations performed throughout this part.

1. What is soot

1.1. Flame systems

A flame is a complex and localized chemical system in which rapid heat-producing oxidoreduction and chain reactions occur. It requires the mixture of a couple of oxidative and reductive species such as O_2/H_2 , or O_2/CH_4 , commonly used in laboratory flame systems.

Flame chemistry is dependent on the amount of oxidizer present in the mix. On Figure II. 1 are shown flames from a Bunsen burner with various amounts of premixed oxygen. The flame with the highest amount (on the right) shows a typical blue colour due to the emission of radical species such as C_2^* , CH^* or OH^* , [208] whereas low oxygen flames display the other typical yellow colour originating from the black body radiation of soot particles.



Figure II. 1: Flames of a Bunsen burner with varying premixed oxygen quantities, from the lowest (left), to the highest (right)

1.2. Environmental concerns

According to the Intergovernmental Panel on Climate Change (IPCC), soot is present in the atmosphere as short-lived climate forcers contributing to climate change. [209]

Soot is emitted by combustion processes such as in diesel engines or residential solid fuel burning (wood, coal, *etc.*). In 2000, diesel engines contributed to around 20% of soot emissions and it is assumed with good confidence that the reduction of these

emissions would help reduce short-term climate forcing. [210, 211] For instance, the reduction of economic activity due to the COVID-19 pandemic has led to a dramatic decrease of pollutant emissions, including soot. Accordingly, simulations have shown that the reduction of soot emissions during this period, mostly due to a reduction of surface transport (using diesel engines) around the globe, had a cooling effect on climate. [212]

Soot has both direct and indirect forcing effects. As a strongly light absorbing material, the direct effect is its heat absorption which can further heat the atmosphere, but it also has indirect effects. For example, it has complex interactions with cloud systems such as the modification of the amount of cloud droplets, which is considered to cool down the atmosphere. [213] Also, it has the ability to deposit on snow and glaciers, which induces a warming effect. Indeed, it darkens the surface which enhances snowmelt in the Arctic which, in turn, reduces Earth's albedo. This is particularly concerning because soot emissions from shipping activities are expected to increase in the future, especially in the Arctic. [214] Overall, those indirect effects are hard to assess but simulations suggest a warming effect too. [211]

1.3. Chemical nature

Soot is a black solid material mainly composed of carbon with around 10 mole percent hydrogen, this percentage being higher at the early stages of the particle formation.

It has been shown that soot particles underwent vast changes during growth and their structure, represented on Figure II. 2 can be described as follows [215]

- A soot particle is an aggregate of primary particles of around 20 to 30 nm in diameter
- The primary particles are composed of an outer shell and an inner core
- The outer shell is composed of graphitic microcrystallites, following the curvature of the particle
- The inner core is of around 10 nm and lays at the centre of the primary particle

- The inner core is composed of fine particles with a diameter of around 3 to 4 nm
- The fine particles are composed of a nucleus of 1 nm diameter, covered by disordered layers of carbon materials

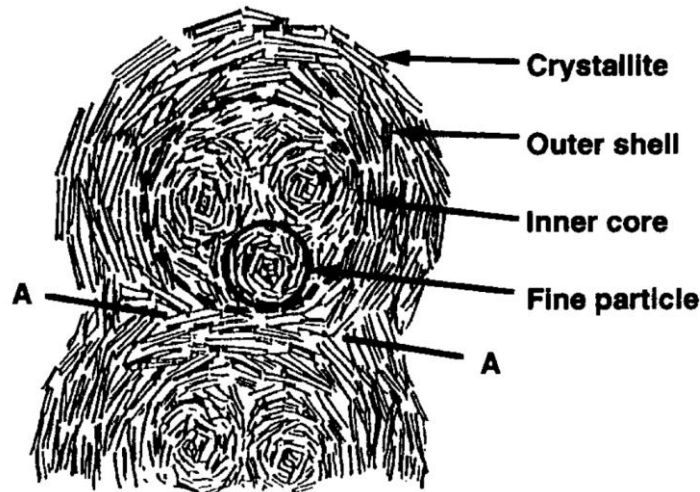


Figure II. 2: Representation of a soot particle, taken from reference [215]

From Figure II. 1, it could clearly be seen that the blackbody radiation appears at a certain height above the burner (HAB). This implies that the first particles are formed by chemical processes happening at these HABs. Indeed, the main steps required to obtain a soot particle can be summarized as follows: [216]

- Formation of molecular precursors
- Particle inception (the transitioning from gaseous molecules, to solid particles)
- Surface growth
- Particle coagulation

1.4. Reducing soot emissions

In order to reduce soot emissions, it is important to understand all of its formation steps. It is established that the inception is one of the least understood steps in the process, [217] and numerous studies are published every year focusing on this particular subject. [218–221] Although PAHs are known to play a major role in soot formation, [222–225] the actual inception mechanism of the particle remains

unknown. [226]. Authors regularly suggest new mechanisms, which involve a wide variety of soot precursor candidates of which a good overview can be found in the review published recently by Martin *et. al.* [226]

The optimization of combustion systems to reduce their soot emissions is a hot topic in the literature and multiple strategies are considered. The most obvious one is the optimization of the air-fuel ratio, soot being formed from the incomplete combustion of hydrocarbons. Accordingly, an excess of air reduces soot production as shown on Figure II. 1. [227] Although well-mixed fuels may be used in diesel engines, non-equilibrium zones with low air-fuel ratio can lead to heavy soot formations. [228] Thus, better engine designs with better fuel injections strategies could help reduce soot emissions, and have been shown to attain good results. [227, 229, 230] Finally, the use of fuel additives is also a common strategy. Fuel additives include metal-based ones such as lead tetramethyl and lead tetraethyl, [231, 232] which have been banned for health issues. [233] Other additives are alcohols aiming to increase the oxygen content of the mix such as methanol, ethanol, etc. [234, 235]

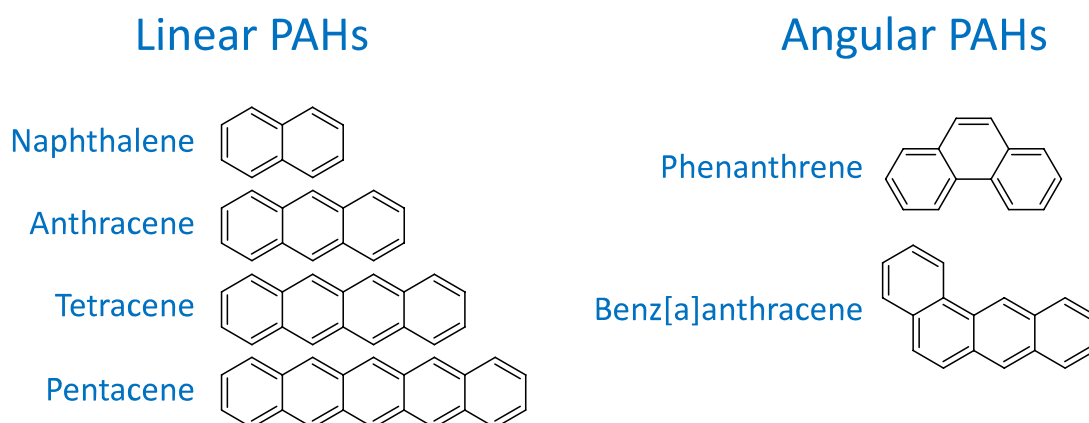
A better understanding of soot inception mechanisms could help develop new strategies to limit or reduce soot emissions. [226] Part II of this thesis is dedicated to the study of these mechanisms at a molecular level. PAHs are observed to be the building blocks of fine particles and soot inception mechanisms suggested by authors always involve their participation in the process. Thus, an introduction on them is given hereafter.

2. Polycyclic aromatic hydrocarbons

2.1. General properties

PAHs are hydrocarbons made of multiple aromatic rings. In the strictest definition, PAHs bear only 6-membered rings and no substituents. However, the definition is often loosened to include more complex systems with 5-membered rings, or even aliphatic substituents. [236, 237] More specifically, the condensed PAHs subclass is composed of PAHs in which at least two aromatic rings have a bond in common. According to this definition, the smallest condensed PAH is naphthalene, consisting of two fused benzene rings from which the addition of additional rings yields anthracene, tetracene, pentacene etc. Angular isomers as opposed to the latter linear ones also exist, such as phenanthrene and benz[a]anthracene.

Cata-condensed PAHs



Peri-condensed PAHs

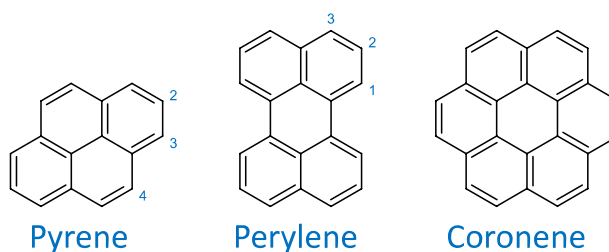


Figure II. 3: Example of PAH compounds

This subclass can further be divided into two family of compounds: the cata-condensed (the previously mentioned PAHs are all cata-condensed PAHs) and peri-condensed PAHs. The peri-condensed PAHs differ from the fact that at least one of

their carbon atoms is common to three aromatic rings. [238] Common peri-condensed PAHs include pyrene, perylene and coronene. Several example structures are shown on Figure II. 3.

Peri-condensed PAHs are particularly interesting in the context of flame chemistry. Because of their thermodynamic stability, [239] they are often considered to play an important role in the soot inception. Pyrene, for example, has been proposed to react with other PAHs to form bigger and more complex PAHs as suggested on Figure II. 4.

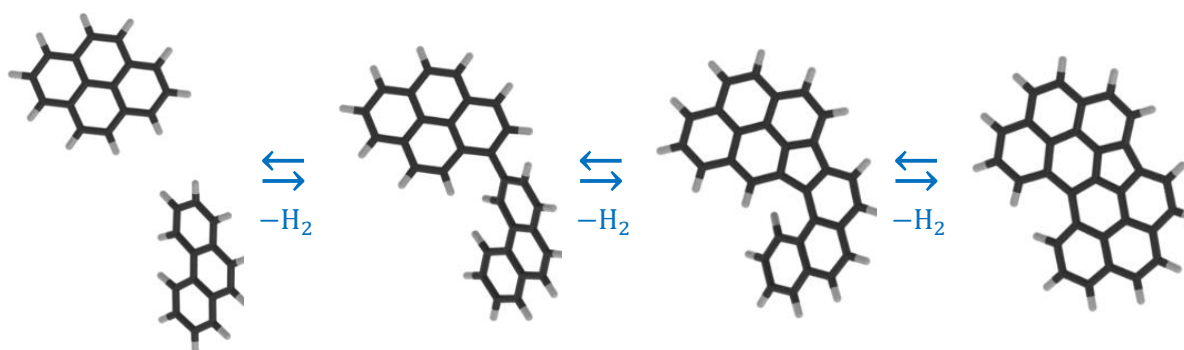


Figure II. 4: Formation of bigger PAHs through dehydrogenation as suggested in the literature [226]

2.2. Their excited-states

2.2.1. Platt's nomenclature

In 1948, John R. Platt applied the free electron model to the π -system of cata-condensed hydrocarbons. [240] This work is at the basis of the nomenclature of PAH ESs. In cata-condensed PAHs, every carbon is on the edge of the π -system which allows to describe the electrons as freely rotating along a circle of the same length as the PAH perimeter. The orbital energies are then obtained from the following formula

$$E = \frac{q^2 h^2}{2ml^2}$$

In which h is Planck's constant, m is the mass of the electron and l is the length of the perimeter. Finally, q is an integer called the orbital ring quantum number. It represents the quantization of the angular momentum which is convenient for describing the electron properties and spectra of PAHs because it gives the number of nodes of wavefunctions as well as the electronic transition selection rules. All orbitals

with non-zero q values are doubly degenerate since the electrons can go one way or the other, and q changes sign accordingly.

If n is the number of rings in the molecule, the system has $2(2n + 1) \pi$ electrons. The highest filled shell is noted f regardless of the number of rings in the system and corresponds to $q = n$. The next one to $q = n + 1$, and so on, according to the energy diagram represented on Figure II. 5.

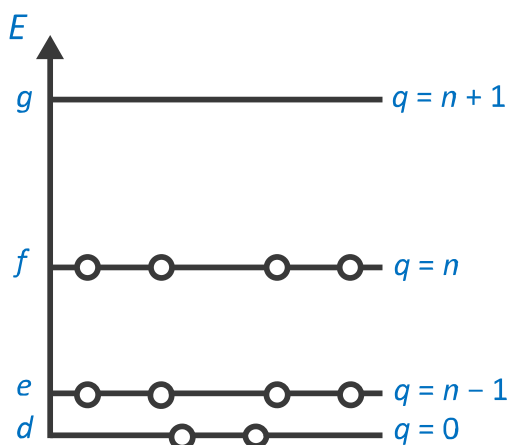


Figure II. 5: Energy diagram representing the states of 10 freely rotating electrons (here, $n = 2$)

The total momentum quantum number Q represents the electronic state of the system, and, in the GS, $Q = 0$. If an electron f is promoted to the g virtual shell (with $q = n + 1$), the total momentum quantum number becomes $Q = (n + 1) \pm n = 1$ or $(2n + 1)$. Thus, Q can take values of $0, 1, 2, \dots$, (the states are noted A, B, C, ...) or $2n + 1, 2n + 2, \dots$, (the states are noted K, L, M, ...).

Once the electrostatic potential from the nuclei is added to the system, the degeneracy is split and the resulting states are denoted “a” and “b”: B_a, B_b, L_a, L_b .

Although this nomenclature was developed for cata-condensed PAHs, the authors had already suggested the possibility of using it for other systems such as peri-condensed PAHs. Nowadays it is commonly used in the literature and will be used throughout this thesis.

2.2.2. The L_a and L_b states

The L_a and L_b states are particularly important in electronic spectroscopy studies since they are the two lowest energy states. The study of PAH absorption spectra is complexified by the fact that the L_a and L_b states are almost degenerate. Furthermore,

the transition to the L_a state is allowed and well visible on the spectrum, whereas that to L_b is forbidden, meaning that it is often hard to know where the L_b absorption lies on the spectrum.

L_a and L_b are so close in energy that for some systems the L_b is the S_1 (such as in naphthalene and pyrene), whereas it is the S_2 in others (such as in anthracene). Also, the small energy gap between L_a and L_b in some PAHs allows them to exhibit a dual fluorescence, violating Kasha's rule. This is for example the case for pyrene and benzo[a]pyrene. [241–243] On their experimental spectra (Figure II. 6), a weak vibronic emission band lies close to the L_a absorption 0–0 peak at around 328 and 370 nm for pyrene and benzo[a]pyrene, respectively.

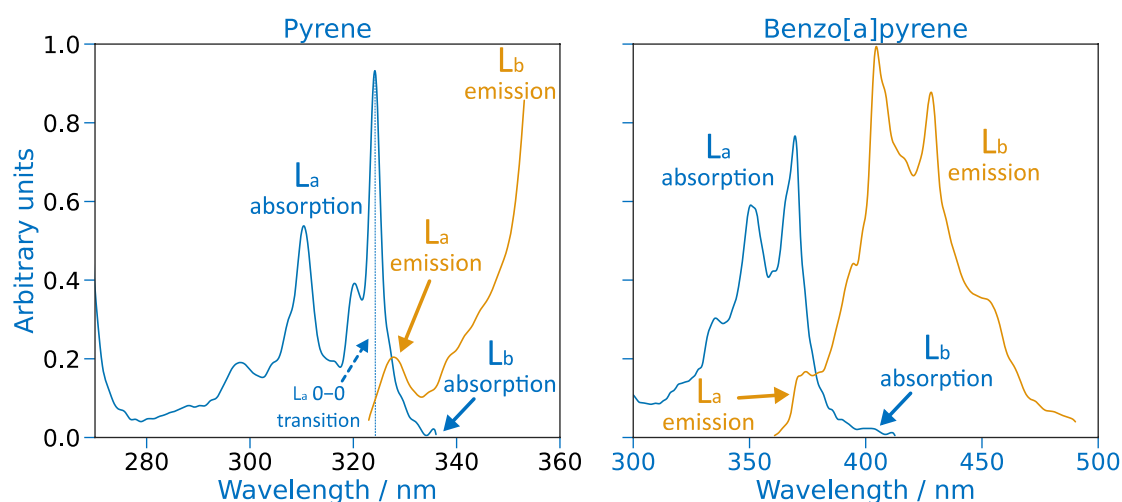


Figure II. 6: Experimental absorption (blue) and fluorescence (orange) spectra of vapours of pyrene and benzo[a]pyrene at 443 K and 533 K, respectively. Taken from reference [241]

In addition to the difficulties in the experimental observations, the closeness of L_a and L_b makes the computation of the ESs of PAHs more complex because theoretical frameworks often switch their order. For example, CIS(D) and LC-PBE predict correctly the L_b to be the S_1 , whereas CIS and PBE0 incorrectly predict it is the L_b . [244] This may lead researchers to study the wrong state.

For example, the prediction of the vibronic shape of a transition (absorption or emission) between states A (usually the GS) and B requires the obtention of the Franck-Condon factors. This is done by optimizing the molecule in both states to obtain the vibrational frequencies. However, if one of the states was misidentified on the spectrum, the Franck-Condon factors are meaningless and the vibronic shape is incorrect. Such misidentifications occurred for example in reference [245] where the vibronic emission spectrum of pyrene and naphthalene ($L_b \rightarrow S_0$) were computed as

$L_a \rightarrow S_0$. In general, it is possible to verify that the transitions were correctly attributed by verifying that the L_a transition is a HOMO \rightarrow LUMO with a large oscillator strength, and that the L_b transition is a HOMO $- 1 \rightarrow$ LUMO and HOMO \rightarrow LUMO $+ 1$ with zero oscillator strength. [246]

Another complexity can be encountered when trying to understand the electronic spectra of PAHs. To illustrate it, the vibronic spectra of naphthalene, pyrene and anthracene were computed using PBE0/6-31+G(d,p) and the time-independent (at 0 K) [247] as well as the time-dependent (at 298 K) [248] frameworks implemented in Gaussian 16, with default broadening parameters. The $S_0 \rightarrow L_a$ transition is the only one visible on the absorption spectra, so, the absorption vibronic shape was computed using the vibrational frequencies of the optimized S_0 and L_a geometries. In emission, the L_b frequencies were used for pyrene and naphthalene emission spectra, as opposed to that of L_a for anthracene emission. The results are shown on Figure II. 7 overlapped with the experimental spectra.

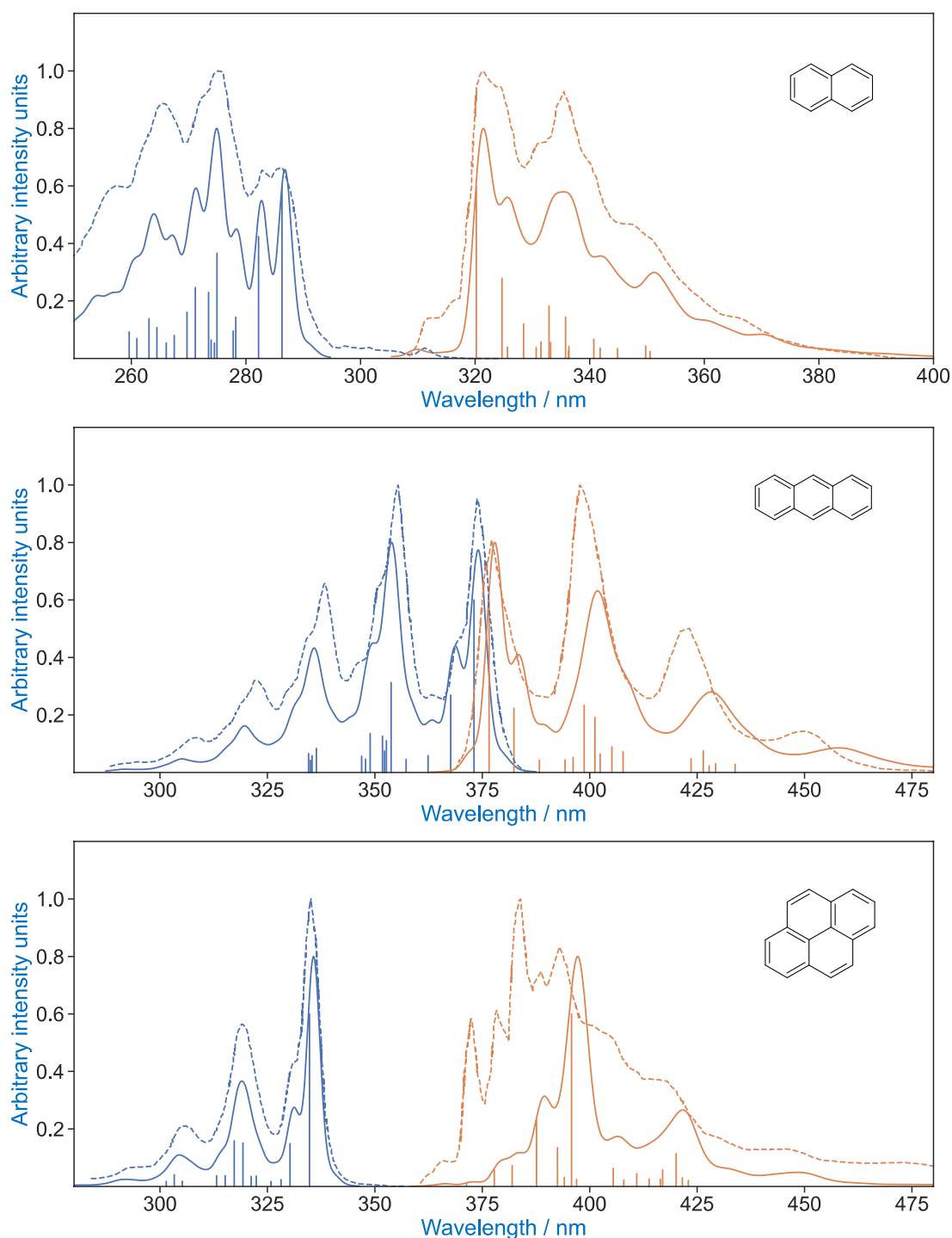


Figure II. 7: Vibronic absorption (blue) and fluorescence (orange) spectra of naphthalene, anthracene and pyrene computed using the time-independent framework (at 0 K, solid vertical lines) as well as the time-dependent framework (at 298 K, solid curve), compared to the experimental spectra in cyclohexane (dashed lines) taken from the literature. [249] The computed spectra were shifted to make the experimental and computed 0–0 transitions match

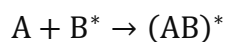
The computed spectra for naphthalene and anthracene match the experiments closely. However, the pyrene emission spectrum differs significantly, despite the correct choice of ES.

This is due to the dependence of pyrene vibronic emission band intensities on solute-solvent interactions, also known as the “Ham effect”. [250, 251] In 2014, Freidzon *et. al.* calculated the emission spectrum of pyrene in a water cluster using a similar procedure to the one used for Figure II. 7. Doing so, the authors obtained a spectrum closer to the experimental one which confirmed the importance of simulating accurately the environment of pyrene. [252]

2.2.3. Excimer fluorescence

A final complex behaviour can be observed on the emission spectra of PAHs. Indeed in 1955, Förster noticed a concentration-dependent broad visible fluorescence band in the spectrum of pyrene, at around 480 nm. [253] To explain this fluorescence, he suggested the binding of an excited pyrene with another pyrene in its GS, a species known as an excimer (exciplex in case of a heterodimer), This dimer would dissociate in the GS as suggested by the structureless shape of the band. Because the excimer formation occurs after the excitation of a monomer, the excitation spectrum recorded at the maximum emission wavelength of the band is that of the monomer.

The photophysical scheme of exciplex formation can be represented as follows: [254]



with $A = B$ and $AB = AA$ in the case of an excimer. The idea is that a molecule electronically excited can bind to a nearby molecule in its GS. Then, the electronic density and geometry can relax until deexcitation, which dissociates the dimer.

Förster suggested the first set of conditions for excimer formation as [255]

- The S_1 must be L_b so that the molecule can remain in its ES as long as possible (due to the weakness of the $L_b \rightarrow S_0$ transition)
- The S_2 must be L_a and there must be a small $S_2 - S_1$ energy gap. The reason is that the splitting into symmetric and antisymmetric combinations of L_a upon excimer formation is greater than that of L_b . Thus, the lowest singlet state becomes the symmetric combination of L_a upon excimer formation, which yields fluorescence emission due to its larger transition dipole moment

The requirements were refined later on to better account for excimer fluorescence of some species such as benzene. [255]

The molecular forces that bind A and B* can be thought of as a combination of two interactions [254, 256]

- A dipole – dipole (or multipole – multipole) interaction between A and B* due to the dipole moment change upon local monomer excitation, resulting in an interaction known as exciton-resonance (ER) ($A^*B \leftrightarrow AB^*$).
- An electrostatic interaction between positive and negative ions due a charge-transfer (CT) excitation of an electron from one moment to the other, resulting in an interaction known as charge-resonance (CR) ($A^+B^- \leftrightarrow A^-B^+$)

Thus, two ER states and two CR states are obtained upon relaxation

$$\psi_{ER,s} = (\psi_{A,i}\psi_{B,0} + \psi_{A,0}\psi_{B,i})$$

$$\psi_{ER,as} = (\psi_{A,i}\psi_{B,0} - \psi_{A,0}\psi_{B,i})$$

$$\psi_{CR,s} = (\psi_{A^+}\psi_{B^-} + \psi_{A^-}\psi_{B^+})$$

$$\psi_{CR,as} = (\psi_{A^+}\psi_{B^-} - \psi_{A^-}\psi_{B^+})$$

In which $\psi_{A,i}$ and $\psi_{A,0}$ are the electronic singlet ES i and GS of species A, respectively, and ψ_{A^+} and ψ_{A^-} are the electronic states of the molecular ion species (B denote those of species B). [255, 257, 258] A simple representation of the possible states is shown on Figure II. 8.

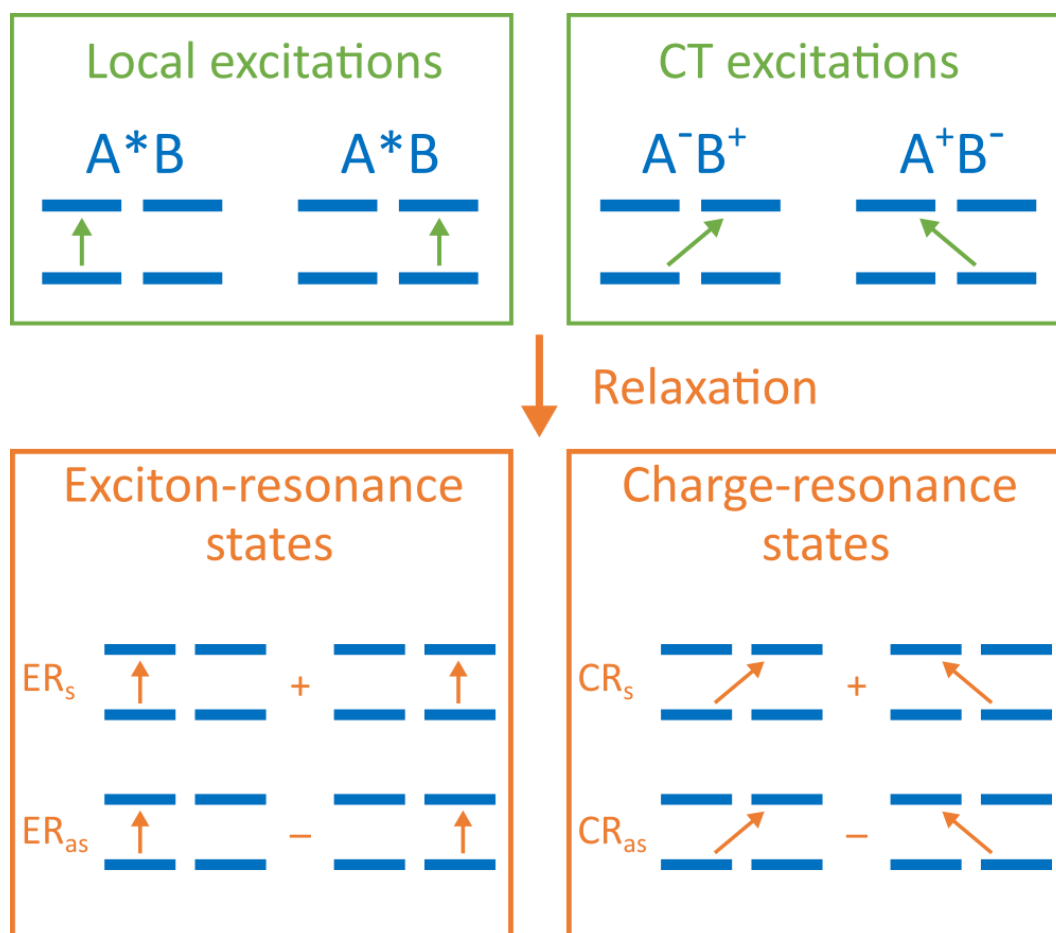


Figure II. 8: Representation of the possible excimer states, inspired by reference [258]. The arrows represent the charge movement during the excitation so that a vertical arrow represents a local excitation, whereas a diagonal arrow represents a charge transfer

However in real life systems, major state mixing occur so that the identification of each state can become difficult. [254, 255, 257–259] For example, it was found that the excimer fluorescence in naphthalene originated from a L_a parentage state with 40% CR character. [260] Similar results were found for benzene, [261] and pyrene. [262–264]

In this work, L_a and L_b systematically yielded two low energy states each which were written L_a^- , L_a^+ , L_b^- and L_b^+ , regardless of their ER or CR character (that was not quantified).

3. The inception of soot particles

3.1. PAH formation

3.1.1. The HACA mechanism

While studying flame systems during the 19th century, Berthelot and others quickly found that the formation acetylene had an important role in increasing the luminosity of flames. [265] For example, the propargyl radical $\text{H}-\text{C}^{\bullet}=\text{C}=\text{CH}_2$ can be obtained from the reaction of the methylene radical (CH_2^{\bullet}) with acetylene. Then, two propargyl radicals can recombine which, after a cyclization, leads to the formation of a first benzene ring. [226, 266, 267]

Then, the growth of PAH can be described using the Hydrogen-Abstraction-Acetylene-Addition, or more generally the Hydrogen-Abstraction-Carbon-Addition (HACA) mechanism. For example, naphthalene can be obtained by a HACA mechanism such as shown on Figure II. 9.

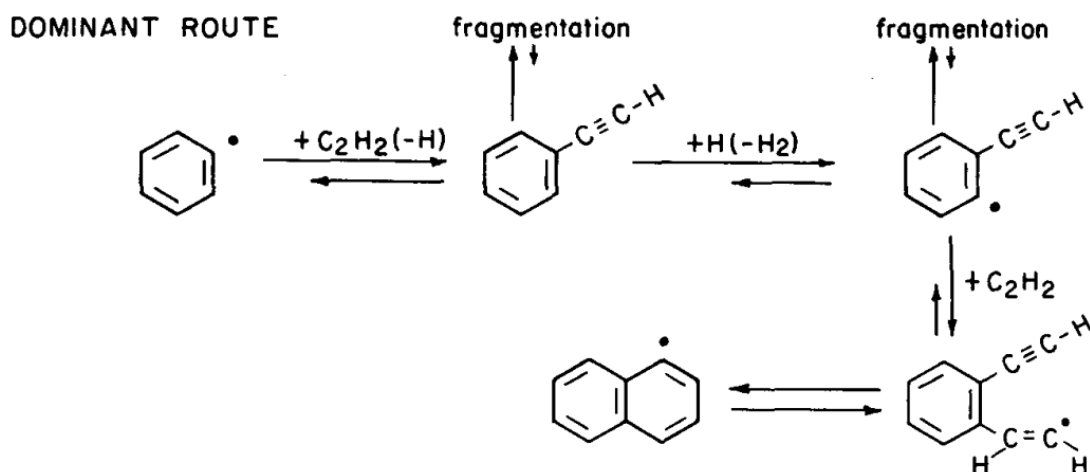


Figure II. 9: Example of a HACA mechanism for the formation of naphthalene as suggested in reference [267]

This mechanism is only one of the possibilities and other pathways to PAH growth have been suggested but are usually derivatives of the HACA mechanism. [226]

3.1.2. More complex PAH structures

It has often been assumed that mostly 6-membered pericondensed PAHs were formed because of their stability. For example, mass spectrometry measurements of various

flame aerosols often display high intensity signals at $m/z = 200 - 400$, [268, 269] and the $m/z = 202$ signals are usually attributed to pyrene. However, simulations showed that this m/z signal originated from several 5-membered containing isomers such as fluoranthene. [270]

In the 2010s, Atomic Force Microscopy (AFM) have shed light on the structure of soot precursors and showed the presence of aliphatic substituents, 5-membered rings and non-aromatic rings. [271, 272] Some examples of small structures are shown on Figure II. 10 and others are given in reference [271].

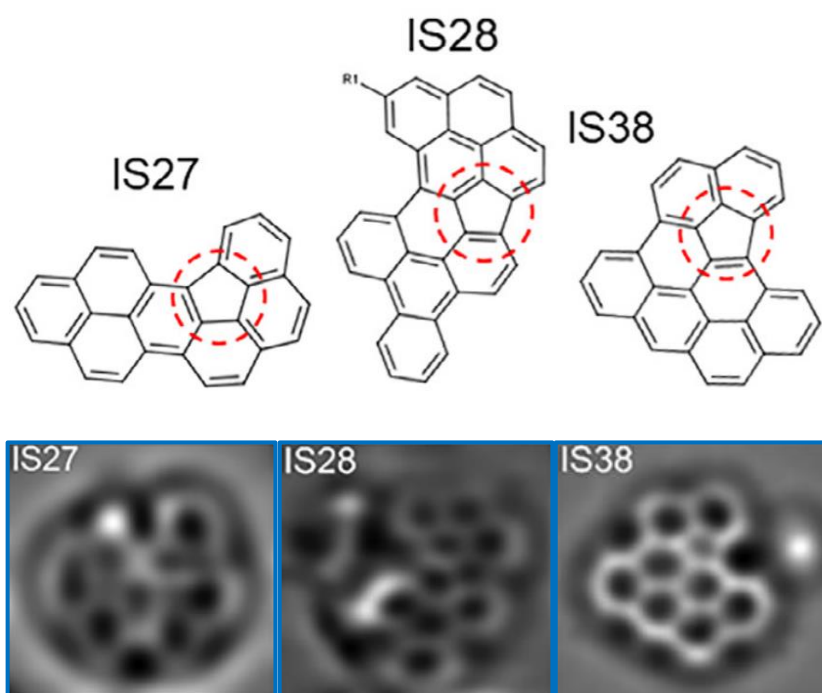


Figure II. 10: Example AFM images of structures observed in ethylene-air diluted samples extracted from the soot inception zone (from reference [271]). Red circles emphasize on the existence of partially internal 5-membered rings

3.2. Soot inception mechanisms

3.2.1. Physical oligomers

Among the simplest mechanisms to explain the particle inception is the physical stacking of PAHs. This involves van der Waals (vdW) forces (without covalent bond formation) to yield dimers, trimers and so on. This idea is backed up by experimental observations of the internal structure of soot particles resembling that of disordered PAH clusters. [272–274] Also, physical dimers were observed at ambient temperature for some PAHs such as anthracene, [275] perylene, [276] and pyrene. [277] However,

it can be assumed for the entropic term to favour dimer dissociation at flame temperature.

The scientific community had a debate on the importance of vdW clustering of pyrene dimers as the first step to soot inception. In 1991, simulating structureless balls interacting through a Lennard-Jones potential, Miller concluded on the impossibility for PAHs below 800 amu to form stable clusters. [278] Later on in 2002, Schuetz and Frenklach used more complete molecular dynamics to show that pyrene clusters were actually able to survive at flame temperature. [279] The missing ingredient in Miller's simulations was the internal rotation induced by PAH collision.

However, with the further increase in computational power and the improvement of static calculations and molecular dynamics algorithms, it became more unlikely for the pure physical clustering to be the main mechanism of inception. Indeed, the pyrene dimer (Figure II. 11) was specifically studied by Sabbah *et. al.* in 2010 using a mixed experimental and theoretical approach. [224] Their conclusions were that pyrene physical dimerization could not be a key step for soot particle formation in flames. The same year, Chung and Violi used atomistic molecular dynamics and attained the same conclusion and suggested that only PAHs as large as ovalene (Figure II. 12) were able to form physical clusters even at 1000 K. [280] Nowadays, researchers studying the physical stacking hypothesis mostly focus on bigger PAHs around the size of circumpyrene (Figure II. 12). [281, 282]

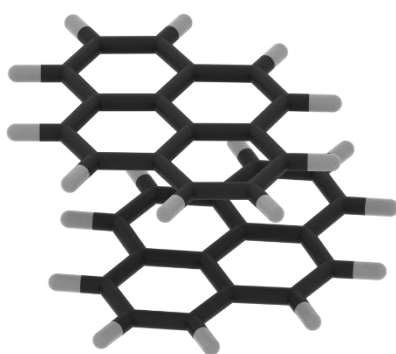


Figure II. 11: The pyrene physical dimer

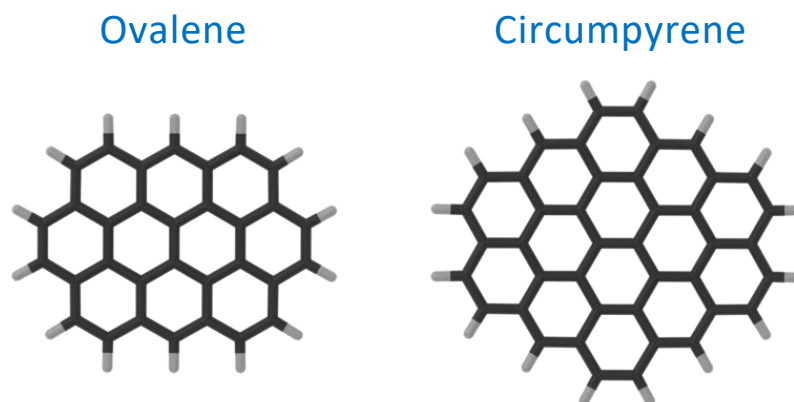


Figure II. 12: The structures of ovalene and circumphyrene

To make up for the poor stability of physical clusters, it has appeared important to take into account the existence of aliphatic chains at the edge of peri-condensed PAHs. Indeed, they were shown to induce stronger attractive forces between the PAH building blocks. [280, 283]

Finally, during the 2010s, several theoretical studies started suggesting that chemical bond formation between the PAH monomers had to occur to explain soot particle inception. [221, 283–288]

3.2.2. Chemical oligomers

The chemical oligomer hypothesis was suggested to better explain the stability of intermediate species before particle inception. In a series of 3 papers, Frenklach and Mebel studied the thermodynamics and kinetics of covalently bonded PAHs and considered the formation of ethylene-bridged PAHs (E-bridged). [218, 223, 289]

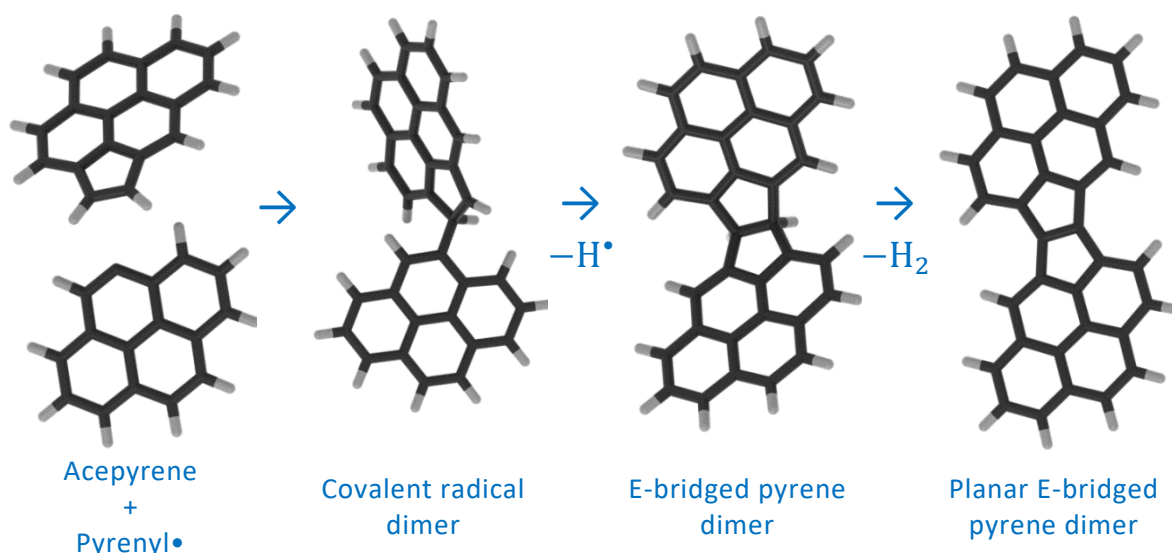


Figure II. 13: Reaction scheme of acepyrene and pyrenyl as suggested in references [223], [289] and [218]

Their findings were that reaction schemes such as that on Figure II. 13 could reproduce the experimental kinetics of soot inception. The E-bridged dimer quickly loses H₂ to form the planar E-bridged dimer. The reaction scheme does not give any insight on how the species can further react to form 3-dimensional particles, but, the suggested mechanism explains the formation of structures similar to those observed in AFM images (Figure II. 10), and involves peripheral 5-membered rings which are commonly observed.

Similar chemical oligomerizations are also possible if aliphatic chains are present at the edge of PAHs. Indeed, they can be expected to further react through the HACA mechanism to form aliphatically bridged PAHs (ABPAH), which are good molecular candidates for the formation of incipient particles. Interestingly, in 2018 Adamson *et. al.*, evidenced by the use of high-resolution tandem mass spectrometry the possible existence of ABPAHs such as shown on Figure II. 14. [290] Also, the AFM and STM images from references [272] and [271] show what looks like PAH cores bridged together by aliphatic chains which would have further reacted through cyclization.

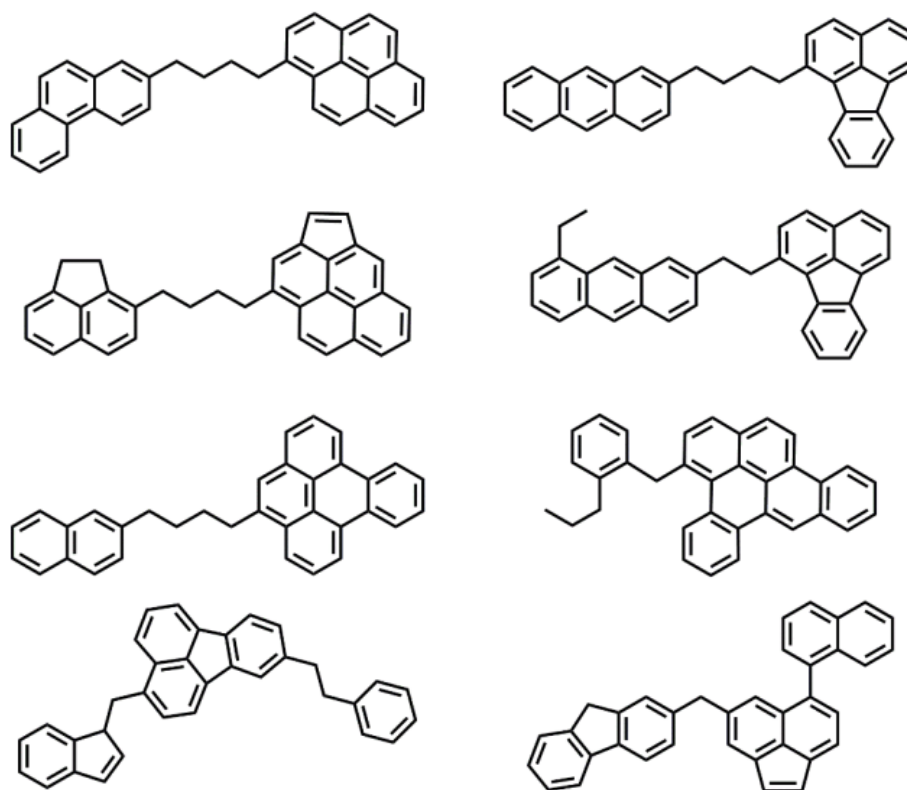


Figure II. 14: Examples of ABPAHs, taken from reference [290]

The thermodynamic stability of ABPAHs was studied and it was shown that the aliphatic linkage could overcome the entropic disadvantages of pure vdW clustering. [291] They were also observed in ReaxFF molecular dynamics studies. [221, 286]

4. Spectroscopic evidences of PAH dimerization

4.1. Laser induced fluorescence (LIF)

Among the possibilities available to track the formation of soot, LIF represents an interesting *in situ* technic that allows to probe a desired region of the flame and record its emission spectrum at a given excitation wavelength. [292] For example, PAH formation can easily be observed because of their typical UV excitation and emission signature. [293–296] A representation of a LIF setup is shown on Figure II. 15, with the emitted fluorescence being collected at a right angle to the laser. Typically, the LIF spectra are measured along the centreline of a laboratory flame at various HABs so that the formation of various chemical species depending on the flame regime can be observed.

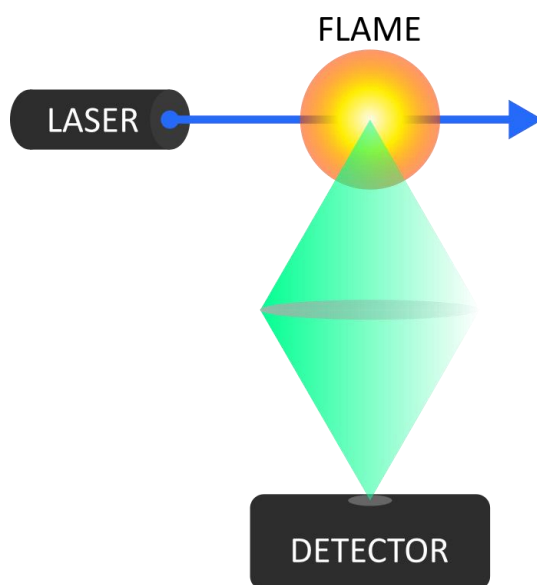


Figure II. 15: Simplified scheme of a LIF setup inspired by reference [297]

4.2. LIF signals in sooting flames

In reference [298], LIF measurements were performed using a Nd:YAG laser as excitation source. It delivers 1064, 532 and 355 nm wavelengths which can further pump an optical parametric oscillator (OPO) to obtain a 213 – 532 nm range of excitation wavelengths. Using a 213.5 nm excitation wavelength, the low HAB

(10 mm) fluorescence emission of the PAHs is evidenced at around 350 nm, as shown on the $\lambda_{\text{exc}} = 213.5$ nm spectrum on Figure II. 16.

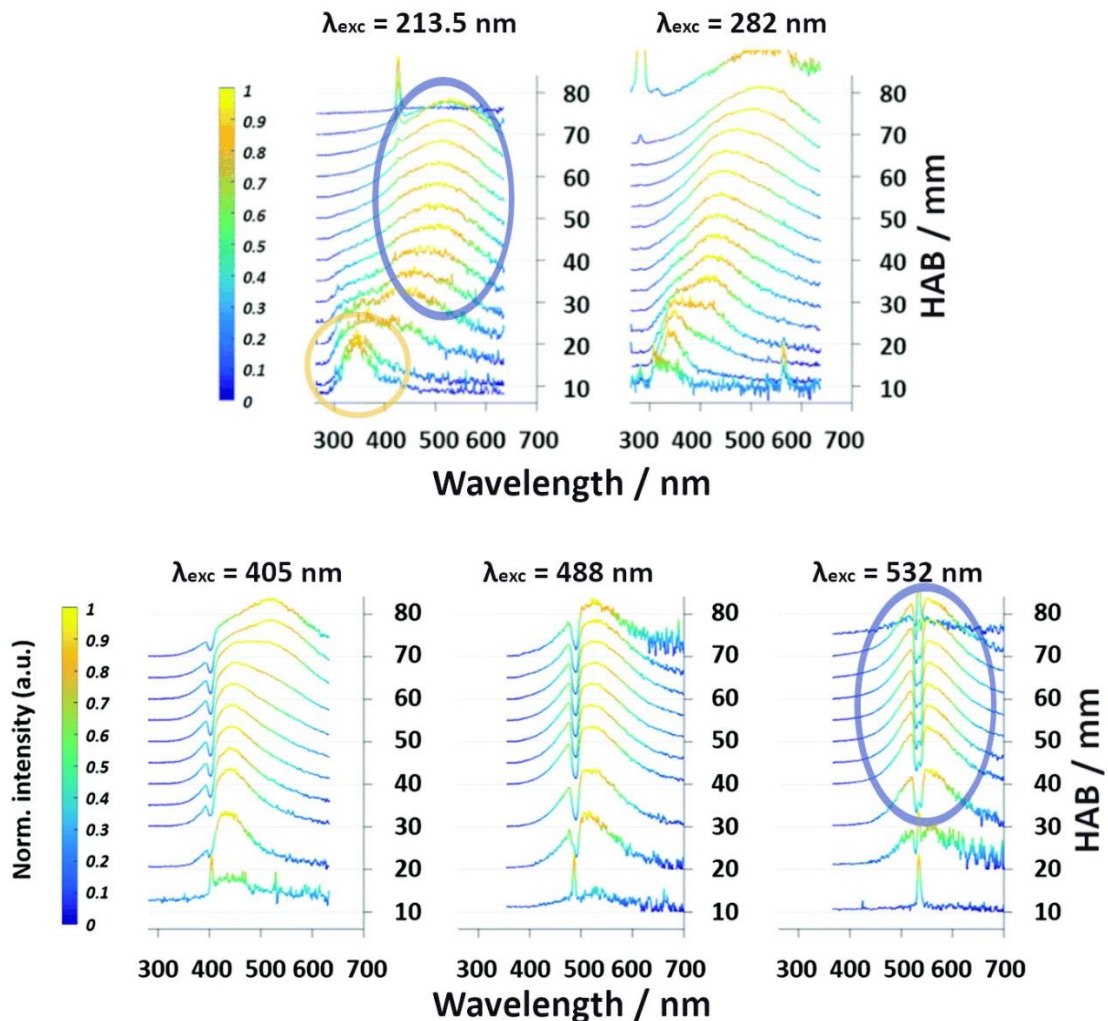


Figure II. 16: Laser induced fluorescence spectra recorded along the flame vertical centre-line at five excitation wavelengths. The spectrum intensities were normalized to better see the weak PAH UV fluorescence. Taken from reference [298]

Moreover, the first soot particles could be detected at around 60 mm HAB by the apparition of a Laser Induced Incandescence (LII) (not shown and not discussed in this work). Thus, it can be assumed for intermediate chemical species responsible for the inception process to be detectable between 10 and 60 mm HABs. Indeed, using the same excitation wavelength of 213.5 nm, a red-shift of the emission spectrum is observed upon an increase in HAB. Thus, intermediate species that could play a role in the process can absorb at 213.5 nm to yield a broad and structureless fluorescence emission band at around 530 nm. This broad-band (BB) can be observed using excitation wavelengths up to 532 nm (680 nm in reference [295]), at maximum emission wavelengths of around 550 nm (630 nm at 680 nm excitation wavelength),

with large Stokes components due to the high temperatures in flames. This represents around 200 – 300 nm (1.3 – 1.6 eV) wavelength shift from the excitation of PAHs in the UV range to excitations that can induce the BB.

4.3. Hypotheses on the origin of the broad-band

4.3.1. Acenaphthylene fluorescence

The BB was first reported in the early 80s by several authors. [299, 300] The first attribution that was given is the fluorescence from acenaphthylene, whose emission signature resembles the BB (its emission maximum lies at around 550 nm). [301, 302] However in 1989, Petarca and Marconi fed a flame with saturated acenaphthylene methanol solution and did not observe the BB, [303] although the comparison of the emission spectra let us think that acenaphthene was injected instead of acenaphthylene. [304, 305]

Nevertheless, acenaphthylene is only weakly fluorescent which raises questions based on the remarkably high intensity of the BB. [298] Moreover, acenaphthylene is a small PAH which can be expected to form rapidly in the flame, contrarily to the HABs corresponding to the apparition of the BB. [295]

4.3.2. Other PAHs

The fact that acenaphthylene can yield such a low energy fluorescence suggested that 5-membered rings would significantly modify PAHs electronic properties. Indeed, such PAHs were shown to have significantly red-shifted emission spectra compared to 6-membered ring-containing only PAHs. [245] Similarly, unsaturated aliphatic chains at the edge of PAHs were also shown to display these shifts. [294] Finally, the progressive growth of PAHs into bigger 2-dimensional structures (up to graphene for infinite growth) is known to extend the π -system, which lowers electronic transition energies. [306]

However, all those systems are planar and monomeric, which cannot account for the 3-dimensional growth of soot. Thus, it was chosen to exclude them from the study.

4.3.3. Excimers and exciplexes fluorescence

A third hypothesis is the fluorescence from excimers or exciplexes, [225, 307] since excimers exhibit a strong fluorescence emission, similar to the BB. Unfortunately, the

literature is unclear on the subject. Indeed, “excimer fluorescence” is sometimes referred to as the fluorescence obtained from the excitation of vdW dimers in their GS, although “excimer” is a term reserved to the fluorescence from photo-formed species that dissociate in the GS.

Strictly speaking, an excimer is formed from the excitation of a monomer in a “pre-oriented” dimerized conformation so that the monomers can interact once in the ES. [308] The pre-orientation is induced by very weak forces (and the Brownian motion), and the excitation spectrum of the pre-oriented dimer is simply that of the monomer.

However, the BB can be observed with low energy lasers of up to 680 nm, far from the absorption range of typical PAHs. This seriously contradicts the hypothesis of an excimer fluorescence despite its acceptance by several research groups. [309–311]

4.3.4. Stable vdW dimers

On the contrary, the excitation of stable vdW PAH dimers would be feasible using low energy lasers, which would yield a fluorescence similar to that of excimers and thus, similar to the BB. It was already mentioned that physical oligomers were unlikely to contribute strongly to soot formation because of their instability. However, it must be pointed out that the physical dimerization as a starting point to soot inception cannot completely be ruled out. Indeed, some authors suggest that both physical and chemical oligomerization regimes might coexist depending on flame conditions. [221, 223] Also, they were mostly studied in thermodynamics and kinetics studies and the possibility of their electronic excitation to yield the BB was, to our knowledge, never investigated by computational methods.

5. Objectives of the study

In the following chapters, the optical properties of some candidates for the explanation of the BB are explored using DFT and TD-DFT. This study was conducted on pyrene, fluoranthene and perylene (of structure given on Figure II. 17), which were chosen as base structures for more complex chemical species.

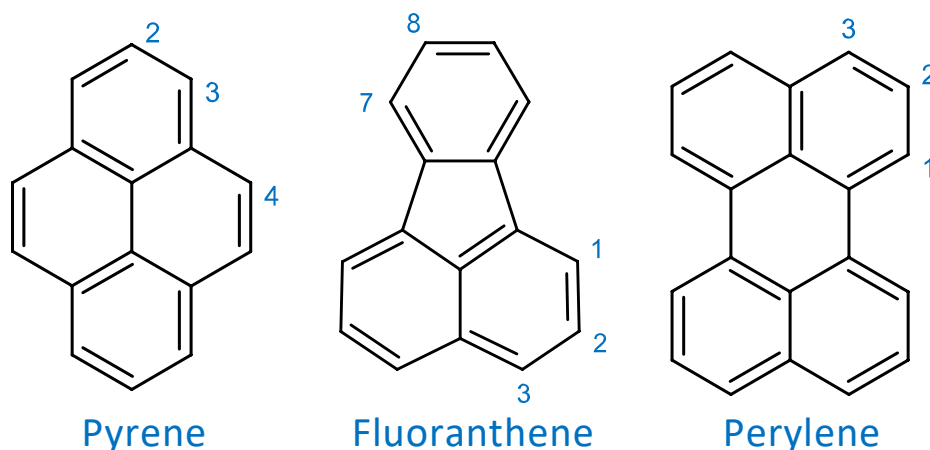


Figure II. 17: The studied PAHs with the labelling of the carbon atoms that can be implied in the aliphatic bonding

In Chapter 2, the vdW oligomers of the aforementioned PAHs are studied, and the effect of their clustering on their electronic properties is investigated. The calculation of emission spectra can be expensive, especially for dimerized systems. Thus, a particular focus is put on the calculation of absorption spectra. Indeed, the vdW dimerization of PAH can be expected to red-shift the electronic transitions, and the calculated red-shifts will be compared to the 200 – 300 nm (1.3 – 1.6 eV) shifts observed experimentally. It is also in this chapter that the performances of three functionals (*i.e.*, PBE0, CAM-B3LYP and LC- ω PBE) are assessed for ES calculations, which will serve as a benchmark for the two remaining chapters.

In Chapter 3, the same considerations are explored for ABPAHs of structure similar to those shown on Figure II. 14. To our knowledge, the implication of bridged structures for the observation of the BB is rarely considered, and the effect of the aliphatic bridging on the electronic spectra has never been studied. Moreover, ABPAHs can be expected to be found in a “folded” conformation which should yield electronic properties similar to pure vdW dimers, with improved thermodynamic stability. Thus, the objectives were to assess the effect of the aliphatic bridging on the

monomers structure, and to explore the differences between purely physically bound PAHs and ABPAHs on the absorption spectra.

Finally, in Chapter 4, a recent and promising hypothesis for the origin of the BB is discussed, *i.e.*, PAH-based radicals. The study is performed on σ - and π -radicals of either monomeric or dimeric, pyrene, fluoranthene and perylene-based structures. To this aim, a more detailed introduction of the importance of PAH radicals for soot inception is given in the corresponding chapter.

6. Methodologies

6.1. Interaction in PAH dimers

The accurate description of non-covalent interactions is a major topic in computational chemistry and it has been shown that the second-order Møller-Plesset perturbation theory (MP2), [312–314] the most lightweight wave function method taking electron correlation into account, described poorly the π -interaction. [315, 316]

Likewise, DFT includes close to no London dispersion forces and also fails at describing non-covalent interactions. However, it can be corrected in a lightweight manner using an atom pairwise correction. [317] Moreover, DFT and TD-DFT are lightweight enough to conduct studies on relatively large systems, and the first part of this thesis highlighted their good performances for the study of organic dyes structures and spectra.

A set of empirical dispersion terms are available to correct DFT functionals deficiency. The D2 [318] and D3 [319] terms are well tested and implemented in most chemistry codes, whereas the D4 correction only slightly improves the results and is rather recent. [320] Thus, it was chosen in this work to focus on the more standard D2 and D3 terms. The D3 correction is expected to perform better compared to D2 because it takes into account the hybridization of atoms which have been shown to yield significant differences, especially when comparing the interaction in saturated dimers *vs.* that in unsaturated dimers. [321] The importance of the π -system in PAH is highlighted there, but one must be cautious when using the term “ π -stacking” because it is misleading. For example, it can vehiculate the idea that PAH homo dimers would stack in a perfectly parallel manner, which is known to be incorrect. [322, 323] Actually, the interaction between PAHs is better understood now. Using dispersion corrected double-hybrid density functionals, it was shown that the stabilization of dimers was mostly due to dispersion. A small “ π -stacking” effect (due to the π orbitals) was indeed observed for systems of at least 10 carbon atoms, but was shown to remain small. [324]

6.2. Excited-states of PAHs

The accurate reproduction of electronic spectra of PAHs can be challenging. It was shown that GHs such as PBE0 and B3LYP struggled with the description of the transitions to L_a , although it is the absorbing state. [244, 246, 325] On the contrary, RSHs struggle with the description of L_b transitions and the accurate description of both states simultaneously cannot be attained by varying the amount of exact exchange in the functional. It was shown that using DHs improved the description of both states, [326] with a major drawback being the extra cost of the calculation of the perturbative term. This study implying a large number of calculations on relatively large systems, these functionals were put aside.

In this work, the spectra are interpreted in a relative manner (monomer *vs.* dimer) so that error compensations can be expected to occur. Also, the aim of this work is to study the electronic properties of dimeric systems in which significant state modifications might occur, potentially improving the situation. Thus, in this work, TD-DFT using standard GHs and RSHs used its performances carefully assessed. To this aim, it was chosen to perform a benchmark (given in the technical details below) to select the best functional among several for accurately reproducing the L_a transition in pyrene vapor.

6.3. Computational details

The software and methods are similar to those used in Part I and will not be further introduced.

For the geometry optimizations, the following functionals were tested: PBE0(D3), B3LYP(D3), CAM-B3LYP(D3), LC- ω PBE(D3), B97D [318], and ω B97XD [327] (the two latter using D2 type dispersion corrections). This was done by performing a relaxed scan with 6-31G(d) that is displayed on Figure II. 23, for which an interpretation is given in Chapter 2. A bigger basis-set (6-311++G(d,p)) and a DH (B2PLYP(D3)) were also tested by performing single-point energy calculations on the PBE0(D3) geometries obtained during the scan.

The performances in the ES were assessed by the mean of a benchmark, the results of which are given in Table II. 1.

Focusing on the performances of the functional with the biggest basis-set, *i.e.*, 6-311++G(d,p), PBE0 is the best performer with a low 0.075 eV difference. Switching to a double-valence basis-set, the PBE0/6-31++G(d,p) yields a 0.057 eV difference and removing polarization functions on hydrogen atoms reduces the error to 0.050 eV. The reduction of absolute difference is entirely due to error cancelling. However, the small absolute error change of only 0.025 eV despite a major reduction of computational cost is interesting. On a side note, the 6-31++G and 6-31G(d,p) basis-sets might have been good candidates based on the results of the benchmark. However, the inclusion of polarization functions on carbon atoms and diffuse functions is required, especially for extending the study to dimers of PAHs interacting through long-range vdW forces as well as radicals.

Ultimately, the PBE0(D3)/6-31++G(d) was chosen as a base theoretical framework for ES calculations. that was backed up by calculations using CAM-B3LYP(D3) and LC- ω PBE(D3).

As will be shown in Chapter 2, PBE0(D3) struggles with the description of the ESs of dimers. Thus, it was chosen to perform the TD-DFT calculations of Chapter 3 using CAM-B3LYP(D3) instead, with the 6-31++G(d) basis-set. The geometries on the other hand were optimized using PBE0(D3)/6-31++G(d) for better comparison with the structures of Chapter 2.

Finally, the results of Chapter 4 were obtained later on during the thesis and, in order to harmonize the results, it was chosen to perform the DFT and TD-DFT using CAM-B3LYP(D3)/6-31++G(d), including geometry optimizations.

	λ / nm	E / eV	$\Delta E / \text{eV}$
PBE0			
6-31++G(d,p)	328	3.782	0.057
6-31++G(d)	327	3.789	0.050
6-31++G	319	3.882	0.042
6-31G(d,p)	323	3.836	0.003
6-31G	315	3.933	0.093
6-311++G(d,p)	329	3.765	0.075
6-311++G(d)	329	3.773	0.067
6-311++G	319	3.883	0.043
6-311G(d,p)	327	3.796	0.044
6-311G	317	3.909	0.069
B3LYP			
6-31++G(d,p)	336	3.692	0.148
6-31++G(d)	335	3.698	0.142
6-31++G	328	3.782	0.058
6-31G(d,p)	331	3.750	0.090
6-31G	323	3.837	0.003
6-311++G(d,p)	337	3.676	0.164
6-311++G(d)	337	3.682	0.157
6-311++G	328	3.782	0.058
6-311G(d,p)	334	3.709	0.131
6-311G	325	3.810	0.029
ωB97XD			
6-31++G(d,p)	309	4.014	0.175
6-31++G(d)	308	4.021	0.181
6-31++G	301	4.125	0.285
6-31G(d,p)	305	4.070	0.231
6-31G	297	4.178	0.338
6-311++G(d,p)	310	3.994	0.154
6-311++G(d)	310	4.000	0.161
6-311++G	301	4.125	0.286
6-311G(d,p)	308	4.023	0.184
6-311G	299	4.151	0.311
CAM-B3LYP			
6-311++G(d,p)	312	3.972	0.133
LC-ωPBE			
6-311++G(d,p)	294	4.215	0.375
M06-2X			
6-311++G(d,p)	308	4.029	0.189

Table II. 1 electronic vertical excitation energies using various functionals and basis-sets. In the third column ($\Delta E / \text{eV}$), the computed values are compared to the gas phase absorption maximum (323 nm) obtained from reference [276]

CHAPTER 2.

Van der Waals dimers

The first hypothesis explored in this work is the vdW dimerization of small PAH species. The idea is that PAH dimerization would increase the delocalization of molecular orbitals and red-shift the electronic excitation and emission spectra in flames. Also, the 3-dimensional structure obtained can be expected to serve as a good nucleation core for soot growth.

VdW dimers of pyrene, fluoranthene and perylene were studied using DFT and TD-DFT. Their stability and electronic properties were studied and the performances of the functionals assessed.

1. Conformers of the pyrene dimer

1.1. Optimization of the structures

As a starting point for a more extensive work, it was chosen to study the vdW dimer of pyrene (**PYPY**). The PAHs are usually flat and rigid meaning that an overview of the interaction energy landscape between monomers can be explored by focusing on a few key structures that are shown on Figure II. 18.

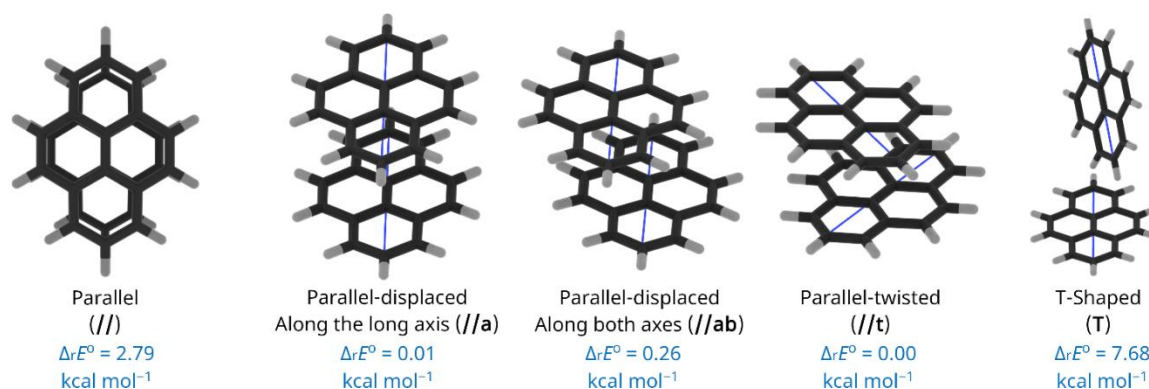


Figure II. 18: Key structures in the study of **PYPY** and their energies

The $\Delta_r E^\circ$ are given according to the chemical equation $\text{Ref} \rightleftharpoons \text{X}$ with Ref, the // geometry since it is the lowest energy conformation, and X the considered geometry.

First of all, the // geometry could not be optimized as the algorithm always converged to one of the other geometries. So, its energy was obtained by positioning two optimized monomers in front of one another and performing multiple single point energy calculations to find the minimum of energy (the scan is shown and discussed in the next section). It has an energy of 2.79 kcal mol⁻¹. Also, the //t, //a, and //ab geometries are almost isoenergetic with energies of 0.00, 0.01 and 0.26 kcal mol⁻¹, respectively. Finally, an energy value of 7.68 kcal mol⁻¹ for **T** was obtained by optimizing its structure without including the dispersion correction and performing a single-point energy calculation including the dispersion on the obtained geometry. This result contrasts with the benzene dimer for which **T** is one of the most stable geometries, [328, 329] but it is consistent with geometries that were found by other authors for **PYPY**. [330, 331] Also, less extensive investigations carried out on the fluoranthene (**FLUFLU**) and perylene (**PERPER**) dimers showed that the minimum

energy is obtained for the **//ab** geometry for **FLUFLU** and **//a** for **PERPER**. However, the other conformations could have probably been observed too.

1.2. Geometry analysis

In order to investigate the effect that the vdW dimerization has on the structure of the pyrene monomers, a structural analysis was performed on the optimized geometries. Several important bond lengths and angles in the **//a**, **//ab** and **//t** geometries are given in Table II. 2, compared to those in pyrene.

Bond lengths / Å							
	//a		//ab		//t		Pyrene
1	1.391	1.392	1.391	1.392	1.391	1.391	1.392
2	1.434	1.434	1.434	1.434	1.434	1.434	1.435
3	1.359	1.359	1.360	1.360	1.360	1.360	1.360
4	1.401	1.401	1.401	1.401	1.401	1.401	1.401
5	1.423	1.423	1.424	1.424	1.423	1.423	1.424
6	1.423	1.423	1.423	1.423	1.423	1.423	1.423
Angles / °							
	//a		//ab		//t		Pyrene
a	120.4	120.5	120.6	120.5	120.5	120.5	120.5
b	119.8	119.9	119.9	119.9	119.9	119.9	119.9
Intermonomer distance / Å							
	//a		//ab		//t		
	3.83		3.81		3.62		

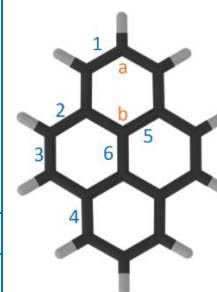


Table II. 2: Some important geometric parameters in the optimized **//a**, **//ab** and **//t** structures. The **T** geometry parameters were not included in the table because it was optimized without dispersion and is not comparable to the others. The two columns correspond to each monomer in the dimeric form

In the dimers, the geometric parameters were gathered for each monomer (corresponding to the two columns) in case one monomer was more impacted than in the other. The structural analysis shows that the dimerization has effects on neither the bond lengths nor the angles of the monomers. Indeed, the geometric parameters are equal up to ± 0.001 Å for the bonds and up to $\pm 0.1^\circ$ for the angles. Finally, the intermonomer distance, defined as the distance between the centre of mass of the two monomers,² is reported in the table. Interestingly, the distance is similar in the **//a** and **//ab** geometries, but not in **//t**. This is surprising since the three energies are almost isoenergetic.

² This definition is disputable but the non-perfect parallelism of both monomers prevents a rigorous one. Moreover, it is quite simple and reasonable since **T** dimers are not investigated.

Based on this structural analysis, two interesting facts can be highlighted. First, the fact that **//a**, **//ab** and **//t** are almost isoenergetic suggests that the monomers are relatively free to move on a flat potential energy surface. This is particularly important considering the difference in intermonomer distance between the three structures. Thus, it can be interesting to further investigate the energy landscape and to search for energy barriers. This is done later in this chapter by the mean of translation and rotation scans. Second, the effect of the dimerization appears to have close to no effect on the structure of the monomers. This is particularly surprising since pyrene is a prototypical system expected to display relatively strong π -interactions. Thus, if any π -interaction is present, it has no structural effect on the monomers.

2. Electronic properties

2.1. Technical details on the translation scan

The // and //t geometries of **PYPY** were further studied by running two scans of the intermonomer distance in each geometry, from 3.00 to 16.00 Å intermonomer distances. The potential energy curves (PEC) were sampled using translation steps of: 0.05 Å near the minima of energy, 1.00 Å at the longest distances, and values in between for intermediate sections.

The // scan was performed by placing two optimized pyrene molecules next to one another (in a // geometry), and by running single-point calculations with a variety of intermonomer distances. In the case of the //t scan, it was obtained by using the optimized //t geometry, and translating one of the monomers along the normal vector of the plane of the other monomer.

Along the PECs, the energies of the electronic ESs were computed. This procedure allows to investigate the dimer properties in the GS as well as its excimer formation. This methodology was applied by other groups to multiple systems, such as benzene, [261] tetracene, [259] and pyrene. [263, 263, 264] Because CTs can be expected when studying the ESs of PAH dimers, PBE0(D3) was anticipated to struggle. Thus, the scan was complemented by the use of 2 RSHs: CAM-B3LYP(D3) and LC- ω PBE(D3).

Finally, before studying the scan results, it will be convenient to define a notation for the molecular orbitals to better describe the orbital contributions to the electronic transitions. Indeed, upon dimerization, the orbitals of the monomers are split into symmetric and antisymmetric linear combinations. Thus, in the next sections on this chapter, the monomers orbitals will be denoted H and L (for HOMO and LUMO, respectively), so that the orbitals of the dimer are $\text{HOMO} - 1 = \text{H} - \text{H}$, $\text{HOMO} = \text{H} + \text{H}$, etc., as shown on Figure II. 19

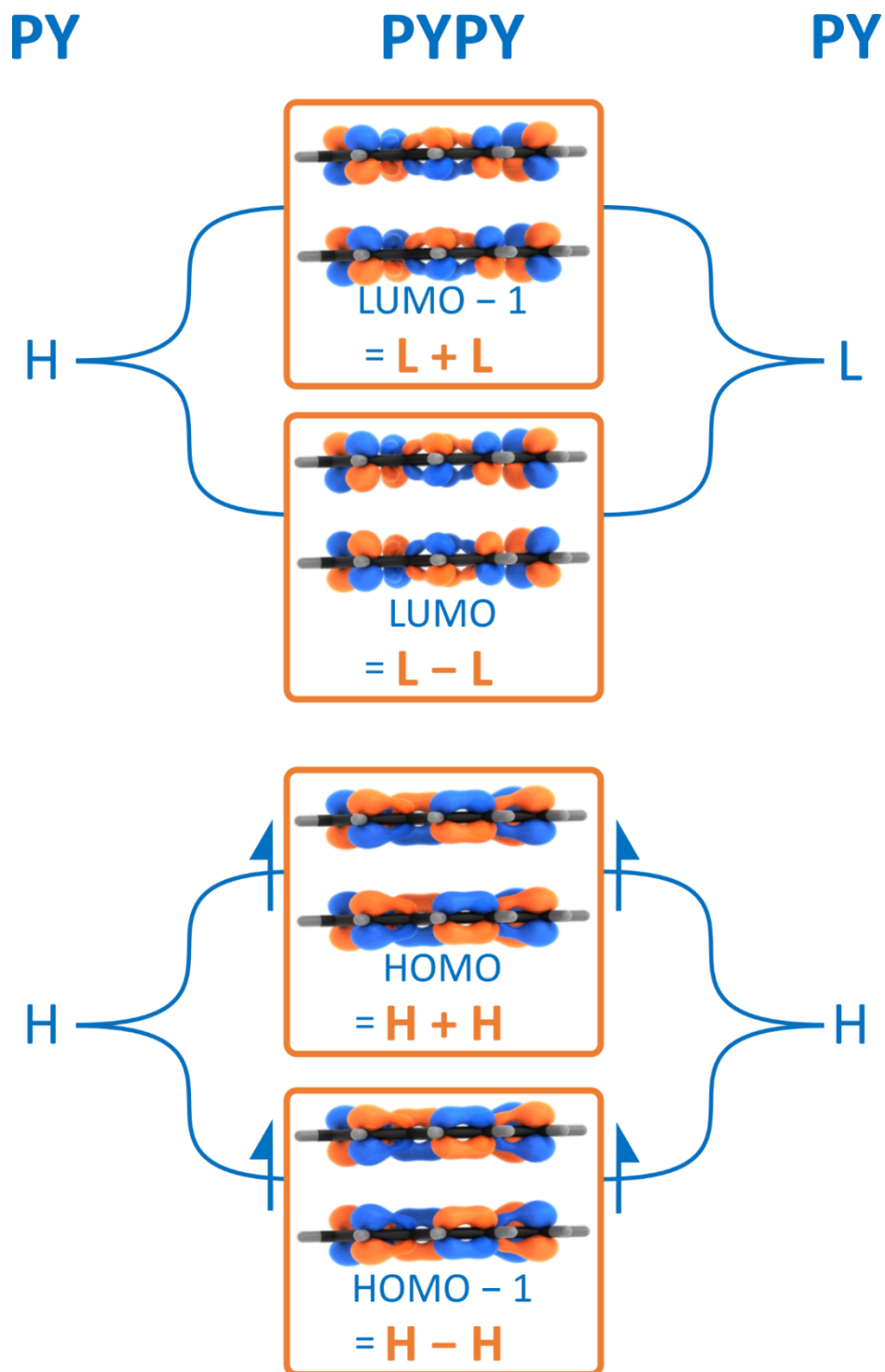


Figure II. 19: Representation of the molecular orbital splitting into symmetric and antisymmetric linear combinations upon dimerization in a // geometry

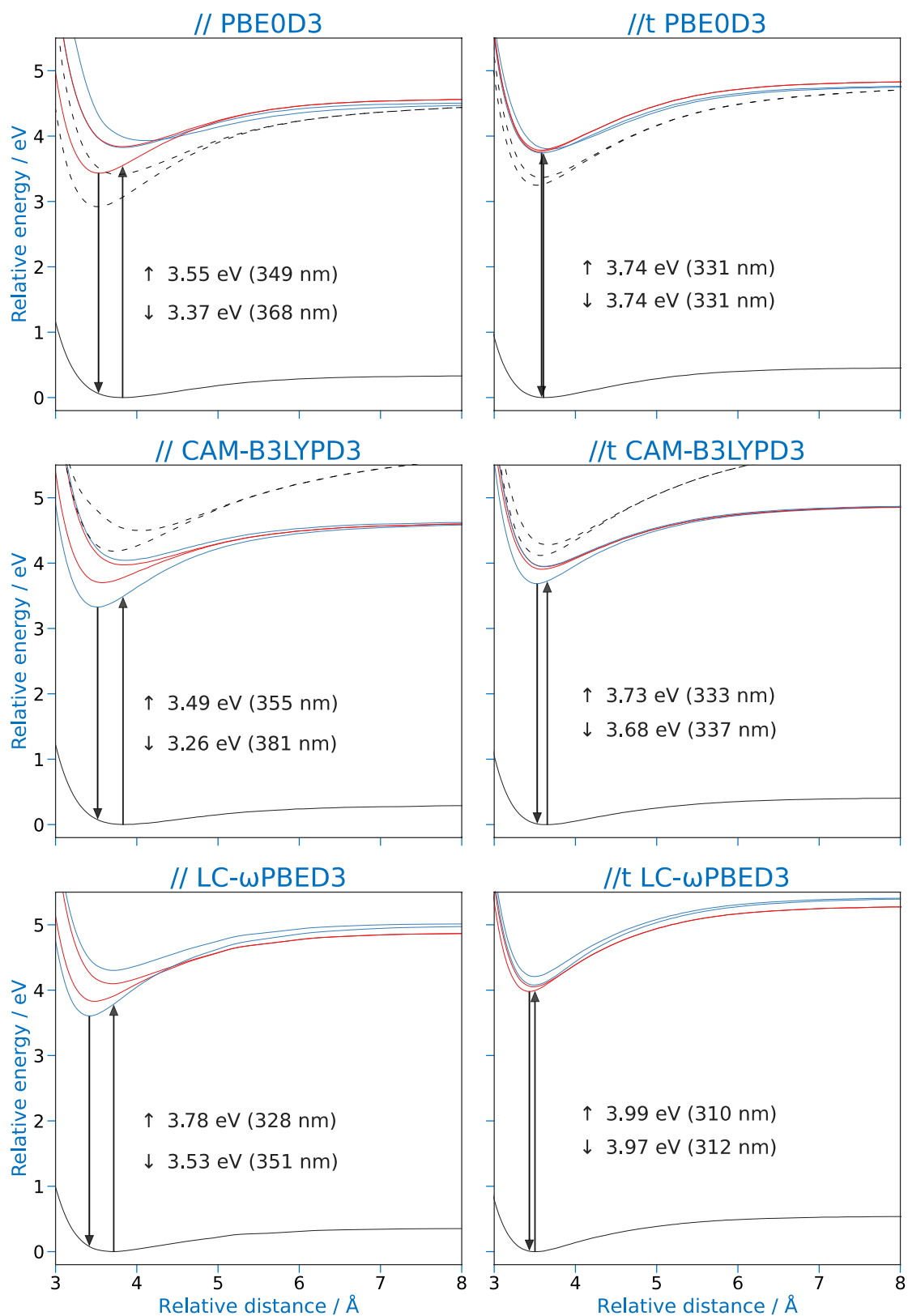


Figure II. 20: PECs of the GS and lowest energy ESs of **PYPY** // (left) and //t (right) along the intermonomer distance. The low-lying excited states originating from L_a and L_b are in blue and red, respectively. The origin of the states drawn as dashed lines is discussed in the text

2.2. The identification of excited-states

2.2.1. The CR states

The PECs are represented on Figure II. 20.

First of all, PBE0(D3) yields two low ESs (in dashed lines). They are induced by HOMO \rightarrow LUMO transitions, meaning that they are of L_a parentage. Interestingly, they are observed at higher energies using CAM-B3LYP(D3) and even more with LC- ω PBE(D3). This behaviour is consistent with CT states since GHs tend to over-stabilize them and an increase of the exact exchange percentage in the functional tends to improve the description. [138] Also, **PYPY** was specifically studied by Hunenerbein and Grimme with BH-LYP (50% exact exchange) and did not report their presence. [263] Thus, it can be assumed that they are CR states that should not be observed at such low energies. This is confirmed by looking at iso-surfaces of the electron density rearrangements upon excitation to one of them, as shown on Figure II. 21. They can easily be identified since their energy keeps rising at infinite distance (not shown), which is a behaviour that was also observed for the CR states of the tetracene dimer. [259]



Figure II. 21: Electron density rearrangements upon the excitation to one of the CR states in the //t pyrene dimer. The orange and blue colours indicate electron density depletions and increase, respectively

This work is focused on the effect of the dimerization on the absorption spectrum of several species, and more specifically, on the red-shift induced. Thus, the CR states were ignored in the remaining part of this study.

2.2.2. The low-lying excited states

Since the CR states have been identified, a focus can be put on the ER ones, in blue and red on the figure. As stated in the introduction, major state-mixing occur at small intermonomer distances so that the states are no longer 100% ER, but display partial CR components. Thus, the term ER is avoided in the remaining part of this work in favour of the term “low-lying excited states” (LLES).

The information on the transitions to the four LLES in the // geometry is given in Table II. 3. Upon dimerization, the ESs are only slightly split to yield a gap of 62 nm between the lower and higher energy states. Only the fourth electronic transition is allowed with an oscillator strength of 0.4507.

λ / nm	f	Dimer orbitals	Monomer orbitals	%
368	0.0000	HOMO \rightarrow LUMO	H \rightarrow L	100 L_a^-
335	0.0000	HOMO - 3 \rightarrow LUMO + 1 HOMO - 2 \rightarrow LUMO HOMO - 1 \rightarrow LUMO + 7 HOMO \rightarrow LUMO + 2	H - 1 \rightarrow L H - 1 \rightarrow L H \rightarrow L + 3 H \rightarrow L + 1	6 37 6 50 L_b^-
312	0.0003	HOMO - 3 \rightarrow LUMO HOMO - 2 \rightarrow LUMO + 1 HOMO - 1 \rightarrow LUMO + 2 HOMO \rightarrow LUMO + 7 HOMO \rightarrow LUMO + 10	H - 1 \rightarrow L H - 1 \rightarrow L H \rightarrow L + 1 H \rightarrow L + 3 H \rightarrow L + 5	24 23 28 23 3 L_b^+
306	0.4507	HOMO - 3 \rightarrow LUMO + 2 HOMO - 2 \rightarrow LUMO + 7 HOMO - 1 \rightarrow LUMO HOMO \rightarrow LUMO + 1	H - 1 \rightarrow L + 1 H - 1 \rightarrow L + 3 H \rightarrow L H \rightarrow L	7 5 54 34 L_a^+

Table II. 3: Wavelengths (nm) and oscillator strengths to the transitions to the four LLESs and their molecular orbital contributions. The attributions of the LLESs (L_a^- , L_a^+ , L_b^- and L_b^+) are given at the right of the figure

The first and fourth transitions are 100 and 88% H \rightarrow L, respectively. Thus, they are of L_a parentage and will be written L_a^- and L_a^+ , respectively. The second transition is a 43% H - 1 \rightarrow L and 50% H \rightarrow L + 1 and can be attributed to a L_b state and will be written L_b^- . Finally, the composition of the third transition is more complex, but is close to a L_b transition, with 47% H - 1 \rightarrow L and 28% H \rightarrow L + 1. Thus, it will be written L_b^+ .

This analysis has also been performed on the results of other functionals and with the //t geometry, which allowed attribution of states. On the scans, the L_a and L_b parentage states are shown in blue and red, respectively.

2.3. Comparison between the functionals

The functionals display different results for the LLESs in the // geometry. To illustrate, the electronic transition wavelengths at 3.7 Å are given in Table II. 4.

	PBE0(D3)	CAM-B3LYP(D3)	LC- ω PBE(D3)
Wavelength / nm (energy / eV)			
L_a^-	323 (3.84)	366 (3.39)	329 (3.77)
L_a^+	304 (4.07)	305 (4.06)	288 (4.30)
L_b^-	358 (3.46)	334 (3.71)	318 (3.90)
L_b^+	322 (3.85)	311 (3.99)	303 (4.10)
State splitting / nm (eV)			
L_a	19 (0.23)	61 (0.67)	41 (0.53)
L_b	36 (0.39)	23 (0.27)	15 (0.20)

Table II. 4: The four LLES electronic transition wavelengths in nm (and energies in eV), and state L_a and L_b splitting upon dimerization. The values are given for the // geometry, at 3.7 Å

First of all, the transition wavelengths are mainly ordered as PBE0(D3) > CAM-B3LYP(D3) > LC- ω PBE(D3). This is expected since the exact exchange component in the functional at long range increases in this order, which is known to blue-shift the transitions. The results are particularly coherent between the three functionals since the transition wavelengths are relatively close, within ± 22 , 9, 20 and 10 nm (± 0.23 , 0.12, 0.22 and 0.13 eV) for L_a^- , L_a^+ , L_b^- and L_b^+ , respectively.

However, taking a closer look to the L_a^- state shows that the results are more contrasted than one may think. Indeed, whereas CAM-B3LYP(D3) and LC- ω PBE(D3) give a $L_a^- < L_b^- < L_b^+ < L_a^+$ state energy ordering, PBE0(D3) predicts that L_a^- is isoenergetic with L_b^+ and that L_b^- is the lowest energy state, *i.e.*, the excimer state.

The state ordering found using RSHs is the same as the one found by Huenerbein and Grimme (using BH-LY), [263] and by do Casal and Cardozo (using RI-SOS-ADC(2)). [262] Moreover, the excimer state is usually considered to be of L_a

parentage due to the strong L_a splitting upon dimerization. [332, 333] Thus, the RSH description of the ESs of **PYPY** appear more realistic.

2.4. Nature of the interaction

2.4.1. Orbital overlap

The π -interaction in PAH dimers is usually thought of as an overlap between π orbitals. For example, it was shown that the H orbitals (HOMO of the monomers) split upon dimerization into symmetric and antisymmetric linear combinations to yield $\text{HOMO} - 1 = \text{H} - \text{H}$ and $\text{HOMO} = \text{H} + \text{H}$.

The splitting is dependent on the orbital overlap of the orbital pair. Thus, in order to assess this effect, orbital overlaps were computed by using the secular equations of orbital pairs:

$$\begin{pmatrix} H_{11} - E & H_{12} - ES \\ H_{12} - ES & H_{22} - E \end{pmatrix} \begin{pmatrix} c_1 \\ c_2 \end{pmatrix} = \begin{pmatrix} 0 \\ 0 \end{pmatrix}$$

In which H_{11} and H_{22} are the energies of orbitals 1 and 2 in the monomers ($H_{22} = H_{11}$), H_{12} is the off-diagonal element of the Hamiltonian matrix which can be approximated as $H_{12} = kH_{11}S$, (k is a constant) and S is the overlap between the two orbitals. Solving for E yields the energies of the two orbitals in the dimer system:

$$E_1 = \frac{H_{11} + kH_{11}S}{1 + S}$$

$$E_2 = \frac{H_{11} - kH_{11}S}{1 - S}$$

Which, finally, using $\Delta E = E_2 - E_1$ and solving for S yields the quadratic equation:

$$\Delta ES^2 + 2H_{11}S(1 - k) - \Delta E = 0$$

The equation can be fitted using the least-squared method with k and H_{11} set as free parameters. The equation is valid only for 2-orbital interactions, which limits its application to not too diffuse orbitals and symmetric systems, so the method was applied on the // scan. The results are shown on Figure II. 22.

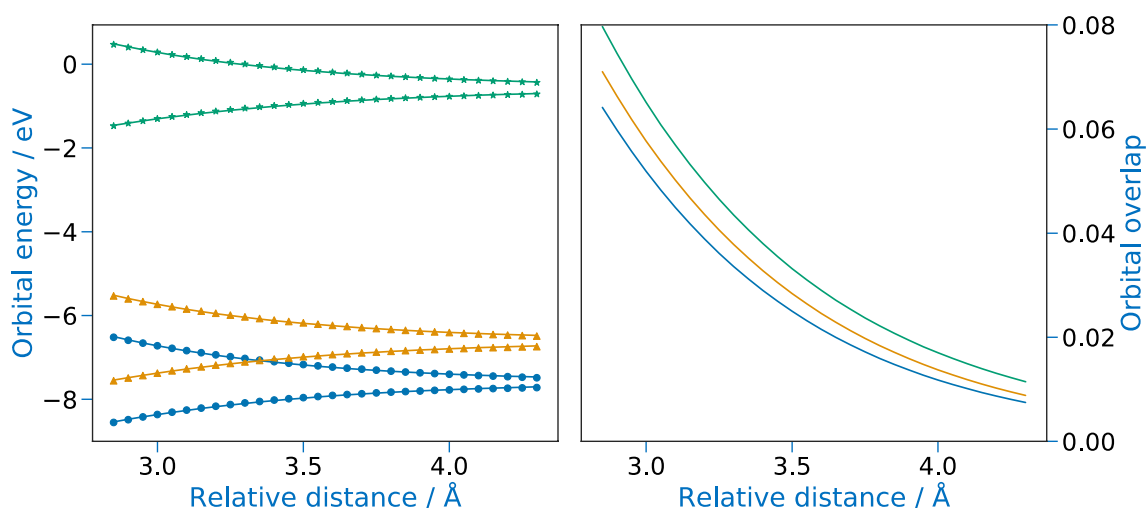


Figure II. 22: Evolution of the HOMO – 1 (blue, ●), HOMO (orange, ▲) and LUMO (green, ★) orbital energies (left) upon dimerization to the // geometry. The computed energy values are given by the scatter points and the line represents the fit. On the right are shown the orbital overlaps using the same colour scheme

The method could not be applied to the $L + 1$ orbital because of its too diffuse character which makes it interact with more than one orbital. On the left is shown the orbital splitting upon dimerization, and on the right, the computed overlap with respect to the intermonomer distance. At the minimum of energy (3.83 Å), the overlap values are of 0.015, 0.017 and 0.021 for HOMO – 1, HOMO and LUMO, respectively. Those values can be compared to the ~ 0.5 overlap values typically encountered in covalent bonds, [334] and a value of 0.7 was obtained for H_2 .

The overlap values suggest a relatively weak π -orbital interaction, which is surprising considering that the pyrene dimer is usually thought of as a prototypical example of a π -stacking system.

2.4.2. Importance of the dispersion forces

The PECs shows that all four LLESs are binding states, with a binding character more pronounced in L_a^- and L_b^- than in L_a^+ and L_b^+ . However, in the //t geometry, they remain almost degenerate. Among possible explanations, the empirical dispersion correction is a simple term added to the total energy of the molecule, regardless of the electronic state considered. Actually, earlier this year Hancock and Goerigk showed that state-specific approaches to apply dispersion corrections should be developed to better account for the differences in the ESs of PAH dimers. [335] Thus, this degeneracy can be a calculation artifact and will not be further discussed.

That being said, two energetic parameters were used to investigate the PECs:

- The **dissociation energy** is defined as the energy of the electronic state of interest at the furthest distance, minus that at the minimum of energy of the state
- The **absolute dispersion energy change upon dimerization** is defined as the absolute difference between the value of the D3 term at the furthest distance, and that at the minimum of energy of the state of interest

They are reported in Table II. 5.

Overall, the dispersion and dissociation energies are of similar orders of magnitudes. This highlights the particular importance of the dispersion forces in the interaction between PAH species, as already suggested by other groups. [321, 331] In particular, L_a^- and L_b^- have greater dissociation than dispersion energies suggesting an important π -interaction, whereas the GS and L_a^+ and L_b^+ have smaller ones. This suggests that the GS and L_a^+ and L_b^+ would be dissociative if it was not for the dispersion forces.

		Dissociation energy / eV				
		GS	L_a^-	L_a^+	L_b^-	L_b^+
	PBE0(D3)	0.336	0.346	0.262	0.903	0.396
//	CAM-B3LYP(D3)	0.292	1.116	0.291	0.703	0.345
	LC- ω PBE(D3)	0.358	1.163	0.356	0.764	0.421
	PBE0(D3)	0.457	0.570	0.508	0.624	0.599
//t	CAM-B3LYP(D3)	0.410	0.795	0.520	0.516	0.557
	LC- ω PBE(D3)	0.544	0.787	0.666	0.776	0.691
		Absolute dispersion energy change upon dimerization / eV				
		GS	L_a^-	L_a^+	L_b^-	L_b^+
	PBE0(D3)	0.466	0.466	0.278	0.643	0.466
//	CAM-B3LYP(D3)	0.453	0.682	0.414	0.653	0.433
	LC- ω PBE(D3)	0.529	0.758	0.529	0.758	0.529
	PBE0(D3)	0.580	0.627	0.536	0.627	0.627
//t	CAM-B3LYP(D3)	0.585	0.701	0.585	0.585	0.613
	LC- ω PBE(D3)	0.714	0.714	0.714	0.776	0.714

Table II. 5: GS and LLES dissociation energies and absolute dispersion energy change upon dimerization of **PYPY**, as defined in the text, in eV

2.4.3. DFT and TD-DFT performances

This analysis is true for CAM-B3LYP(D3) and LC- ω PBE(D3), but not for PBE0(D3) for which we already showed that the L_a^- was poorly described. This is particularly striking here, since the dissociation energies are computed as 1.116 and 1.163 eV for CAM-B3LYP(D3) and LC- ω PBE(D3), respectively, compared to 0.346 eV for PBE0(D3).

The pyrene dimer was studied recently by do Casal and Cardozo. [262] They calculated the same PECs as those on Figure II. 20 using RI-SOS-ADC(2), CAM-B3LYP(D3) and ω B97XD with the def2-SV(P) basis-set. The very small single ζ valence basis-set was used to assess its performances in ES molecular dynamics studies (that requires cheap computational frameworks). They found that TD-DFT severely over-bound the excimer compared to experimental data and that an incorrect ordering of states was predicted. The use of the def2-SV(P) was probably the culprit since the correct state ordering is obtained on Figure II. 20 with either CAM-B3LYP(D3) or LC- ω PBE(D3) functionals and the 6-31++G(d) basis-set. Moreover, they found a 1.70 eV dissociation energy (with the same definition as ours) using CAM-B3LYP(D3) to be compared to the experimental 0.73 eV. [254] In this work, values of 1.12 and 1.16 eV are found using CAM-B3LYP(D3) and LC- ω PBE(D3), respectively, which is a strong improvement compared to their findings. Moreover, part of the remaining error can be attributed to solvation effects since the experiments were carried out in cyclohexane whereas the calculations were performed in a vacuum.

In summary, CAM-B3LYP(D3) and LC- ω PBE(D3) along with the 6-31++G(d) basis-set not only predict the correct state ordering in the pyrene monomer, but also predict the correct $L_a^- < L_b^- < L_b^+ < L_a^+$ state ordering in its ESs. Moreover, it shifts CR states to higher energies as expected, and give realistic dissociation energy for the excimer.

We showed that D3 corrected RSHs are valuable tools for these kinds of studies and it was chosen to use CAM-B3LYP(D3) and LC- ω PBE(D3) for the remaining calculations on ESs of PAH dimers in this chapter.

3. Potential energy landscape

3.1. Rotation scan

In order to further explore the PES and to assess the differences between functionals on the dimer geometries, relaxed rotation scans were performed and the results are displayed on Figure II. 23.

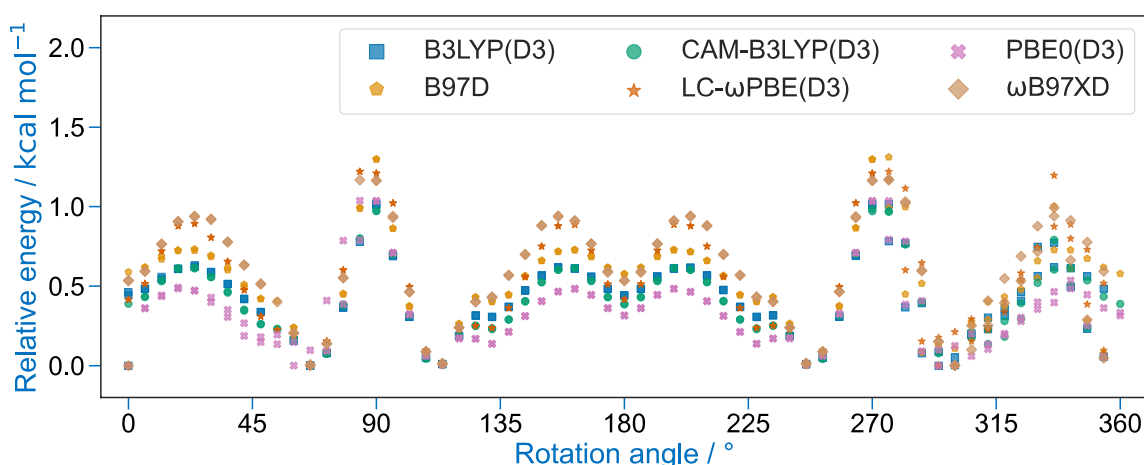


Figure II. 23: PECs of the relaxed rotational scan, using several functionals

Some key results can be extracted from the scan. First of all, notice that the global minima are the same whatever the functional used. Also, the maximum deviation in relative energy given by the functionals is of only $0.37 \text{ kcal mol}^{-1}$. In terms of geometry, there is a mean absolute deviation between the functionals for the intermonomer distance of 0.19 \AA with an average of 3.70 \AA for *//t*. Overall, the results are consistent with the literature findings, [331] with the global minimum being confirmed as *//t*. The three minima are retrieved, corresponding to the *//t*, *//a* and *//ab* geometries with a maximum energy barrier of $1.31 \text{ kcal mol}^{-1}$ obtained for the B97D functional. As illustration, the 84° geometry obtained with PBE0(D3) (noted *//t*(84°)) is shown on Figure II. 24, compared to the *//ab* and *//t* geometries. As a final and most important result, the PES is confirmed to be flat, with energy barriers of around $1.3 \text{ kcal mol}^{-1}$.

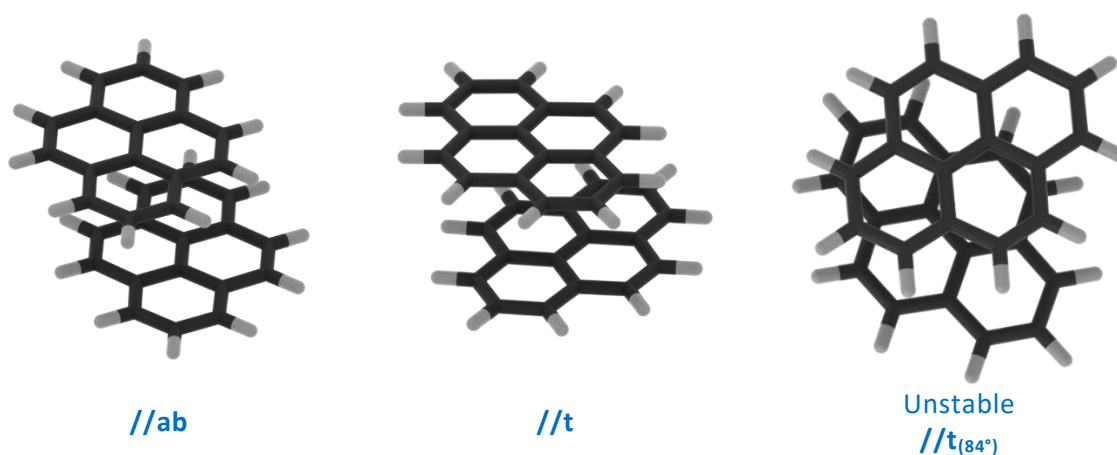


Figure II. 24: The **//ab** and **//t** geometries, compared to the unstable **//t(84°)** geometry, obtained with PBE0(D3)

The relaxed rotation scan was performed using the 6-31G(d) which is rather small. Thus, single-point energy calculations were performed on the set of PBE0(D3) geometries, using a bigger basis-set, *i.e.* 6-311++G(d,p). Also, in order to assess the importance of the perturbative term introduced in DHs, single-point energy calculations were performed on the same geometries using B2PLYP(D3)/6-311++G(d,p). The results are reported on Figure II. 25.

Overall, it can be seen that changing the basis-set has close to no effect on the relative energies and it can be assumed that optimizing with a larger basis-set would not lead to a different conclusion. Also, the use of a DH does not change the overall shape of the curves as well as give energy barriers similar to those obtained with GHs and RSHs.

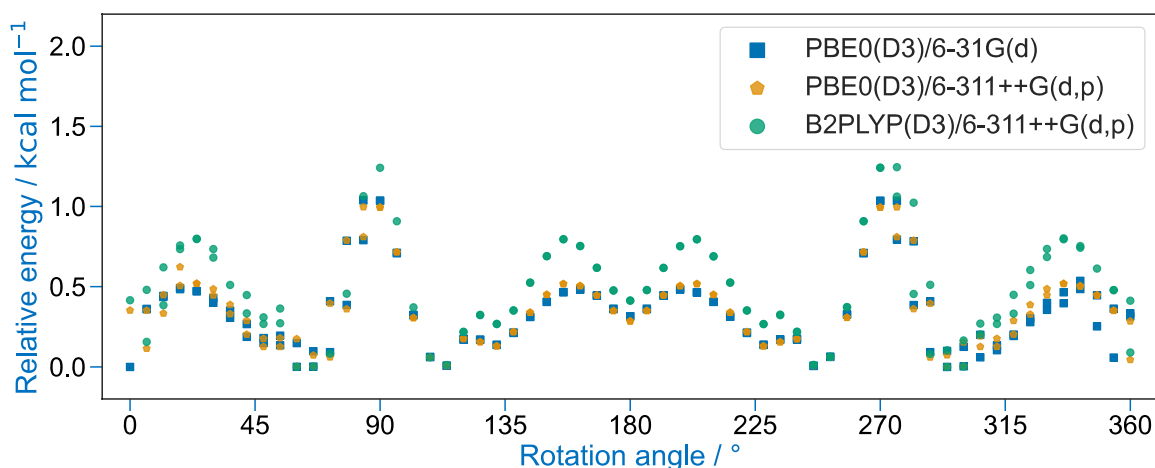


Figure II. 25: Single-point energy calculations on the PBE0(D3)/6-31G(d) geometries using a bigger basis-set and a DH

Thus, the effect of the functional on the geometries is very limited and the PBE0(D3) functional was kept for the geometry optimizations of the remaining part of this chapter, and for Chapter 3.

3.2. Binding energies

PAHs interact on the flat potential energy surface, with the majority of the stabilization coming from dispersion forces.

The stability of **PYPY**, **FLULU** and **PERPER** were investigated by optimizing their structure with three functionals and their binding free energies were calculated using the chemical equation $2M \rightleftharpoons D$, with M and D denoting the monomer and dimer, respectively. The values were computed at ambient and flame temperatures and are reported in Table II. 6.

The dimers are predicted to be observable at ambient temperature, which is consistent with experimental evidences of pyrene and perylene dimer formation in saturated solutions. [276, 277, 336] However, the interaction between the monomers appears quite weak.

The pyrene and fluoranthene dimers have similar binding energies, whereas the perylene dimer is more stable. This is expected since pyrene and fluoranthene are isomers (C₁₆H₁₀), whereas perylene is bigger (C₂₀H₁₂) which induces stronger dispersion forces. [225, 282]

		PYPY	FLUFLU	PERPER
298 K	PBE0(D3)	0.00	0.10	-2.34
	CAM-B3LYP(D3)	1.00	0.34	-1.21
	LC- ω PBE(D3)	-1.44	-0.91	-3.94
1500 K	PBE0(D3)	44.91	43.01	45.41
	CAM-B3LYP(D3)	45.19	39.52	49.73
	LC- ω PBE(D3)	47.31	46.71	55.90

Table II. 6: Binding Gibbs free energies (in kcal mol⁻¹) computed using the 6-31++G(d).

Switching to 1500 K, the dimers are unstable, which is due to entropy. This is a well-known result as discussed in Part II. Indeed, it led scientists to believe that, if vdW dimers of PAHs played a role in the inception of soot, it would be through kinetically-controlled processes. For example, it could be assumed for dimer

formation to only be the first step of the mechanism before further oligomerization into bigger and more stable clusters.

Also, based on these results, researchers suggested the formation of covalent bonds between PAH entities as an intermediate step. This would add irreversibility to the mechanisms and overcome some of the entropic disadvantages. This chemical pathway to soot inception is explored in more depth in Chapter 3.

4. Electronic absorption spectra

As a result of the previous potential energy landscape and structural analysis, three key results were obtained. First, vdW PAH dimers interact on a flat potential energy surface, to yield three stable structures //a, //ab and //t with small energy barriers between them. Second, the ESs of pyrene appear to be accurately described by CAM-B3LYP(D3) and LC- ω PBE(D3), which predicts the correct state ordering and coherent dissociation energies.

Finally, the π -interaction in vdW PAH dimers is quite weak and their interaction is mostly due to dispersion forces. Taking into account the dispersion forces, the binding is still weak and the dimers are barely stable at ambient temperature, and completely unstable in flame conditions. However, vdW PAH dimers are not excluded to temporarily be observed before further oligomerization, and the question whether vdW dimers of PAHs are at the origin of the BB or not remains unknown. Thus, in this section, the effect that the dimerization has on the absorption spectra of PAH is investigated.

4.1. Dimerization effect on the low energy excitations

The electronic transitions of **PYPY**, **FLUFLU** and **PERPER** were computed and compared to the lowest energy electronic transition (LEET) of the respective monomer. The results are shown on the spectra of Figure II. 26.

Although it could have been expected that the dimerization would extend the delocalization of the electrons and induce strong red-shifts on the absorption spectrum, the calculated shift is rather small. Indeed, the computed values are of 22, 7 and 35 nm (0.26, 0.07 and 0.25 eV) for pyrene, fluoranthene and perylene, respectively, using CAM-B3LYP(D3) and 13, 14 and 40 nm (0.18, 0.19 and 0.37 eV) using LC- ω PBE(D3). The shifts are far below the $\sim 1.3 - 1.6$ eV experimental excitation energy shift and the transitions remain below the 500 nm range.

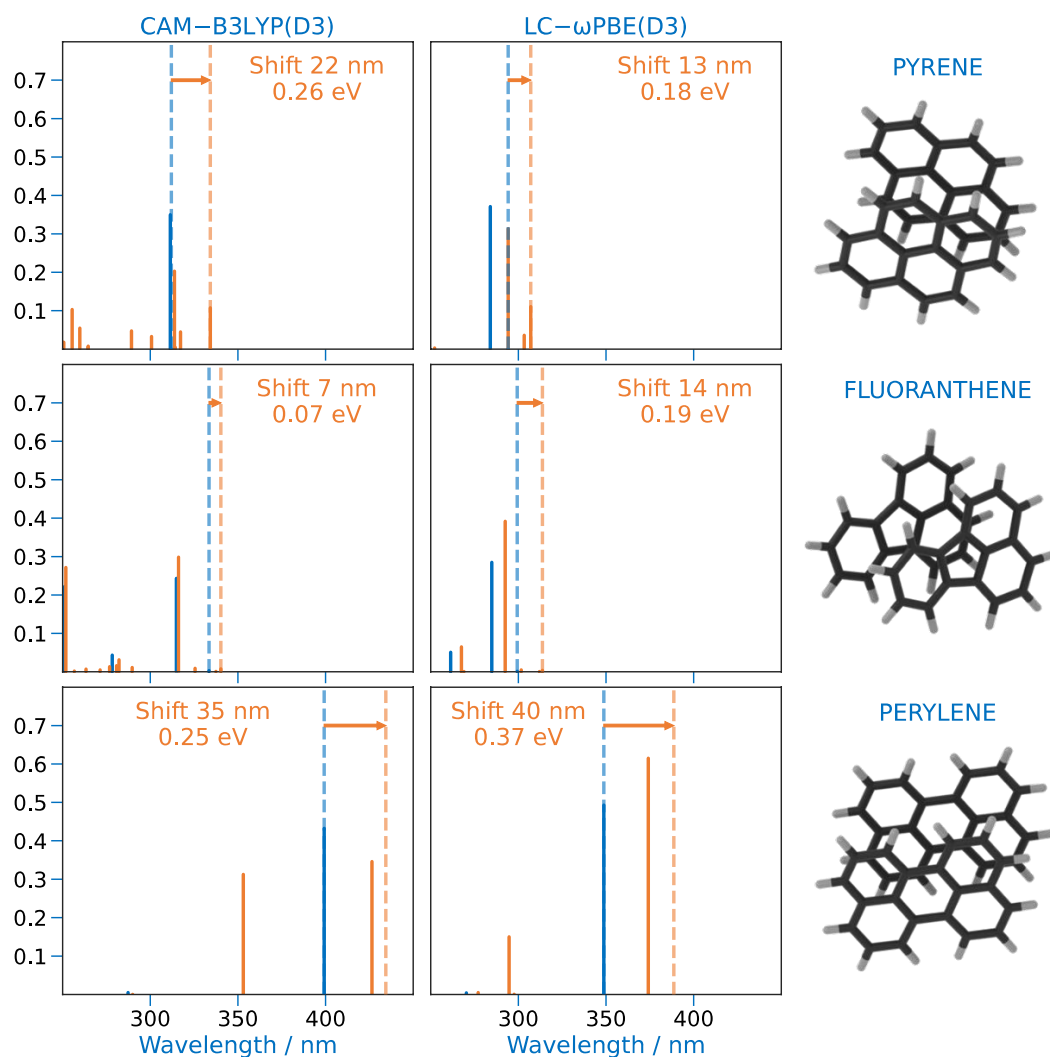


Figure II. 26: Electronic transitions of **PYPY**, **FLUFLU** and **PERPER** using the CAM-B3LYP(D3) and LC- ω PBE(D3) functionals (in orange) compared to those of the respective monomers (in blue). The vertical dashed lines indicate the position of the LEET in each monomeric (blue) or dimeric (orange) system

4.2. Effect of the geometry

The LEET in the **PYPY** dimer has a non-zero oscillator as opposed to **FLUFLU** and **PERPER**. It is however hard to conclude on this property because it is dependent on the symmetry. Indeed, the **PYPY**, **FLUFLU** and **PERPER** geometries have //t, //ab and //a geometries, respectively. For example, switching to a //ab geometry for **PERPER** leads to a modification of the spectrum which changes the shift from 35 to 11 nm (0.25 to 0.08 eV) and 40 to 17 nm (0.37 to 0.17 eV) for CAM-B3LYP(D3) and LC- ω PBE(D3), respectively, as shown on Figure II. 27.

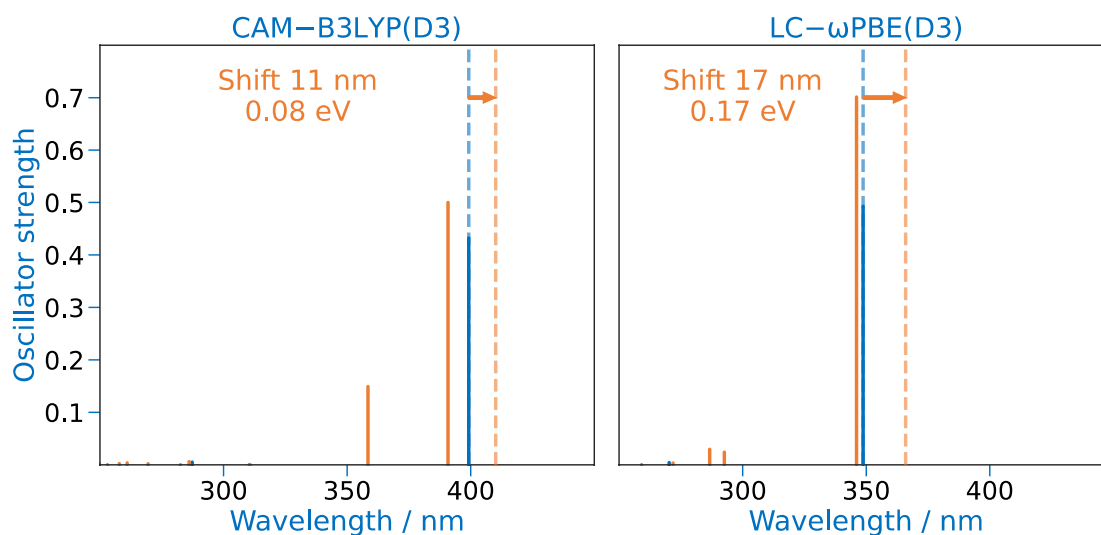


Figure II. 27: Electronic transitions of **PERPER** using the CAM-B3LYP(D3) and LC- ω PBE(D3) functionals (in orange) compared to those of perylene (in blue). The vertical dashed lines indicate the position of the LEET in each system. The geometry of the perylene dimer is that of a //ab geometry

Similarly, in order to better assess the effect of the geometry in **PYPY**, the electronic transitions of the PBE0(D3) optimized //t, //a and //ab geometries were computed using CAM-B3LYP(D3) and compared. The results are shown on Figure II. 28.

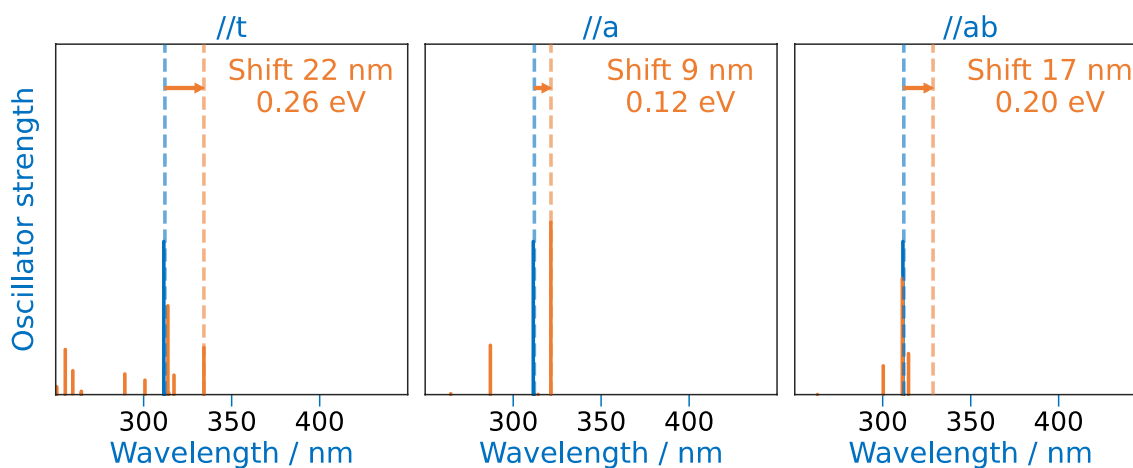


Figure II. 28: Electronic transitions computed using CAM-B3LYP(D3) of the //t, //a and //ab geometries of **PYPY** (orange) obtained using PBE0(D3), compared to those of pyrene (blue). The vertical dashed lines indicate the position of the LEET in each system.

The shifts are of 22, 9 and 17 nm (0.26, 0.12 and 0.20 eV) for //t, //a and //ab, respectively. Although the differences in the shift appear small, the oscillator strengths vastly change. This can be due to symmetry or because the nature of the ES changes.

To investigate these changes, the LEETs were studied and their properties given in Table II. 7.

	//t	S ₁	//a	S ₂	//ab
$\lambda_{exc} /$ nm	334	321	321	321	329
f	0.1075	0.0000	0.3934	0.3934	0.0000
nature	H → L (100%) (L _a ⁻)	H → L (97%) (L _a ⁻)	H → L (93%) (L _a ⁺)	H → L (93%) (L _a ⁺)	H → L (90%) (L _a ⁻)

Table II. 7: Excitation wavelengths (nm), oscillator strengths and nature of the LEET in the //t, //a and //ab geometries of **PYPY**. H and L stand for HOMO and LUMO in the monomers (using the monomers notation, previously defined), respectively.

In //a, there are two transitions with the same energy. Both states can unambiguously be attributed to L_a⁻ and L_a⁺ by looking at the orbital contributions. When laterally translating one of the monomers to obtain //ab, the states split in energy and the transition to the L_a⁻ is red-shifted. Finally, the S₁ in //t has 97% contribution from H → L and is thus the transition to L_a⁻. //t is the only geometry with non-zero oscillator strength S₀ → S₁ (L_a⁻), despite it has the same nature as in the other geometries. Thus, the only explanation is that the introduction of an intermonomer angle allows the transition to acquire intensity due to a breaking of symmetry.

5. Trimerization effect

5.1. Structures

The thermodynamics as well as the spectral properties of vdW dimers of PAH species appear to discredit the hypothesis of their presence for the origin of the BB of the emission spectrum. The hypothesis of the physical clustering of PAH usually suggests higher order oligomers to be more and more stabilized due to an increase of dispersion forces. To go further on the hypothesis of a physical interaction, the trimers of pyrene, fluoranthene and perylene were optimized and studied. The obtained structures are shown on Figure II. 29 and the intermonomer distances and binding Gibbs free energies are reported in Table II. 8.

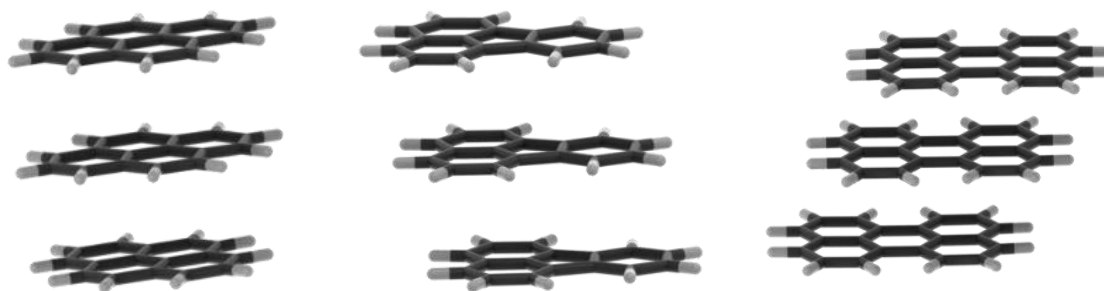


Figure II. 29: Optimized structures of the pyrene, fluoranthene and perylene trimers

		Pyrene	Fluoranthene	Perylene
Intermonomer distances / Å		3.73 and 3.81 <i>vs.</i> 3.62	3.84 and 3.84 <i>vs.</i> 3.83	3.79 and 3.81 <i>vs.</i> 3.80
Binding Gibbs free energies / kcal mol ⁻¹	298 K	-0.13 <i>vs.</i> 0.00	0.07 <i>vs.</i> 0.10	-4.47 <i>vs.</i> -2.34
Binding Gibbs free energies / kcal mol ⁻¹	1500 K	89.41 <i>vs.</i> 44.91	86.33 <i>vs.</i> 43.01	93.84 <i>vs.</i> 45.41

Table II. 8: Intermonomer distances and binding Gibbs free energies at 298 and 1500 K of the pyrene, fluoranthene and perylene vdW trimers, compared (*vs.*) to the respective dimers. All geometries were optimised using PBE0(D3)

Upon trimerization, the monomers could have been expected to further stack through the effect of stronger dispersion forces. However, no effect on the intermonomer

distance is observed. On the contrary for pyrene, the distances are even larger in the trimer than in the dimer. The enthalpic component of the stabilization could have also been expected to increase, but the effect is once again small. This leads to a completely unstable trimer at flame temperature showing that higher order vdW oligomers are highly unlikely to form in flames and to participate in the soot nucleation process.

5.2. Red-shift due to trimerization

The vdW trimers are unstable at flame temperature which seriously question the possibility to observe them in LIF experiments. To confirm this, the electronic transitions of the trimers were computed and are shown on Figure II. 30.

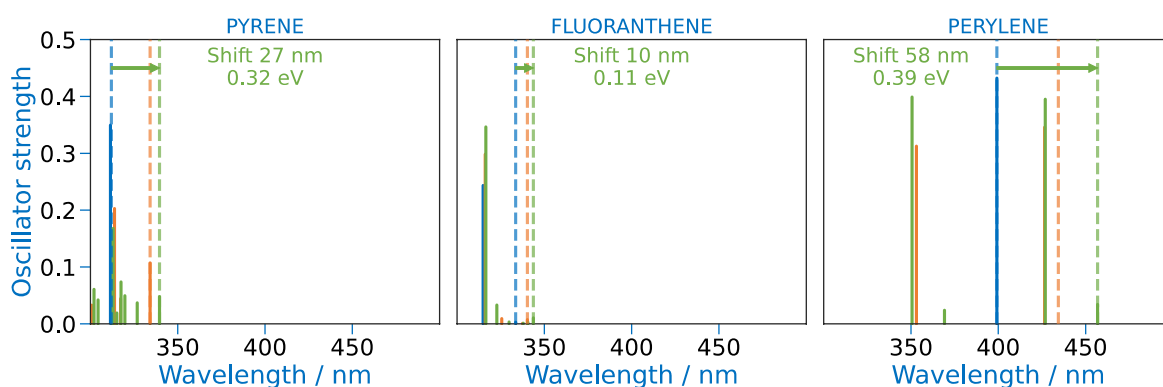


Figure II. 30: Electronic transitions of the pyrene, fluoranthene and perylene monomers (blue), dimers (orange) and trimers (green). The vertical dashed lines indicate the position of the LEET in each system. The calculations were done with CAM-B3LYP(D3) on the PBE0(D3) optimized geometries

Upon trimerization, the pyrene, fluoranthene and perylene electronic transitions undergo small red-shifts of 27, 10 and 58 nm (0.32, 0.11 and 0.39 eV). Thus, the effects are too weak compared to experimental observations and the observation of vdW oligomers to explain the BB is unlikely.

6. Conclusion

In this chapter, vdW dimers of **PYPY**, **FLUFLU** and **PERPER** were studied to investigate their implications in the observation of the BB during LIF measurements in flames.

It was found that **PYPY** had three stable conformers: //a, //ab and //t, in which the dimerization had close to no effect on the monomers structure.

The ESs of **PYPY** were extensively studied using three functionals. It was observed that CR states appeared at too low energies when using PBE0(D3), which suggests that this functional should be used with caution when studying the ESs of these systems. Four LLESs were also evidenced, in agreement with the literature. The description of the L_a^+ , L_b^- and L_b^+ states appear quite good with all three functionals. However, in the case of the L_a^- state, the results are more contrasted. Indeed, it is predicted to be weakly stabilized using PBE0(D3) and that the L_b^- is the excimer state (the lowest energy state). This is in contradiction with most interpretations in the literature. [263, 333]

On the other hand, CAM-B3LYP(D3) and LC- ω PBE(D3) predict the correct state ordering, shift the CR states to higher energies, and give realistic dissociation energies for the excimer state. Thus, we believe that TD-DFT with RSHs corrected in dispersion is a valuable tool to describe the electronic properties of vdW PAH systems.

The nature of the interaction between the monomers was investigated by computing the orbital overlap for the linear combinations of HOMO – 1, HOMO and LUMO orbitals in **PYPY**. It was shown that the orbital overlap was rather small, which seriously questions the importance of π -interactions, as suggested by other authors. [337] On the other hand, the dispersion forces appear to be an important contribution to the stability of the dimers. Still, the dimers are quite weakly bonded and are predicted to be unstable at flame temperature.

This does not prevent them to be observed as intermediate species in flames, so, in order to investigate their possible implications in the observation of the BB, their absorption spectra were calculated and studied. A particular focus was put on the

lowest energy state in each system to assess whether the dimerization would reduce excitation energies enough so that such dimeric species could be excited by visible sources. The effects on the spectra were quite small, and the dimerization was shown to induce red-shifts of the LEET of at most (for PERPER) 0.37 eV, compared to the 1.3 – 1.6 eV shifts observed experimentally. Thus, the hypothesis of the vdW dimerization of PAHs to explain experimental LIF signals is unlikely.

The further oligomerization of PAHs to yield trimers was also studied. The investigated trimers of pyrene, fluoranthene and perylene display similar thermodynamic stabilities and absorption spectra to their respective monomers. Thus, this hypothesis is also unlikely.

CHAPTER 3.

Aliphatically-bridged polycyclic aromatic hydrocarbons

The vdW dimers of PAHs are unstable at flame temperature. This lead researches suggest the formation of covalent bonds between monomers, which would add irreversibility to the mechanism and overcome some of the entropic disadvantages. Thus, in this chapter, aliphatically-bridge PAHs are studied (ABPAH)

The effect of the vdW dimerization was shown to induce close to no modifications on the structure of the monomers. To verify if the same results are found for ABPAHs, the effect of the aliphatic bridging on the structure of a variety of pyrene, fluoranthene and perylene ABPAHs is studied Also, their absorption spectra are computed to assess their possible implications in the BB in LIF spectra.

1. Optimization procedure

The possible importance of ABPAHs in soot inception mechanisms was previously introduced. The presence of chemical bonds between PAH entities in ABPAHs has the advantage of reducing the entropic Gibbs free energy term compared to vdW dimers. If the monomers are bridged by a single sp^3 carbon atom, the dimeric structure is rigid and the monomers are not allowed to stack. However, the resulting dimers might still interact through long distances. On the other hand, when at least two sp^3 carbon atoms are present, the bridging induces enough freedom for the monomers to orient themselves and maximize the long-range interaction. In this case, two categories of conformations can be assumed: the “folded” and “unfolded” conformations, as shown on Figure II. 31.

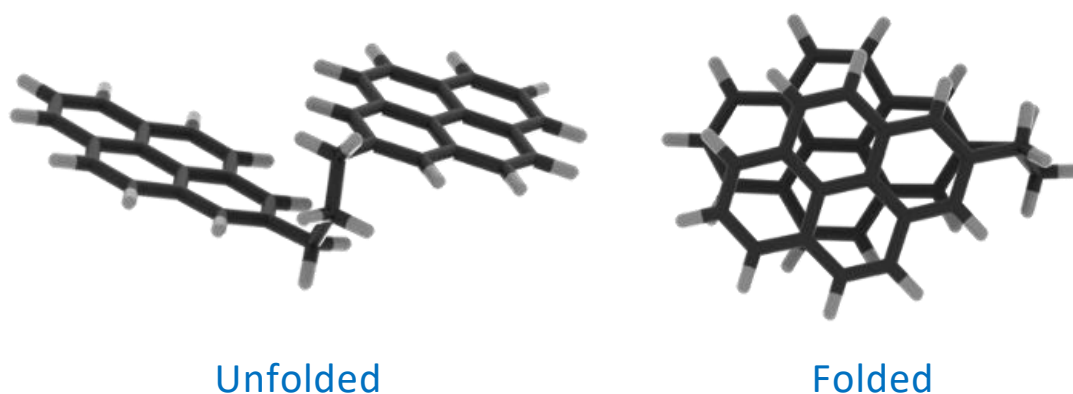


Figure II. 31: Example of a **PYPY ABPAH** in either unfolded or folded configurations

The folded configuration can be expected to be less entropically stable due to the degrees of freedom offered by the AB, however, the entropic term can be assumed to be smaller than in the case of pure vdW dimers.

In this work, it was chosen to study ABPAHs with 1 to 4 sp^3 carbon atoms in the bridge (named **1C**, **2C**, **3C** and **4C**) to evaluate the influence of the bridge on the structures and the spectral properties. On Figure II. 32, the carbon atoms that give no duplicate geometries (for symmetry reasons) upon formation of an aliphatic bridge are highlighted.

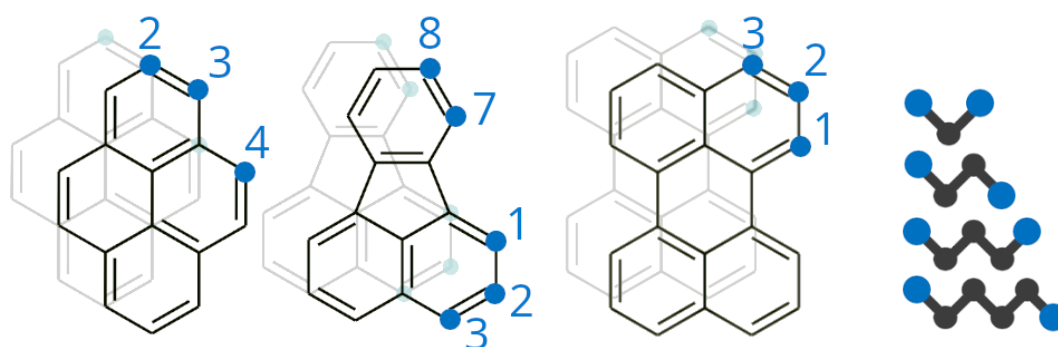


Figure II. 32: On the left, blue circles indicate the carbon atoms that can be bonded by an AB without giving redundant geometries by symmetry. On the right are schemed the four ABs, **1C**, **2C**, **3C** and **4C**, considered in this study

The bridging of these carbon atoms yields 6 structures of pyrene and perylene homodimers, and 15 structures of fluoranthene dimers. The geometries will be termed by the carbon atoms bonded to the bridged and the bridge type *i.e.*, **2C-2PYPY2**, **3C-FLUFLU8**, *etc.*

Including the 4 AB types, 24 structures are obtained for pyrene and perylene, and 60 for fluoranthene. The structures were optimized by pre-orienting the monomers to maximize the stacking interaction. This was done because it can be assumed that the greatest effects will be observed for folded structures, rather than unfolded ones. However, few structures were tested in unfolded conformations to perform a thermodynamical study.

2. Thermodynamics

In order to explore the stability of the folded structures compared to the unfolded ones, unfolded versions of the **2C** and **3C** pyrene dimers were optimized, and their energies compared to the folded counterparts according to the chemical equations shown on Figure II. 33.

The $\Delta_r G^\circ$ are of 0.02 and -3.07 kcal mol⁻¹ at 298 K, and 10.01 and 5.33 kcal mol⁻¹ at 1500 K, for the reactions describing the folding of **2C** and **3C**, respectively. Although the entropic terms still disfavour the dimerization, the destabilization is much smaller than for the pure vdW dimers (44.91 kcal mol⁻¹). The increase in bridge length strongly lowers the enthalpy due to a better interaction between monomers, with a diminution of 2.70 kcal mol⁻¹, and a small effect of the entropy with a decrease of the $-T\Delta S$ term of 1.98 kcal mol⁻¹ at 1500 K.

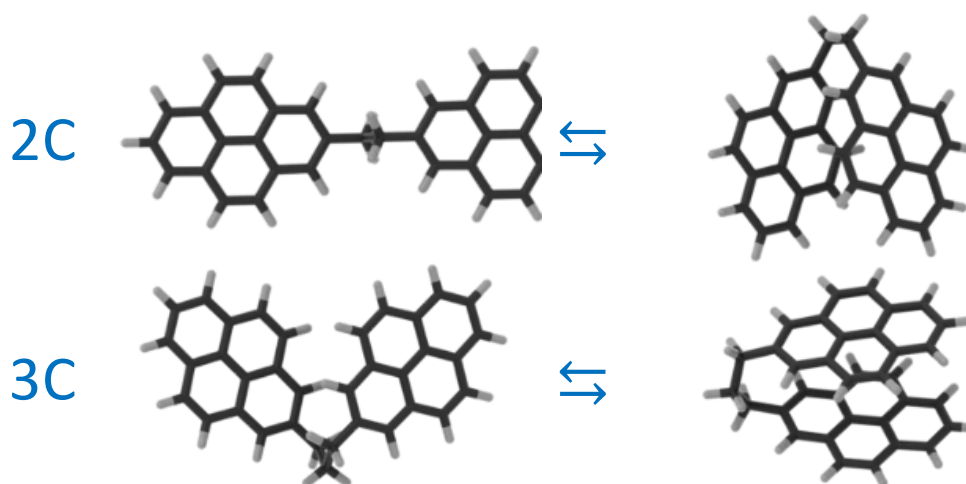


Figure II. 33: Examples of switching from an unfolded to a folded structure with 2 and 3 carbon ABs (**2C** and **3C**) for **2PYPY2**

Based on these results, such systems can be expected to form at lower flame temperatures, or with bigger PAHs.

3. Geometry analysis

To characterize the dimers and quantify the effect of PAH dimerization on the monomers structures, geometrical parameters were defined and are presented here after.

3.1. Definition of geometrical parameters

3.1.1. The intermonomer distance (ID)

The ID was defined as the distance between each centre of mass of monomers, not taking into account the aliphatic bridge. This is the same definition that was used in Chapter 2 and the same difficulties apply since the monomers are not perfectly parallel (especially for **1C** ABPAHs), which makes it impossible to define a rigorous distance. A depiction of the ID is given on Figure II. 34. This parameter is a good indication of the stacking of the monomers.

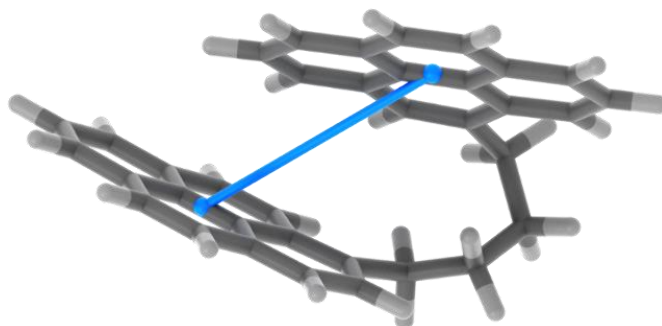


Figure II. 34: Depiction of the ID geometrical parameter

3.1.2. Plane fit residuals (PFR)

Upon dimerization, a decrease in the flatness of the monomers can be expected due to structural tensions induced by the AB and dispersion forces. To quantify this decrease in planarity, the carbon atom positions were considered as a cloud of points that was fitted by a plane. This was done by performing an SVD as defined in the methods section in Part I, with the data matrix \mathbf{M} corresponding to carbon atom positions of the monomers.

For a perfect plane, the z -axis associated singular value in Σ (s_z) should be zero and any deviation from zero quantifies the deviation from a plane. Thus, the PFR parameter was computed as the sum of the s_z values of the Σ matrices. A representation of the planes fitted onto the monomer carbon positions is shown on Figure II. 35.

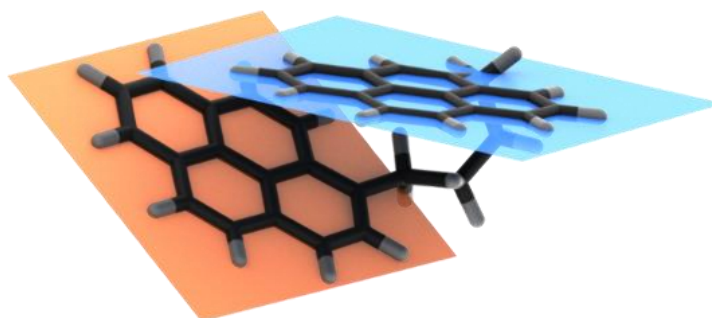


Figure II. 35: Depiction of the planes fitted onto the monomer carbon positions. A deviation from the plane gives large PFR values

3.1.3. Sum of internal angles (SIA)

An alternative way to quantify the deviation from a plane in ring systems is the sum of the internal angles. As shown on Figure II. 36, the out-of-plane distortion of a ring diminishes the sum of its internal angles.

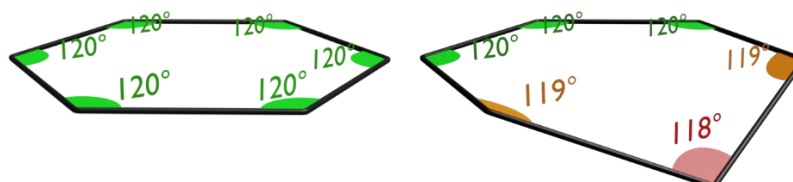


Figure II. 36: Depiction of the internal angle values on normal and out-of-plane distorted benzenes

Subtracting the sum of the internal angles of a distorted ring from that of a perfectly planar one gives an indicator value of deviation from the plane of the distorted ring. Summing up the values of all rings of a molecular system gives its SIA. A representation of the dimerization effect on the SIA parameter is represented on Figure II. 37.

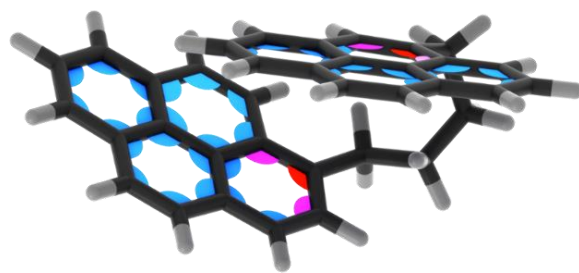


Figure II. 37: Depiction of the SIA parameter, a red colour (bigger values) indicates a stronger effect of the dimerization on the internal angle

3.1.4. Root-mean-square deviation of carbon atom positions (RMSDC)

The aim of the study being to quantify the effect of the dimerization of PAHs, it is possible to compare the geometry of a monomer in a dimer, to that of the optimized monomer geometry. The RMSDC parameter is defined as

$$\text{RMSDC} = \sqrt{\frac{1}{N_{C,1}} \sum_{i=1}^{N_{C,1}} d_i^2} + \sqrt{\frac{1}{N_{C,2}} \sum_{i=1}^{N_{C,2}} d_i^2}$$

With $N_{C,1}$ (and $N_{C,2}$) being the number of carbon atoms in the first (and second) monomer, and d_i being the distance between carbon atom i in the optimized monomer and the dimer. For this to work, the monomers were superimposed using the Kabsch algorithm as shown on Figure II. 38.

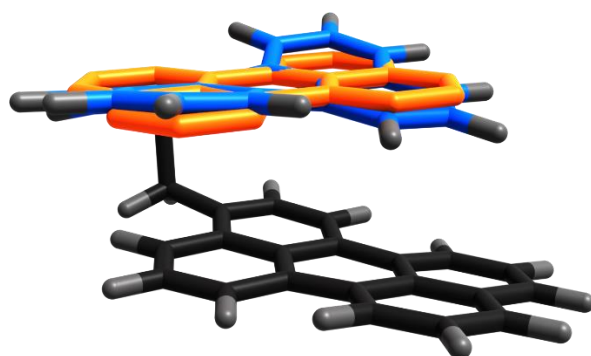


Figure II. 38: Depiction of the superimposition using the Kabsch algorithm. The orange structure is the optimized monomer carbon skeleton, which is compared to the blue carbon skeleton. The analysis is performed on both monomers.

3.2. Effect of dimerization on the structure

To visualize the effect of the dimerization on the structure of PAHs, the structural parameters are shown on Figure II. 39

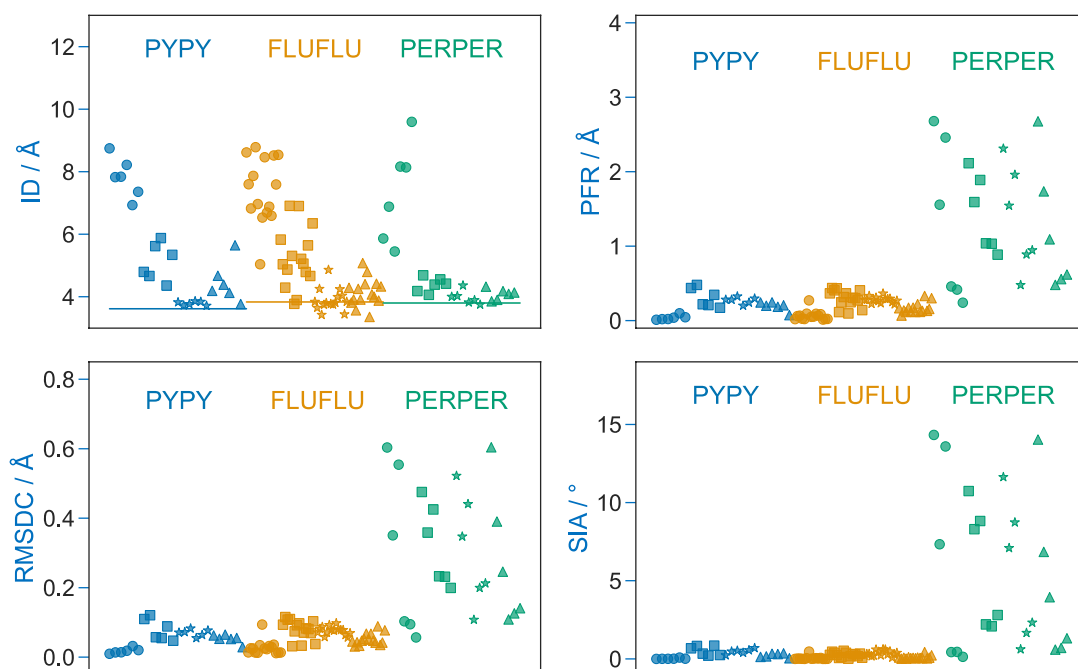
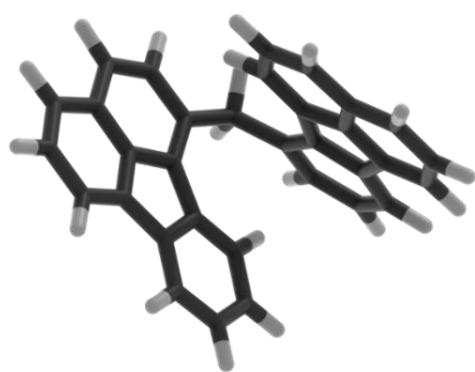
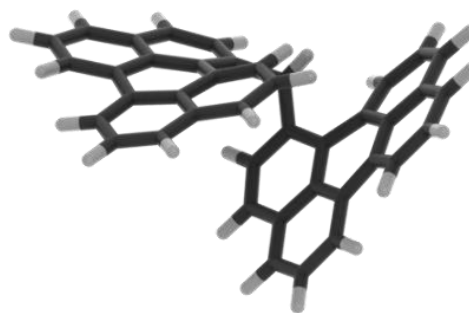


Figure II. 39: Effect of the dimerization on the four structural parameters ID, PFR, RMSDC, and SIA. AB types are indicated (in order) by the markers: **1C** ●, **2C** ■, **3C** ★, **4C** ▲. The horizontal line on the ID parameter figure indicates the ID parameter in the vdW dimer.

First, looking at the ID parameter, it can be seen that **1C** ABs are too rigid to allow a stacking of the monomers, as stated before. Also, the stacking is better with the **2C** ABs and appears to be minimum for a **3C** AB. For **3C** and **4C** ABs, the ID values in the ABPAH dimers are roughly the same as that in the vdW dimer, and even be smaller. However, this result must be interpreted with caution since the ID parameter is dependent on the orientation of the monomers. This is especially the case for fluoranthene whose curved-edge structure allows a better stacking (as shown on the left of Figure II. 40, where a **1C** **FLUFLU** dimer displays a rather stacked geometry). This explains why many **FLUFLU** geometries display smaller ID values than the vdW one. **PERPER** behaves slightly differently compared to **PYPY** and **FLUFLU** as 2 carbon atom ABs appear to be enough to bring the monomers as close as in the vdW structure.



1C-1FLUFLU7
RMSDC = 0.094 Å



1C-1PERPER1
RMSDC = 0.603 Å

Figure II. 40: Example of structures with relatively large RMSDC values

Now switching to the 3 other parameters, the singular behaviour of **PERPER** is even clearer. Indeed, **PERPER** undergoes much larger structural changes compared to the other two dimer types. Also, no correlation between the AB type and the structural changes is evidenced for **PERPER**. This means that its dimerization leads to large effects even when perylene monomers interact through long distances such as with **1C** ABs. Indeed, looking at one of the structures with the largest structural changes, *i.e.*, **1C-1PERPER1** (Figure II. 40, right), perylene is able to bend so that one of the naphthalene moieties gets superimposed onto the other monomer. To get a better view of the dimerization effect on **PYPY** and **FLULFU**, it is necessary to normalize the data. This is done on Figure II. 41.

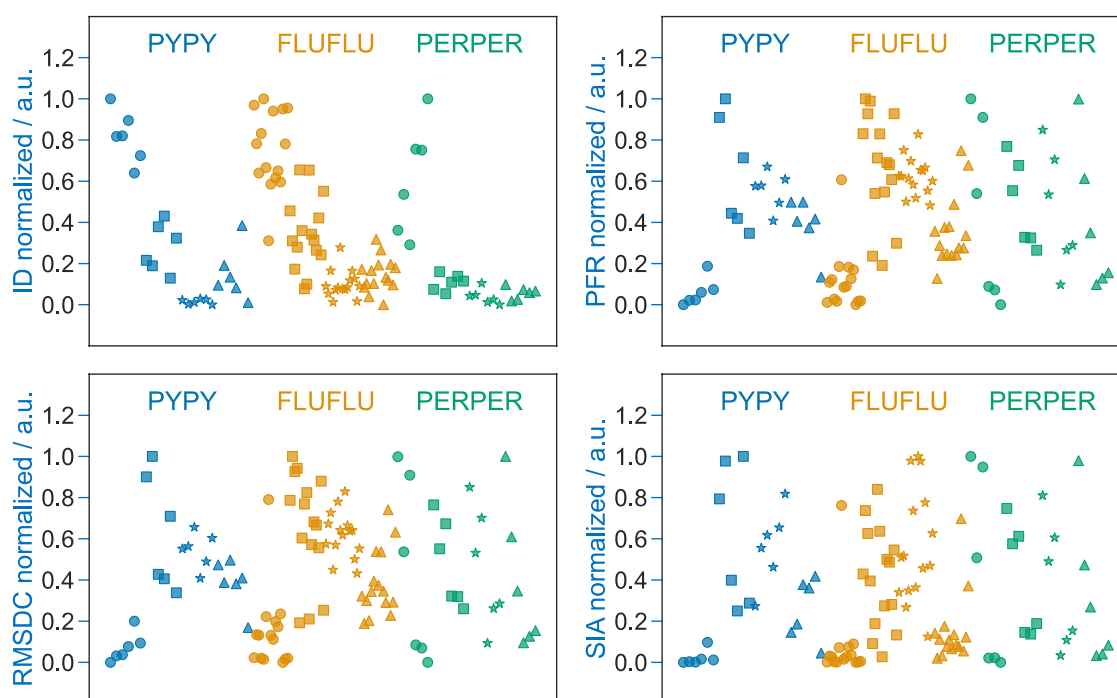


Figure II. 41: Effect of the dimerization on the four normalized structural parameters ID, PFR, RMSDC, and SIA. AB types are indicated by the markers: **1C** ●, **2C** ■, **3C** ★, **4C** ▲

On the normalized data, a striking observation is that the PFR, RMSDC and SIA parameters yield very close results. It could have been expected from SIA and PFR to give close results because they both quantify the deviation from the plane. It is more surprising for RMSDC, because it should encompass all structural changes. The similarities between the PFR, RMSDC and SIA parameters shows that most of the structural changes on the monomers upon dimerization occur as a deviation from a plane.

Taking a closer look at the values of the parameters for **PYPY** and **FLUFLU**, shows that contrarily to **PERPER**, there is a correlation between the AB type and the structural changes. For dimers with a **1C** AB, the monomers are too far away to interact and thus show close to no changes. With a **2C** AB, the structural modifications are the largest, the rigidity of the AB forces the monomers to bend to maximize the interaction. From here, the addition of carbon atoms in the bridge increases the freedom of movement of the monomers, which releases the structural tension. The effect is less pronounced in **FLUFLU**, which is once again due to its curved-edge structure. For example, the largest RMSDC value for **1C-FLUFLU** is 0.094 Å and is obtained for the **1C-1FLUFLU7** dimer shown on Figure II. 40 (left).

4. Electronic properties

4.1. Spectral range of ABPAHs

In order to investigate the possibility of ABPAH species to induce significant red-shifts on the LIF excitation spectra of flames, their electronic transitions were computed and compared to the respective monomers. The results are shown on Figure II. 42.

First, **PYPY** and **FLUFLU** have similar spectra with a majority of bright transitions around 325 nm. The **PERPER** dimers on the other hand absorb mostly around 400 nm. Second, the LEETs are found 32, 22 and 38 nm (0.37, 0.23 and 0.27 eV) to longer wavelengths compared to those of the monomers, which is limited red-shift, similar to those found for the pure vdW systems. Finally, apart from reducing the excitation energy of the transitions, the dimerization appears to reduce the oscillator strengths.

Thus, these calculations seriously contradict the possibility of small ABPAHs to yield the LIF signals in flames.

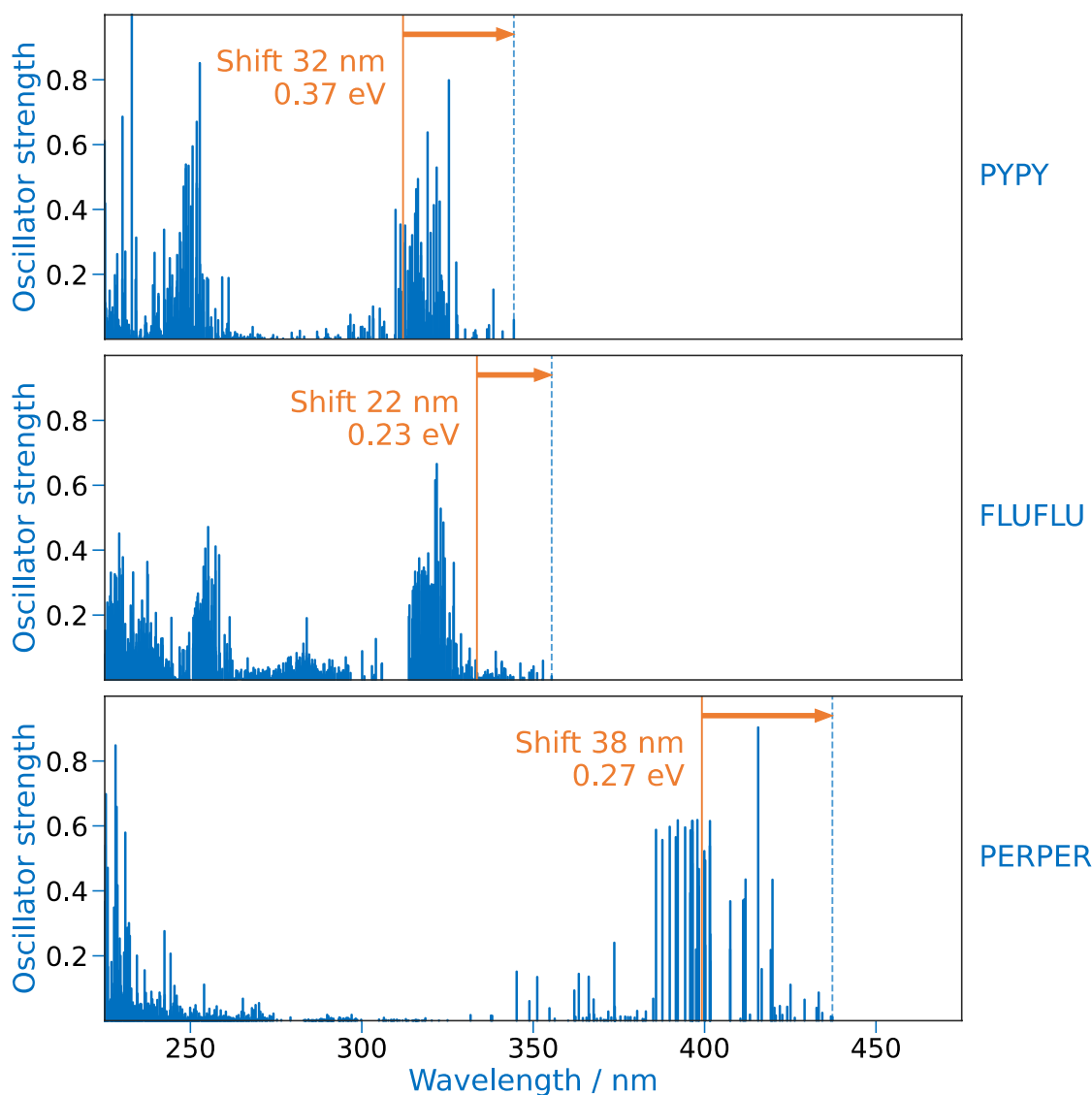


Figure II. 42: Electronic transitions of all ABPAHs (blue vertical lines), compared to the LEET of the corresponding monomer (orange vertical line)

4.2. Structure – electronic properties relationship

4.2.1. Origin of the red-shift

A relatively large panel of 3 vdW dimers and 108 ABPAHs was investigated in terms structure and absorption spectra. The **PERPER** structures were shown to display rather large structural changes compared to **PYPY** and **FLUFLU**. However, the red-shifts are similar in the three dimer types. Thus, it can be interesting to investigate the relationship between the structure and the red-shift, to get insights into the possible structures of the species responsible for the BB in LIF experiments.

The correlation between dimerization effects on the structure and the LEET of each dimer was studied. On, Figure II. 43 the red-shift in eV is plotted against the ID and

RMSDC parameters. The SIA and PFR parameters were excluded because they give redundant information with RMSDC.

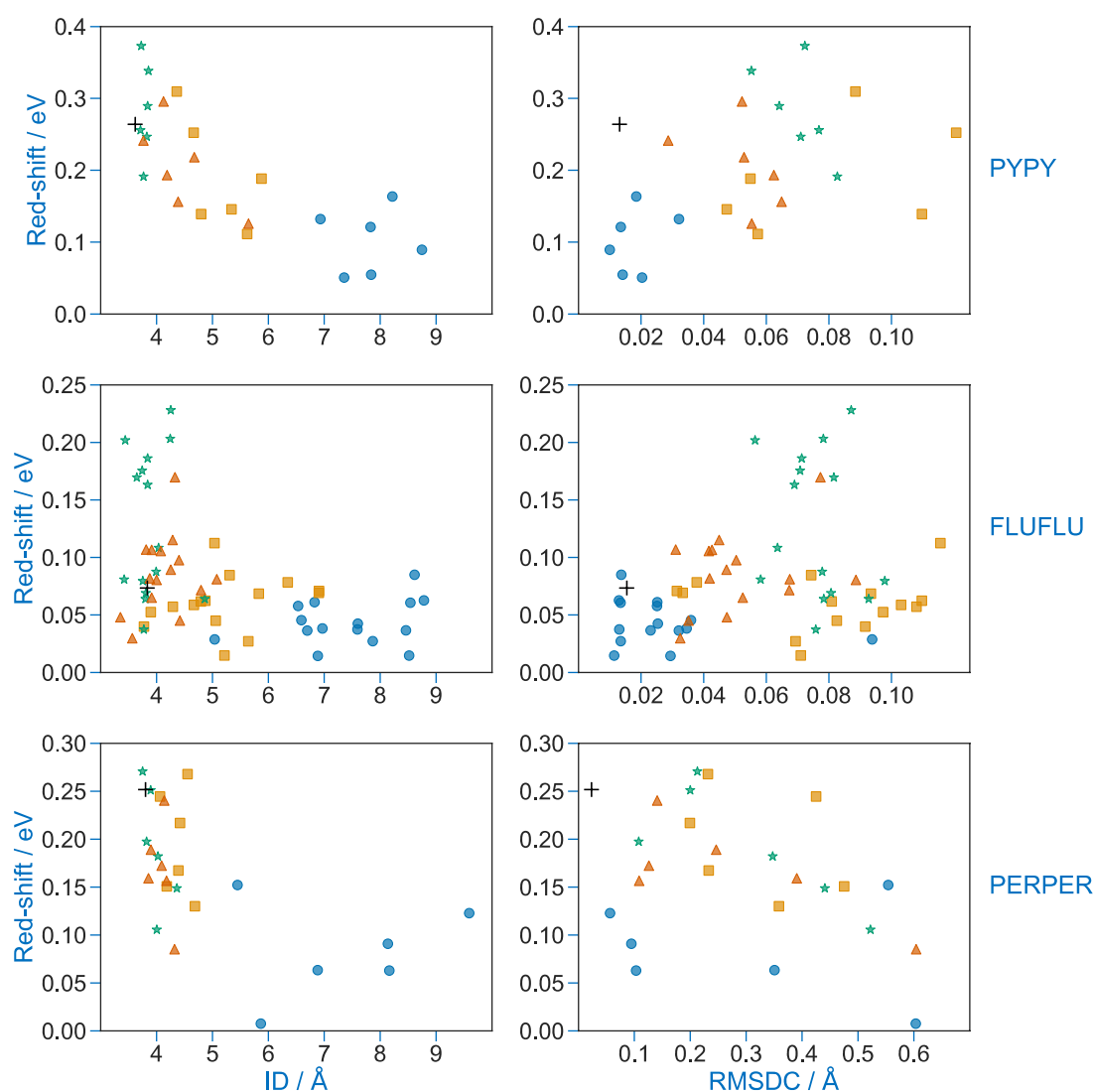


Figure II. 43: Red-shift of the LEET (eV) induced by the dimerization with respect to the ID (left) and RMSDC (right) parameters. AB types are given by the markers: vdW +, 1C ●, 2C ■, 3C ★, 4C ▲

Looking at the RMSDC values for **PYPY**, larger RMSDC values appear to be correlated with increased red-shifts. However, this effect is not recovered in **FLUFLU** and **PERPER**. This is especially obvious when looking at the RMSDC values for the three vdW dimers. Indeed, the vdW dimers show close to no structural changes on the monomers despite having relatively strong red-shifts. Thus, the effect of the RMSDC parameter appears to be at least partially due to its underlying dependence on the ID parameter.

Now looking at the ID values, there is a clear correlation showing that smallest IDs yield the strongest red-shifts. This is especially the case of **PYPY** and **PERPER** for

which the **1C** AB cannot bring the monomers close enough to maximize the interaction, which induces close to no changes on the spectrum. On the contrary, bigger ABs can induce red-shifts similar to those in vdW dimers. However, the vdW dimers are not those with the biggest shifts observed. This suggests that other structural effects can help further red-shift the transitions.

Overall, the most important results are the low red-shift values of less than 0.4 eV. Also, although 5-membered ring containing systems such as fluoranthene have often been considered important in flame chemistry, the dimerization of fluoranthene yields even smaller shifts as those observed for pyrene. Perylene is different compared to the other two PAHs because its LEET is already near the visible spectral range before dimerization. However, even the perylene dimers were not able to explain the possibility to excite species at more than 500 nm in LIF measurements.

4.2.2. Decorrelating RMSDC and ID

The previous section highlighted correlation between ID and the structural modifications on monomers (RMSDC). This makes it hard to know whether deformations on monomers were responsible for some of the observed red-shifts.

However, from the set of 108 geometries, it is possible to form three additional set of geometries to quantify this effect, consisting of:

- Non-optimized monomer (**NO-M**): By substituting the AB and one monomer by a hydrogen atom, a non-optimized monomer is obtained. This way it is possible to quantify the effect of the structural changes on a monomer on the red-shift.
- Non-optimized monomer + AB (**NO-MAB**): By doing the same substitution while keeping the AB, it is possible to add the effect of the aliphatic chain on the red-shift.
- Non-optimized vdW dimer (**NO-VDW**): Finally, substituting the AB by hydrogen atoms while keeping both monomers yields a non-optimized vdW dimer that allows to compare the effect of the chemical bonding mode to the physical one.

On Figure II. 44 are represented the obtained structure for the **2C-3PERPER3** system for example purposes.

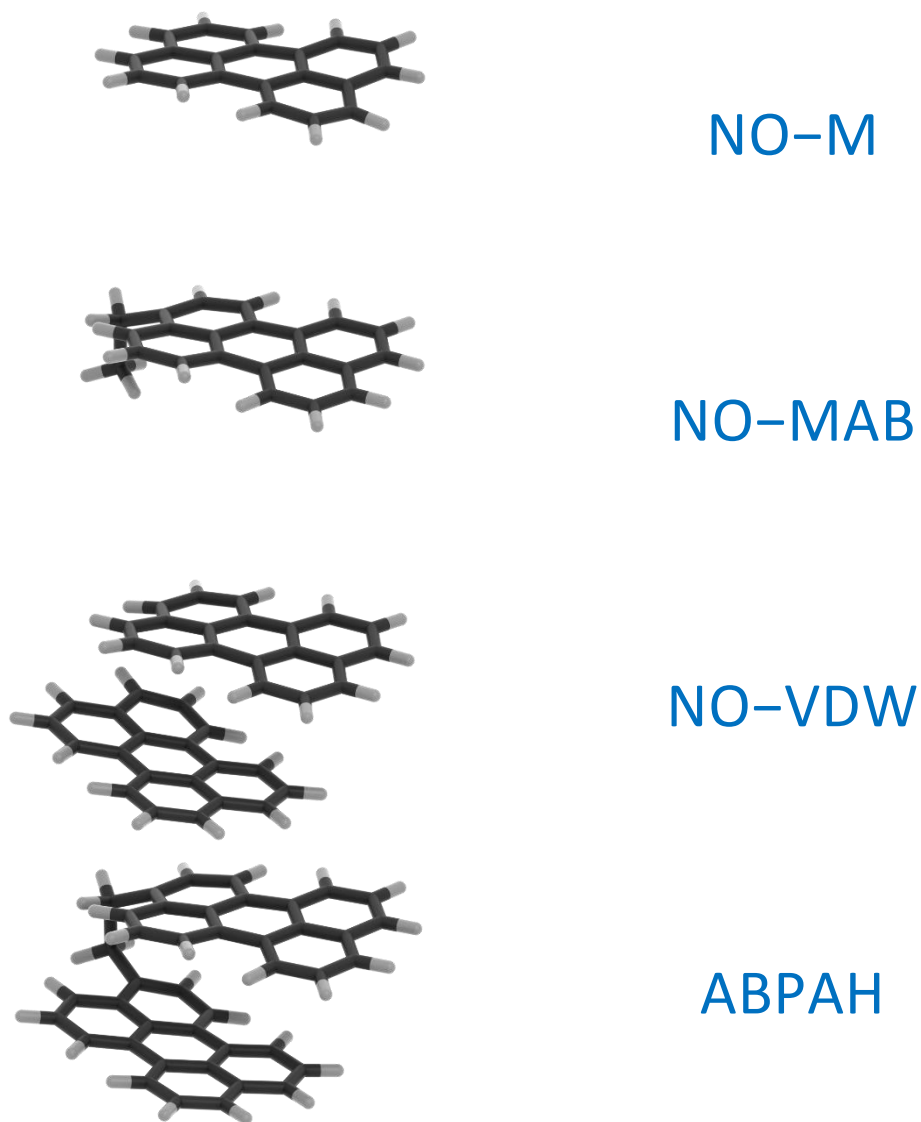


Figure II. 44: The decomposed geometries of the **2C-3PERPER3** structure

The electronic transitions of the new sets of geometries were calculated and the LEETs were compared to those in the optimized monomers. The results are shown on Figure II. 45.

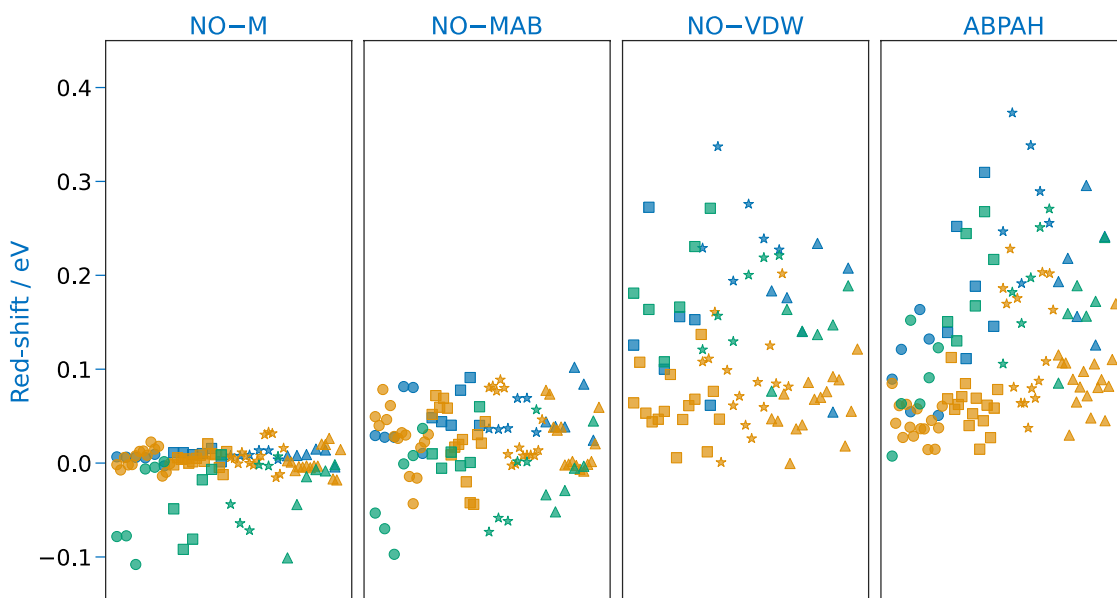


Figure II. 45: Red-shift of the LEET upon going from the optimized monomer to one of the decomposed geometries. AB types are indicated by the markers: **1C** ●, **2C** ■, **3C** ★, **4C** ▲. For **PYPY** (blue), **FLUFLU** (orange) and **PERPER** (green)

Starting with the **NO-M** results (first column), the deformation of the monomer induces relatively small changes that are proportional to the deformations on the monomer. Indeed, the perylene monomers are those with the most structural modifications and are those with the most spectral changes. The distortions on the monomer geometries tend to blue shift the transitions, as shown on Figure II. 46 for the perylene example. This is due to a decrease of electron delocalization on the molecule.

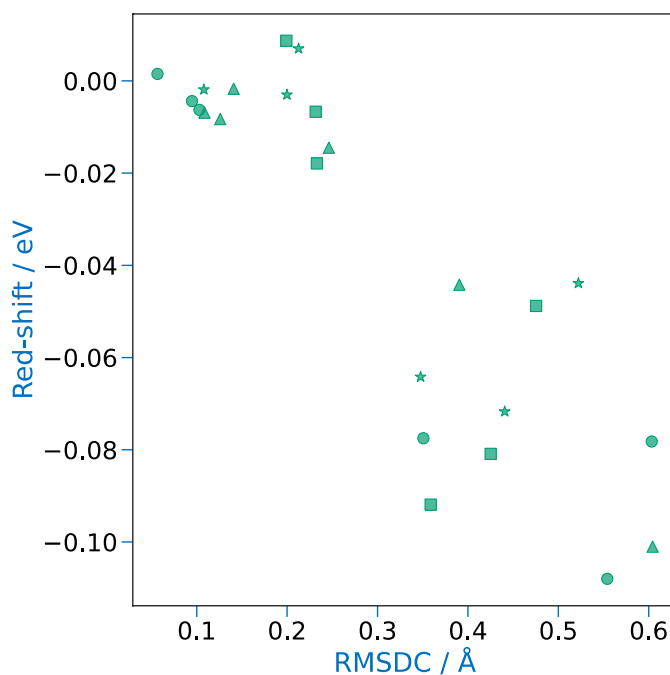


Figure II. 46: **NO-M** red-shift plotted against RMSDC. **1C** ●, **2C** ■, **3C** ★, **4C** ▲

The addition of the AB (second column of Figure II. 45) on the monomer mostly tends to red-shift the LEET by around 1.0 eV. Thus, the effect is rather small and the **NO-MAB** geometries display similar absorption spectra to the optimized monomers.

Switching to a purely vdW interacting system (**NO-VDW** or **ABPAH**) immediately induces the largest effects on the spectrum. The geometrical decomposition shows that the structural distortions have only limited effects on the spectrum of chemical dimers and that most of their spectral properties are due to the physical interaction between monomers.

4.3. Molecular orbitals

On Figure II. 47 are shown the HOMO – 1, HOMO, LUMO and LUMO + 1 orbitals in the **3C-4PYPY4** system for example purposes. Although the orbitals look like those in the vdW dimer, they are more localized on single monomers. For example, the HOMO – 1 is more located on the left monomer, whereas the HOMO is more located on the right monomer. This indicates that electron delocalization occurs to a lesser extent than in the vdW dimer.

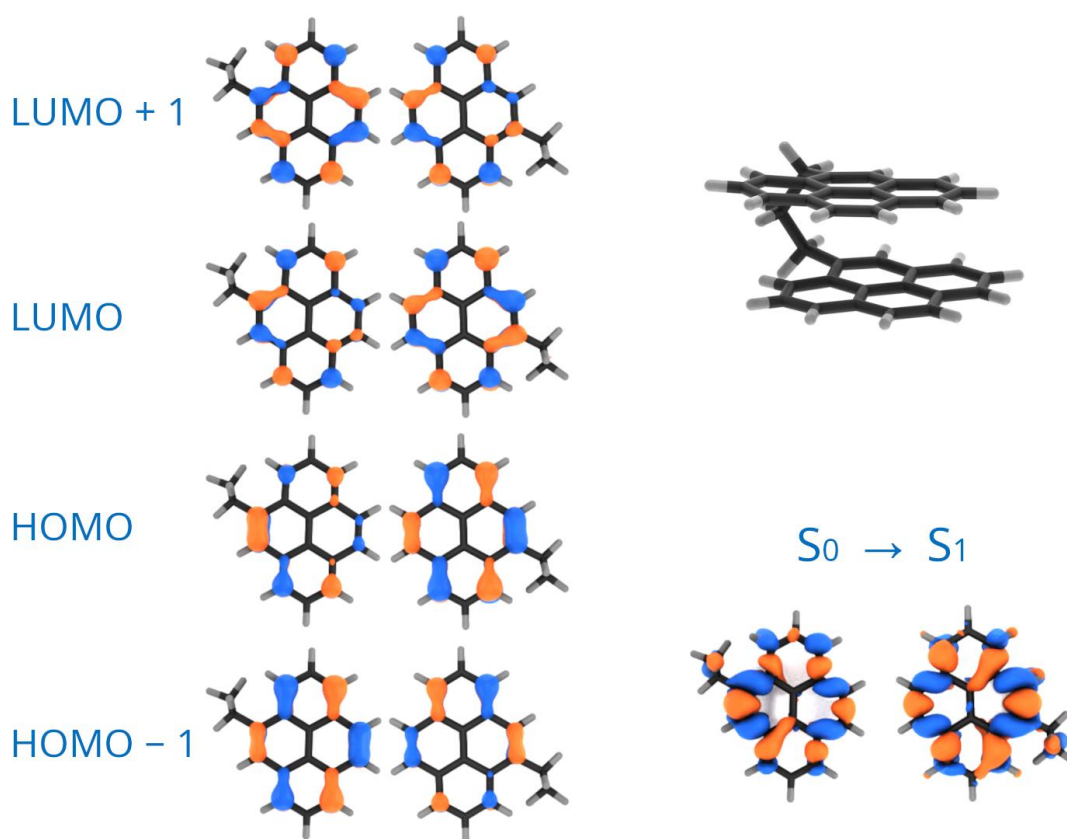


Figure II. 47: HOMO - 1, HOMO, LUMO and LUMO + 1 (left) in each monomer forming the **3C-4PYPY4** dimer (shown at the top right). The monomers are separated for better visualization. Variation of the electron density upon excitation to the S_1 (bottom right), the orange colour indicates an electron density depletion, and blue an electron density increase.

An even more obvious case of orbital localization is given on Figure II. 48. Indeed, in the **3C-2PYPY4** system, the LUMO and LUMO + 1 orbitals are entirely localized on single monomers. The transition has a major CT component from the HOMO of one monomer, to the LUMO of the other.

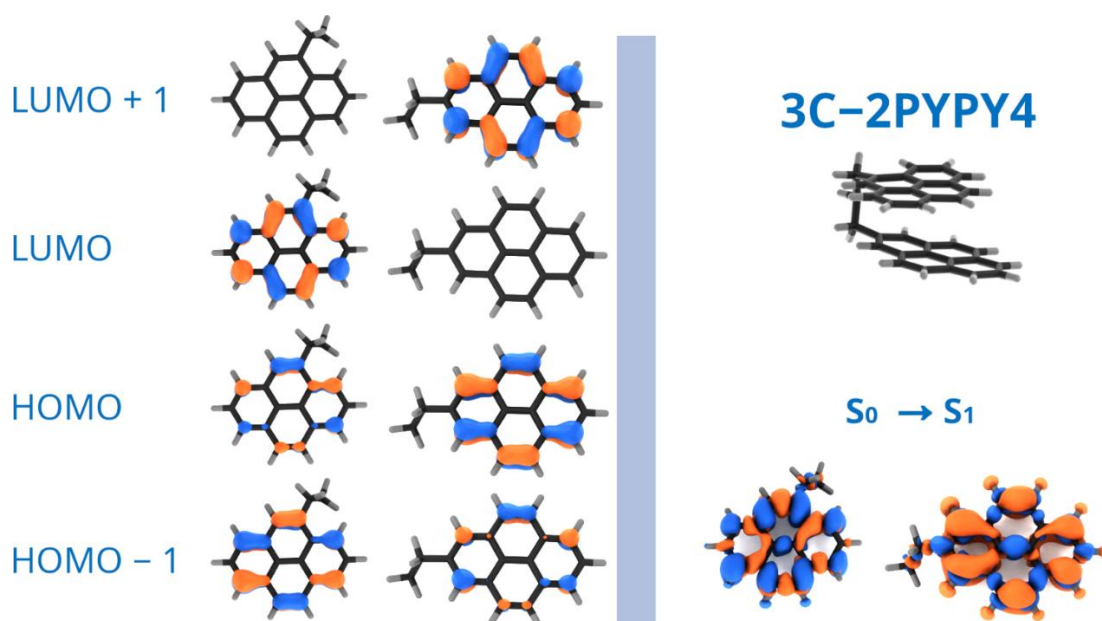


Figure II. 48: HOMO - 1, HOMO, LUMO and LUMO + 1 (left) in each monomer forming the **3C-2PYPY4** dimer (shown at the top right). The monomers are separated for better visualization. Variation of the electron density upon excitation to the S_1 (bottom right), the orange colour indicates an electron density depletion, and blue an electron density increase.

5. Conclusion

The hypothesis of chemically bonded dimers to explain LIF spectra was investigated in this chapter by the study of 108 ABPAH structures. If the AB is long enough (at least **2C**) the dimers can stack and interact in the same way as purely vdW dimers. However, the folding of ABPAHs is less entropically disfavoured compared to the stacking of pure vdW dimers, and they could be observed at low temperature regimes in flames.

With long ABs, structural distortions are observed on PAH monomers. In this manner, perylene is special because its central anti-aromatic 6-membered ring allows for the structure to bend and maximize the interaction between monomers. Interestingly, the structural flexibility is a feature often thought to be necessary to initiate the inception of a soot particle. Thus, perylene (among other flexible structures) could lead to further exciting studies.

The computed electronic transition wavelengths do not vary much, or in the opposite direction (hypsochromic effect) to what would be required to explain LIF experiments. Indeed, the computed energies of the LEETs are similar to those in the vdW dimers, and thus, are too large. Therefore, the chemical bonding of pyrene, fluoranthene and perylene is not the most plausible explanation for the LIF signals and other hypotheses are presented in the next chapter.

CHAPTER 4.

PAH-based radicals

This chapter concerns an alternative explanation for the LIF signals. The results presented herein are the first attempts of such study and will require further computational and experimental work.

The hypothesis is the presence of PAH radicals that would lead to the presence of the BB in LIF experiments. Indeed, PAHs are known to be formed in flames through the HACA mechanism. This involves neutral σ and π -radical PAH intermediates (σ R and π R), [338–340] and radical cations. [341]

In this chapter, an introduction on PAH radicals and their implications for soot formation is given. Then, following the work performed in Chapter 2 and Chapter 3, σ Rs and π Rs of the already suggested structures are studied in terms of electronic properties. Implications for interpreting LIF experiments are given alongside.

1. Introduction

1.1. State of the art

The mechanisms of formation of PAHs in flames involve neutral σ and π -radical PAH intermediates (σ R and π R), [338–340] and radical cations. [341]

Most of the studies that can be found regarding PAH radicals electronic properties concern the radical cations due to the great importance of spectroscopic technics for astrochemical studies. [342–347]

On the other hand, the electronic spectra of σ Rs and π Rs remain mostly unknown although they are known to exist in flames. For example, a computational study showed that π Rs were formed on saturated rim-based 5-membered rings (Figure II. 49) at low temperature regimes, whereas higher temperatures favoured the formation of σ Rs. [348]

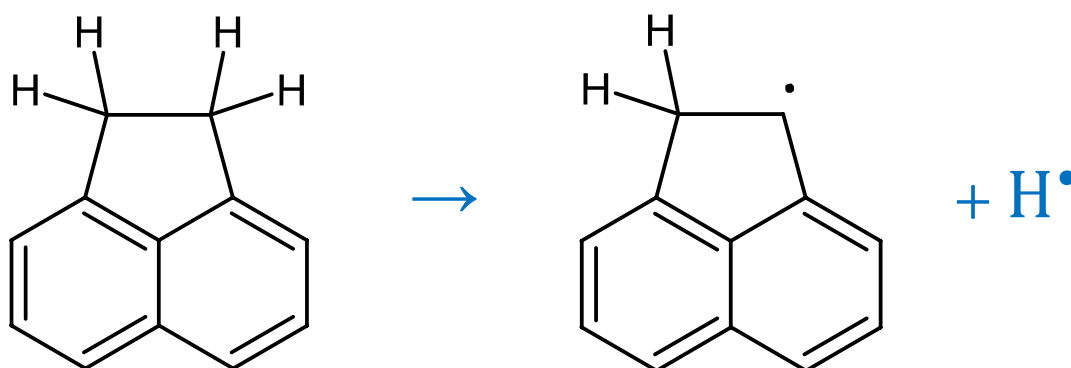


Figure II. 49: Example of the formation of a π R on the saturated rim-based 5-membered ring in acenaphthene

Experimentally they were suspected to be observed in mass spectrometry measurements using molecular beams. [349] Also, AFM images have evidenced their probable existence in sooting flames. Indeed, an AFM image from reference [272] and shown on Figure II. 50 shows a condensed PAH embedding a π R.³

π Rs are particularly important because they can be resonantly stabilized. Thus they are more stable and display longer lifetimes in flames. Their production rates are also

³ On the image, the bright contrast is due to an sp^3 carbon, which gives an odd number of electrons. This implies the existence of a resonantly-stabilized radical on the molecule as depicted on the skeletal structures

faster compared to σ Rs, [339, 350–352] and promising mechanisms of soot nucleation involving the reaction of π Rs with closed-shell PAHs to form larger radical clusters have been recently suggested. [226, 353] To this regard, methylene groups (R–CH₂–R) can also yield stable π Rs and are currently being studied for their implications in soot nucleation processes. [354]

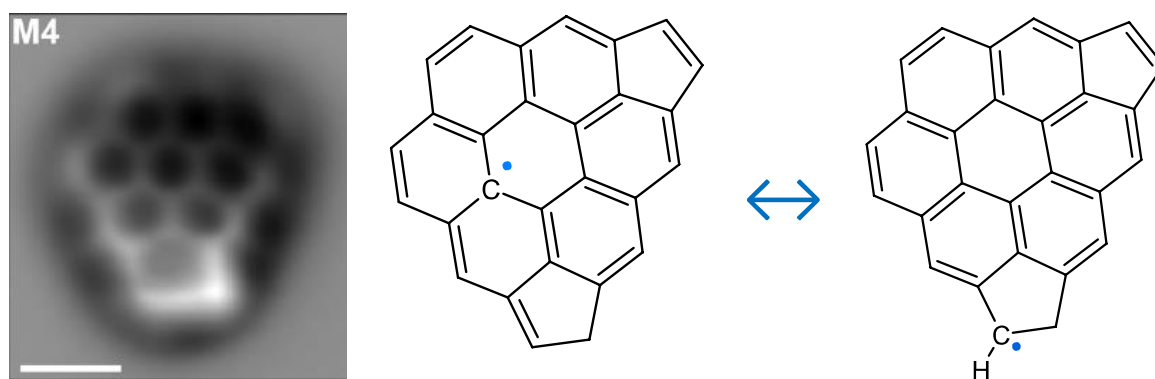


Figure II. 50: AFM image of the evidence for the existence of π Rs in sooting flames (obtained and modified from reference [272])

Some probable π and σ radical sites, including the methylene group (noted “partially embedded pentagonal ring π -radical”) are given in reference [226] and shown on Figure II. 51.

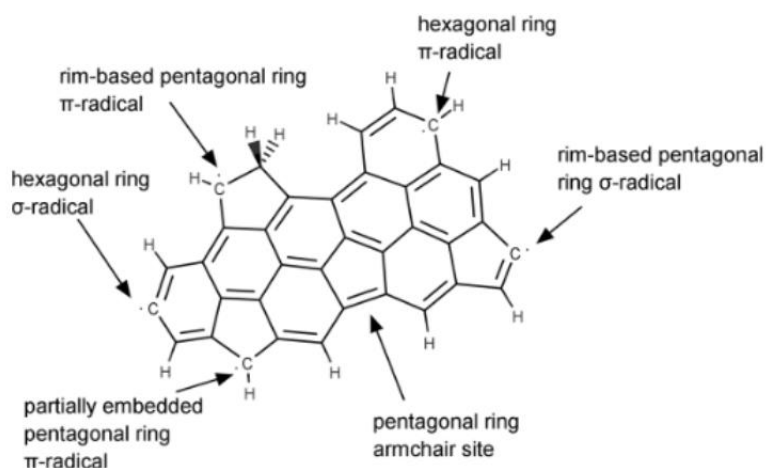


Figure II. 51: Examples of σ and π radical sites on PAHs according to reference [226]

1.2. Studied structures

This chapter being an extension of the work performed on vdW dimers and ABPAHs in Chapter 2 and Chapter 3, only σ Rs and π Rs of the already studied structures were investigated. This was for example done by adding small aliphatic chains on monomers to study π Rs, or removing hydrogens in the ABs of chemical dimers. This

means that the study of radical cations is out of the scope of this work. Also, diradicals were excluded from the study because of the difficulties of modelling such systems using DFT.

The σ -radical monomers were studied by abstracting a hydrogen atom of the molecule. This was done by randomly picking one carbon on the edge of the molecule and removing its hydrogen, regardless of thermodynamic nor kinetic plausibility of the abstraction. This way the 2-pyrenyl, 3-perylenyl and 8-fluoranthenyl (σ PY, σ PER and σ FLU) were obtained according to the nomenclature given on Figure II. 52. The same procedure was applied on the vdW dimers to obtain the pyrene/2-pyrenyl, perylene/2-perylenyl and fluoranthene/2-fluoranthenyl (PY/ σ PY, PER/ σ PER and FLU/ σ FLU).

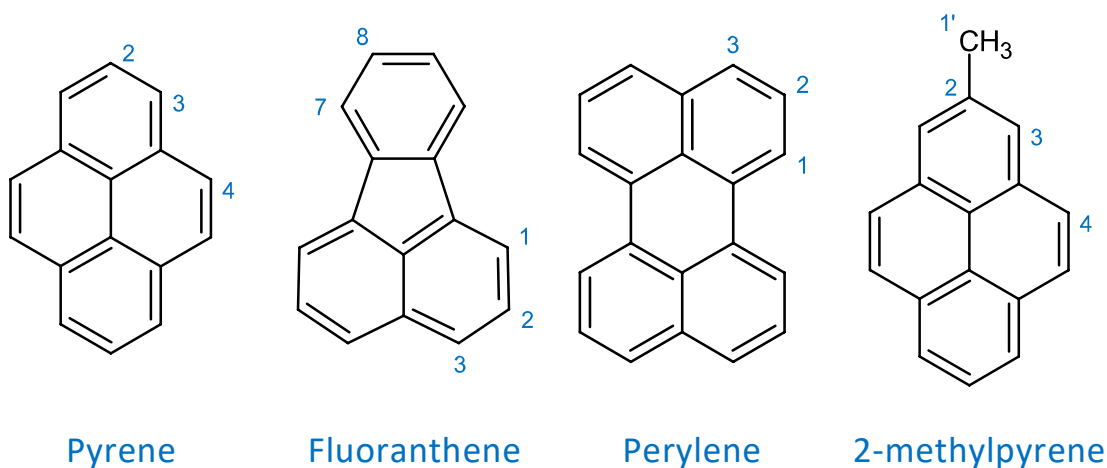


Figure II. 52: The studied PAHs with the carbon atom labelling used in this work

The formation of π Rs requires sp^3 carbon atoms neighbouring the π -system of the molecule. This happens for molecules bearing saturations in rim-based rings as shown on Figure II. 50, or more simply, for molecules bearing aliphatic groups. For this reason and in order to study π Rs, methyl or ethyl groups were added to each species and a hydrogen atom abstracted from the 1' carbon atom (according to the IUPAC labelling given on Figure II. 52) to obtain π Me-PY, π Et-PY, PY/ π Me-PY and PY/ π Et-PY (and analogously for perylene and fluoranthene).

The hydrogen abstraction from the ethyl group can also be performed from the 2' carbon which yields sigma radicals, named σ Et-PY and PY/ σ Et-PY.

Finally, π Rs were obtained from the abstraction of a H atom in the AB of chemical dimers with either 1C or 4C AB. The 1C AB allows the delocalization of the radical

on both monomers at the cost of strong structure tensions, whereas the **4C** AB yields more flexibility, but the radical is delocalized on only one of the monomers. The species will be referred to as $\pi\text{XC-2PYPY2}$, $\pi\text{XC-2FLUFLU2}$ and $\pi\text{XC-2PERPER2}$ (with **X** being **1** or **4**).

The 30 structures are shown in Appendix 8 and some examples are shown on Figure II. 53.

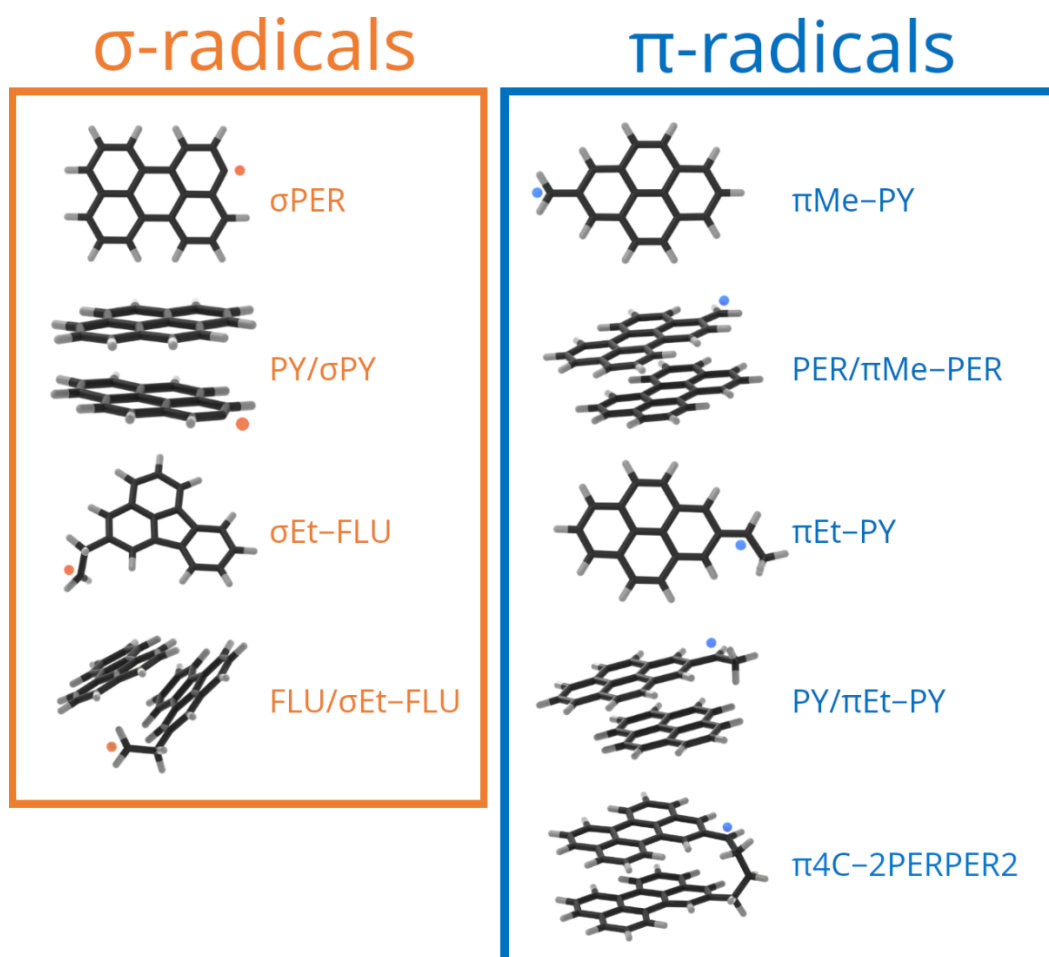


Figure II. 53: Examples of σR and πR species studied in this work

2. Stability of radical containing vdW dimers

In ReaxFF studies, $\sigma\text{R}/\sigma\text{R}$ vdW dimers were observed to remain in purely physical dimeric forms, rather than to form covalent bonds. [355] Using DFT, $\pi\text{R}/\pi\text{R}$ vdW dimers were shown to be more stable than their non-radical (NR) counterpart. [220] However, to our knowledge, the stability of the vdW dimerization of σR or πR with NR counterparts was never studied.

In Table II. 9 are reported the binding Gibbs free energies of each vdW system: with or without aliphatic groups and in their radical form or not.

			Binding Gibbs free energies / kcal mol ⁻¹		
			Pyrene	Fluoranthene	Perylene
M + M	\rightleftharpoons	M/M	1.00	0.34	-1.21
M + Me-M	\rightleftharpoons	M/Me-M	0.59	0.15	-0.47
M + M-Et	\rightleftharpoons	M/M-Et	0.48	0.43	-0.51
M + σM	\rightleftharpoons	M/ σM	0.52	0.53	-1.98
M + $\pi\text{Me-M}$	\rightleftharpoons	M/ $\pi\text{Me-M}$	0.25	0.16	-4.47
M + $\sigma\text{Et-M}$	\rightleftharpoons	M/ $\sigma\text{Et-M}$	0.70	0.66	-0.05
M + $\pi\text{Et-M}$	\rightleftharpoons	M/ $\pi\text{Et-M}$	-0.10	-0.33	-2.23

Table II. 9: Binding Gibbs free energies (kcal mol⁻¹) of every vdW dimer species studied. In the chemical equations, M stands for **PY**, **FLU** or **PER**

The addition of a methyl or ethyl group on one NR monomer has close to no effect on the binding energy. Similarly, the implication of σR or πR species yields no changes on the stability of the dimers. This is contradiction with the previously mentioned studies in which $\sigma\text{R}/\sigma\text{R}$ and $\pi\text{R}/\pi\text{R}$ dimers displayed unusual stability, which might indicate that the involvement of two radical species is necessary for an improved stability. Note there during optimization, the **FLU/ $\sigma\text{Et-FLU}$** converged into a peculiar geometry (shown on Figure II. 54), in which one monomer stacked onto the radical tip of the ethyl group. Moreover, the binding energy of **FLU/ $\sigma\text{Et-FLU}$** is 0.66 kcal mol⁻¹ which is almost the same as in **FLU/Et-FLU** (0.43 kcal mol⁻¹), and the same progression is observed for the pyrene-based systems (0.70 kcal mol⁻¹ and 0.48 kcal mol⁻¹ for **PY/ $\sigma\text{Et-PY}$** and **PY/Et-PY**, respectively), although they converged to more standard stacked geometries. This confirms that the orientation of

the molecule has no effect on the binding strength in vdW dimers of PAH as concluded in Chapter 2.

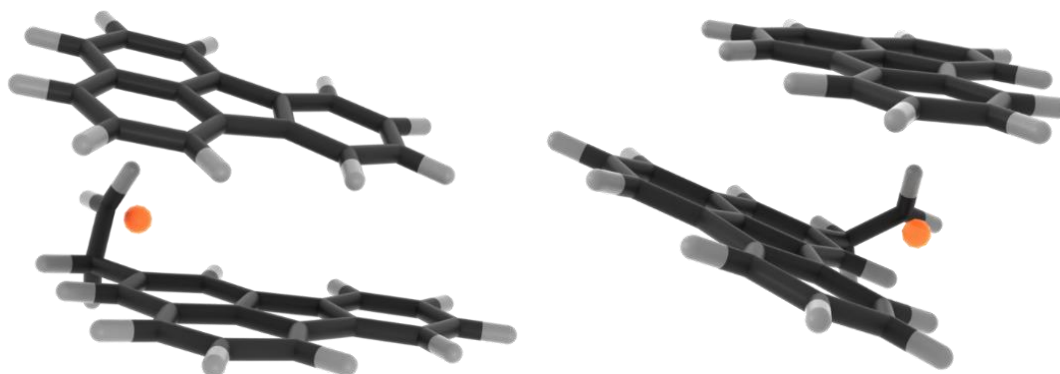


Figure II. 54: The **FLU/σEt-FLU** geometry from two camera angles

Finally, the **PER/πMe-PER** dimer is particularly stable. Looking at the structure on Figure II. 55 shows that the radical methyl group lies on top of a naphthalene moiety of the other monomer. However, this structural feature is also present on the **FLU/πMe-FLU** structure, which display regular binding energies. Thus, this unusual stability remains unexplained.

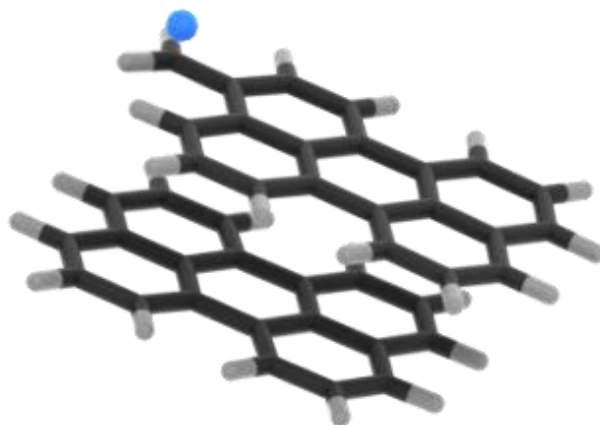


Figure II. 55: The **PER/πMe-PER** dimer

3. Electronic properties

3.1. σ -radicals

The σ -radicals of PAH-based species involves the removal of a hydrogen atom from an sp^2 carbon atom. Because the electron is not delocalized on the π system, σ R species can be expected to display similar excitation spectra to their NR counterpart.

On Figure II. 56 are shown the vertical electronic transitions of **PY**, **FLU** and **PER** compared to σ **PY**, σ **FLU** and σ **PER** (on the left), as well as those of **PY/PY**, **FLU/FLU** and **PER/PER** compared to **PY/ σ PY**, **FLU/ σ FLU** and **PER/ σ PER** (on the right). On both the monomeric and dimeric systems, the electronic transitions of the σ R match closely those of the NRs. However, additional low energy and low oscillator strength transitions appear in the σ R. This is interesting because it indicates that some electronic transitions could explain the significant red-shifts observed experimentally in LIF measurements. For example, of all systems, the maximum energy shift is observed when going from **PY** to σ **PY** with a value of 2.02 eV. However, the oscillator strength of the transition is rigorously zero, due to a change of spin during the transition. When keeping the non-zero oscillator strengths only, the largest shift is obtained for the same system and is of 1.07 eV with an oscillator strength of 0.0014. Although it is a low oscillator strength, it means that the system can indeed be excited to induce a fluorescence. The low energy transitions are better observed on Figure II. 57 in which the oscillator strengths axis was zoomed in.

The non-zero oscillator strength LEET for σ **PY** lies at 421 nm whereas that of its vdW dimer **PY/ σ PY** is at 430 nm, still below the experimental excitation wavelengths. However, σ **PER** has a transition at 572 nm with a 0.0007 oscillator strength, suggesting that σ R could be at the origin of the BB.

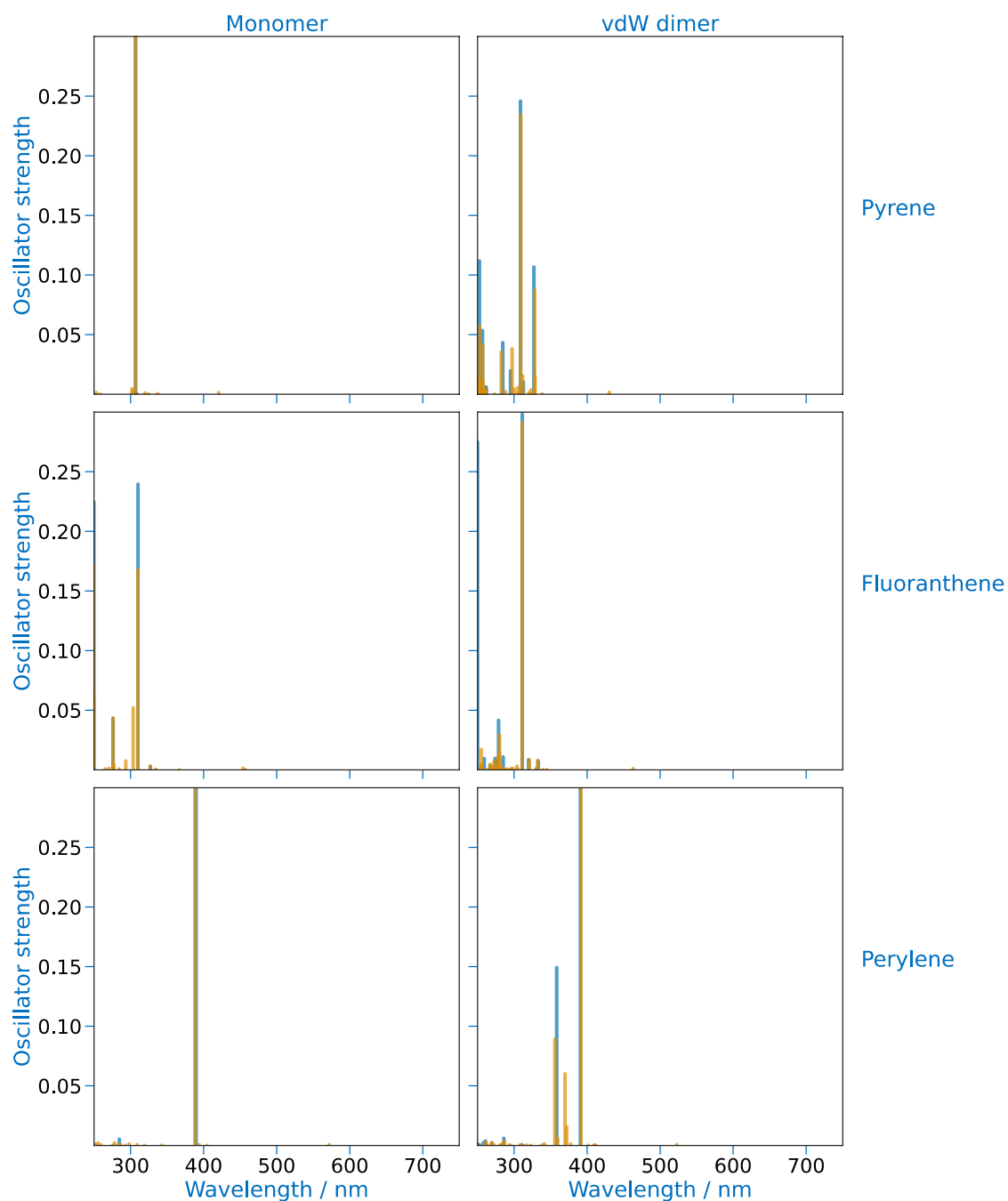


Figure II. 56: Computed electronic transitions of monomer (left) and vdW dimer species (right) of pyrene, fluoranthene and perylene (blue) compared to those of the σR species (orange):

\mathbf{M} compared to $\sigma\mathbf{M}$ (left) and \mathbf{M}/\mathbf{M} compared to $\mathbf{M}/\sigma\mathbf{M}$ (right)

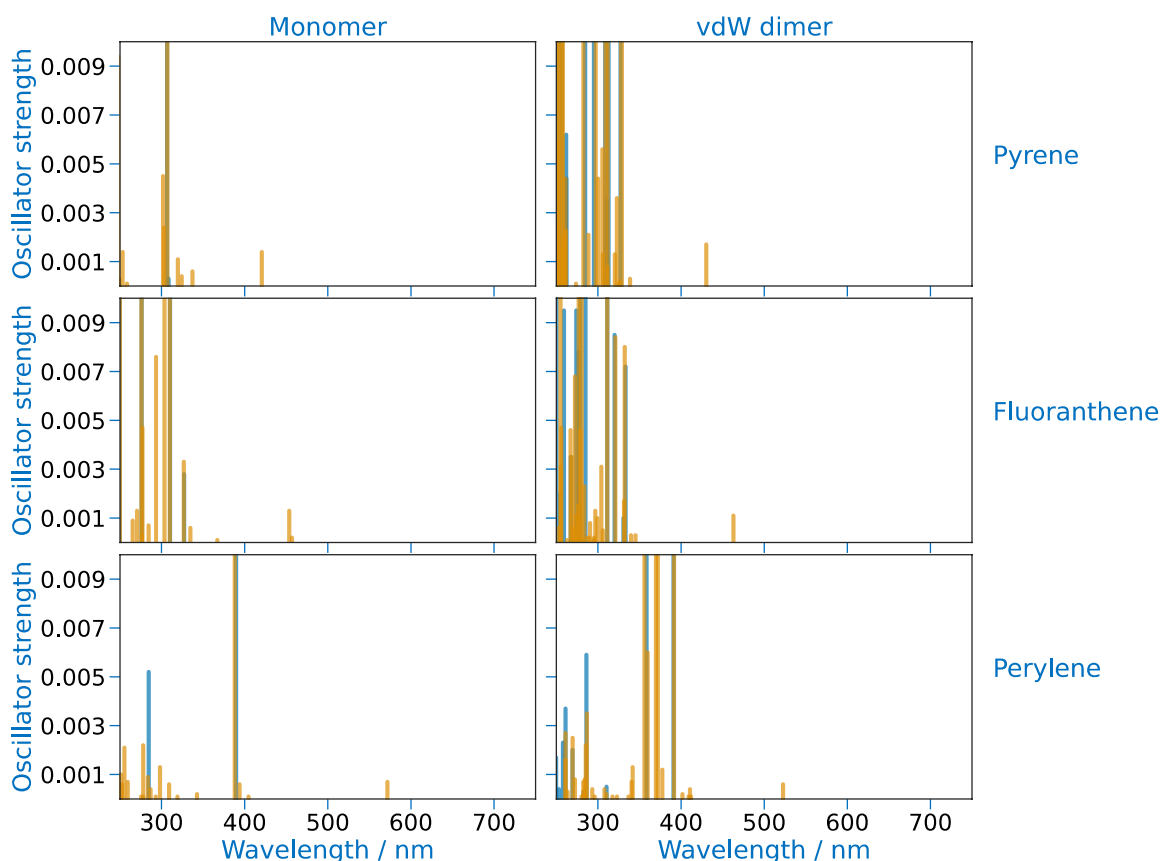


Figure II. 57: Zoom on the low energy transitions shown on Figure II. 56

On the other hand, it is possible to form σ Rs by abstracting a hydrogen atom at the tip of the ethyl group (to yield $\mathbf{M}/\sigma\text{Et}-\mathbf{M}$ systems). Doing so yields the electronic transitions shown in Appendix 10. The removal of such a hydrogen has no effect on the low energy transitions whatsoever meaning that such species cannot be responsible for the observation of the BB.

3.2. π -radicals

As stated in the introduction to this chapter, the π Rs were studied by substituting the molecules with methyl or ethyl groups. Before studying the effect of π Rs on the spectra, it is necessary to quantify the effect of the substitution. To this aim, the electronic transitions of **NR PY**, **FLU**, **PER**, **PY/PY**, **FLU/FLU** and **PER/PER** are shown in Appendix 9 compared to their methylated and ethylated counterparts. The alkylation has close to no effect on the spectrum except for **PY/PY** whose LEET is blue-shifted upon substitution. This shows that the alkylation effect can safely be ignored when studying π R formation.

On Figure II. 58 are shown the electronic transitions of the alkylated systems compared to their π R counterpart. The maximum energy shifts obtained are of

1.93 and 1.29 eV with LEETs at 623 and 618 nm for **PY/ π Et-PY** and **PY/ π Me-PY**, respectively. However, those are transitions with exactly 0 oscillator strengths and keeping only the non-zero oscillator strengths, the maximum red-shift is of 1.78 eV with a transition at 561 nm and 0.0002 oscillator strength obtained for **π Et-PY**. Interestingly, this is a transition to the first ES meaning that fluorescence could be obtained after excitation. The non-zero oscillator strength ($f = 0.0002$) LEET is obtained for **π Et-PER** with a transition at 713 nm, which is a lower energy than the laser energies used in LIF experiments.

Fluoranthene forms particularly interesting systems and, for example, **π Et-FLU** has its LEET at 518 nm with an oscillator strength of 0.0103. Thus, its electronic properties could explain the observation of the BB.

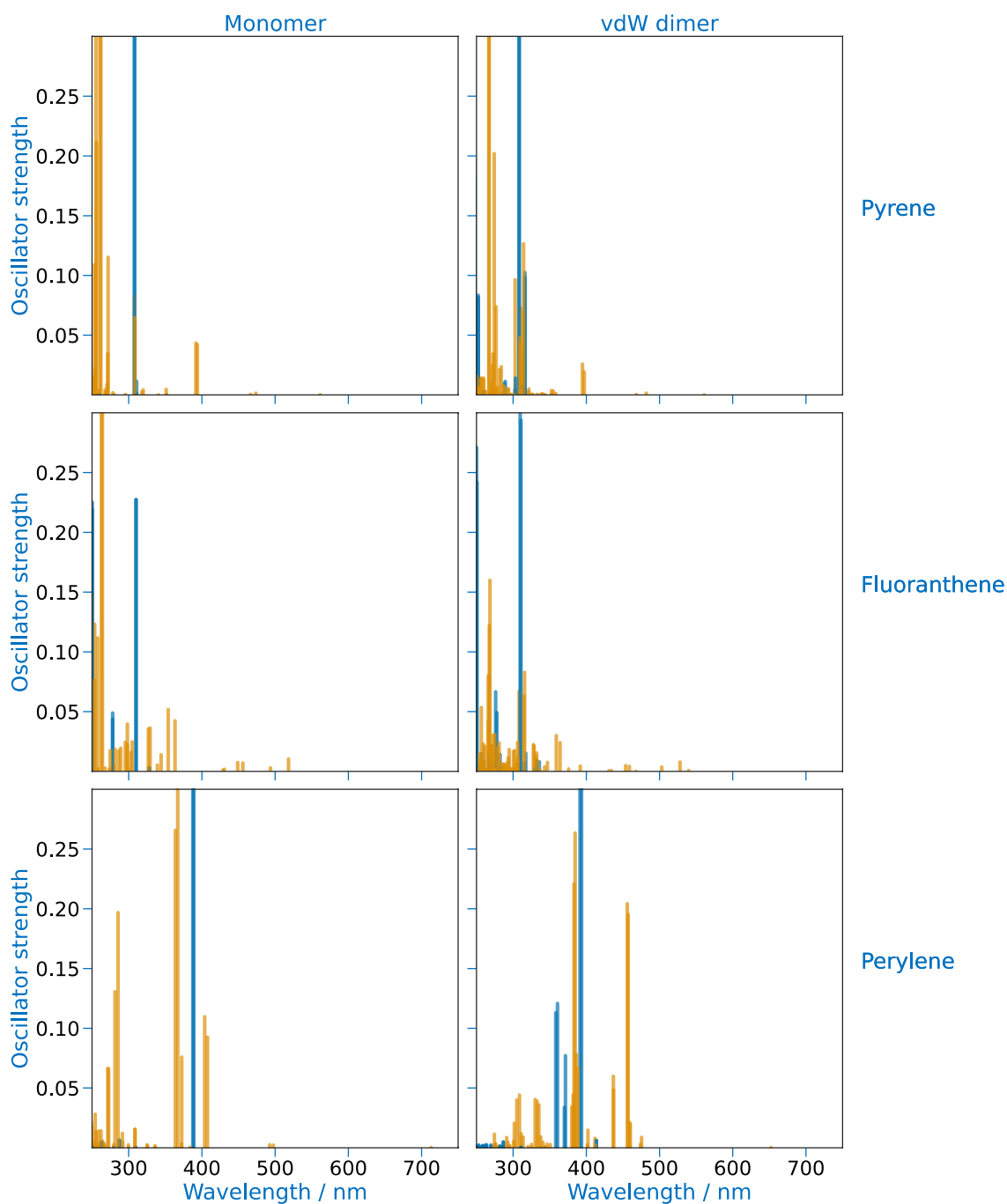


Figure II. 58: Computed electronic transitions of the monomer (left) and vdW dimer (right) species of methylated and ethylated pyrene, fluoranthene and perylene (blue, regardless of the alkyl group) compared to the π R species (orange):

Alkyl-M compared to $\pi\text{Alkyl-M}$ (left) and $\text{M}/\pi\text{Alkyl-M}$ compared to $\text{M}/\pi\text{Alkyl-M}$ (right)

3.3. Chemical dimer π -radicals

Finally, π -radicals formed from the abstraction of a hydrogen atom from the AB of chemical dimers were studied. This was done by studying a subset of the ABPAH structures from Chapter 3 containing one conformer per monomer with either **1C** or **4C** ABs. The structures are shown on Figure II. 59

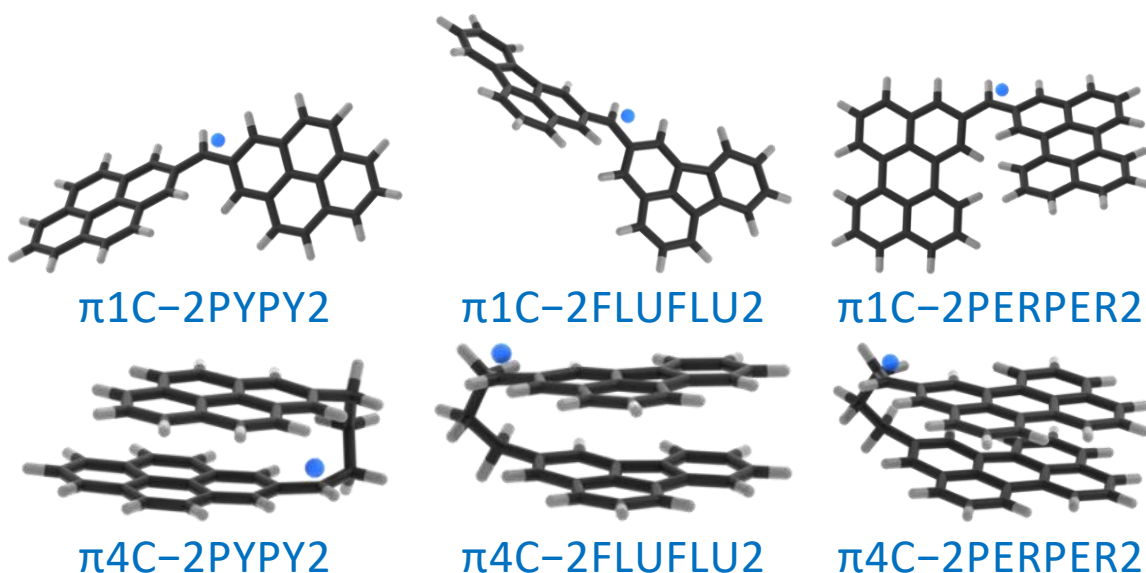


Figure II. 59: The πR chemical dimers studied in this chapter

The $\pi 4C$ systems converged to stacked geometries similar to those of their NR counterpart. In the case of the $\pi 1C$ systems, it could have been expected for them to converge into planar structures due to the sp^2 hybridization of the bonding carbon atom which allows electron delocalization on the whole system. However, this is not the case because steric hindrance prevents planarity. Note that the $\pi 1C-2PERPER2$ structure converged to a *cis* geometry with both perylene monomers put aside along their long-axis, although the *trans* geometry would probably be another minimum on the PES.

The electronic transitions of each system are shown on Figure II. 60, compared to those of their NR counterpart. Upon radical formation, the transitions are red-shifted similarly to the $M/\pi Alkyl-M$ systems. The maximum energy shift is of 1.87 eV, obtained for $\pi 4C-2PYPY2$ with a transition at 593 nm.

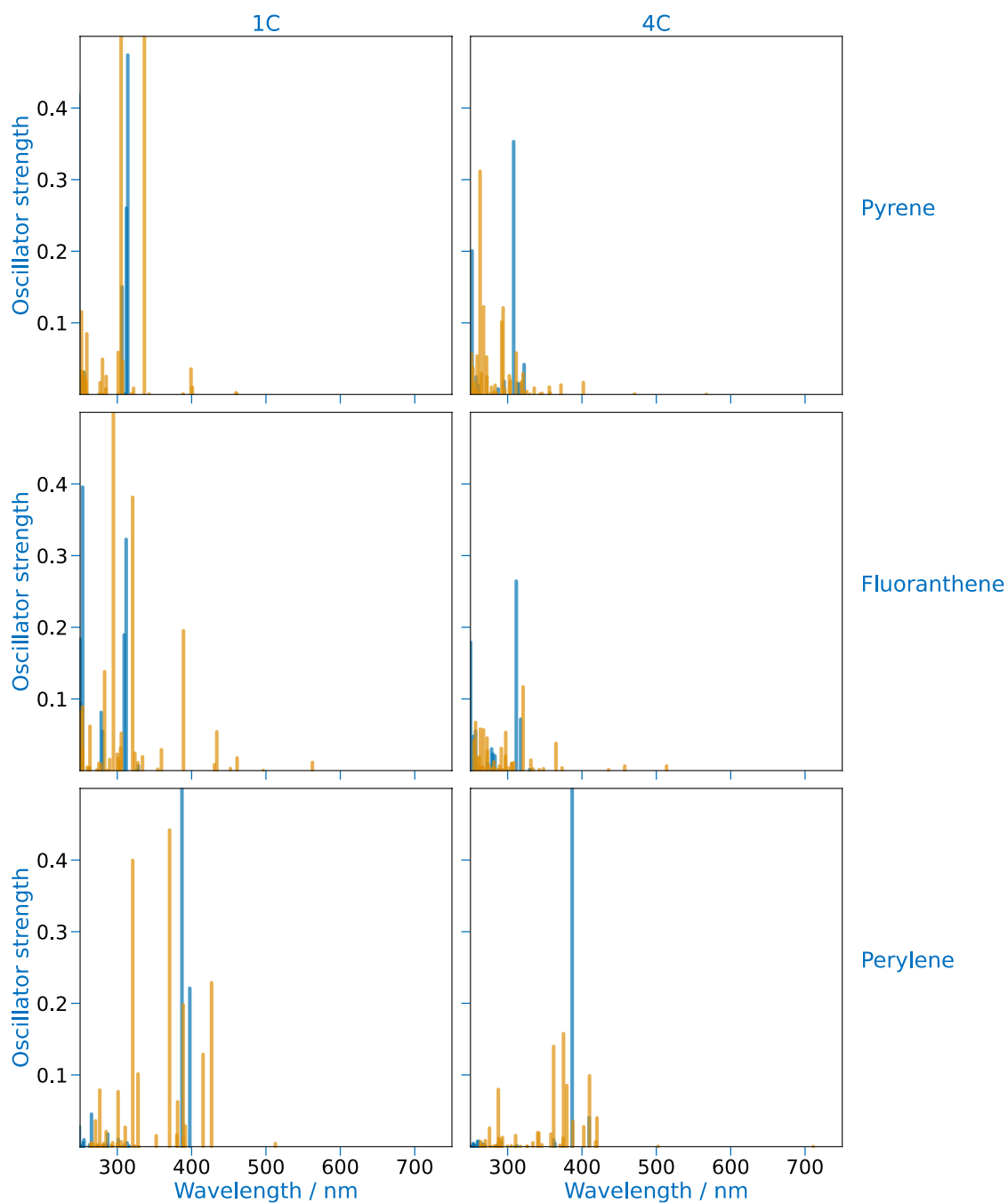


Figure II. 60: Computed electronic transitions of the **1C** (left) and **4C** (right) chemical dimers of pyrene, fluoranthene and perylene (blue) compared to the π R species (orange)

The non-zero oscillator strength transitions are given in Table II. 1.

	Red-shift / eV	Wavelength / nm	Oscillator strength
		1C	
PY	1.26	461	0.0006
FLU	1.57	562	0.0114
PER	0.70	513	0.0042
		4C	
PY	1.66	567	0.0002
FLU	1.33	514	0.0064
PER	1.28	711	0.0001

Table II. 10: First non-zero oscillator strength transitions in the π 1C and π 4C systems. The red-shift value corresponds to that observed upon abstracting a hydrogen in the AB of the studied system.

The LEET calculated with the smallest wavelength is obtained for π 1C–2PYPY2 at 461 nm, which is already a strong improvement over the NR counterpart. π 4C–2PERPER2 has a calculated LEET at 711 nm which is below the laser energies used experimentally for LIF measurements. Finally, the fluoranthene-based systems are once again the most interesting ones with larger oscillator strengths. The 562 nm transition with 0.0114 oscillator strength in π 1C–2FLUFLU2 is a transition to the lowest energy ES showing that fluorescence might occur upon excitation of this molecule.

4. Conclusion

Physical and chemical dimers of PAHs were studied to verify whether they could be at the origin of the BB observed in LIF experiments. Although the dimerization could have been expected to red-shift the electronic transitions to yield visible fluorescence excitation and emission, the computed transitions for the **PY**, **FLU** and **PER** dimers are far below the experimental values. Instead in this chapter, σ Rs and π Rs were studied in monomeric and dimer forms of the same monomers.

σ Rs obtained from the removal of a hydrogen atom “far” from the π system of the molecule, such as at the tip of an ethyl group, has no effect on the wavelengths of the electronic transitions. Thus, such molecules cannot be at the origin of the BB.

Instead, all the other studied radicals have interesting electronic properties. Indeed, the abstraction of hydrogen atoms on the edge of PAHs yields visible electronic transitions, and **σ PER**, for example has a transition at 572 nm with a 0.0007 oscillator strength. Resonant excitations of these kind of electronic transitions could yield the visible BB in LIF measurements. However, It can be noted that the oscillator strengths are quite low meaning that if they display fluorescence, the signals could be quite low.

The most interesting radicals in terms of electronic properties are the π Rs. Indeed, **π Et-PY**, **π Et-FLU** and **π 1C-2FLUFLU2** have their LEETs at 561, 518 and 562 nm, respectively. This is particularly interesting for the fluoranthene transitions that have 0.0103 and 0.0114 oscillator strengths, which could yield measurable fluorescence signals.

The hypothesis developed in this chapter appears as the best match to experimental data which echoes the recent experimental and theoretical advancements in the field, suggesting that studies on open-shell PAH systems are key for understanding the soot inception mechanisms. [220, 271, 272, 353, 354]

General conclusion on Part II.

The observation of visible LIF signals in flames has raised questions since the 80s. The signals appear right before the apparition of a laser-induced incandescence signal, suggesting that the emitting species play an important role in the inception of a particle.

In this Part II. were gathered the results of a theoretical investigation that was undertaken in collaboration with Xavier Mercier's team from the PhysicoChimie des Processus de Combustion et de l'Atmosphère laboratory (PC2A). The aim was to investigate the possible implication of three PAH-based classes of molecules in the observation of the broad visible fluorescence band, *i.e.*, vdW dimers of PAHs, ABPAHs and radicals of PAH-based species.

In Chapter 2, the performances of DFT and TD-DFT for the study of vdW dimers of PAHs were assessed. A variety of dispersion corrected functionals were tested, which showed that the choice of the functional had little impact on the geometries. Calculations on the ESs showed that PBE0(D3) struggles with these systems, whereas the use of RSH functionals such as CAM-B3LYP(D3) or LC- ω PBE(D3) significantly improves the results. Indeed, they shift CR states to higher energies, predict a correct LLES ordering ($L_a^- < L_b^- < L_b^+ < L_a^+$) and give realistic dissociation energies for the excimer state. The orbital overlap between monomer entities is small, and dispersion forces account for most of the interaction between the monomers. Still, the intermonomer interaction is quite weak and **PYPY**, **FLUFLU** and **PERPER** are unstable at flame temperature. In electronic absorption, the dimerization red-shifts the LEET by 0.37 eV, in the best-case scenario. This value is to be compared to the 1.3 – 1.6 eV shifts observed experimentally. Similarly, the trimers are unstable and display similar absorption spectra. Thus, the vdW oligomerization of PAHs cannot explain the observation of the BB in LIF measurements.

Then, ABPAHs were studied in Chapter 3. This type of chemical dimerization allows to obtain “folded” structures that resemble pure vdW dimers, with less disadvantageous entropic terms. The dimerization can induce strong structural deformations on flexible molecules such as perylene. However, neither the structural

modifications nor the vdW interaction appear to induce strong enough changes on the absorption spectrum to explain LIF measurements.

Finally, a promising hypothesis was explored in Chapter 4: σ R_s and π R_s of PAH-based structures. Although the formation of σ R_s on the edge of a pyrene, fluoranthene or perylene can induce visible electronic transitions (572 nm for σ PER), these transitions display low oscillator strengths (0.0007 for σ PER), which cannot account for the large experimental emission intensities. On the other hand, π R_s can display low energy transitions such as 518 and 562 nm for π Et-FLU and π 1C-2FLUFLU2, respectively, with larger oscillator strengths of 0.0103 and 0.0114. This latter hypothesis fits experimental observations particularly well and is very promising.

Conclusion

In this thesis were reported the results of an experimental and theoretical study of two molecular systems of environmental interest: 2'3HF and PAHs. Electronic spectroscopic techniques, including absorption and fluorescence, were employed in conjunction with quantum chemical calculations, utilizing DFT and TD-DFT, to gain a comprehensive understanding of the properties and behavior of these systems. These methods once again proved themselves valuable to provide insights into complex systems at a reasonable computational cost.

The aim of the first part of this thesis was to study the complexation of metal cations with organic matter, with a focus on the properties of 2'3HF. Through a series of experiments and calculations, it was determined that the decrease of pK_a by several units compared to 3HF was attributed to the presence of a HB network within the molecule. Furthermore, an extensive study of the Ca(II), Mn(II) and Zn(II) complexes of 2'3HF was conducted and it was found that chelates were formed with the α -hydroxyketone function. In light of the results of this part, a crucial finding can be highlighted. Indeed, the study concluded that the reactivity of organic matter cannot entirely be reduced to that of its functional groups, since a vicinal hydroxyl group such as the 2' one greatly influences the properties of the α -hydroxyketone function.

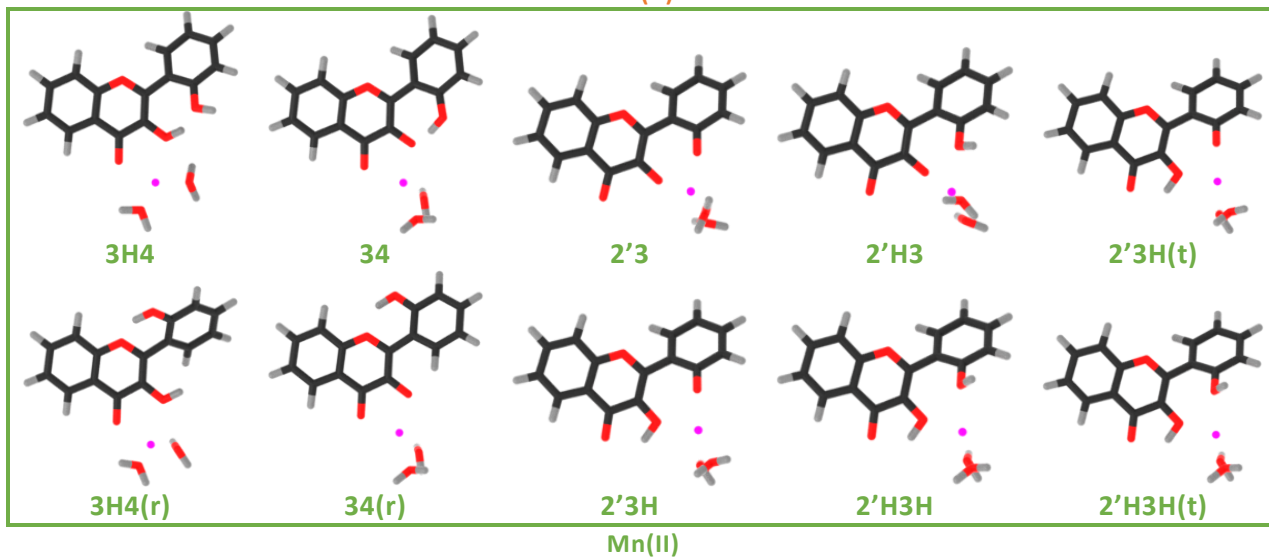
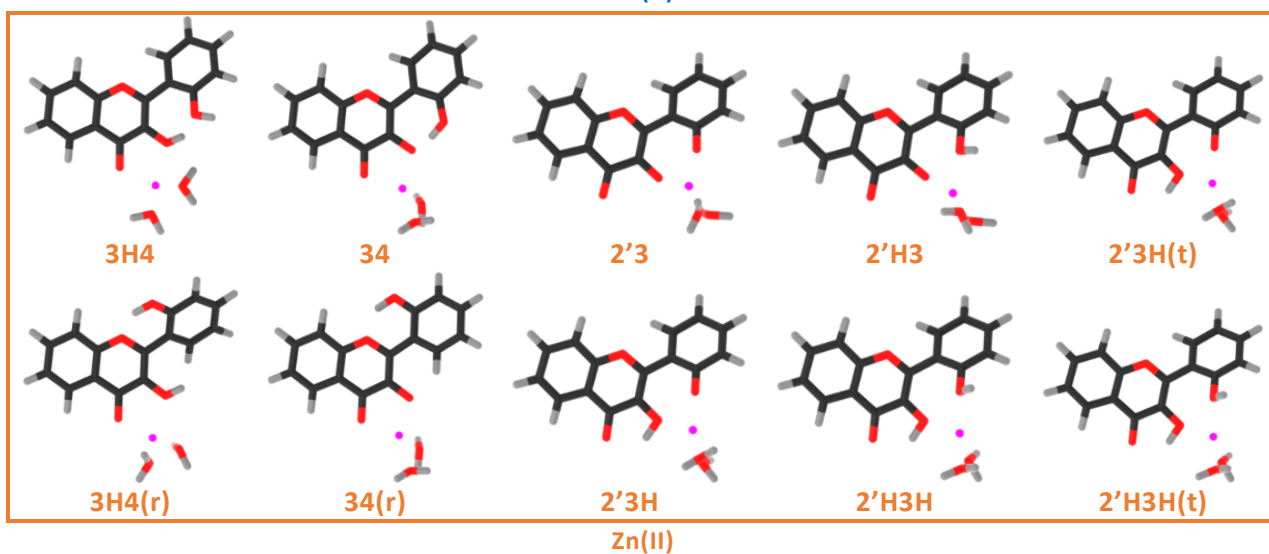
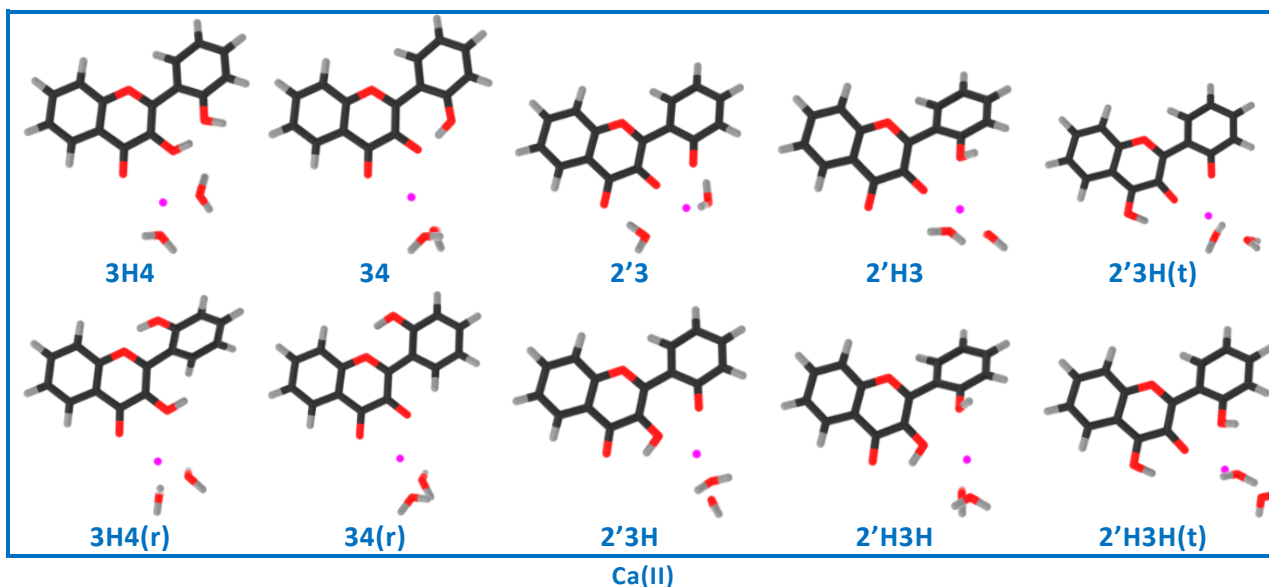
The second part of this thesis focused on the investigation of PAHs, which are known to be important environmental pollutants. In particular, the origin of the LIF signals observed in flames was investigated. To this end, three structural hypotheses were explored. The first hypothesis that was proposed is that vdW dimers of PAHs were responsible for the LIF signals. However, the calculated electronic transitions indicated that this hypothesis was unlikely. Aliphatically bridged PAHs were suggested as a second hypothesis, but the results were similar to those obtained for vdW dimers, thus ruling out their involvement in the observed fluorescence. The third hypothesis proposed that the LIF signals were emitted from PAH radicals. This hypothesis was found to be highly promising and opened the way for further experimental and theoretical studies. These future studies on PAH radicals could help unravel the way gaseous PAH molecules transition to solid particles and nucleate to form soot.

Appendices

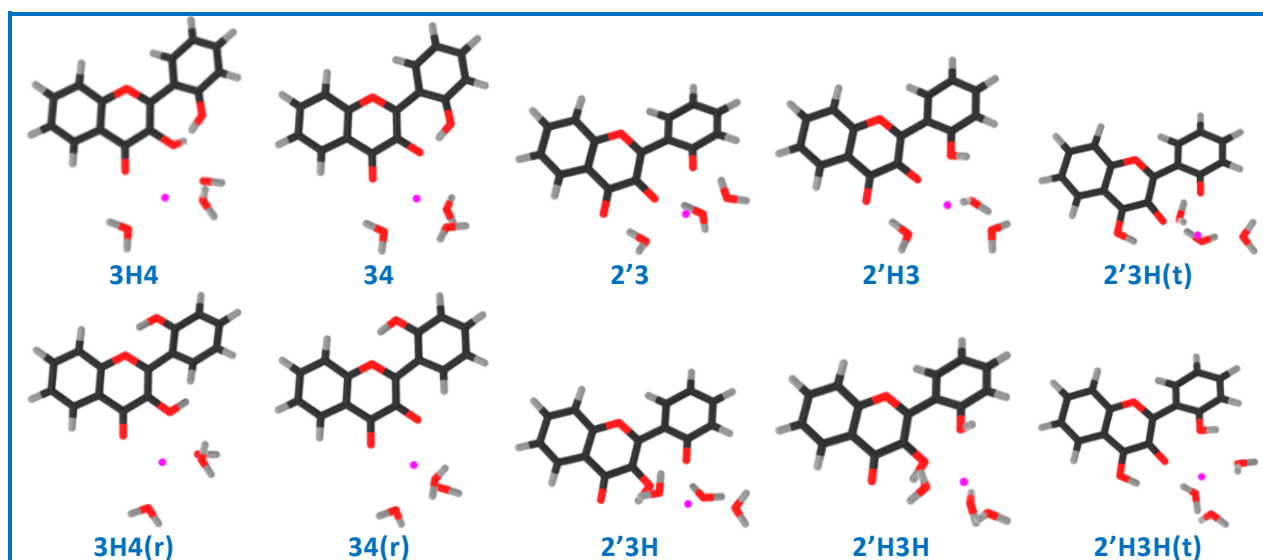
Table of appendices

2'3HF–MII(H ₂ O) ₂ optimized complexes	268
2'3HF–MII(H ₂ O) ₃ optimized complexes	269
2'3HF–MII(H ₂ O) ₄ optimized complexes	270
The Metrohm Titrando automate and its programs	271
Computed transitions for all 2'3HF complex geometries for Ca(II)	274
Computed transitions for all 2'3HF complex geometries for Zn(II)	275
Computed transitions for all 2'3HF complex geometries for Mn(II)	276
The PAH-based radical structures studied in this work	277
Alkylation effect on the electronic transitions of PAH-based structure	279
Effect on the electronic transitions of σ radicals in alkyl groups of PAH-based structures	280

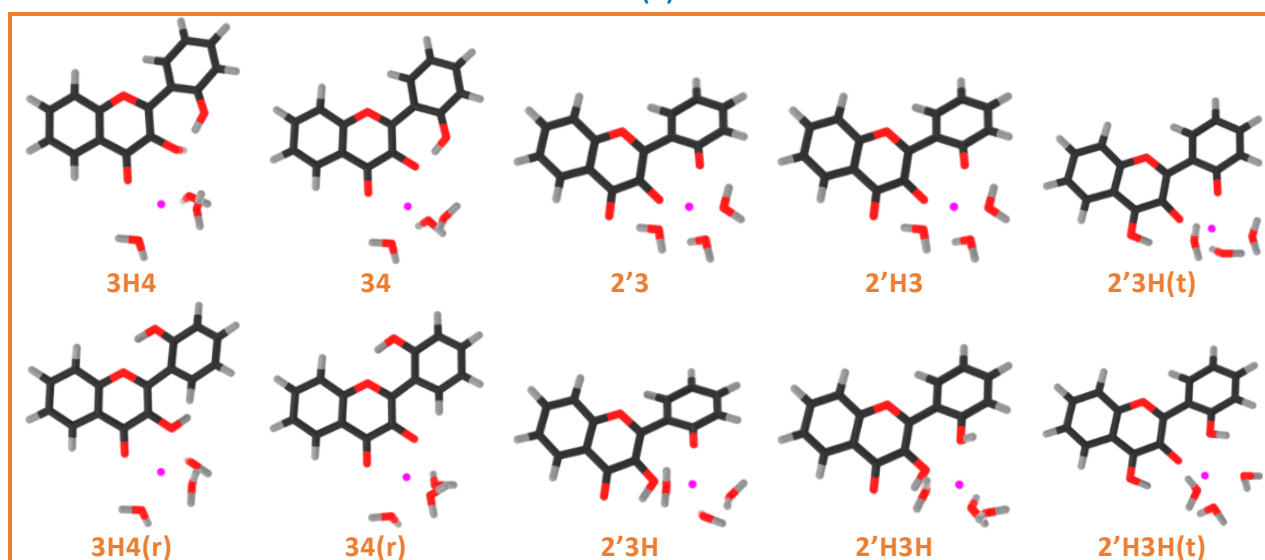
Appendix 1.2'3HF-M^{II}(H₂O)₂ optimized complexes



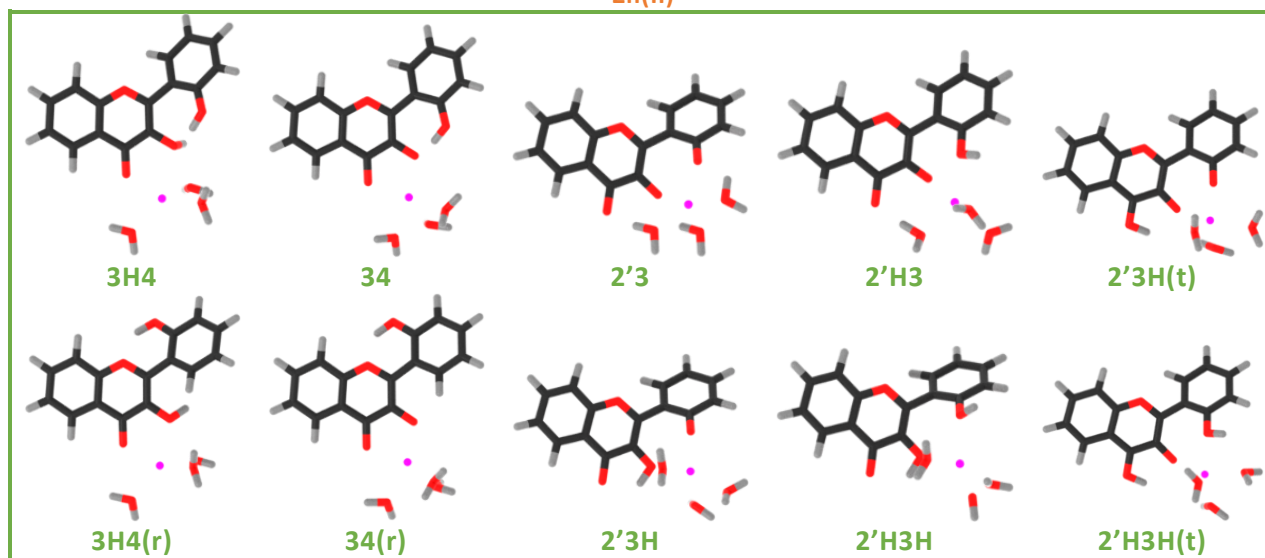
Appendix 2.2'3HF-M^{II}(H₂O)₃ optimized complexes



Ca(II)

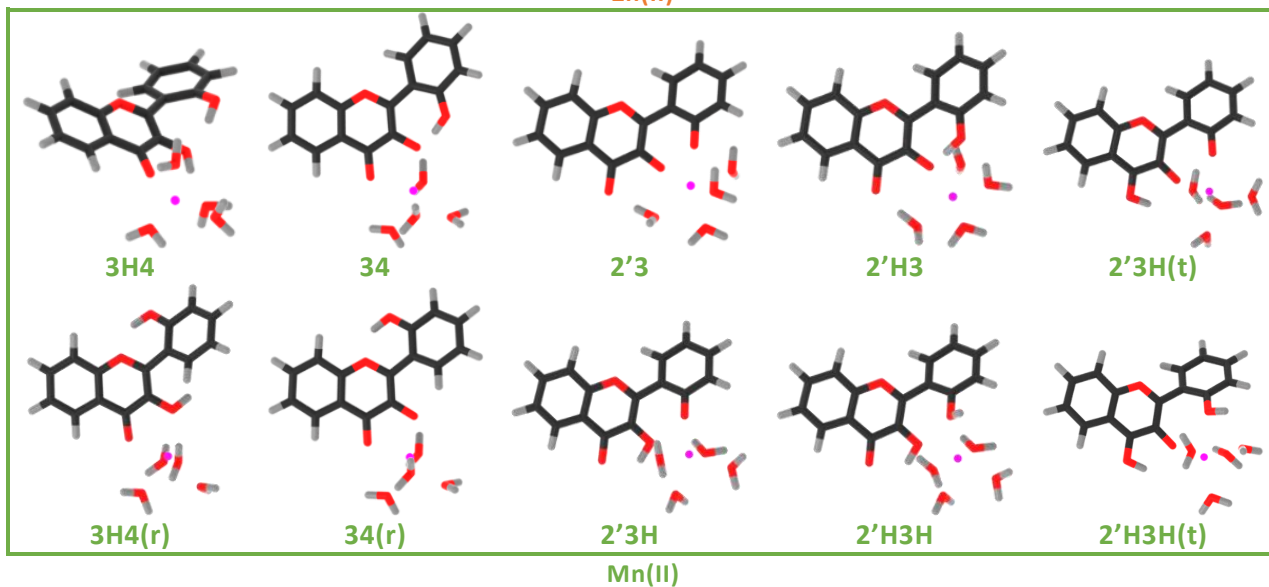
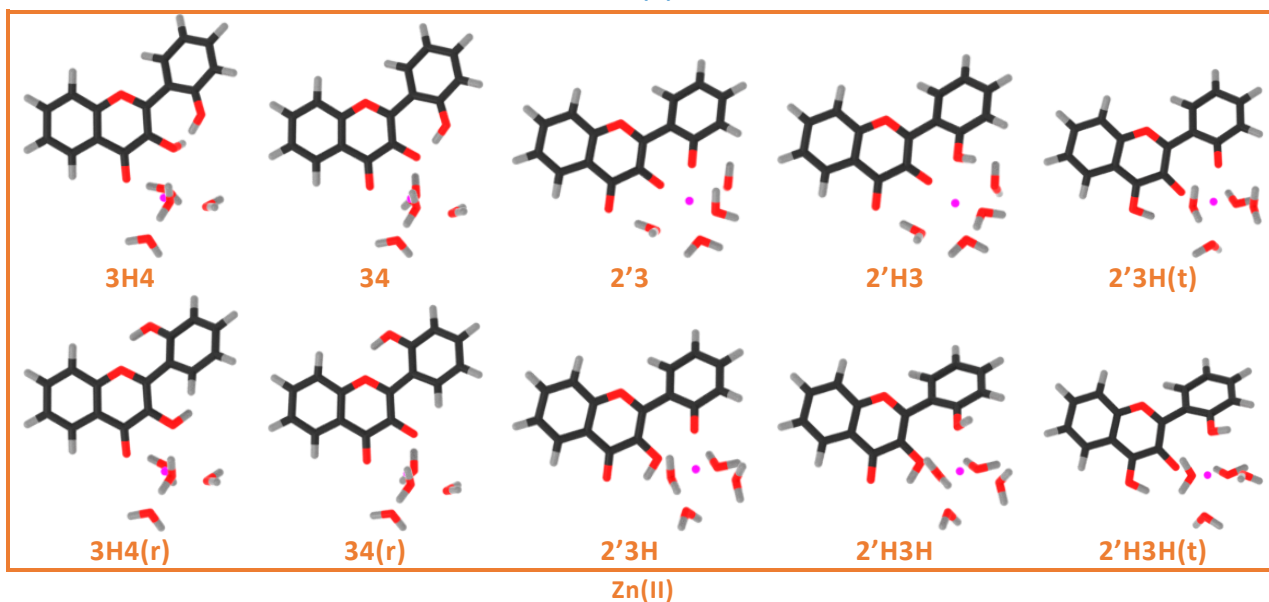
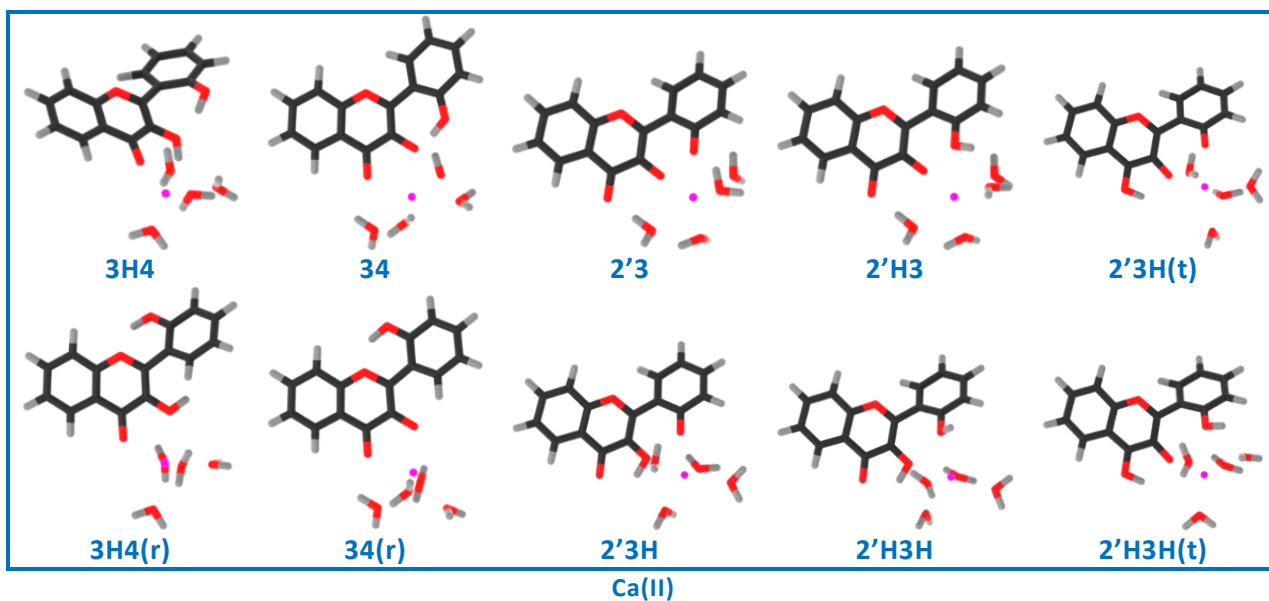


Zn(II)



Mn(II)

Appendix 3. 2'3HF-M^{II}(H₂O)₄ optimized complexes



Appendix 4. The Metrohm Titrande automate and its programs

The Metrohm Titrande system is a titrator that can be customized with modules and can be programmed to perform experiments. The version used in this thesis is composed of three burettes, a pH-meter and a computer. For the sake of this study, custom programs were developed to perform two types of experiments: complexometric dosages at fixed pH, and acid-base titrations. A scheme of the setup is shown on Figure 1.

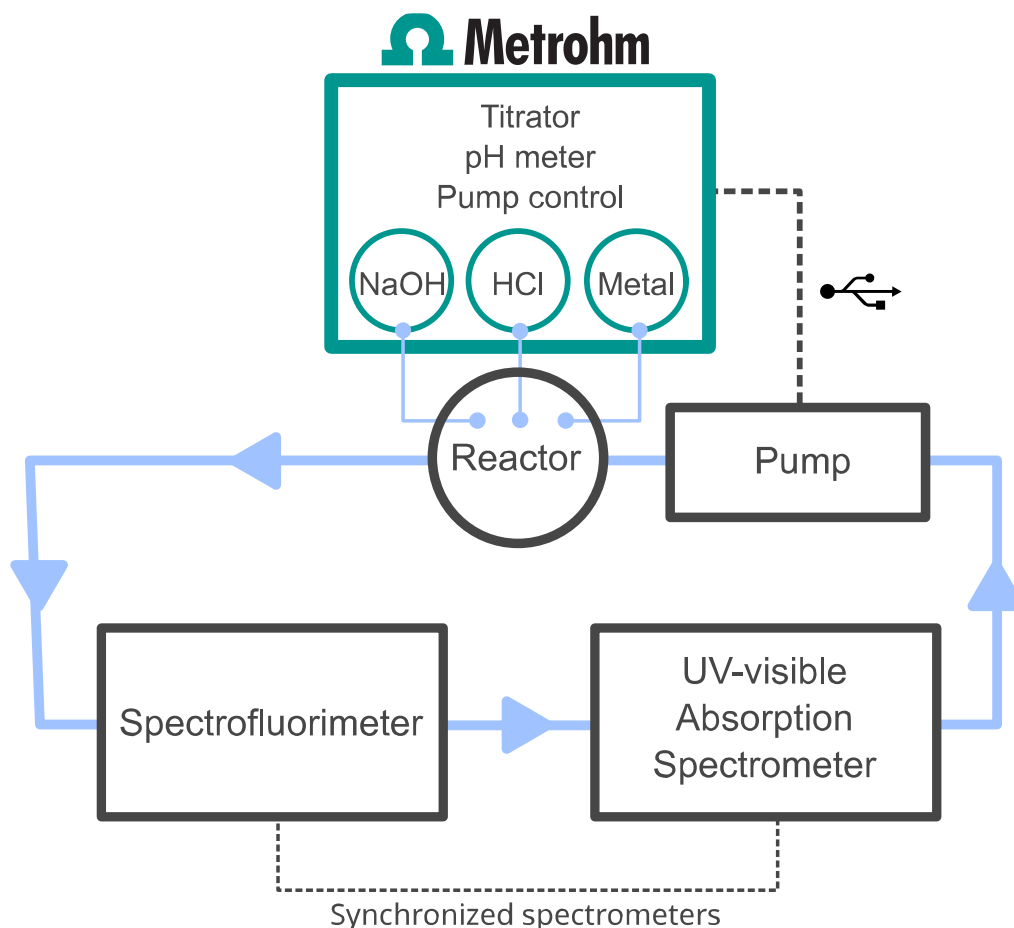


Figure 1: The experimental setup used for complexometric dosages and acid-base titrations

In both types of measurements, the automate automatically controls the flow of solution from the reactor, to a Cary Eclipse spectrofluorometer, followed by a Cary 3500 absorption spectrometer, back to the reactor. This allows the recording of emission and absorption spectra simultaneously, during which the automate is program to stop the solution flow to avoid interfering with the measurements. Between each spectrum recording (every 30 or 60 minutes depending on the experiment), the pH is measured and set to the appropriate value by small incremental additions of 0.1 mol L^{-1} aqueous solutions of NaOH or HCl. At the beginning of each spectrum recording, the final pH and added quantities of NaOH and HCl are exported to a file on the computer.

The programs were implemented in the Tiamo software (shipped with the Metrohm Titrand system) which offers a graphics user interface and a visual programming language to control the automate. An example of program is shown on Figure 2.

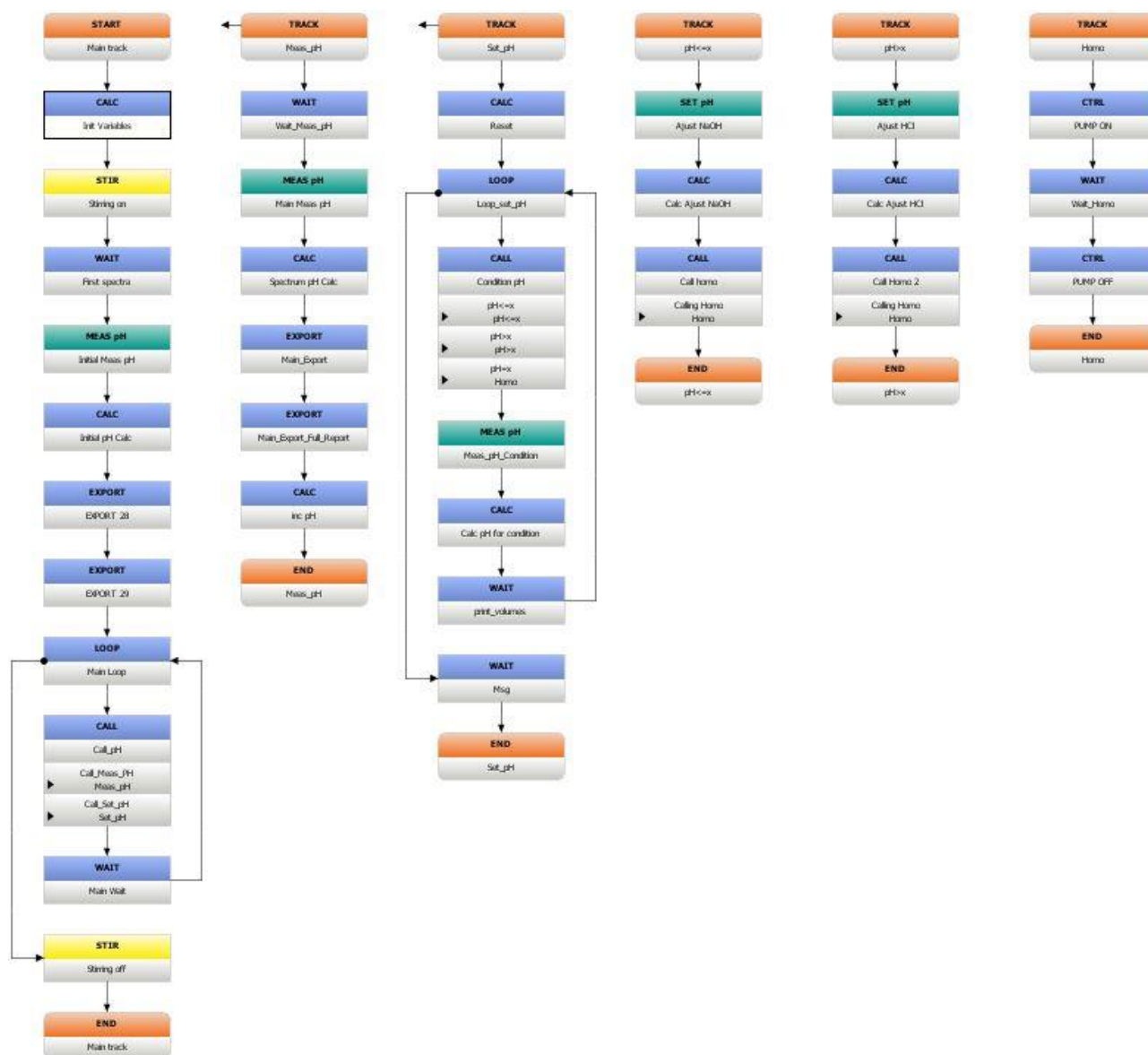


Figure 2: The pH titration program developed using the visual programming language provided by the Tiamo software

The complexometric dosage was performed by adding successive quantities of a metal (methanol) solution to a 2'3HF methanol solution at fixed pH. This was done using the following program

- The main track of the program (first column on Figure 2) initializes the experiment and all its parameters, starts the two sub-tracks in a loop, and ends the experiment.

Some examples of parameters include the stirring rate, the target pH (set to 4.0), the tolerance on pH (set to 0.02), the duration between each spectrum recording (set to 1 hour), and the sensitivity

of the pH setting track which controls how fast NaOH and HCl solutions are added to reach the target pH.

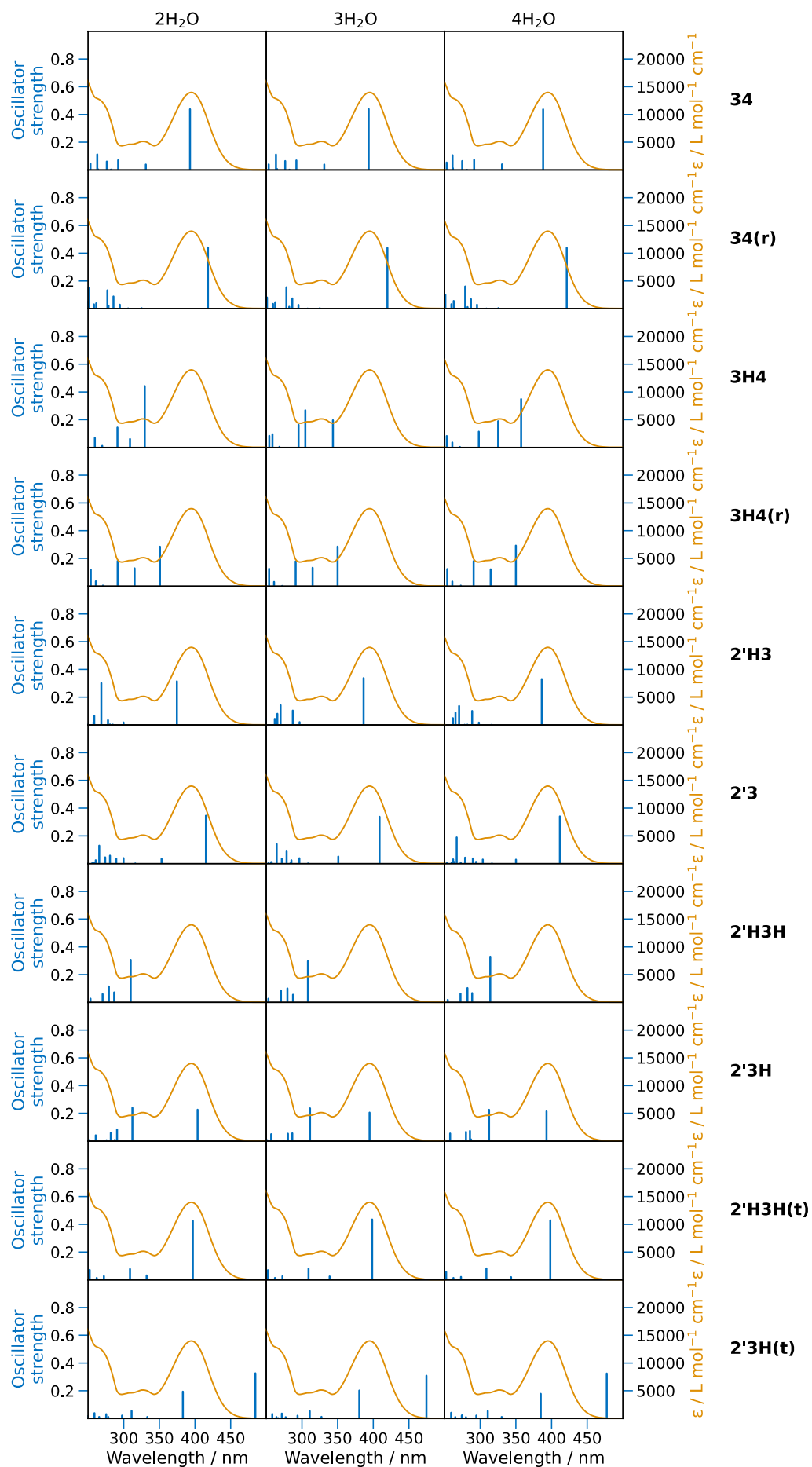
The main track is a loop in which, at the beginning of each turn, the metal solution volume to be added to the reactor is set (so that the volume increments are increased progressively during the experiment), and the main sub-tracks are started to run in parallel with the main track.

- The first sub-track consists of a waiting time of around 55 minutes, followed by a pH measurement consisting of the pH of the solution at the recording of the spectra.
- The second sub-track adds the metal solution to the reactor, then goes in a loop which measures the pH, and starts the appropriate sub-track to set the pH depending on whether NaOH or HCl solutions should be added. If the pH is already at the target value, it starts an empty sub-track which simply consists of flowing the solution. This is performed in a loop so that the solution can be circulated multiple times and to ensure that the pH is the same in the reactor and in the measurement cuvettes.

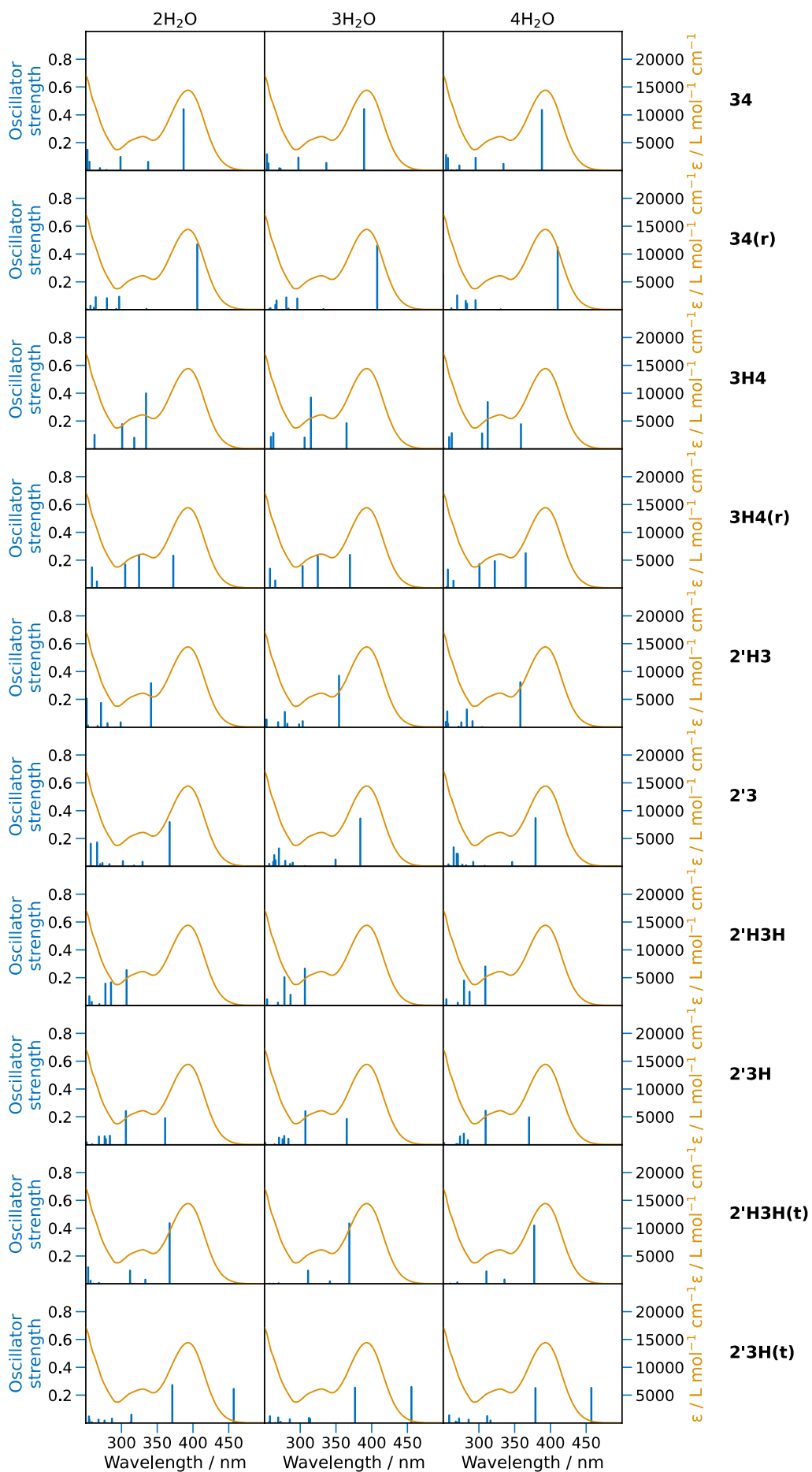
The tracks and the spectrometers are synchronized so that upon reaching the 55 minutes of waiting time, the automate stops the solution flow to let the spectrometers perform the measurements.

In the case of the pH titration experiment, the program is similar, except that the main loop increments the target pH value at each turn, and no metal solution is added. Also, the spectra are recorded every 30 minutes.

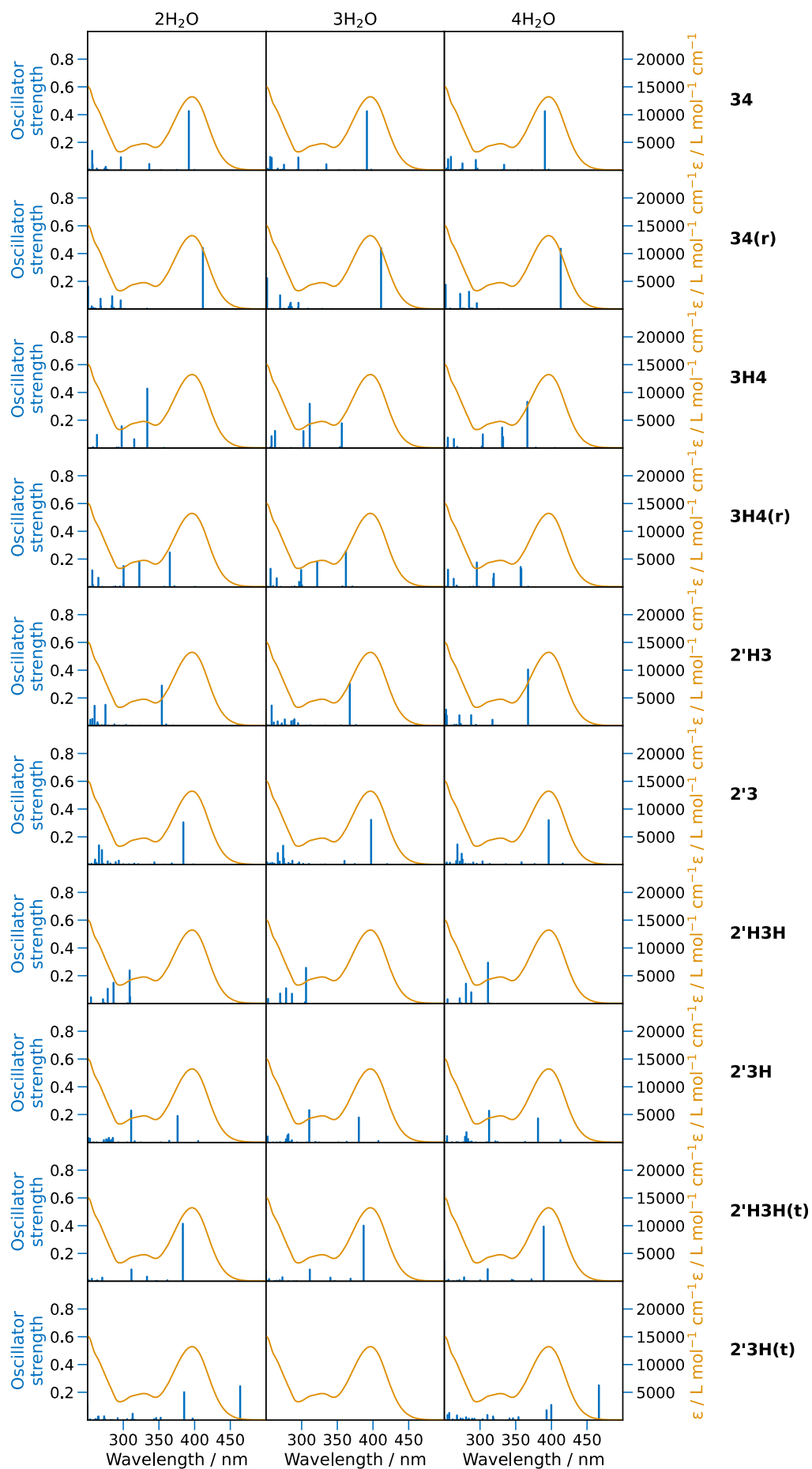
Appendix 5. Computed transitions for all 2'3HF complex geometries for Ca(II)



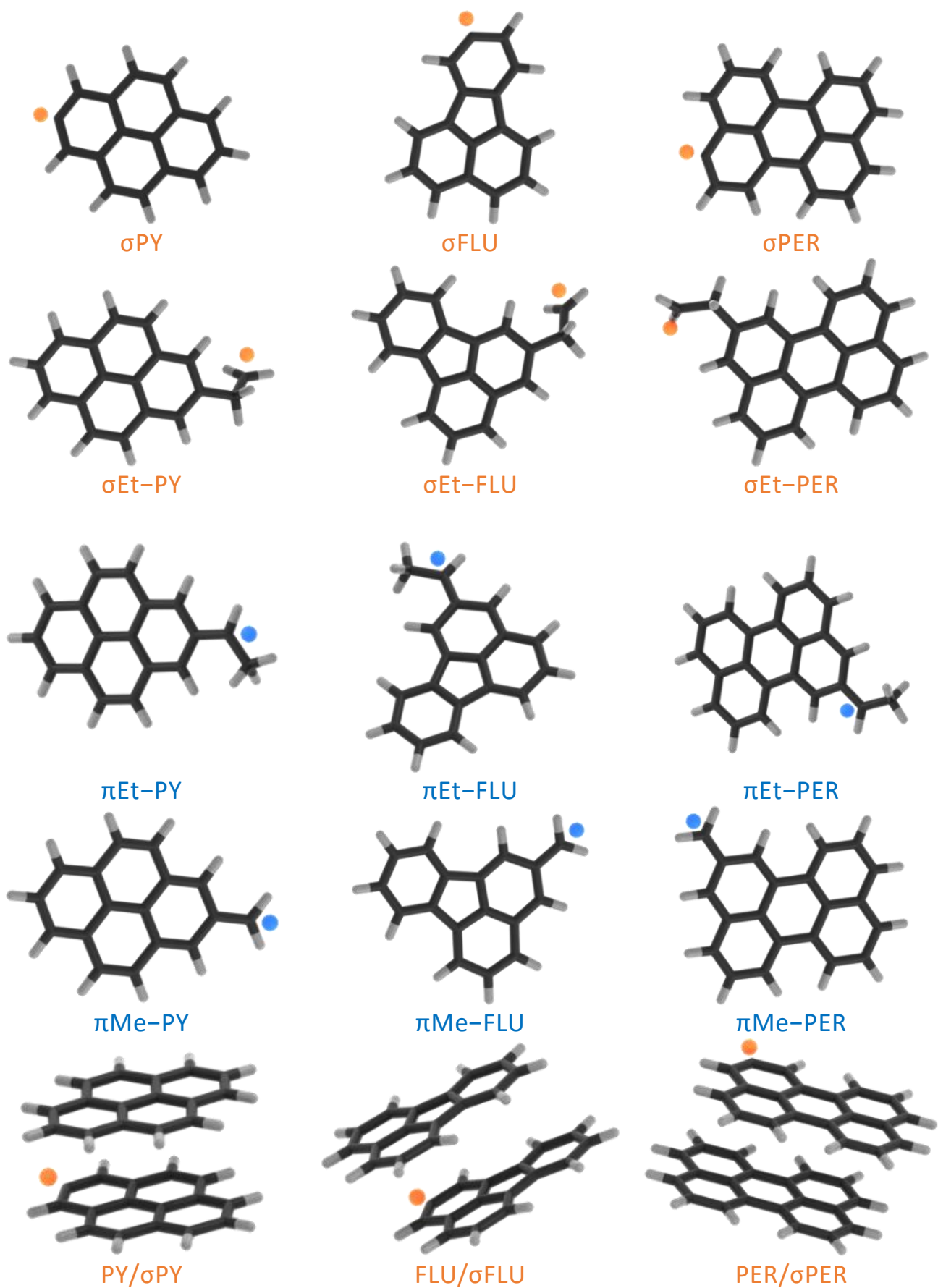
Appendix 6. Computed transitions for all 2'3HF complex geometries for Zn(II)

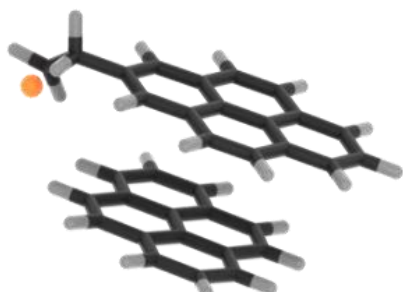


Appendix 7. Computed transitions for all 2'3HF complex geometries for Mn(II)

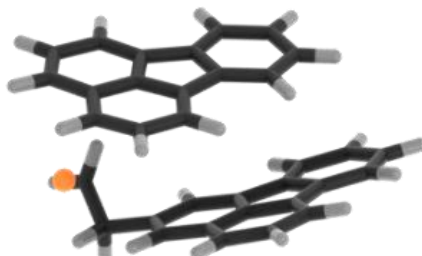


Appendix 8. The PAH-based radical structures studied in this work

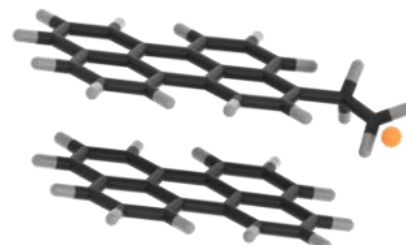




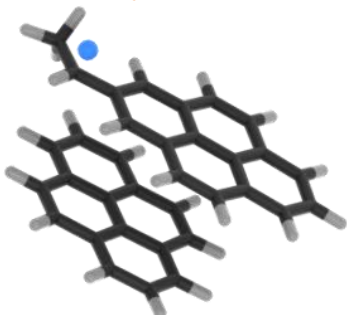
PY/σEt-PY



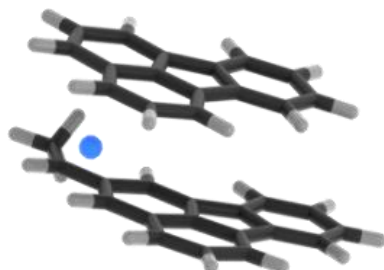
FLU/σEt-FLU



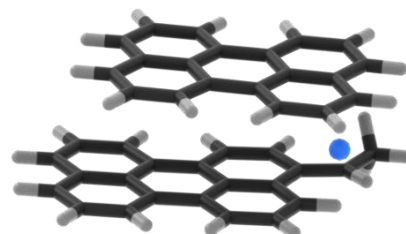
PER/σEt-PER



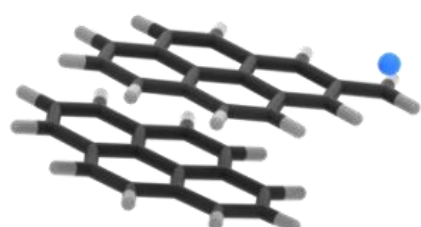
PY/πEt-PY



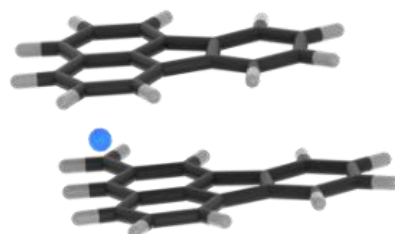
FLU/πEt-FLU



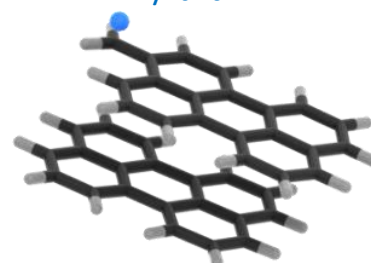
PER/πEt-PER



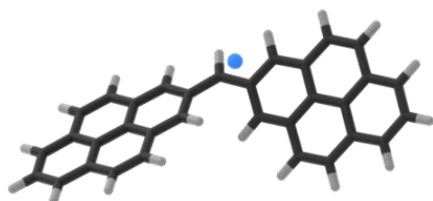
PY/πMe-PY



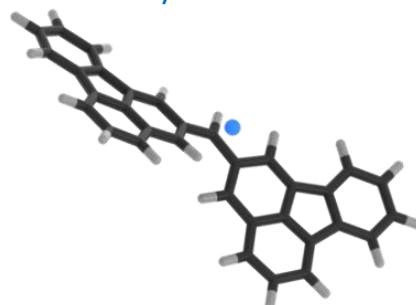
FLU/πMe-FLU



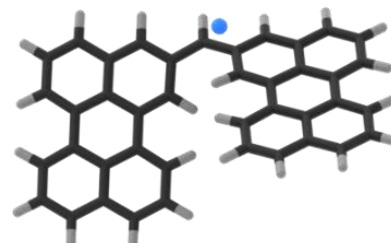
PER/πMe-PER



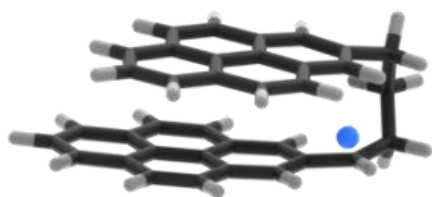
π1C-2PYPY2



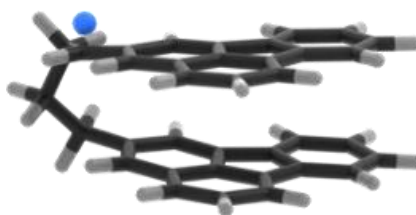
π1C-2FLUFLU2



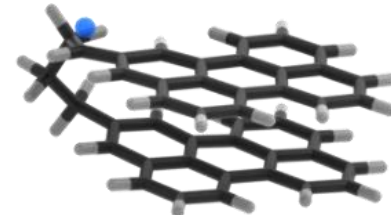
π1C-2PERPER2



π4C-2PYPY2

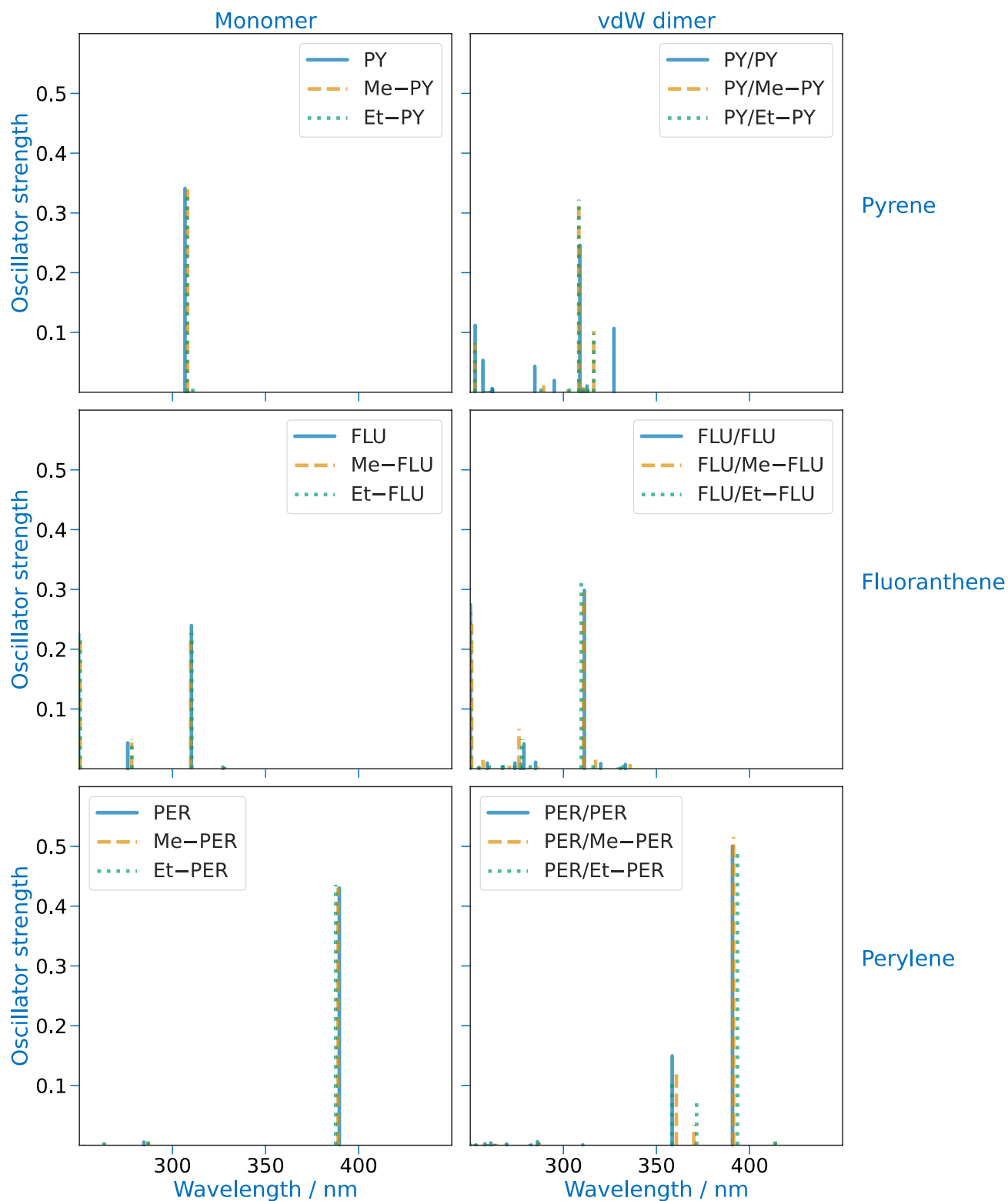


π4C-2FLUFLU2



π4C-2PERPER2

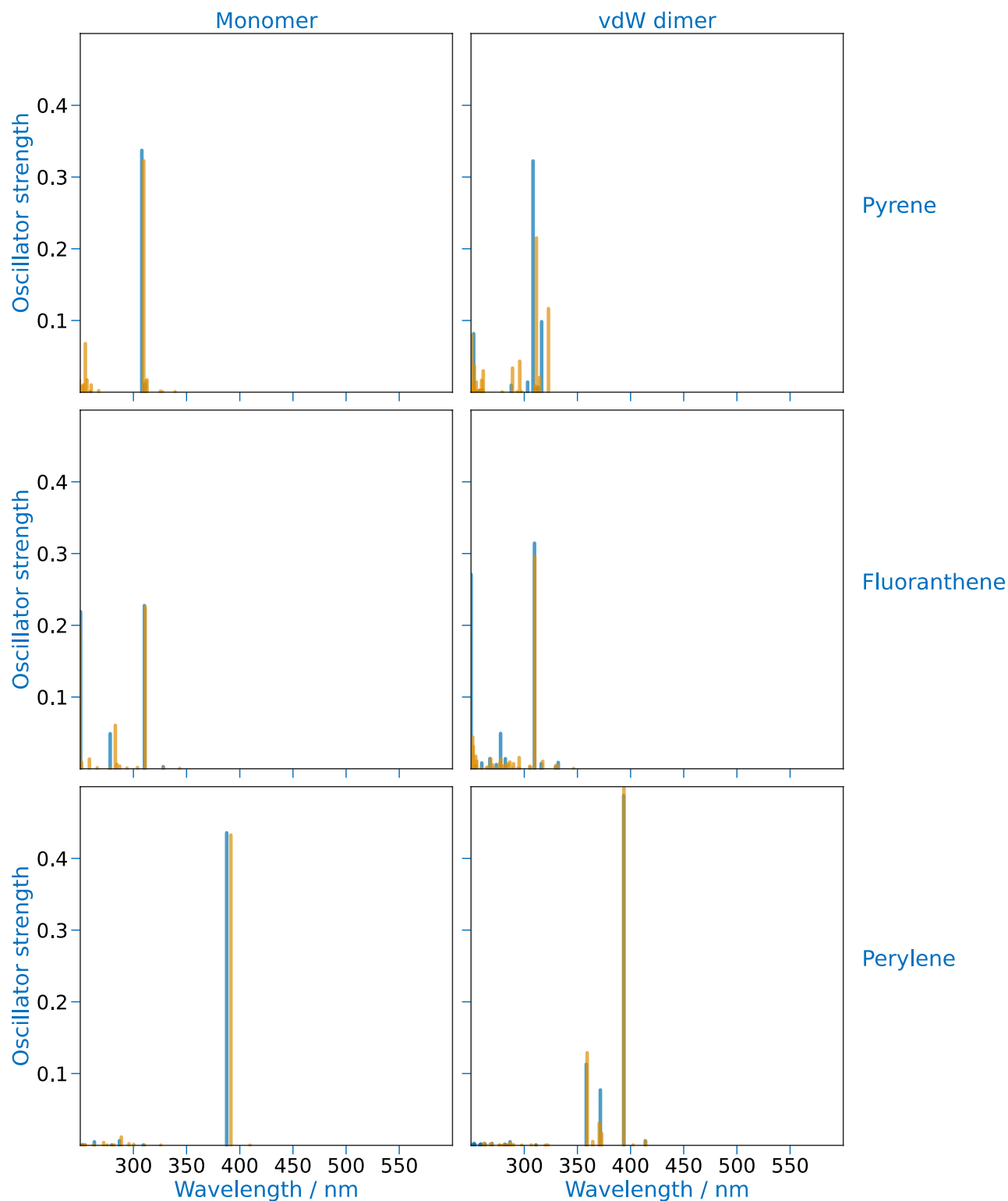
Appendix 9. Alkylation effect on the electronic transitions of PAH-based structure



Computed electronic transitions of monomer (left) and vdW dimer species (right) of pyrene, fluoranthene and perylene (blue) compared to those of the methylated and ethylated systems (orange and green, respectively):

M compared to **Alkyl-M** (left) and **M/M** compared to **M/Alkyl-M** (right)

Appendix 10. Effect on the electronic transitions of σ radicals in alkyl groups of PAH-based structures



Computed electronic transitions of the monomer (left) and vdW dimer (right) species of methylated and ethylated pyrene, fluoranthene and perylene (blue, regardless of the alkyl group) compared to the σ R species (orange):

Alkyl-M compared to **σ Alkyl-M** (left) and **X/Alkyl-M** compared to **M/ σ Alkyl-M** (right)

References

- [1] Thaviligadu, D. J.; Labarrière, L.; Moncomble, A.; Cornard, J.-P. Spectroscopic and Theoretical Study of the PH Effect on the Optical Properties of the Calcium–Morin System. *Spectrochimica Acta Part A: Molecular and Biomolecular Spectroscopy* **2020**, *225*, 117492. <https://doi.org/10.1016/j.saa.2019.117492>.
- [2] Aiken, G. R.; McKnight, D. M.; Wershaw, R. L.; MacCarthy, P. *Humic Substances in Soil, Sediment, and Water: Geochemistry, Isolation, and Characterization*; Krieger Publishing Company, 1991.
- [3] Lehmann, J.; Kleber, M. The Contentious Nature of Soil Organic Matter. *Nature* **2015**, *528* (7580), 60–68. <https://doi.org/10.1038/nature16069>.
- [4] de Melo, B. A. G.; Motta, F. L.; Santana, M. H. A. Humic Acids: Structural Properties and Multiple Functionalities for Novel Technological Developments. *Materials Science and Engineering: C* **2016**, *62*, 967–974. <https://doi.org/10.1016/j.msec.2015.12.001>.
- [5] Junek, R.; Morrow, R.; Schoenherr, J. I.; Schubert, R.; Kallmeyer, R.; Phull, S.; Klöcking, R. Bimodal Effect of Humic Acids on the LPS-Induced TNF- α Release from Differentiated U937 Cells. *Phytomedicine* **2009**, *16* (5), 470–476. <https://doi.org/10.1016/j.phymed.2008.10.003>.
- [6] Neyts, J.; Snoeck, R.; Wutzler, P.; Cushman, M.; Klöcking, R.; Helbig, B.; Wang, P.; De Clercq, E. Poly(Hydroxy)Carboxylates as Selective Inhibitors of Cytomegalovirus and Herpes Simplex Virus Replication. *Antivir Chem Chemother* **1992**, *3* (4), 215–222. <https://doi.org/10.1177/095632029200300404>.
- [7] Hassett, D. J.; Bisesi, M. S.; Hartenstein, R. Bactericidal Action of Humic Acids. *Soil Biology and Biochemistry* **1987**, *19* (1), 111–113. [https://doi.org/10.1016/0038-0717\(87\)90134-9](https://doi.org/10.1016/0038-0717(87)90134-9).
- [8] Raber, B.; Kögel-Knabner, I. Influence of Origin and Properties of Dissolved Organic Matter on the Partition of Polycyclic Aromatic Hydrocarbons (PAHs). *European Journal of Soil Science* **1997**, *48* (3), 443–455. <https://doi.org/10.1111/j.1365-2389.1997.tb00210.x>.
- [9] Stempvoort, D. R. V.; Lesage, S. Binding of Methylated Naphthalenes to Concentrated Aqueous Humic Acids. **2002**, *10*.
- [10] Lassen, P.; Carlsen, L. The Effect of Humic Acids on the Water Solubility and Water — Organic Carbon Partitioning of Fluorene and Its NSO-Heteroanalogues: Carbazole, Dibenzofuran, and Dibenzothiophene. *Chemosphere* **1999**, *38* (13), 2959–2968. [https://doi.org/10.1016/S0045-6535\(98\)00498-6](https://doi.org/10.1016/S0045-6535(98)00498-6).
- [11] Lassen, P.; Carlsen, L. Solubilization of Phenanthrene by Humic Acids. *Chemosphere* **1997**, *34* (4), 817–825. [https://doi.org/10.1016/S0045-6535\(97\)00010-6](https://doi.org/10.1016/S0045-6535(97)00010-6).
- [12] Tejada-Agredano, M.-C.; Mayer, P.; Ortega-Calvo, J.-J. The Effect of Humic Acids on Biodegradation of Polycyclic Aromatic Hydrocarbons Depends on the Exposure Regime. *Environmental Pollution* **2014**, *184*, 435–442. <https://doi.org/10.1016/j.envpol.2013.09.031>.
- [13] Stathi, P.; Deligiannakis, Y. Humic Acid-Inspired Hybrid Materials as Heavy Metal Absorbents. *Journal of Colloid and Interface Science* **2010**, *351* (1), 239–247. <https://doi.org/10.1016/j.jcis.2010.06.023>.

- [14] Yates, L. M.; Von Wandruszka, R. Decontamination of Polluted Water by Treatment with a Crude Humic Acid Blend. *Environ. Sci. Technol.* **1999**, *33* (12), 2076–2080. <https://doi.org/10.1021/es980408k>.
- [15] De la Rosa, J. M.; Santos, M.; Araújo, M. F. Metal Binding by Humic Acids in Recent Sediments from the SW Iberian Coastal Area. *Estuarine, Coastal and Shelf Science* **2011**, *93* (4), 478–485. <https://doi.org/10.1016/j.ecss.2011.05.029>.
- [16] Chen, Y.; Stevenson, F. J. Soil Organic Matter Interactions with Trace Elements. In *The Role of Organic Matter in Modern Agriculture*; Chen, Y., Avnimelech, Y., Eds.; Developments in Plant and Soil Sciences; Springer Netherlands: Dordrecht, 1986; pp 73–116. https://doi.org/10.1007/978-94-009-4426-8_5.
- [17] Li, A.-N.; Li, S.; Zhang, Y.-J.; Xu, X.-R.; Chen, Y.-M.; Li, H.-B. Resources and Biological Activities of Natural Polyphenols. *Nutrients* **2014**, *6* (12), 6020–6047. <https://doi.org/10.3390/nu6126020>.
- [18] Panche, A. N.; Diwan, A. D.; Chandra, S. R. Flavonoids: An Overview. *Journal of Nutritional Science* **2016**, *5*, e47. <https://doi.org/10.1017/jns.2016.41>.
- [19] Kasprzak, M. M.; Erxleben, A.; Ochocki, J. Properties and Applications of Flavonoid Metal Complexes. *RSC Adv.* **2015**, *5* (57), 45853–45877. <https://doi.org/10.1039/C5RA05069C>.
- [20] Uivarosi, V.; Munteanu, A. C.; Sharma, A.; Singh Tuli, H. Metal Complexation and Patent Studies of Flavonoid. In *Current Aspects of Flavonoids: Their Role in Cancer Treatment*; Singh Tuli, H., Ed.; Springer: Singapore, 2019; pp 39–89. https://doi.org/10.1007/978-981-13-5874-6_4.
- [21] Ramešová, Š.; Sokolová, R.; Tarábek, J.; Degano, I. The Oxidation of Luteolin, the Natural Flavonoid Dye. *Electrochimica Acta* **2013**, *110*, 646–654. <https://doi.org/10.1016/j.electacta.2013.06.136>.
- [22] Jäger, A. K.; Saaby, L. Flavonoids and the CNS. *Molecules* **2011**, *16* (2), 1471–1485. <https://doi.org/10.3390/molecules16021471>.
- [23] Haddad, A. Q.; Venkateswaran, V.; Viswanathan, L.; Teahan, S. J.; Fleshner, N. E.; Klotz, L. H. Novel Antiproliferative Flavonoids Induce Cell Cycle Arrest in Human Prostate Cancer Cell Lines. *Prostate Cancer Prostatic Dis* **2006**, *9* (1), 68–76. <https://doi.org/10.1038/sj.pcan.4500845>.
- [24] Salucci, M.; Stivala, L. A.; Maiani, G.; Bugianesi, R.; Vannini, V. Flavonoids Uptake and Their Effect on Cell Cycle of Human Colon Adenocarcinoma Cells (Caco2). *Br J Cancer* **2002**, *86* (10), 1645–1651. <https://doi.org/10.1038/sj.bjc.6600295>.
- [25] Kawabata, K.; Tanaka, T.; Honjo, S.; Kakumoto, M.; HARA, A.; Makita, H.; Tatematsu, N.; Ushida, J.; Tsuda, H.; Mori, H. Chemopreventive Effect of Dietary Flavonoid Morin on Chemically Induced Rat Tongue Carcinogenesis. *7*.
- [26] Cushnie, T. P. T.; Lamb, A. J. Antimicrobial Activity of Flavonoids. *International Journal of Antimicrobial Agents* **2005**, *26* (5), 343–356. <https://doi.org/10.1016/j.ijantimicag.2005.09.002>.
- [27] Young, J.; Park, Y.; Lee, Y. U.; Kim, H.; Shim, Y. H.; Ahn, J. H.; Lim, Y. Antimicrobial Effects of Flavone Analogues and Their Structure-Activity Relationships. *J Microbiol Biotechnol* **2007**, *17* (3), 530–533.
- [28] Liu, A.-L.; Wang, H.-D.; Lee, S. M.; Wang, Y.-T.; Du, G.-H. Structure–Activity Relationship of Flavonoids as Influenza Virus Neuraminidase Inhibitors and Their in Vitro Anti-Viral Activities. *Bioorganic & Medicinal Chemistry* **2008**, *16* (15), 7141–7147. <https://doi.org/10.1016/j.bmc.2008.06.049>.
- [29] Javed, H.; Khan, M. M.; Ahmad, A.; Vaibhav, K.; Ahmad, M. E.; Khan, A.; Ashafaq, M.; Islam, F.; Siddiqui, M. S.; Safhi, M. M.; Islam, F. Rutin Prevents Cognitive Impairments by Ameliorating Oxidative Stress and Neuroinflammation in Rat Model

- of Sporadic Dementia of Alzheimer Type. *Neuroscience* **2012**, *210*, 340–352.
<https://doi.org/10.1016/j.neuroscience.2012.02.046>.
- [30] Wu, T.-W.; Zeng, L. H.; Wu, J.; Fung, K. P. Morin Hydrate Is a Plant-Derived and Antioxidant-Based Hepatoprotector. *Life Sciences* **1993**, *53* (13), PL213–PL218.
[https://doi.org/10.1016/0024-3205\(93\)90266-6](https://doi.org/10.1016/0024-3205(93)90266-6).
- [31] Kumar, A.; Singh, A.; Ekavali. A Review on Alzheimer’s Disease Pathophysiology and Its Management: An Update. *Pharmacological Reports* **2015**, *67* (2), 195–203.
<https://doi.org/10.1016/j.pharep.2014.09.004>.
- [32] Panche, A.; Chandra, S.; Ad, D.; Harke, S. Alzheimer’s and Current Therapeutics: A Review. *Asian J Pharm Clin Res* **2015**, *8* (3), 14–19.
- [33] Sun, A. Y.; Simonyi, A.; Sun, G. Y. The “French Paradox” and beyond: Neuroprotective Effects of Polyphenols. *Free Radic. Biol. Med.* **2002**, *32* (4), 314–318. [https://doi.org/10.1016/s0891-5849\(01\)00803-6](https://doi.org/10.1016/s0891-5849(01)00803-6).
- [34] Corder, R.; Mullen, W.; Khan, N. Q.; Marks, S. C.; Wood, E. G.; Carrier, M. J.; Crozier, A. Red Wine Procyanidins and Vascular Health. *Nature* **2006**, *444* (7119), 566–566. <https://doi.org/10.1038/444566a>.
- [35] Renaud, S.; de Lorgeril, M. Wine, Alcohol, Platelets, and the French Paradox for Coronary Heart Disease. *The Lancet* **1992**, *339* (8808), 1523–1526.
[https://doi.org/10.1016/0140-6736\(92\)91277-F](https://doi.org/10.1016/0140-6736(92)91277-F).
- [36] Lippi, G.; Franchini, M.; Favalaro, E. J.; Targher, G. Moderate Red Wine Consumption and Cardiovascular Disease Risk: Beyond the “French Paradox.” *Semin Thromb Hemost* **2010**, *31* (1), 59–70. <https://doi.org/10.1055/s-0030-1248725>.
- [37] Jordan, B. R. Review: Molecular Response of Plant Cells to UV-B Stress. *Functional Plant Biol.* **2002**, *29* (8), 909–916. <https://doi.org/10.1071/fp02062>.
- [38] Barnes, P. W.; Flint, S. D.; Ryel, R. J.; Tobler, M. A.; Barkley, A. E.; Wargent, J. J. Rediscovering Leaf Optical Properties: New Insights into Plant Acclimation to Solar UV Radiation. *Plant Physiology and Biochemistry* **2015**, *93*, 94–100.
<https://doi.org/10.1016/j.plaphy.2014.11.015>.
- [39] Li, J.; Ou-Lee, T. M.; Raba, R.; Amundson, R. G.; Last, R. L. Arabidopsis Flavonoid Mutants Are Hypersensitive to UV-B Irradiation. *The Plant Cell* **1993**, *5* (2), 171–179.
<https://doi.org/10.1105/tpc.5.2.171>.
- [40] Olsson, L. C.; Veit, M.; Weissenböck, G.; Bornman, J. F. Differential Flavonoid Response to Enhanced Uv-b Radiation in Brassica Napus. *Phytochemistry* **1998**, *49* (4), 1021–1028. [https://doi.org/10.1016/S0031-9422\(98\)00062-4](https://doi.org/10.1016/S0031-9422(98)00062-4).
- [41] Ballaré, C. L.; Caldwell, M. M.; Flint, S. D.; Robinson, S. A.; Bornman, J. F. Effects of Solar Ultraviolet Radiation on Terrestrial Ecosystems. Patterns, Mechanisms, and Interactions with Climate Change. *Photochem. Photobiol. Sci.* **2011**, *10* (2), 226–241.
<https://doi.org/10.1039/C0PP90035D>.
- [42] Sengupta, P. K.; Kasha, M. Excited State Proton-Transfer Spectroscopy of 3-Hydroxyflavone and Quercetin. *Chemical Physics Letters* **1979**, *68* (2–3), 382–385.
[https://doi.org/10.1016/0009-2614\(79\)87221-8](https://doi.org/10.1016/0009-2614(79)87221-8).
- [43] Woolfe, G. J.; Thistlethwaite, P. J. Direct Observation of Excited State Intramolecular Proton Transfer Kinetics in 3-Hydroxyflavone. *J. Am. Chem. Soc.* **1981**, *103* (23), 6916–6923. <https://doi.org/10.1021/ja00413a026>.
- [44] Strandjord, A. J. G.; Barbara, P. F. The Proton-Transfer Kinetics of 3-Hydroxyflavone: Solvent Effects. *J. Phys. Chem.* **1985**, *89* (11), 2355–2361.
<https://doi.org/10.1021/j100257a041>.
- [45] Salaeh, R.; Prommin, C.; Chansen, W.; Kerdpol, K.; Daengngern, R.; Kungwan, N. The Effect of Protic Solvents on the Excited State Proton Transfer of 3-

- Hydroxyflavone: A TD-DFT Static and Molecular Dynamics Study. *Journal of Molecular Liquids* **2018**, *252*, 428–438. <https://doi.org/10.1016/j.molliq.2017.12.148>.
- [46] Arnaut, L. G.; Formosinho, S. J. Excited-State Proton Transfer Reactions I. Fundamentals and Intermolecular Reactions. *Journal of Photochemistry and Photobiology A: Chemistry* **1993**, *75* (1), 1–20. [https://doi.org/10.1016/1010-6030\(93\)80157-5](https://doi.org/10.1016/1010-6030(93)80157-5).
- [47] Formosinho, S. J.; Arnaut, L. G. Excited-State Proton Transfer Reactions II. Intramolecular Reactions. *Journal of Photochemistry and Photobiology A: Chemistry* **1993**, *75* (1), 21–48. [https://doi.org/10.1016/1010-6030\(93\)80158-6](https://doi.org/10.1016/1010-6030(93)80158-6).
- [48] Brucker, G. A.; Kelley, D. F. Proton Transfer in Matrix-Isolated 3-Hydroxyflavone and 3-Hydroxyflavone Complexes. *J. Phys. Chem.* **1987**, *91* (11), 2856–2861. <https://doi.org/10.1021/j100295a040>.
- [49] Tomin, V. I.; Ushakou, D. V. Use of 3-Hydroxyflavone as a Fluorescence Probe for the Controlled Photopolymerization of the E-Shell 300 Polymer. *Polymer Testing* **2017**, *64*, 77–82. <https://doi.org/10.1016/j.polymertesting.2017.09.036>.
- [50] Buffa, M.; Carturan, S.; Quaranta, A.; Maggioni, G.; Della Mea, G. Spectral Properties of 3-Hydroxyflavone Embedded in Polysiloxane: Effects of the Polymerization Method. *Optical Materials* **2012**, *34* (7), 1219–1224. <https://doi.org/10.1016/j.optmat.2012.01.038>.
- [51] Matei, I.; Ionescu, S.; Hillebrand, M. Interaction of Fisetin with Human Serum Albumin by Fluorescence, Circular Dichroism Spectroscopy and DFT Calculations: Binding Parameters and Conformational Changes. *Journal of Luminescence* **2011**, *131* (8), 1629–1635. <https://doi.org/10.1016/j.jlumin.2011.03.073>.
- [52] Park, J.-M.; Do, V. Q.; Seo, Y.-S.; Duong, M. T. H.; Ahn, H.-C.; Huh, H. J.; Lee, M.-Y. Application of Fisetin to the Quantitation of Serum Albumin. *Journal of Clinical Medicine* **2020**, *9* (2), 459. <https://doi.org/10.3390/jcm9020459>.
- [53] He, X.; Xiong, W.; LileiZhang; Xu, C.; Fan, J.; Qian, Y.; Wen, J.; Ding, F.; Shen, J. ES IPT-Based Ratiometric Fluorescent Probe for Highly Selective and Sensitive Sensing and Bioimaging of Group IIIA Ions in Living Cancer Cells and Zebrafish. *Dyes and Pigments* **2020**, *174*, 108059. <https://doi.org/10.1016/j.dyepig.2019.108059>.
- [54] Wu, Q.; Wang, K.; Wang, Z.; Sun, Y.; Cao, D.; Liu, Z.; Guan, R.; Zhao, S.; Yu, X. Two 3-Hydroxyflavone Derivatives as Two-Photon Fluorescence Turn-on Chemosensors for Cysteine and Homocysteine in Living Cells. *Talanta* **2018**, *181*, 118–124. <https://doi.org/10.1016/j.talanta.2017.12.062>.
- [55] Samsonowicz, M.; Regulska, E. Spectroscopic Study of Molecular Structure, Antioxidant Activity and Biological Effects of Metal Hydroxyflavonol Complexes. *Spectrochimica Acta Part A: Molecular and Biomolecular Spectroscopy* **2017**, *173*, 757–771. <https://doi.org/10.1016/j.saa.2016.10.031>.
- [56] Grazul, M.; Budzisz, E. Biological Activity of Metal Ions Complexes of Chromones, Coumarins and Flavones. *Coordination Chemistry Reviews* **2009**, *253* (21–22), 2588–2598. <https://doi.org/10.1016/j.ccr.2009.06.015>.
- [57] Boudet, A.-C.; Cornard, J.-P.; Merlin, J.-C. Conformational and Spectroscopic Investigation of 3-Hydroxyflavone–Aluminium Chelates. *Spectrochimica Acta Part A: Molecular and Biomolecular Spectroscopy* **2000**, *56* (4), 829–839. [https://doi.org/10.1016/S1386-1425\(99\)00284-X](https://doi.org/10.1016/S1386-1425(99)00284-X).
- [58] Cornard, J. P.; Merlin, J. C. Spectroscopic and Structural Study of Complexes of Quercetin with Al(III). *Journal of Inorganic Biochemistry* **2002**, *92* (1), 19–27. [https://doi.org/10.1016/S0162-0134\(02\)00469-5](https://doi.org/10.1016/S0162-0134(02)00469-5).
- [59] Moncomble, A.; Jani Thaviligadu, D.; Raoumbé Djendja, A.; Cornard, J.-P. The Crucial Role of the Inter-Ring Hydrogen Bond to Explain the Properties of Morin.

New Journal of Chemistry **2018**, 42 (10), 7691–7702.
<https://doi.org/10.1039/C7NJ04579D>.

- [60] Jani Thaviligadu, D. Réactivité de La Morine et Photophysique Des Hydrocarbures Aromatiques Polycycliques Par Chimie Quantique et Spectroscopie Électronique. These de doctorat, Université de Lille (2018-2021), 2020.
- [61] Grubel, K.; Rudzka, K.; Arif, A. M.; Klotz, K. L.; Halfen, J. A.; Berreau, L. M. Synthesis, Characterization, and Ligand Exchange Reactivity of a Series of First Row Divalent Metal 3-Hydroxyflavonolate Complexes. *Inorg. Chem.* **2010**, 49 (1), 82–96. <https://doi.org/10.1021/ic901405h>.
- [62] Ghosh, N.; Chakraborty, T.; Mallick, S.; Mana, S.; Singha, D.; Ghosh, B.; Roy, S. Synthesis, Characterization and Study of Antioxidant Activity of Quercetin–Magnesium Complex. *Spectrochimica Acta Part A: Molecular and Biomolecular Spectroscopy* **2015**, 151, 807–813. <https://doi.org/10.1016/j.saa.2015.07.050>.
- [63] Wei, Y.; Guo, M. Zinc-Binding Sites on Selected Flavonoids. *Biol Trace Elem Res* **2014**, 161 (2), 223–230. <https://doi.org/10.1007/s12011-014-0099-0>.
- [64] Primikyri, A.; Mazzone, G.; Lekka, C.; Tzakos, A. G.; Russo, N.; Gerotheranassis, I. P. Understanding Zinc(II) Chelation with Quercetin and Luteolin: A Combined NMR and Theoretical Study. *The Journal of Physical Chemistry B* **2015**, 119 (1), 83–95. <https://doi.org/10.1021/jp509752s>.
- [65] Cornard, J. P.; Merlin, J. C. Comparison of the Chelating Power of Hydroxyflavones. *Journal of Molecular Structure* **2003**, 651–653, 381–387. [https://doi.org/10.1016/S0022-2860\(02\)00655-5](https://doi.org/10.1016/S0022-2860(02)00655-5).
- [66] Boilet, L.; Cornard, J. P.; Lapouge, C. Determination of the Chelating Site Preferentially Involved in the Complex of Lead(II) with Caffeic Acid: A Spectroscopic and Structural Study. *J. Phys. Chem. A* **2005**, 109 (9), 1952–1960. <https://doi.org/10.1021/jp047703d>.
- [67] Porter, L. J.; Markham, K. R. The Aluminium(III) Complexes of Hydroxy-Flavones in Absolute Methanol. Part I. Ligands Containing Only One Chelating Site. *J. Chem. Soc. C* **1970**, No. 2, 344–349. <https://doi.org/10.1039/J39700000344>.
- [68] Le Person, A.; Moncomble, A.; Cornard, J.-P. The Complexation of Al^{III}, Pb^{II}, and Cu^{II} Metal Ions by Esculetin: A Spectroscopic and Theoretical Approach. *The Journal of Physical Chemistry A* **2014**, 118 (14), 2646–2655. <https://doi.org/10.1021/jp412291z>.
- [69] Lapouge, C.; Dangleterre, L.; Cornard, J.-P. Spectroscopic and Theoretical Studies of the Zn(II) Chelation with Hydroxyflavones. *The Journal of Physical Chemistry A* **2006**, 110 (45), 12494–12500. <https://doi.org/10.1021/jp064362q>.
- [70] Cornard, J. P.; Boudet, A. C.; Merlin, J. C. Complexes of Al(III) with 3'4'-Dihydroxy-Flavone: Characterization, Theoretical and Spectroscopic Study. *Spectrochimica Acta Part A: Molecular and Biomolecular Spectroscopy* **2001**, 57 (3), 591–602. [https://doi.org/10.1016/S1386-1425\(00\)00412-1](https://doi.org/10.1016/S1386-1425(00)00412-1).
- [71] World Health Organization; Agency, I. A. E.; Nations, F. and A. O. of the U. *Trace elements in human nutrition and health*; World Health Organization, 1996.
- [72] Mishra, V. Biosorption of Zinc Ion: A Deep Comprehension. *Appl Water Sci* **2014**, 4 (4), 311–332. <https://doi.org/10.1007/s13201-013-0150-x>.
- [73] Kumar, Y. P.; King, P.; Prasad, V. S. R. K. Zinc Biosorption on Tectona Grandis L.f. Leaves Biomass: Equilibrium and Kinetic Studies. *Chemical Engineering Journal* **2006**, 124 (1), 63–70. <https://doi.org/10.1016/j.cej.2006.07.010>.
- [74] Kresovich, J. K.; Erdal, S.; Chen, H. Y.; Gann, P. H.; Argos, M.; Rauscher, G. H. Metallic Air Pollutants and Breast Cancer Heterogeneity. *Environmental Research* **2019**, 177, 108639. <https://doi.org/10.1016/j.envres.2019.108639>.

- [75] Rutter, M. Raised Lead Levels and Impaired Cognitive/Behavioural Functioning: A Review of the Evidence. *Dev Med Child Neurol Suppl* **1980**, *42*, 1–26.
- [76] Needleman, H. L.; Gunnoe, C.; Leviton, A.; Reed, R.; Peresie, H.; Maher, C.; Barrett, P. Deficits in Psychologic and Classroom Performance of Children with Elevated Dentine Lead Levels. *New England Journal of Medicine* **1979**, *300* (13), 689–695. <https://doi.org/10.1056/NEJM197903293001301>.
- [77] Moon, C.; Marlowe, M.; Stellem, J.; Errera, J. Main and Interaction Effects of Metallic Pollutants on Cognitive Functioning. *J Learn Disabil* **1985**, *18* (4), 217–221. <https://doi.org/10.1177/002221948501800407>.
- [78] Wei, Z.; Gu, H.; Van Le, Q.; Peng, W.; Lam, S. S.; Yang, Y.; Li, C.; Sonne, C. Perspectives on Phytoremediation of Zinc Pollution in Air, Water and Soil. *Sustainable Chemistry and Pharmacy* **2021**, *24*, 100550. <https://doi.org/10.1016/j.scp.2021.100550>.
- [79] Avila, D. S.; Puntel, R. L.; Aschner, M. Manganese in Health and Disease. In *Interrelations between Essential Metal Ions and Human Diseases*; Sigel, A., Sigel, H., Sigel, R. K. O., Eds.; Metal Ions in Life Sciences; Springer Netherlands: Dordrecht, 2013; pp 199–227. https://doi.org/10.1007/978-94-007-7500-8_7.
- [80] Srivastava, J. *Environmental Contamination*; BoD – Books on Demand, 2012.
- [81] Gorell, J. M.; Johnson, C. C.; Rybicki, B. A.; Peterson, E. L.; Kortsha, G. X.; Brown, G. G.; Richardson, R. J. Occupational Exposures to Metals as Risk Factors for Parkinson’s Disease. *Neurology* **1997**, *48* (3), 650–658. <https://doi.org/10.1212/WNL.48.3.650>.
- [82] Barbeau, A. Manganese and Extrapyrmidal Disorders (a Critical Review and Tribute to Dr. George C. Cotzias). *Neurotoxicology* **1984**, *5* (1), 13–35.
- [83] Khanlarian, M.; Roshanfar, M.; Rashchi, F.; Motesharezadeh, B. Phyto-Extraction of Zinc, Lead, Nickel, and Cadmium from Zinc Leach Residue by a Halophyte: *Salicornia Europaea*. *Ecological Engineering* **2020**, *148*, 105797. <https://doi.org/10.1016/j.ecoleng.2020.105797>.
- [84] Chandra, R.; Yadav, S.; Bharagava, R. N.; Murthy, R. C. Bacterial Pretreatment Enhances Removal of Heavy Metals during Treatment of Post-Methanated Distillery Effluent by *Typha Angustata* L. *Journal of Environmental Management* **2008**, *88* (4), 1016–1024. <https://doi.org/10.1016/j.jenvman.2007.05.001>.
- [85] Sethurajan, M.; Huguenot, D.; Lens, P. N. L.; Horn, H. A.; Figueiredo, L. H. A.; van Hullebusch, E. D. Fractionation and Leachability of Heavy Metals from Aged and Recent Zn Metallurgical Leach Residues from the Três Marias Zinc Plant (Minas Gerais, Brazil). *Environ Sci Pollut Res* **2016**, *23* (8), 7504–7516. <https://doi.org/10.1007/s11356-015-6014-1>.
- [86] Haarstad, K.; Bavor, H. J.; Mæhlum, T. Organic and Metallic Pollutants in Water Treatment and Natural Wetlands: A Review. *Water Science and Technology* **2012**, *65* (1), 76–99. <https://doi.org/10.2166/wst.2011.831>.
- [87] Yue, X.; Ma, N. L.; Sonne, C.; Guan, R.; Lam, S. S.; Van Le, Q.; Chen, X.; Yang, Y.; Gu, H.; Rinklebe, J.; Peng, W. Mitigation of Indoor Air Pollution: A Review of Recent Advances in Adsorption Materials and Catalytic Oxidation. *Journal of Hazardous Materials* **2021**, *405*, 124138. <https://doi.org/10.1016/j.jhazmat.2020.124138>.
- [88] Klimek, B. Effect of Long-Term Zinc Pollution on Soil Microbial Community Resistance to Repeated Contamination. *Bull Environ Contam Toxicol* **2012**, *88* (4), 617–622. <https://doi.org/10.1007/s00128-012-0523-0>.
- [89] Padoan, E.; Romè, C.; Ajmone-Marsan, F. Bioaccessibility and Size Distribution of Metals in Road Dust and Roadside Soils along a Peri-Urban Transect. *Science of The*

- Total Environment* **2017**, 601–602, 89–98.
<https://doi.org/10.1016/j.scitotenv.2017.05.180>.
- [90] Le Gall, M.; Ayrault, S.; Evrard, O.; Laceby, J. P.; Gateuille, D.; Lefèvre, I.; Mouchel, J.-M.; Meybeck, M. Investigating the Metal Contamination of Sediment Transported by the 2016 Seine River Flood (Paris, France). *Environmental Pollution* **2018**, 240, 125–139. <https://doi.org/10.1016/j.envpol.2018.04.082>.
- [91] Iordache, A. M.; Nechita, C.; Voica, C.; Pluháček, T.; Schug, K. A. Climate Change Extreme and Seasonal Toxic Metal Occurrence in Romanian Freshwaters in the Last Two Decades—Case Study and Critical Review. *npj Clean Water* **2022**, 5 (1), 1–9. <https://doi.org/10.1038/s41545-021-00147-w>.
- [92] Forbes, R. M.; Cooper, A. R.; Mitchel, H. H. The Composition of the Adult Human Body as Determined by Chemical Analysis. 9.
- [93] Peacock, M. Calcium Metabolism in Health and Disease. *CJASN* **2010**, 5 (Supplement 1), S23–S30. <https://doi.org/10.2215/CJN.05910809>.
- [94] Bootman, M. D.; Collins, T. J.; Peppiatt, C. M.; Prothero, L. S.; MacKenzie, L.; De Smet, P.; Travers, M.; Tovey, S. C.; Seo, J. T.; Berridge, M. J.; Ciccolini, F.; Lipp, P. Calcium Signalling—an Overview. *Seminars in Cell & Developmental Biology* **2001**, 12 (1), 3–10. <https://doi.org/10.1006/scdb.2000.0211>.
- [95] Cali, T.; Ottolini, D.; Brini, M. Mitochondrial Ca²⁺ and Neurodegeneration. *Cell Calcium* **2012**, 52 (1), 73–85. <https://doi.org/10.1016/j.ceca.2012.04.015>.
- [96] Tsuneda, T. *Density Functional Theory in Quantum Chemistry*; Springer Japan: Tokyo, 2014. <https://doi.org/10.1007/978-4-431-54825-6>.
- [97] Jones, R. O.; Gunnarsson, O. The Density Functional Formalism, Its Applications and Prospects. *Rev. Mod. Phys.* **1989**, 61 (3), 689–746. <https://doi.org/10.1103/RevModPhys.61.689>.
- [98] Perdew, J. P. Accurate Density Functional for the Energy: Real-Space Cutoff of the Gradient Expansion for the Exchange Hole. *Phys. Rev. Lett.* **1985**, 55 (16), 1665–1668. <https://doi.org/10.1103/PhysRevLett.55.1665>.
- [99] Becke, A. D. Density-Functional Exchange-Energy Approximation with Correct Asymptotic Behavior. *Phys. Rev. A* **1988**, 38 (6), 3098–3100. <https://doi.org/10.1103/PhysRevA.38.3098>.
- [100] Lee, C.; Yang, W.; Parr, R. G. Development of the Colle-Salvetti Correlation-Energy Formula into a Functional of the Electron Density. *Phys. Rev. B* **1988**, 37 (2), 785–789. <https://doi.org/10.1103/PhysRevB.37.785>.
- [101] Perdew, J. P.; Burke, K.; Ernzerhof, M. Generalized Gradient Approximation Made Simple. *Phys. Rev. Lett.* **1996**, 77 (18), 3865–3868. <https://doi.org/10.1103/PhysRevLett.77.3865>.
- [102] Perdew, J. P.; Burke, K.; Ernzerhof, M. Generalized Gradient Approximation Made Simple [Phys. Rev. Lett. 77, 3865 (1996)]. *Phys. Rev. Lett.* **1997**, 78 (7), 1396–1396. <https://doi.org/10.1103/PhysRevLett.78.1396>.
- [103] Becke, A. D. A New Mixing of Hartree–Fock and Local Density-functional Theories. *J. Chem. Phys.* **1993**, 98 (2), 1372–1377. <https://doi.org/10.1063/1.464304>.
- [104] Becke, A. D. Density-functional Thermochemistry. IV. A New Dynamical Correlation Functional and Implications for Exact-exchange Mixing. *The Journal of Chemical Physics* **1998**, 104 (3), 1040. <https://doi.org/10.1063/1.470829>.
- [105] Cortona, P. Note: Theoretical Mixing Coefficients for Hybrid Functionals. *J. Chem. Phys.* **2012**, 136 (8), 086101. <https://doi.org/10.1063/1.3690462>.
- [106] Becke, A. D. Density-functional Thermochemistry. III. The Role of Exact Exchange. *J. Chem. Phys.* **1993**, 98 (7), 5648–5652. <https://doi.org/10.1063/1.464913>.

- [107] Adamo, C.; Barone, V. Toward Reliable Density Functional Methods without Adjustable Parameters: The PBE0 Model. *J. Chem. Phys.* **1999**, *110* (13), 6158–6170. <https://doi.org/10.1063/1.478522>.
- [108] Yanai, T.; Tew, D. P.; Handy, N. C. A New Hybrid Exchange–Correlation Functional Using the Coulomb-Attenuating Method (CAM-B3LYP). *Chemical Physics Letters* **2004**, *393* (1), 51–57. <https://doi.org/10.1016/j.cplett.2004.06.011>.
- [109] Iikura, H.; Tsuneda, T.; Yanai, T.; Hirao, K. A Long-Range Correction Scheme for Generalized-Gradient-Approximation Exchange Functionals. *The Journal of Chemical Physics* **2001**, *115* (8), 3540–3544. <https://doi.org/10.1063/1.1383587>.
- [110] Vydrov, O. A.; Scuseria, G. E. Assessment of a Long-Range Corrected Hybrid Functional. *J. Chem. Phys.* **2006**, *125* (23), 234109. <https://doi.org/10.1063/1.2409292>.
- [111] Vydrov, O. A.; Scuseria, G. E.; Perdew, J. P. Tests of Functionals for Systems with Fractional Electron Number. *J. Chem. Phys.* **2007**, *126* (15), 154109. <https://doi.org/10.1063/1.2723119>.
- [112] Grimme, S. Semiempirical Hybrid Density Functional with Perturbative Second-Order Correlation. *J. Chem. Phys.* **2006**, *124* (3), 034108. <https://doi.org/10.1063/1.2148954>.
- [113] Tomasi, J.; Mennucci, B.; Cammi, R. Quantum Mechanical Continuum Solvation Models. *Chem. Rev.* **2005**, *105* (8), 2999–3094. <https://doi.org/10.1021/cr9904009>.
- [114] van Duin, A. C. T.; Dasgupta, S.; Lorant, F.; Goddard, W. A. ReaxFF: A Reactive Force Field for Hydrocarbons. *J. Phys. Chem. A* **2001**, *105* (41), 9396–9409. <https://doi.org/10.1021/jp004368u>.
- [115] Iftimie, R.; Minary, P.; Tuckerman, M. E. *Ab Initio* Molecular Dynamics: Concepts, Recent Developments, and Future Trends. *Proceedings of the National Academy of Sciences* **2005**, *102* (19), 6654–6659. <https://doi.org/10.1073/pnas.0500193102>.
- [116] Maeder, M.; Zilian, A. Evolving Factor Analysis, a New Multivariate Technique in Chromatography. *Chemometrics and Intelligent Laboratory Systems* **1988**, *3* (3), 205–213. [https://doi.org/10.1016/0169-7439\(88\)80051-0](https://doi.org/10.1016/0169-7439(88)80051-0).
- [117] Frisch, M. J.; Trucks, G. W.; Schlegel, H. B.; Scuseria, G. E.; Robb, M. A.; Cheeseman, J. R.; Scalmani, G.; Barone, V.; Petersson, G. A.; Nakatsuji, H.; Li, X.; Caricato, M.; Marenich, A. V.; Bloino, J.; Janesko, B. G.; Gomperts, R.; Mennucci, B.; Hratchian, H. P.; Ortiz, J. V.; Izmaylov, A. F.; Sonnenberg, J. L.; Williams-Young, D.; Ding, F.; Lipparini, F.; Egidi, F.; Goings, J.; Peng, B.; Petrone, A.; Henderson, T.; Ranasinghe, D.; Zakrzewski, V. G.; Gao, J.; Rega, N.; Zheng, G.; Liang, W.; Hada, M.; Ehara, M.; Toyota, K.; Fukuda, R.; Hasegawa, J.; Ishida, M.; Nakajima, T.; Honda, Y.; Kitao, O.; Nakai, H.; Vreven, T.; Throssell, K.; Montgomery, J. A., Jr.; Peralta, J. E.; Ogliaro, F.; Bearpark, M. J.; Heyd, J. J.; Brothers, E. N.; Kudin, K. N.; Staroverov, V. N.; Keith, T. A.; Kobayashi, R.; Normand, J.; Raghavachari, K.; Rendell, A. P.; Burant, J. C.; Iyengar, S. S.; Tomasi, J.; Cossi, M.; Millam, J. M.; Klene, M.; Adamo, C.; Cammi, R.; Ochterski, J. W.; Martin, R. L.; Morokuma, K.; Farkas, O.; Foresman, J. B.; Fox, D. J. *Gaussian 16 Revision A.03*; 2016.
- [118] Krishnan, R.; Binkley, J. S.; Seeger, R.; Pople, J. A. Self-consistent Molecular Orbital Methods. XX. A Basis Set for Correlated Wave Functions. *J. Chem. Phys.* **1980**, *72* (1), 650–654. <https://doi.org/10.1063/1.438955>.
- [119] McLean, A. D.; Chandler, G. S. Contracted Gaussian Basis Sets for Molecular Calculations. I. Second Row Atoms, Z=11–18. *J. Chem. Phys.* **1980**, *72* (10), 5639–5648. <https://doi.org/10.1063/1.438980>.
- [120] Hariharan, P. C.; Pople, J. A. The Influence of Polarization Functions on Molecular Orbital Hydrogenation Energies. *Theoret. Chim. Acta* **1973**, *28* (3), 213–222. <https://doi.org/10.1007/BF00533485>.

- [121] Clark, T.; Chandrasekhar, J.; Spitznagel, G. W.; Schleyer, P. V. R. Efficient Diffuse Function-Augmented Basis Sets for Anion Calculations. III. The 3-21+G Basis Set for First-Row Elements, Li–F. *Journal of Computational Chemistry* **1983**, *4* (3), 294–301. <https://doi.org/10.1002/jcc.540040303>.
- [122] Li, X.; Frisch, M. J. Energy-Represented Direct Inversion in the Iterative Subspace within a Hybrid Geometry Optimization Method. *J. Chem. Theory Comput.* **2006**, *2* (3), 835–839. <https://doi.org/10.1021/ct050275a>.
- [123] Pulay, P.; Fogarasi, G.; Pang, F.; Boggs, J. E. Systematic Ab Initio Gradient Calculation of Molecular Geometries, Force Constants, and Dipole Moment Derivatives. *J. Am. Chem. Soc.* **1979**, *101* (10), 2550–2560. <https://doi.org/10.1021/ja00504a009>.
- [124] Peng, C.; Schlegel, H. B. Combining Synchronous Transit and Quasi-Newton Methods to Find Transition States. *Israel Journal of Chemistry* **1993**, *33* (4), 449–454. <https://doi.org/10.1002/ijch.199300051>.
- [125] Fukui, K. The Path of Chemical Reactions - the IRC Approach. *Acc. Chem. Res.* **1981**, *14* (12), 363–368. <https://doi.org/10.1021/ar00072a001>.
- [126] Foster, J. P.; Weinhold, F. Natural Hybrid Orbitals. *J. Am. Chem. Soc.* **1980**, *102* (24), 7211–7218. <https://doi.org/10.1021/ja00544a007>.
- [127] Reed, A. E.; Weinstock, R. B.; Weinhold, F. Natural Population Analysis. *J. Chem. Phys.* **1985**, *83* (2), 735–746. <https://doi.org/10.1063/1.449486>.
- [128] Wiberg, K. B. Application of the Pople-Santry-Segal CNDO Method to the Cyclopropylcarbinyl and Cyclobutyl Cation and to Bicyclobutane. *Tetrahedron* **1968**, *24* (3), 1083–1096. [https://doi.org/10.1016/0040-4020\(68\)88057-3](https://doi.org/10.1016/0040-4020(68)88057-3).
- [129] Case, D.; Betz, R.; Cerutti, D. S.; Cheatham, T.; Darden, T.; Duke, R.; Giese, T. J.; Gohlke, H.; Götz, A.; Homeyer, N.; Izadi, S.; Janowski, P.; Kaus, J.; Kovalenko, A.; Lee, T.-S.; LeGrand, S.; Li, P.; Lin, C.; Luchko, T.; Kollman, P. *Amber 16, University of California, San Francisco.*; 2016. <https://doi.org/10.13140/RG.2.2.27958.70729>.
- [130] Berendsen, H. J. C.; Postma, J. P. M.; van Gunsteren, W. F.; DiNola, A.; Haak, J. R. Molecular Dynamics with Coupling to an External Bath. *J. Chem. Phys.* **1984**, *81* (8), 3684–3690. <https://doi.org/10.1063/1.448118>.
- [131] VandeVondele, J.; Krack, M.; Mohamed, F.; Parrinello, M.; Chassaing, T.; Hutter, J. Quickstep: Fast and Accurate Density Functional Calculations Using a Mixed Gaussian and Plane Waves Approach. *Computer Physics Communications* **2005**, *167* (2), 103–128. <https://doi.org/10.1016/j.cpc.2004.12.014>.
- [132] Kühne, T. D.; Iannuzzi, M.; Del Ben, M.; Rybkin, V. V.; Seewald, P.; Stein, F.; Laino, T.; Khaliullin, R. Z.; Schütt, O.; Schiffmann, F.; Golze, D.; Wilhelm, J.; Chulkov, S.; Bani-Hashemian, M. H.; Weber, V.; Borštnik, U.; TAILLEFUMIER, M.; Jakobovits, A. S.; Lazzaro, A.; Pabst, H.; Müller, T.; Schade, R.; Guidon, M.; Andermatt, S.; Holmberg, N.; Schenter, G. K.; Hehn, A.; Bussy, A.; Belleflamme, F.; Tabacchi, G.; Glöß, A.; Lass, M.; Bethune, I.; Mundy, C. J.; Plessl, C.; Watkins, M.; VandeVondele, J.; Krack, M.; Hutter, J. CP2K: An Electronic Structure and Molecular Dynamics Software Package - Quickstep: Efficient and Accurate Electronic Structure Calculations. *J. Chem. Phys.* **2020**, *152* (19), 194103. <https://doi.org/10.1063/5.0007045>.
- [133] Lippert, B. G.; Parrinello, J. H. and M. A Hybrid Gaussian and Plane Wave Density Functional Scheme. *Molecular Physics* **1997**, *92* (3), 477–488. <https://doi.org/10.1080/002689797170220>.
- [134] Goedecker, S.; Teter, M.; Hutter, J. Separable Dual-Space Gaussian Pseudopotentials. *Phys. Rev. B* **1996**, *54* (3), 1703–1710. <https://doi.org/10.1103/PhysRevB.54.1703>.

- [135] Martyna, G. J.; Klein, M. L.; Tuckerman, M. Nosé–Hoover Chains: The Canonical Ensemble via Continuous Dynamics. *J. Chem. Phys.* **1992**, *97* (4), 2635–2643. <https://doi.org/10.1063/1.463940>.
- [136] Lin, I.-C.; Seitsonen, A. P.; Tavernelli, I.; Rothlisberger, U. Structure and Dynamics of Liquid Water from Ab Initio Molecular Dynamics—Comparison of BLYP, PBE, and RevPBE Density Functionals with and without van Der Waals Corrections. *J. Chem. Theory Comput.* **2012**, *8* (10), 3902–3910. <https://doi.org/10.1021/ct3001848>.
- [137] Bankura, A.; Karmakar, A.; Carnevale, V.; Chandra, A.; Klein, M. L. Structure, Dynamics, and Spectral Diffusion of Water from First-Principles Molecular Dynamics. *J. Phys. Chem. C* **2014**, *118* (50), 29401–29411. <https://doi.org/10.1021/jp506120t>.
- [138] Campetella, M.; Maschietto, F.; Frisch, M. J.; Scalmani, G.; Ciofini, I.; Adamo, C. Charge Transfer Excitations in TDDFT: A Ghost-Hunter Index. *Journal of Computational Chemistry* **2017**, *38* (25), 2151–2156. <https://doi.org/10.1002/jcc.24862>.
- [139] Bai, S.; Mansour, R.; Stojanović, L.; Toldo, J. M.; Barbatti, M. On the Origin of the Shift between Vertical Excitation and Band Maximum in Molecular Photoabsorption. *J Mol Model* **2020**, *26* (5), 107. <https://doi.org/10.1007/s00894-020-04355-y>.
- [140] Boumendil, S.; Cornard, J.-P.; Sekkal-Rahal, M.; Moncomble, A. Solvent Effects to Compute UV–Vis Spectra for Ionic Metal Complexes. *Chemical Physics Letters* **2015**, *636*, 39–45. <https://doi.org/10.1016/j.cplett.2015.07.019>.
- [141] Cornard, J. P.; Dangleterre, L.; Lapouge, C. DFT and TD-DFT Investigation and Spectroscopic Characterization of the Molecular and Electronic Structure of the Zn(II)–3-Hydroxyflavone Complex. *Chemical Physics Letters* **2006**, *419* (1–3), 304–308. <https://doi.org/10.1016/j.cplett.2005.11.101>.
- [142] Moncomble, A.; Cornard, J.-P. Elucidation of Complexation Multi-Equilibrium with Mg^{II} and a Multisite Ligand. A Combined Electronic Spectroscopies and DFT Investigation. *RSC Adv.* **2014**, *4* (55), 29050–29061. <https://doi.org/10.1039/C4RA05048G>.
- [143] Cornard, J.-P.; Lapouge, C.; Allet-Bodelot, C. Study of S₀ and S₁ States of Catechol and Catechol–Al(III) Systems in Aqueous Solution by TD-DFT Methods and Electronic Spectroscopies. *Chemical Physics Letters* **2010**, *489* (4–6), 164–168. <https://doi.org/10.1016/j.cplett.2010.02.064>.
- [144] Lapouge, C.; Cornard, J.-P. Theoretical Study of the Pb(II)–Catechol System in Dilute Aqueous Solution: Complex Structure and Metal Coordination Sphere Determination. *Journal of Molecular Structure* **2010**, *969* (1–3), 88–96. <https://doi.org/10.1016/j.molstruc.2010.01.047>.
- [145] Labarrière, L.; Moncomble, A.; Cornard, J.-P. pH Dependency of the Structural and Photophysical Properties of the Atypical 2',3'-Dihydroxyflavone. *RSC Adv.* **2020**, *10* (58), 35017–35030. <https://doi.org/10.1039/D0RA06833K>.
- [146] Hossain, M. K.; Choi, H. Y.; Hwang, J.-S.; Dayem, A. A.; Kim, J.-H.; Kim, Y. B.; Poo, H.; Cho, S.-G. Antiviral Activity of 3,4'-Dihydroxyflavone on Influenza A Virus. *J Microbiol.* **2014**, *52* (6), 521–526. <https://doi.org/10.1007/s12275-014-4212-z>.
- [147] Brinkworth, R. I.; Stoermer, M. J.; Fairlie, D. P. Flavones Are Inhibitors of HIV-1 Proteinase. *Biochemical and Biophysical Research Communications* **1992**, *188* (2), 631–637. [https://doi.org/10.1016/0006-291X\(92\)91103-W](https://doi.org/10.1016/0006-291X(92)91103-W).
- [148] Lee, E.-R.; Kang, G.-H.; Cho, S.-G. Effect of Flavonoids on Human Health: Old Subjects but New Challenges. *Recent patents on biotechnology* **2007**, *1*, 139–150. <https://doi.org/10.2174/187220807780809445>.

- [149] Hyun, J.; Woo, Y.; Hwang, D.; Jo, G.; Eom, S.; Lee, Y.; Park, J. C.; Lim, Y. Relationships between Structures of Hydroxyflavones and Their Antioxidative Effects. *Bioorganic & Medicinal Chemistry Letters* **2010**, *20* (18), 5510–5513. <https://doi.org/10.1016/j.bmcl.2010.07.068>.
- [150] Kim, K.; Abdal Dayem, A.; Gil, M.; Yang, G.-M.; Lee, S. B.; Kwon, O.-H.; Choi, S.; Kang, G.-H.; Lim, K. M.; Kim, D.; Cho, S.-G. 3,2'-Dihydroxyflavone Improves the Proliferation and Survival of Human Pluripotent Stem Cells and Their Differentiation into Hematopoietic Progenitor Cells. *Journal of Clinical Medicine* **2020**, *9* (3), 669. <https://doi.org/10.3390/jcm9030669>.
- [151] *3,2/-Dihydroxyflavone-Treated Pluripotent Stem Cells Show Enhanced Proliferation, Pluripotency Marker Expression, and Neuroprotective Properties - Dawoon Han, Han Jun Kim, Hye Yeon Choi, Bongwoo Kim, Gwangmo Yang, Jihae Han, Ahmed Abdal Dayem, Hye-Rim Lee, Jin Hoi Kim, Kyung-Mi Lee, Kyu-Shik Jeong, Sun Hee Do, Ssang-Goo Cho, 2015.* <https://journals-sagepub-com.ressources-electroniques.univ-lille.fr/doi/full/10.3727/096368914X683511> (accessed 2020-04-23).
- [152] Kim, K.; Gil, M.; Dayem, A. A.; Choi, S.; Kang, G.-H.; Yang, G.-M.; Cho, S.; Jeong, Y.; Kim, S. J.; Seok, J.; Kwak, H. J.; Kumar Saha, S.; Kim, A.; Cho, S.-G. Improved Isolation and Culture of Urine-Derived Stem Cells (USCs) and Enhanced Production of Immune Cells from the USC-Derived Induced Pluripotent Stem Cells. *Journal of Clinical Medicine* **2020**, *9* (3), 827. <https://doi.org/10.3390/jcm9030827>.
- [153] Molins, E.; Miravittles, C.; Wallet, J.-C.; Gaydou, E. M. 2',6'-Dihydroxyflavone and a New Polymorph of 2'-Hydroxyflavonol. *Acta Cryst C* **1996**, *52* (4), 925–929. <https://doi.org/10.1107/S0108270195013679>.
- [154] Kingston, D. G. I. Mass Spectrometry of Organic Compounds—VI: Electron-Impact Spectra of Flavonoid Compounds. *Tetrahedron* **1971**, *27* (13), 2691–2700. [https://doi.org/10.1016/S0040-4020\(01\)98059-7](https://doi.org/10.1016/S0040-4020(01)98059-7).
- [155] Markham, K. R.; McGhie, T. K. Separation of Flavones by Capillary Electrophoresis: The Influence of PKa on Electrophoretic Mobility. *Phytochemical Analysis* **1996**, *7* (6), 300–304. [https://doi.org/10.1002/\(SICI\)1099-1565\(199611\)7:6%3C300::AID-PCA319%3E3.0.CO;2-%23](https://doi.org/10.1002/(SICI)1099-1565(199611)7:6%3C300::AID-PCA319%3E3.0.CO;2-%23).
- [156] Burns, D. C.; Ellis, D. A.; March, R. E. A Predictive Tool for Assessing ¹³C NMR Chemical Shifts of Flavonoids. *Magnetic Resonance in Chemistry* **2007**, *45* (10), 835–845. <https://doi.org/10.1002/mrc.2054>.
- [157] Falantin, C.; Moncomble, A.; Le Person, A.; Cornard, J.-P. Chalcogen Substitution: Effect of Oxygen-by-Sulfur Exchange on Structural and Spectroscopic Properties of Flavonols. *Spectrochimica Acta Part A: Molecular and Biomolecular Spectroscopy* **2017**, *187*, 49–60. <https://doi.org/10.1016/j.saa.2017.06.022>.
- [158] Aparicio, S. A Systematic Computational Study on Flavonoids. *International Journal of Molecular Sciences* **2010**, *11* (5), 2017–2038. <https://doi.org/10.3390/ijms11052017>.
- [159] Arunan, E.; Desiraju, G. R.; Klein, R. A.; Sadlej, J.; Scheiner, S.; Alkorta, I.; Clary, D. C.; Crabtree, R. H.; Dannenberg, J. J.; Hobza, P.; Kjaergaard, H. G.; Legon, A. C.; Mennucci, B.; Nesbitt, D. J. Definition of the hydrogen bond (IUPAC Recommendations 2011). *Pure and Applied Chemistry* **2011**, *83* (8), 1637–1641. <https://doi.org/10.1351/PAC-REC-10-01-02>.
- [160] Höfener, S.; Kooijman, P. C.; Groen, J.; Ariese, F.; Visscher, L. Fluorescence Behavior of (Selected) Flavonols: A Combined Experimental and Computational Study. *Phys. Chem. Chem. Phys.* **2013**, *15* (30), 12572. <https://doi.org/10.1039/c3cp44267e>.
- [161] Wolfbeis, O. S.; Leiner, M.; Hochmuth, P.; Geiger, H. Absorption and Fluorescence Spectra, pKa Values, and Fluorescence Lifetimes of Monohydroxyflavones and

Monomethoxyflavones. *Berichte der Bunsengesellschaft für physikalische Chemie* **1984**, 88 (8), 759–767. <https://doi.org/10.1002/bbpc.19840880817>.

- [162] da Graça Campos, M.; Markham, K. R. *Structure Information from HPLC and On-Line Measured Absorption Spectra: Flavones, Flavonols and Phenolic Acids*; Imprensa da Universidade de Coimbra/Coimbra University Press, 2007.
- [163] Mabry, T. J.; Markham, K. R.; Thomas, M. B. *The Systematic Identification of Flavonoids*; Springer, 1970.
- [164] Hayashi, T.; Kawai, S.; Ohno, T. Fluorometric Study on the Metal Chelates of Flavone Derivatives. II. Correlation between Fluorescence Emission and the Carbonyl Stretching Frequency. *Chemical and Pharmaceutical Bulletin* **1971**, 19 (4), 792–795.
- [165] Mammone, J.; Sharma, S.; Nicol, M. Raman Spectra of Methanol and Ethanol at Pressures up to 100 Kbar. *The Journal of Physical Chemistry* **1980**, 84 (23), 3130–3134.
- [166] Strandjord, A. J. G.; Smith, D. E.; Barbara, P. F. Structural Effects on the Proton-Transfer Kinetics of 3-Hydroxyflavones. *J. Phys. Chem.* **1985**, 89 (11), 2362–2366. <https://doi.org/10.1021/j100257a042>.
- [167] Skilitsi, A. I.; Agathangelou, D.; Shulov, I.; Conyard, J.; Haacke, S.; Mély, Y.; Klymchenko, A.; Léonard, J. Ultrafast Photophysics of the Environment-Sensitive 4'-Methoxy-3-Hydroxyflavone Fluorescent Dye. *Phys. Chem. Chem. Phys.* **2018**, 20 (11), 7885–7895. <https://doi.org/10.1039/C7CP08584B>.
- [168] Wolfbeis, O. S.; Knierzinger, A.; Schipfer, R. PH-Dependent Fluorescence Spectroscopy XVII: First Excited Singlet State Dissociation Constants, Photoautomerism and Dual Fluorescence of Flavonol. *Journal of Photochemistry* **1983**, 21 (1), 67–79. [https://doi.org/10.1016/0047-2670\(83\)80009-4](https://doi.org/10.1016/0047-2670(83)80009-4).
- [169] McMorro, D.; Kasha, M. Intramolecular Excited-State Proton Transfer in 3-Hydroxyflavone. Hydrogen-Bonding Solvent Perturbations. *J. Phys. Chem.* **1984**, 88 (11), 2235–2243. <https://doi.org/10.1021/j150655a012>.
- [170] Frolov, Y. L.; Sapozhnikov, Y. M. SS Barev, NN Pogodaeva, NA Tyukavkina. *Izv. Akad. Nauk SSSR, Ser. Khim* **1974**, 10, 2364.
- [171] McMorro, D.; Kasha, M. Proton-Transfer Spectroscopy of 3-Hydroxychromones. Extreme Sensitivity to Hydrogen-Bonding Perturbations. *J. Am. Chem. Soc.* **1983**, 105 (15), 5133–5134. <https://doi.org/10.1021/ja00353a047>.
- [172] Dereka, B.; Letrun, R.; Svehkarev, D.; Rosspeintner, A.; Vauthey, E. Excited-State Dynamics of 3-Hydroxyflavone Anion in Alcohols. *J. Phys. Chem. B* **2015**, 119 (6), 2434–2443. <https://doi.org/10.1021/jp507311n>.
- [173] Protti, S.; Mezzetti, A.; Cornard, J.-P.; Lapouge, C.; Fagnoni, M. Hydrogen Bonding Properties of DMSO in Ground-State Formation and Optical Spectra of 3-Hydroxyflavone Anion. *Chemical Physics Letters* **2008**, 467 (1–3), 88–93. <https://doi.org/10.1016/j.cplett.2008.11.005>.
- [174] Lazzaroni, S.; Dondi, D.; Mezzetti, A.; Protti, S. Role of Solute-Solvent Hydrogen Bonds on the Ground State and the Excited State Proton Transfer in 3-Hydroxyflavone. A Systematic Spectrophotometric Study. *Photochem. Photobiol. Sci.* **2018**, 17 (7), 923–933. <https://doi.org/10.1039/C8PP00053K>.
- [175] Loco, D.; Protti, S.; Mennucci, B.; Mezzetti, A. Critical Assessment of Solvent Effects on Absorption and Fluorescence of 3HF in Acetonitrile in the QM/PCM Framework: A Synergic Computational and Experimental Study. *Journal of Molecular Structure* **2019**, 1182, 283–291. <https://doi.org/10.1016/j.molstruc.2018.12.085>.
- [176] Seitsonen, A. P.; Idrissi, A.; Protti, S.; Mezzetti, A. Solvent Effects on the Vibrational Spectrum of 3-Hydroxyflavone. *Journal of Molecular Liquids* **2019**, 275, 723–728. <https://doi.org/10.1016/j.molliq.2018.11.020>.

- [177] Loco, D.; Gelfand, N.; Jurinovich, S.; Protti, S.; Mezzetti, A.; Mennucci, B. Polarizable QM/Classical Approaches for the Modeling of Solvation Effects on UV–Vis and Fluorescence Spectra: An Integrated Strategy. *J. Phys. Chem. A* **2018**, *122* (1), 390–397. <https://doi.org/10.1021/acs.jpca.7b10463>.
- [178] Li, Y.; Siddique, F.; Aquino, A. J. A.; Lischka, H. Molecular Dynamics Simulation of the Excited-State Proton Transfer Mechanism in 3-Hydroxyflavone Using Explicit Hydration Models. *J. Phys. Chem. A* **2021**, *125* (26), 5765–5778. <https://doi.org/10.1021/acs.jpca.1c03687>.
- [179] Smortsova, Y.; Gaillard, J.; Miannay, F.-A.; Cornard, J.-P. A Picosecond Time-Resolved Spectroscopic Investigation of the Effect of PH on Morin Fluorescence. *ChemPhysChem* **2020**, *21* (24), 2680–2691. <https://doi.org/10.1002/cphc.202000608>.
- [180] Taft, R. W.; Kamlet, M. J. *The solvatochromic comparison method. 2. The .alpha.-scale of solvent hydrogen-bond donor (HBD) acidities*. ACS Publications. <https://pubs.acs.org/doi/pdf/10.1021/ja00426a036> (accessed 2022-06-25). <https://doi.org/10.1021/ja00426a036>.
- [181] Kamlet, M. J.; Taft, R. W. The Solvatochromic Comparison Method. I. The .Beta.-Scale of Solvent Hydrogen-Bond Acceptor (HBA) Basicities. *J. Am. Chem. Soc.* **1976**, *98* (2), 377–383. <https://doi.org/10.1021/ja00418a009>.
- [182] Kamlet, M. J.; Abboud, J. L.; Taft, R. W. The Solvatochromic Comparison Method. 6. The .Pi.* Scale of Solvent Polarities. *J. Am. Chem. Soc.* **1977**, *99* (18), 6027–6038. <https://doi.org/10.1021/ja00460a031>.
- [183] Marcus, Y. The Properties of Organic Liquids That Are Relevant to Their Use as Solvating Solvents. *Chem. Soc. Rev.* **1993**, *22* (6), 409–416. <https://doi.org/10.1039/CS9932200409>.
- [184] Mandal, P. K.; Samanta, A. Evidence of Ground-State Proton-Transfer Reaction of 3-Hydroxyflavone in Neutral Alcoholic Solvents. *J. Phys. Chem. A* **2003**, *107* (32), 6334–6339. <https://doi.org/10.1021/jp027613d>.
- [185] Sulpizi, M.; Sprik, M. Acidity Constants from DFT-Based Molecular Dynamics Simulations. *J. Phys.: Condens. Matter* **2010**, *22* (28), 284116. <https://doi.org/10.1088/0953-8984/22/28/284116>.
- [186] Houari, Y.; Jacquemin, D.; Laurent, A. D. TD-DFT Study of the PKa* for Coumarins. *Chemical Physics Letters* **2013**, *583*, 218–221. <https://doi.org/10.1016/j.cplett.2013.08.002>.
- [187] Arbelo-González, W.; Crespo-Otero, R.; Barbatti, M. Steady and Time-Resolved Photoelectron Spectra Based on Nuclear Ensembles. *J. Chem. Theory Comput.* **2016**, *12* (10), 5037–5049. <https://doi.org/10.1021/acs.jctc.6b00704>.
- [188] Hu, Z.; Sun, Z.; Sun, H. Simulation of Negative Ion Photoelectron Spectroscopy Using a Nuclear Ensemble Approach: Implications from a Nuclear Vibration Effect. *J. Phys. Chem. A* **2021**, *125* (30), 6621–6628. <https://doi.org/10.1021/acs.jpca.1c04246>.
- [189] Bryenton, K. R.; Adeleke, A. A.; Dale, S. G.; Johnson, E. R. Delocalization Error: The Greatest Outstanding Challenge in Density-Functional Theory. *WIREs Computational Molecular Science* *n/a* (n/a), e1631. <https://doi.org/10.1002/wcms.1631>.
- [190] Jacquemin, D.; Perpète, E. A.; Scuseria, G. E.; Ciofini, I.; Adamo, C. TD-DFT Performance for the Visible Absorption Spectra of Organic Dyes: Conventional versus Long-Range Hybrids. *J. Chem. Theory Comput.* **2008**, *4* (1), 123–135. <https://doi.org/10.1021/ct700187z>.
- [191] Jacquemin, D.; Wathélet, V.; Perpète, E. A.; Adamo, C. Extensive TD-DFT Benchmark: Singlet-Excited States of Organic Molecules. *J. Chem. Theory Comput.* **2009**, *5* (9), 2420–2435. <https://doi.org/10.1021/ct900298e>.

- [192] Ahmed, M. Spectrophotometric Determination of Aluminium by Morin. *Talanta* **1995**, *42* (8), 1135–1142. [https://doi.org/10.1016/0039-9140\(95\)01554-O](https://doi.org/10.1016/0039-9140(95)01554-O).
- [193] Qi, Z.; Liufang, W.; Xiang, L.; Shuben, L.; Fengying, H. Synthesis, Characterization and Antitumour Properties of Metal(II) Solid Complexes with Morin. *Transition Met Chem* **1996**, *21* (1), 23–27. <https://doi.org/10.1007/BF00166007>.
- [194] Payán-Gómez, S. A.; Flores-Holguín, N.; Pérez-Hernández, A.; Piñón-Miramontes, M.; Glossman-Mitnik, D. Computational Molecular Characterization of the Flavonoid Morin and Its Pt(II), Pd(II) and Zn(II) Complexes. *Journal of Molecular Modeling* **2011**, *17* (5), 979–985. <https://doi.org/10.1007/s00894-010-0789-2>.
- [195] Zhang, H.; Mei, P. Synthesis of Morin–Zinc(II) Complex and Its Interaction with Serum Albumin. *Biol Trace Elem Res* **2011**, *143* (2), 677–687. <https://doi.org/10.1007/s12011-010-8903-y>.
- [196] Jabeen, E.; Janjua, N. K.; Ahmed, S.; Murtaza, I.; Ali, T.; Masood, N.; Rizvi, A. S.; Murtaza, G. DFT Predictions, Synthesis, Stoichiometric Structures and Anti-Diabetic Activity of Cu (II) and Fe (III) Complexes of Quercetin, Morin, and Primuletin. *Journal of Molecular Structure* **2017**, *1150*, 459–468. <https://doi.org/10.1016/j.molstruc.2017.09.003>.
- [197] Jomova, K.; Lawson, M.; Drostinova, L.; Lauro, P.; Poprac, P.; Brezova, V.; Michalik, M.; Lukes, V.; Valko, M. Protective Role of Quercetin against Copper(II)-Induced Oxidative Stress: A Spectroscopic, Theoretical and DNA Damage Study. *Food and Chemical Toxicology* **2017**, *110*, 340–350. <https://doi.org/10.1016/j.fct.2017.10.042>.
- [198] Šimunková, M.; Valko, M.; Bučinský, L.; Malček, M. Structure Functionality Relationship of Flavonoids (Myricetin, Morin, Taxifolin and 3',4'-Dihydroxyflavone). A Computational Study via the Cupric Ion Probe. *Journal of Molecular Structure* **2020**, *1222*, 128923. <https://doi.org/10.1016/j.molstruc.2020.128923>.
- [199] Halevas, E.; Mavroidi, B.; Kaplanis, M.; Hatzidimitriou, A. G.; Moschona, A.; Litsardakis, G.; Pelecanou, M. Hydrophilic Bis-MPA Hyperbranched Dendritic Scaffolds as Nanocarriers of a Fully Characterized Flavonoid Morin-Zn(II) Complex for Anticancer Applications. *Journal of Inorganic Biochemistry* **2022**, *232*, 111832. <https://doi.org/10.1016/j.jinorgbio.2022.111832>.
- [200] Zeng, Q.; Jones, M. R.; Brooks, B. R. Absolute and Relative PKa Predictions via a DFT Approach Applied to the SAMPL6 Blind Challenge. *J Comput Aided Mol Des* **2018**, *32* (10), 1179–1189. <https://doi.org/10.1007/s10822-018-0150-x>.
- [201] Cornard, J.-P.; Lapouge, C. Absorption Spectra of Caffeic Acid, Caffeate and Their 1:1 Complex with Al(III): Density Functional Theory and Time-Dependent Density Functional Theory Investigations. *J. Phys. Chem. A* **2006**, *110* (22), 7159–7166. <https://doi.org/10.1021/jp060147y>.
- [202] Lapouge, C.; Cornard, J.-P. Reaction Pathways Involved in the Mechanism of Al(III) Chelation with Caffeic Acid: Catechol and Carboxylic Functions Competition. *ChemPhysChem* **2007**, *8* (3), 473–479. <https://doi.org/10.1002/cphc.200600620>.
- [203] Adams, M. L.; O'Sullivan, B.; Downard, A. J.; Powell, K. J. Stability Constants for Aluminum(III) Complexes with the 1,2-Dihydroxyaryl Ligands Caffeic Acid, Chlorogenic Acid, DHB, and DASA in Aqueous Solution. *J. Chem. Eng. Data* **2002**, *47* (2), 289–296. <https://doi.org/10.1021/je010279e>.
- [204] Cornard, J.-P.; Caudron, A.; Merlin, J.-C. UV–Visible and Synchronous Fluorescence Spectroscopic Investigations of the Complexation of Al(III) with Caffeic Acid, in Aqueous Low Acidic Medium. *Polyhedron* **2006**, *25* (11), 2215–2222. <https://doi.org/10.1016/j.poly.2006.01.013>.
- [205] Hem, J. D. *Chemical Equilibria and Rates of Manganese Oxidation*; U.S. Government Printing Office, 1963.

- [206] Morgan, J. J. Kinetics of Reaction between O₂ and Mn(II) Species in Aqueous Solutions. *Geochimica et Cosmochimica Acta* **2005**, *69* (1), 35–48. <https://doi.org/10.1016/j.gca.2004.06.013>.
- [207] Fifen, J. J.; Nsangou, M.; Dhaouadi, Z.; Motapon, O.; Jaidane, N.-E. Solvation Energies of the Proton in Methanol. *J. Chem. Theory Comput.* **2013**, *9* (2), 1173–1181. <https://doi.org/10.1021/ct300669v>.
- [208] Kotal, M. R.; De, S.; Das, S.; Sen, S. Characterization of Laminar Flame Using High Speed Camera and Spectrometer. *Sādhanā* **2020**, *45* (1), 230. <https://doi.org/10.1007/s12046-020-01465-4>.
- [209] Naik, V.; Szopa, S.; Adhikary, B.; Artaxo Netto, P. E.; Berntsen, T.; Collins, W. D.; Fuzzi, S.; Gallardo, L.; Kiendler-Scharr, A.; Klimont, Z.; Liao, H.; Unger, N.; Zanis, P. Short-Lived Climate Forcers. In *Climate Change 2021: The Physical Science Basis. Contribution of Working Group I to the Sixth Assessment Report of the Intergovernmental Panel on Climate Change*; Masson-Delmotte, V., Zhai, P., Pirani, A., Connors, S. L., Péan, C., Berger, S., Caud, N., Chen, Y., Goldfarb, L., Gomis, M. I., Huang, M., Leitzell, K., Lonnoy, E., Matthews, J. B. R., Maycock, T. K., Waterfield, T., Yelekçi, Ö., Yu, R., Zhou, B., Eds.; Cambridge University Press, 2021.
- [210] Bowerman, N. H. A.; Frame, D. J.; Huntingford, C.; Lowe, J. A.; Smith, S. M.; Allen, M. R. The Role of Short-Lived Climate Pollutants in Meeting Temperature Goals. *Nature Clim Change* **2013**, *3* (12), 1021–1024. <https://doi.org/10.1038/nclimate2034>.
- [211] Bond, T. C.; Doherty, S. J.; Fahey, D. W.; Forster, P. M.; Berntsen, T.; DeAngelo, B. J.; Flanner, M. G.; Ghan, S.; Kärcher, B.; Koch, D.; Kinne, S.; Kondo, Y.; Quinn, P. K.; Sarofim, M. C.; Schultz, M. G.; Schulz, M.; Venkataraman, C.; Zhang, H.; Zhang, S.; Bellouin, N.; Guttikunda, S. K.; Hopke, P. K.; Jacobson, M. Z.; Kaiser, J. W.; Klimont, Z.; Lohmann, U.; Schwarz, J. P.; Shindell, D.; Storelvmo, T.; Warren, S. G.; Zender, C. S. Bounding the Role of Black Carbon in the Climate System: A Scientific Assessment. *Journal of Geophysical Research: Atmospheres* **2013**, *118* (11), 5380–5552. <https://doi.org/10.1002/jgrd.50171>.
- [212] Weber, J.; Shin, Y. M.; Staunton Sykes, J.; Archer-Nicholls, S.; Abraham, N. L.; Archibald, A. T. Minimal Climate Impacts From Short-Lived Climate Forcers Following Emission Reductions Related to the COVID-19 Pandemic. *Geophysical Research Letters* **2020**, *47* (20), e2020GL090326. <https://doi.org/10.1029/2020GL090326>.
- [213] Smith, S. J.; Chateau, J.; Dorheim, K.; Drouet, L.; Durand-Lasserve, O.; Fricko, O.; Fujimori, S.; Hanaoka, T.; Harmsen, M.; Hilaire, J.; Keramidas, K.; Klimont, Z.; Luderer, G.; Moura, M. C. P.; Riahi, K.; Rogelj, J.; Sano, F.; van Vuuren, D. P.; Wada, K. Impact of Methane and Black Carbon Mitigation on Forcing and Temperature: A Multi-Model Scenario Analysis. *Climatic Change* **2020**, *163* (3), 1427–1442. <https://doi.org/10.1007/s10584-020-02794-3>.
- [214] Polar Regions. In *The Ocean and Cryosphere in a Changing Climate: Special Report of the Intergovernmental Panel on Climate Change*; Intergovernmental Panel on Climate Change (IPCC), Ed.; Cambridge University Press: Cambridge, 2022; pp 203–320. <https://doi.org/10.1017/9781009157964.005>.
- [215] Microstructure of Diesel Soot Particles Probed by Electron Microscopy: First Observation of Inner Core and Outer Shell. *Combustion and Flame* **1997**, *108* (1–2), 231–234. [https://doi.org/10.1016/S0010-2180\(96\)00206-4](https://doi.org/10.1016/S0010-2180(96)00206-4).
- [216] Frenklach, M. Reaction Mechanism of Soot Formation in Flames. *Physical Chemistry Chemical Physics* **2002**, *4* (11), 2028–2037. <https://doi.org/10.1039/B110045A>.
- [217] Wang, H. Formation of Nascent Soot and Other Condensed-Phase Materials in Flames. *Proceedings of the Combustion Institute* **2011**, *33* (1), 41–67. <https://doi.org/10.1016/j.proci.2010.09.009>.

- [218] Frenklach, M.; Semnikhin, A. S.; Mebel, A. M. On the Mechanism of Soot Nucleation. III. The Fate and Facility of the E-Bridge. *J. Phys. Chem. A* **2021**, *125* (31), 6789–6795. <https://doi.org/10.1021/acs.jpca.1c04936>.
- [219] Gleason, K.; Carbone, F.; Gomez, A. PAHs Controlling Soot Nucleation in 0.101–0.811MPa Ethylene Counterflow Diffusion Flames. *Combustion and Flame* **2021**, *227*, 384–395. <https://doi.org/10.1016/j.combustflame.2021.01.015>.
- [220] Gentile, F. S.; Picca, F.; De Falco, G.; Commodo, M.; Minutolo, P.; Causà, M.; D’Anna, A. Soot Inception: A DFT Study of σ and π Dimerization of Resonantly Stabilized Aromatic Radicals. *Fuel* **2020**, *279*, 118491. <https://doi.org/10.1016/j.fuel.2020.118491>.
- [221] Yuan, H.; Kong, W.; Liu, F.; Chen, D. Study on Soot Nucleation and Growth from PAHs and Some Reactive Species at Flame Temperatures by ReaxFF Molecular Dynamics. *Chemical Engineering Science* **2019**, *195*, 748–757. <https://doi.org/10.1016/j.ces.2018.10.020>.
- [222] Richter, H.; Howard, J. B. Formation of Polycyclic Aromatic Hydrocarbons and Their Growth to Soot—a Review of Chemical Reaction Pathways. *Progress in Energy and Combustion Science* **2000**, *26* (4), 565–608. [https://doi.org/10.1016/S0360-1285\(00\)00009-5](https://doi.org/10.1016/S0360-1285(00)00009-5).
- [223] Frenklach, M.; Mebel, A. M. On the Mechanism of Soot Nucleation. *Phys. Chem. Chem. Phys.* **2020**, *22* (9), 5314–5331. <https://doi.org/10.1039/D0CP00116C>.
- [224] Sabbah, H.; Biennier, L.; Klippenstein, S. J.; Sims, I. R.; Rowe, B. R. Exploring the Role of PAHs in the Formation of Soot: Pyrene Dimerization. *J. Phys. Chem. Lett.* **2010**, *1* (19), 2962–2967. <https://doi.org/10.1021/jz101033t>.
- [225] Herdman, J. D.; Miller, J. H. Intermolecular Potential Calculations for Polynuclear Aromatic Hydrocarbon Clusters. *J. Phys. Chem. A* **2008**, *112* (28), 6249–6256. <https://doi.org/10.1021/jp800483h>.
- [226] Martin, J. W.; Salamanca, M.; Kraft, M. Soot Inception: Carbonaceous Nanoparticle Formation in Flames. *Progress in Energy and Combustion Science* **2022**, *88*, 100956. <https://doi.org/10.1016/j.pecs.2021.100956>.
- [227] Howard, J. B.; Kausch, W. J. Soot Control by Fuel Additives. *Progress in Energy and Combustion Science* **1980**, *6* (3), 263–276. [https://doi.org/10.1016/0360-1285\(80\)90018-0](https://doi.org/10.1016/0360-1285(80)90018-0).
- [228] Linded, L. H.; Heywood, J. B. Smoke Emission from Jet Engines. *Combustion Science and Technology* **1971**, *2* (5–6), 401–411. <https://doi.org/10.1080/00102207108952264>.
- [229] Gehmlich, R. K.; Mueller, C. J.; Ruth, D. J.; Nilsen, C. W.; Skeen, S. A.; Manin, J. Using Ducted Fuel Injection to Attenuate or Prevent Soot Formation in Mixing-Controlled Combustion Strategies for Engine Applications. *Applied Energy* **2018**, *226*, 1169–1186. <https://doi.org/10.1016/j.apenergy.2018.05.078>.
- [230] Prasad, R.; Bella, V. R. A Review on Diesel Soot Emission, Its Effect and Control. *Bulletin of Chemical Reaction Engineering & Catalysis* **2011**, *5* (2), 69–86. <https://doi.org/10.9767/bcrec.5.2.794.69-86>.
- [231] Mitchell, J. B. A.; Miller, D. J. M.; Sharpe, M. The Use of Additives in the Control and Elucidation of Soot Formation. *Combustion Science and Technology* **1990**, *74* (1–6), 63–66. <https://doi.org/10.1080/00102209008951680>.
- [232] Yee, K. F.; Mohamed, A. R.; Tan, S. H. A Review on the Evolution of Ethyl Tert-Butyl Ether (ETBE) and Its Future Prospects. *Renewable and Sustainable Energy Reviews* **2013**, *22*, 604–620. <https://doi.org/10.1016/j.rser.2013.02.016>.
- [233] Parekh, P. P.; Khwaja, H. A.; Khan, A. R.; Malik, A.; Khan, K.; Hussain, G. Lead Content of Petrol and Diesel and Its Assessment in an Urban Environment. *8*.

- [234] Wu, J.; Song, K. H.; Litzinger, T.; Lee, S.-Y.; Santoro, R.; Linevsky, M.; Colket, M.; Liscinsky, D. Reduction of PAH and Soot in Premixed Ethylene–Air Flames by Addition of Ethanol. *Combustion and Flame* **2006**, *144* (4), 675–687. <https://doi.org/10.1016/j.combustflame.2005.08.036>.
- [235] Ni, T.; Gupta, S. B.; Santoro, R. J. Suppression of Soot Formation in Ethene Laminar Diffusion Flames by Chemical Additives. *Symposium (International) on Combustion* **1994**, *25* (1), 585–592. [https://doi.org/10.1016/S0082-0784\(06\)80689-2](https://doi.org/10.1016/S0082-0784(06)80689-2).
- [236] Lai, J. Y. W.; Elvati, P.; Violi, A. Stochastic Atomistic Simulation of Polycyclic Aromatic Hydrocarbon Growth in Combustion. *Phys. Chem. Chem. Phys.* **2014**, *16* (17), 7969–7979. <https://doi.org/10.1039/C4CP00112E>.
- [237] Yang, X. J.; Glaser, R.; Li, A.; Zhong, J. X. The Carriers of the Unidentified Infrared Emission Features: Clues from Polycyclic Aromatic Hydrocarbons with Aliphatic Sidegroups. *New Astronomy Reviews* **2017**, *77*, 1–22. <https://doi.org/10.1016/j.newar.2017.01.001>.
- [238] Balaban, A. T.; Harary, F. Chemical Graphs—V: Enumeration and Proposed Nomenclature of Benzenoid Cata-Condensed Polycyclic Aromatic Hydrocarbons. *Tetrahedron* **1968**, *24* (6), 2505–2516. [https://doi.org/10.1016/S0040-4020\(01\)82523-0](https://doi.org/10.1016/S0040-4020(01)82523-0).
- [239] Stein, S. E.; Fahr, A. High-Temperature Stabilities of Hydrocarbons. *J. Phys. Chem.* **1985**, *89* (17), 3714–3725. <https://doi.org/10.1021/j100263a027>.
- [240] Platt, J. R. Classification of Spectra of Cata-Condensed Hydrocarbons. *J. Chem. Phys.* **1949**, *17* (5), 484–495. <https://doi.org/10.1063/1.1747293>.
- [241] Geldof, P. A.; Rettschnick, R. P. H.; Hoytink, G. J. Fluorescence from the Second Excited Singlets of Pyrene and 3,4-Benzopyrene. *Chemical Physics Letters* **1969**, *4* (2), 59–61. [https://doi.org/10.1016/0009-2614\(69\)85066-9](https://doi.org/10.1016/0009-2614(69)85066-9).
- [242] Deinum, T.; Werkhoven, C. J.; Langelaar, J.; Rettschnick, R. P. H.; van Voorst, J. D. W. Intermediate Strong Coupling and Vibrational Redistribution Effects in the S₂ Emission of Pyrene. *Chemical Physics Letters* **1971**, *12* (1), 189–192. [https://doi.org/10.1016/0009-2614\(71\)80647-4](https://doi.org/10.1016/0009-2614(71)80647-4).
- [243] Baba, H.; Aoi, M. Vapor-Phase Fluorescence Spectra from the Second Excited Singlet State of Pyrene and Its Derivatives. *Journal of Molecular Spectroscopy* **1973**, *46* (2), 214–222. [https://doi.org/10.1016/0022-2852\(73\)90037-4](https://doi.org/10.1016/0022-2852(73)90037-4).
- [244] Prlj, A.; Sandoval-Salinas, M. E.; Casanova, D.; Jacquemin, D.; Corminboeuf, C. Low-Lying $\Pi\pi^*$ States of Heteroaromatic Molecules: A Challenge for Excited State Methods. *J. Chem. Theory Comput.* **2016**, *12* (6), 2652–2660. <https://doi.org/10.1021/acs.jctc.6b00245>.
- [245] Liu, P.; He, Z.; Hou, G.-L.; Guan, B.; Lin, H.; Huang, Z. The Diagnostics of Laser-Induced Fluorescence (LIF) Spectra of PAHs in Flame with TD-DFT: Special Focus on Five-Membered Ring. *J. Phys. Chem. A* **2015**, *119* (52), 13009–13017. <https://doi.org/10.1021/acs.jpca.5b10114>.
- [246] Wang, Y.-L.; Wu, G.-S. Improving the TDDFT Calculation of Low-Lying Excited States for Polycyclic Aromatic Hydrocarbons Using the Tamm–Dancoff Approximation. *International Journal of Quantum Chemistry* **2008**, *108* (3), 430–439. <https://doi.org/10.1002/qua.21510>.
- [247] Barone, V.; Bloino, J.; Biczysko, M.; Santoro, F. Fully Integrated Approach to Compute Vibrationally Resolved Optical Spectra: From Small Molecules to Macrosystems. *J. Chem. Theory Comput.* **2009**, *5* (3), 540–554. <https://doi.org/10.1021/ct8004744>.

- [248] Baiardi, A.; Bloino, J.; Barone, V. A General Time Dependent Approach to Vibronic Spectroscopy Including Franck-Condon, Herzberg-Teller and Dushinsky Effects. *J Chem Theory Comput* **2013**, *9* (9), 4097–4115. <https://doi.org/10.1021/ct400450k>.
- [249] Berlman, I. *Handbook of Florescence Spectra of Aromatic Molecules*; Elsevier, 2012.
- [250] Durocher, G.; Sandorfy, C. On the General Occurrence of the Ham Effect in the Electronic Spectra of Aromatic Hydrocarbons. *Journal of Molecular Spectroscopy* **1966**, *20* (4), 410–424. [https://doi.org/10.1016/0022-2852\(66\)90012-9](https://doi.org/10.1016/0022-2852(66)90012-9).
- [251] Nakajima, A. Solvent Effect on the Vibrational Structures of the Fluorescence and Absorption Spectra of Pyrene. *BCSJ* **1971**, *44* (12), 3272–3277. <https://doi.org/10.1246/bcsj.44.3272>.
- [252] Freidzon, A. Y.; Valiev, R. R.; Berezhnoy, A. A. Ab Initio Simulation of Pyrene Spectra in Water Matrices. *RSC Adv.* **2014**, *4* (79), 42054–42065. <https://doi.org/10.1039/C4RA05574H>.
- [253] Ein Konzentrationsumschlag Der Fluoreszenz. *Zeitschrift für Physikalische Chemie* **1954**, *1* (5_6), 275–277. https://doi.org/10.1524/zpch.1954.1.5_6.275.
- [254] Birks, J. B. Excimers. *Rep. Prog. Phys.* **1975**, *38* (8), 903–974. <https://doi.org/10.1088/0034-4885/38/8/001>.
- [255] Azumi, T.; McGlynn, S. P. Energy of Excimer Luminescence. I. A Reconsideration of Excimer Processes. *J. Chem. Phys.* **1964**, *41* (10), 3131–3138. <https://doi.org/10.1063/1.1725686>.
- [256] Kołaski, M.; Arunkumar, C. R.; Kim, K. S. Aromatic Excimers: Ab Initio and TD-DFT Study. *J. Chem. Theory Comput.* **2013**, *9* (1), 847–856. <https://doi.org/10.1021/ct300350m>.
- [257] Azumi, T.; Armstrong, A. T.; McGlynn, S. P. Energy of Excimer Luminescence. II. Configuration Interaction between Molecular Exciton States and Charge Resonance States. *J. Chem. Phys.* **1964**, *41* (12), 3839–3852. <https://doi.org/10.1063/1.1725823>.
- [258] Plasser, F.; Lischka, H. Analysis of Excitonic and Charge Transfer Interactions from Quantum Chemical Calculations. *J. Chem. Theory Comput.* **2012**, *8* (8), 2777–2789. <https://doi.org/10.1021/ct300307c>.
- [259] Valente, D. C. A.; Casal, M. T. do; Barbatti, M.; Niehaus, T. A.; Aquino, A. J. A.; Lischka, H.; Cardozo, T. M. Excitonic and Charge Transfer Interactions in Tetracene Stacked and T-Shaped Dimers. *The Journal of Chemical Physics* **2021**, *154* (4), 044306. <https://doi.org/10.1063/5.0033272>.
- [260] Shirai, S.; Kurashige, Y.; Yanai, T. Computational Evidence of Inversion of 1La and 1Lb-Derived Excited States in Naphthalene Excimer Formation from Ab Initio Multireference Theory with Large Active Space: DMRG-CASPT2 Study. *J. Chem. Theory Comput.* **2016**, *12* (5), 2366–2372. <https://doi.org/10.1021/acs.jctc.6b00210>.
- [261] Messias Cardozo, T.; Pessoa Galliez, A.; Borges, I.; Plasser, F.; A. Aquino, A. J.; Barbatti, M.; Lischka, H. Dynamics of Benzene Excimer Formation from the Parallel-Displaced Dimer. *Physical Chemistry Chemical Physics* **2019**, *21* (26), 13916–13924. <https://doi.org/10.1039/C8CP06354K>.
- [262] do Casal, M. T.; Cardozo, T. M. Impact of Low-Cost Methods in the Description of Excimer and Exciplex Formation: Pyrene–Pyrene and Pyrene–Naphthalene Case Studies. *Theor Chem Acc* **2020**, *139* (8), 144. <https://doi.org/10.1007/s00214-020-02658-0>.
- [263] Huenerbein, R.; Grimme, S. Time-Dependent Density Functional Study of Excimers and Exciplexes of Organic Molecules. *Chemical Physics* **2008**, *343* (2), 362–371. <https://doi.org/10.1016/j.chemphys.2007.08.005>.

- [264] Hoche, J.; Schmitt, H.-C.; Humeniuk, A.; Fischer, I.; Mitrić, R.; S. Röhr, M. I. The Mechanism of Excimer Formation: An Experimental and Theoretical Study on the Pyrene Dimer. *Physical Chemistry Chemical Physics* **2017**, *19* (36), 25002–25015. <https://doi.org/10.1039/C7CP03990E>.
- [265] Berthelot, M. Note Sur Une Nouvelle Série de Composés Organiques, Le Quadricarbure d'Hydrogène et Ses Dérivés. *Comptes Rendus* **1860**, *50*, 805–808.
- [266] Zhao, L.; Lu, W.; Ahmed, M.; Zagidullin, M. V.; Azyazov, V. N.; Morozov, A. N.; Mebel, A. M.; Kaiser, R. I. Gas-Phase Synthesis of Benzene via the Propargyl Radical Self-Reaction. *Science Advances* **2021**, *7* (21), eabf0360. <https://doi.org/10.1126/sciadv.abf0360>.
- [267] Frenklach, M.; Clary, D. W.; Gardiner, W. C.; Stein, S. E. Detailed Kinetic Modeling of Soot Formation in Shock-Tube Pyrolysis of Acetylene. *Symposium (International) on Combustion* **1985**, *20* (1), 887–901. [https://doi.org/10.1016/S0082-0784\(85\)80578-6](https://doi.org/10.1016/S0082-0784(85)80578-6).
- [268] Homann, K.-H. Fullerenes and Soot Formation— New Pathways to Large Particles in Flames. *Angewandte Chemie International Edition* **1998**, *37* (18), 2434–2451. [https://doi.org/10.1002/\(SICI\)1521-3773\(19981002\)37:18<2434::AID-ANIE2434>3.0.CO;2-L](https://doi.org/10.1002/(SICI)1521-3773(19981002)37:18<2434::AID-ANIE2434>3.0.CO;2-L).
- [269] Faccinetto, A.; Desgroux, P.; Ziskind, M.; Therssen, E.; Focsa, C. High-Sensitivity Detection of Polycyclic Aromatic Hydrocarbons Adsorbed onto Soot Particles Using Laser Desorption/Laser Ionization/Time-of-Flight Mass Spectrometry: An Approach to Studying the Soot Inception Process in Low-Pressure Flames. *Combustion and Flame* **2011**, *158* (2), 227–239. <https://doi.org/10.1016/j.combustflame.2010.08.012>.
- [270] Johansson, K. O.; Lai, J. Y. W.; Skeen, S. A.; Popolan-Vaida, D. M.; Wilson, K. R.; Hansen, N.; Violi, A.; Michelsen, H. A. Soot Precursor Formation and Limitations of the Stabilomer Grid. *Proceedings of the Combustion Institute* **2015**, *35* (2), 1819–1826. <https://doi.org/10.1016/j.proci.2014.05.033>.
- [271] Commodo, M.; Kaiser, K.; De Falco, G.; Minutolo, P.; Schulz, F.; D'Anna, A.; Gross, L. On the Early Stages of Soot Formation: Molecular Structure Elucidation by High-Resolution Atomic Force Microscopy. *Combustion and Flame* **2019**, *205*, 154–164. <https://doi.org/10.1016/j.combustflame.2019.03.042>.
- [272] Schulz, F.; Commodo, M.; Kaiser, K.; De Falco, G.; Minutolo, P.; Meyer, G.; D'Anna, A.; Gross, L. Insights into Incipient Soot Formation by Atomic Force Microscopy. *Proceedings of the Combustion Institute* **2019**, *37* (1), 885–892. <https://doi.org/10.1016/j.proci.2018.06.100>.
- [273] Wang, C. S.; Bartelt, N. C.; Ragan, R.; Thürmer, K. Revealing the Molecular Structure of Soot Precursors. *Carbon* **2018**, *129*, 537–542. <https://doi.org/10.1016/j.carbon.2017.12.005>.
- [274] Botero, M. L.; Sheng, Y.; Akroyd, J.; Martin, J.; Dreyer, J. A. H.; Yang, W.; Kraft, M. Internal Structure of Soot Particles in a Diffusion Flame. *Carbon* **2019**, *141*, 635–642. <https://doi.org/10.1016/j.carbon.2018.09.063>.
- [275] Chandross, E. A.; Ferguson, J.; McRae, E. G. Absorption and Emission Spectra of Anthracene Dimers. *The Journal of Chemical Physics* **2004**, *45* (10), 3546. <https://doi.org/10.1063/1.1727371>.
- [276] Ferguson, J. Absorption and Emission Spectra of the Perylene Dimer. *J. Chem. Phys.* **1966**, *44* (7), 2677–2683. <https://doi.org/10.1063/1.1727110>.
- [277] Khakhel', O. A. Absorption Spectra of Pyrene Aggregates in Saturated Solutions. *Journal of Applied Spectroscopy* **2001**, *68* (2), 280–286. <https://doi.org/10.1023/A:1019220303911>.

- [278] Miller, J. H. The Kinetics of Polynuclear Aromatic Hydrocarbon Agglomeration in Flames. *Symposium (International) on Combustion* **1991**, *23* (1), 91–98. [https://doi.org/10.1016/S0082-0784\(06\)80246-8](https://doi.org/10.1016/S0082-0784(06)80246-8).
- [279] Schuetz, C. A.; Frenklach, M. Nucleation of Soot: Molecular Dynamics Simulations of Pyrene Dimerization. *Proceedings of the Combustion Institute* **2002**, *29* (2), 2307–2314. [https://doi.org/10.1016/S1540-7489\(02\)80281-4](https://doi.org/10.1016/S1540-7489(02)80281-4).
- [280] Chung, S.-H.; Violi, A. Peri-Condensed Aromatics with Aliphatic Chains as Key Intermediates for the Nucleation of Aromatic Hydrocarbons. *Proceedings of the Combustion Institute* **2011**, *33* (1), 693–700. <https://doi.org/10.1016/j.proci.2010.06.038>.
- [281] Botero, M. L.; Adkins, E. M.; González-Calera, S.; Miller, H.; Kraft, M. PAH Structure Analysis of Soot in a Non-Premixed Flame Using High-Resolution Transmission Electron Microscopy and Optical Band Gap Analysis. *Combustion and Flame* **2016**, *164*, 250–258. <https://doi.org/10.1016/j.combustflame.2015.11.022>.
- [282] Adkins, E. M.; Giaccari, J. A.; Miller, J. H. Computed Electronic Structure of Polynuclear Aromatic Hydrocarbon Agglomerates. *Proceedings of the Combustion Institute* **2017**, *36* (1), 957–964. <https://doi.org/10.1016/j.proci.2016.06.186>.
- [283] Elvati, P.; Violi, A. Thermodynamics of Poly-Aromatic Hydrocarbon Clustering and the Effects of Substituted Aliphatic Chains. *Proceedings of the Combustion Institute* **2013**, *34* (1), 1837–1843. <https://doi.org/10.1016/j.proci.2012.07.030>.
- [284] Totton, T. S.; Misquitta, A. J.; Kraft, M. A Quantitative Study of the Clustering of Polycyclic Aromatic Hydrocarbons at High Temperatures. *Phys. Chem. Chem. Phys.* **2012**, *14* (12), 4081–4094. <https://doi.org/10.1039/C2CP23008A>.
- [285] Han, S.; Li, X.; Nie, F.; Zheng, M.; Liu, X.; Guo, L. Revealing the Initial Chemistry of Soot Nanoparticle Formation by ReaxFF Molecular Dynamics Simulations. *Energy Fuels* **2017**, *31* (8), 8434–8444. <https://doi.org/10.1021/acs.energyfuels.7b01194>.
- [286] Mao, Q.; van Duin, A. C. T.; Luo, K. H. Formation of Incipient Soot Particles from Polycyclic Aromatic Hydrocarbons: A ReaxFF Molecular Dynamics Study. *Carbon* **2017**, *121*, 380–388. <https://doi.org/10.1016/j.carbon.2017.06.009>.
- [287] Mao, Q.; Ren, Y.; Luo, K. H.; van Duin, A. C. T. Dynamics and Kinetics of Reversible Homo-Molecular Dimerization of Polycyclic Aromatic Hydrocarbons. *J. Chem. Phys.* **2017**, *147* (24), 244305. <https://doi.org/10.1063/1.5000534>.
- [288] Kholghy, M. R.; Kelesidis, G. A.; Pratsinis, S. E. Reactive Polycyclic Aromatic Hydrocarbon Dimerization Drives Soot Nucleation. *Phys. Chem. Chem. Phys.* **2018**, *20* (16), 10926–10938. <https://doi.org/10.1039/C7CP07803J>.
- [289] Semenikhin, A. S.; Savchenkova, A. S.; Chechet, I. V.; Matveev, S. G.; Frenklach, M.; Mebel, A. M. On the Mechanism of Soot Nucleation. II. E-Bridge Formation at the PAH Bay. *Phys. Chem. Chem. Phys.* **2020**, *22* (30), 17196–17204. <https://doi.org/10.1039/D0CP02554B>.
- [290] Adamson, B. D.; Skeen, S. A.; Ahmed, M.; Hansen, N. Detection of Aliphatically Bridged Multi-Core Polycyclic Aromatic Hydrocarbons in Sooting Flames with Atmospheric-Sampling High-Resolution Tandem Mass Spectrometry. *J. Phys. Chem. A* **2018**, *122* (48), 9338–9349. <https://doi.org/10.1021/acs.jpca.8b08947>.
- [291] Giordana, A.; Maranzana, A.; Tonachini, G. Carbonaceous Nanoparticle Molecular Inception from Radical Addition and van Der Waals Coagulation of Polycyclic Aromatic Hydrocarbon-Based Systems. A Theoretical Study. *J. Phys. Chem. C* **2011**, *115* (35), 17237–17251. <https://doi.org/10.1021/jp2010698>.
- [292] Sirignano, M.; Collina, A.; Commodo, M.; Minutolo, P.; D’Anna, A. Detection of Aromatic Hydrocarbons and Incipient Particles in an Opposed-Flow Flame of Ethylene by Spectral and Time-Resolved Laser Induced Emission Spectroscopy.

- Combustion and Flame* **2012**, *159* (4), 1663–1669.
<https://doi.org/10.1016/j.combustflame.2011.11.005>.
- [293] Sun, R.; Zobel, N.; Neubauer, Y.; Cardenas Chavez, C.; Behrendt, F. Analysis of Gas-Phase Polycyclic Aromatic Hydrocarbon Mixtures by Laser-Induced Fluorescence. *Optics and Lasers in Engineering* **2010**, *48* (12), 1231–1237.
<https://doi.org/10.1016/j.optlaseng.2010.06.009>.
- [294] Zhang, Y.; Liu, P.; Li, Y.; Zhan, R.; Huang, Z.; Lin, H. Study on Fluorescence Spectroscopy of PAHs with Different Molecular Structures Using Laser-Induced Fluorescence (LIF) Measurement and TD-DFT Calculation. *Spectrochimica Acta Part A: Molecular and Biomolecular Spectroscopy* **2020**, *224*, 117450.
<https://doi.org/10.1016/j.saa.2019.117450>.
- [295] Bejaoui, S.; Mercier, X.; Desgroux, P.; Therssen, E. Laser Induced Fluorescence Spectroscopy of Aromatic Species Produced in Atmospheric Sooting Flames Using UV and Visible Excitation Wavelengths. *Combustion and Flame* **2014**, *161* (10), 2479–2491. <https://doi.org/10.1016/j.combustflame.2014.03.014>.
- [296] Chi, Z.; Cullum, B. M.; Stokes, D. L.; Mobley, J.; Miller, G. H.; Hajaligol, M. R.; Vo-Dinh, T. Laser-Induced Fluorescence Studies of Polycyclic Aromatic Hydrocarbons (PAH) Vapors at High Temperatures. *Spectrochimica Acta Part A: Molecular and Biomolecular Spectroscopy* **2001**, *57* (7), 1377–1384. [https://doi.org/10.1016/S1386-1425\(00\)00479-0](https://doi.org/10.1016/S1386-1425(00)00479-0).
- [297] Daily, J. W. Laser Induced Fluorescence Spectroscopy in Flames. *Progress in Energy and Combustion Science* **1997**, *23* (2), 133–199. [https://doi.org/10.1016/S0360-1285\(97\)00008-7](https://doi.org/10.1016/S0360-1285(97)00008-7).
- [298] Mercier, X.; Carrivain, O.; Irimiea, C.; Faccinetto, A.; Therssen, E. Dimers of Polycyclic Aromatic Hydrocarbons: The Missing Pieces in the Soot Formation Process. *Phys. Chem. Chem. Phys.* **2019**, *21* (16), 8282–8294.
<https://doi.org/10.1039/C9CP00394K>.
- [299] Di Lorenzo, A.; D'Alessio, A.; Cincotti, V.; Masi, S.; Menna, P.; Venitozzi, C. UV Absorption, Laser Excited Fluorescence and Direct Sampling in the Study of the Formation of Polycyclic Aromatic Hydrocarbons in Rich CH₄/O₂ Flames. *Symposium (International) on Combustion* **1981**, *18* (1), 485–491. [https://doi.org/10.1016/S0082-0784\(81\)80054-9](https://doi.org/10.1016/S0082-0784(81)80054-9).
- [300] Haynes, B. S.; Jander, H.; Wagner, H. Gg. Optical Studies of Soot-Formation Processes in Premixed Flames. *Berichte der Bunsengesellschaft für physikalische Chemie* **1980**, *84* (6), 585–592. <https://doi.org/10.1002/bbpc.19800840613>.
- [301] Beretta, F.; Cincotti, V.; D'Alessio, A.; Menna, P. Ultraviolet and Visible Fluorescence in the Fuel Pyrolysis Regions of Gaseous Diffusion Flames. *Combustion and Flame* **1985**, *61* (3), 211–218. [https://doi.org/10.1016/0010-2180\(85\)90102-6](https://doi.org/10.1016/0010-2180(85)90102-6).
- [302] Coe, D. S.; Haynes, B. S.; Steinfeld, J. I. Identification of a Source of Argon-Ion-Laser Excited Fluorescence in Sooting Flames. *Combustion and Flame* **1981**, *43*, 211–214. [https://doi.org/10.1016/0010-2180\(81\)90018-3](https://doi.org/10.1016/0010-2180(81)90018-3).
- [303] Petarca, L.; Marconi, F. Fluorescence Spectra and Polycyclic Aromatic Species in a N-Heptane Diffusion Flame. *Combustion and Flame* **1989**, *78* (3), 308–325.
[https://doi.org/10.1016/0010-2180\(89\)90020-5](https://doi.org/10.1016/0010-2180(89)90020-5).
- [304] Smith, T. A.; Haines, D. J.; Ghiggino, K. P. Steady-State and Time-Resolved Fluorescence Polarization Behavior of Acenaphthene. *Journal of Fluorescence* **2000**, *10* (4), 365–373. <https://doi.org/10.1023/A:1009478413528>.
- [305] Samanta, A.; Devadoss, C.; Fessenden, R. W. *Picosecond time-resolved absorption and emission studies of the singlet excited states of acenaphthylene*. ACS Publications. <https://pubs.acs.org/doi/pdf/10.1021/j100381a030> (accessed 2022-03-04). <https://doi.org/10.1021/j100381a030>.

- [306] Miller, J. H.; Herdman, J. D.; Green, C. D. O.; Webster, E. M. Experimental and Computational Determinations of Optical Band Gaps for PAH and Soot in a N₂-Diluted, Ethylene/Air Non-Premixed Flame. *Proceedings of the Combustion Institute* **2013**, *34* (2), 3669–3675. <https://doi.org/10.1016/j.proci.2012.05.054>.
- [307] Miller, J. H. Aromatic Excimers: Evidence for Polynuclear Aromatic Hydrocarbon Condensation in Flames. *Proceedings of the Combustion Institute* **2005**, *30* (1), 1381–1388. <https://doi.org/10.1016/j.proci.2004.08.192>.
- [308] Saigusa, H.; Lim, E. C. Excimer Formation in van Der Waals Dimers and Clusters of Aromatic Molecules. *Acc. Chem. Res.* **1996**, *29* (4), 171–178. <https://doi.org/10.1021/ar950169v>.
- [309] Krueger, R. A.; Blanquart, G. Predicting Aromatic Exciplex Fluorescence Emission Energies. *Phys. Chem. Chem. Phys.* **2019**, *21* (20), 10325–10335. <https://doi.org/10.1039/C9CP02027F>.
- [310] Krueger, R. A.; Blanquart, G. Exciplex Stabilization in Asymmetric Acene Dimers. *J. Phys. Chem. A* **2019**, *123* (9), 1796–1806. <https://doi.org/10.1021/acs.jpca.8b11461>.
- [311] Krueger, R. A.; Blanquart, G. Multireference Exciplex Binding Energies: Basis Set Convergence and Error. *International Journal of Quantum Chemistry* **2019**, *119* (5), e25819. <https://doi.org/10.1002/qua.25819>.
- [312] Frisch, M. J.; Head-Gordon, M.; Pople, J. A. A Direct MP2 Gradient Method. *Chemical Physics Letters* **1990**, *166* (3), 275–280. [https://doi.org/10.1016/0009-2614\(90\)80029-D](https://doi.org/10.1016/0009-2614(90)80029-D).
- [313] Frisch, M. J.; Head-Gordon, M.; Pople, J. A. Semi-Direct Algorithms for the MP2 Energy and Gradient. *Chemical Physics Letters* **1990**, *166* (3), 281–289. [https://doi.org/10.1016/0009-2614\(90\)80030-H](https://doi.org/10.1016/0009-2614(90)80030-H).
- [314] Head-Gordon, M.; Pople, J. A.; Frisch, M. J. MP2 Energy Evaluation by Direct Methods. *Chemical Physics Letters* **1988**, *153* (6), 503–506. [https://doi.org/10.1016/0009-2614\(88\)85250-3](https://doi.org/10.1016/0009-2614(88)85250-3).
- [315] Tsuzuki, S.; Honda, K.; Uchimaru, T.; Mikami, M.; Tanabe, K. Origin of Attraction and Directionality of the π/π Interaction: Model Chemistry Calculations of Benzene Dimer Interaction. *J. Am. Chem. Soc.* **2002**, *124* (1), 104–112. <https://doi.org/10.1021/ja0105212>.
- [316] Hohenstein, E. G.; Sherrill, C. D. Wavefunction Methods for Noncovalent Interactions. *WIREs Computational Molecular Science* **2012**, *2* (2), 304–326. <https://doi.org/10.1002/wcms.84>.
- [317] Grimme, S. Density Functional Theory with London Dispersion Corrections. *WIREs Computational Molecular Science* **2011**, *1* (2), 211–228. <https://doi.org/10.1002/wcms.30>.
- [318] Grimme, S. Semiempirical GGA-type density functional constructed with a long-range dispersion correction. *Journal of Computational Chemistry* **2006**, *27* (15), 1787–1799. <https://doi.org/10.1002/jcc.20495>.
- [319] Grimme, S.; Antony, J.; Ehrlich, S.; Krieg, H. A Consistent and Accurate Ab Initio Parametrization of Density Functional Dispersion Correction (DFT-D) for the 94 Elements H-Pu. *J. Chem. Phys.* **2010**, *132* (15), 154104. <https://doi.org/10.1063/1.3382344>.
- [320] Caldeweyher, E.; Ehlert, S.; Hansen, A.; Neugebauer, H.; Spicher, S.; Bannwarth, C.; Grimme, S. A Generally Applicable Atomic-Charge Dependent London Dispersion Correction. *J. Chem. Phys.* **2019**, *150* (15), 154122. <https://doi.org/10.1063/1.5090222>.

- [321] Ehrlich, S.; Moellmann, J.; Grimme, S. Dispersion-Corrected Density Functional Theory for Aromatic Interactions in Complex Systems. *Acc. Chem. Res.* **2013**, *46* (4), 916–926. <https://doi.org/10.1021/ar3000844>.
- [322] Chakarova, S. D.; Schröder, E. Van Der Waals Interactions of the Benzene Dimer: Towards Treatment of Polycyclic Aromatic Hydrocarbon Dimers. *Materials Science and Engineering: C* **2005**, *25* (5), 787–792. <https://doi.org/10.1016/j.msec.2005.06.012>.
- [323] Lee, N. K.; Park, S.; Kim, S. K. Ab Initio Studies on the van Der Waals Complexes of Polycyclic Aromatic Hydrocarbons. II. Naphthalene Dimer and Naphthalene–Anthracene Complex. *J. Chem. Phys.* **2002**, *116* (18), 7910–7917. <https://doi.org/10.1063/1.1468642>.
- [324] Grimme, S. Do Special Noncovalent π – π Stacking Interactions Really Exist? *Angewandte Chemie International Edition* **2008**, *47* (18), 3430–3434. <https://doi.org/10.1002/anie.200705157>.
- [325] Grimme, S.; Parac, M. Substantial Errors from Time-Dependent Density Functional Theory for the Calculation of Excited States of Large π Systems. *ChemPhysChem* **2003**, *4* (3), 292–295. <https://doi.org/10.1002/cphc.200390047>.
- [326] Goerigk, L.; Grimme, S. Double-Hybrid Density Functionals Provide a Balanced Description of Excited 1La and 1Lb States in Polycyclic Aromatic Hydrocarbons. *J. Chem. Theory Comput.* **2011**, *7* (10), 3272–3277. <https://doi.org/10.1021/ct200380v>.
- [327] Chai, J.-D.; Head-Gordon, M. Long-Range Corrected Hybrid Density Functionals with Damped Atom–Atom Dispersion Corrections. *Phys. Chem. Chem. Phys.* **2008**, *10* (44), 6615–6620. <https://doi.org/10.1039/B810189B>.
- [328] Pitoňák, M.; Neogrady, P.; Řezáč, J.; Jurečka, P.; Urban, M.; Hobza, P. Benzene Dimer: High-Level Wave Function and Density Functional Theory Calculations. *J. Chem. Theory Comput.* **2008**, *4* (11), 1829–1834. <https://doi.org/10.1021/ct800229h>.
- [329] Janda, K. C.; Hemminger, J. C.; Winn, J. S.; Novick, S. E.; Harris, S. J.; Klemperer, W. Benzene Dimer: A Polar Molecule. *J. Chem. Phys.* **1975**, *63* (4), 1419–1421. <https://doi.org/10.1063/1.431502>.
- [330] Sinnokrot, M. O.; Valeev, E. F.; Sherrill, C. D. Estimates of the Ab Initio Limit for Π – π Interactions: The Benzene Dimer. *J. Am. Chem. Soc.* **2002**, *124* (36), 10887–10893. <https://doi.org/10.1021/ja025896h>.
- [331] Podaszwa, R.; Szalewicz, K. Physical Origins of Interactions in Dimers of Polycyclic Aromatic Hydrocarbons. *Physical Chemistry Chemical Physics* **2008**, *10* (19), 2735–2746. <https://doi.org/10.1039/B719725J>.
- [332] Birks, J. B.; Christophorou, L. G. Excimer Fluorescence Spectra of Pyrene Derivatives. *Spectrochimica Acta* **1963**, *19* (2), 401–410. [https://doi.org/10.1016/0371-1951\(63\)80051-X](https://doi.org/10.1016/0371-1951(63)80051-X).
- [333] Birks, J. B.; Dyson, D. J.; Munro, I. H.; Flowers, B. H. 'Excimer' Fluorescence II. Lifetime Studies of Pyrene Solutions. *Proceedings of the Royal Society of London. Series A. Mathematical and Physical Sciences* **1963**, *275* (1363), 575–588. <https://doi.org/10.1098/rspa.1963.0187>.
- [334] Krapp, A.; Bickelhaupt, F. M.; Frenking, G. Orbital Overlap and Chemical Bonding. *Chemistry – A European Journal* **2006**, *12* (36), 9196–9216. <https://doi.org/10.1002/chem.200600564>.
- [335] C. Hancock, A.; Goerigk, L. Noncovalently Bound Excited-State Dimers: A Perspective on Current Time-Dependent Density Functional Theory Approaches Applied to Aromatic Excimer Models. *RSC Advances* **2022**, *12* (21), 13014–13034. <https://doi.org/10.1039/D2RA01703B>.

- [336] Winnik, F. M. *Photophysics of preassociated pyrenes in aqueous polymer solutions and in other organized media*. ACS Publications.
<https://pubs.acs.org/doi/pdf/10.1021/cr00018a001> (accessed 2022-08-02).
<https://doi.org/10.1021/cr00018a001>.
- [337] R. Martinez, C.; L. Iverson, B. Rethinking the Term “Pi-Stacking.” *Chemical Science* **2012**, 3 (7), 2191–2201. <https://doi.org/10.1039/C2SC20045G>.
- [338] Reizer, E.; Viskolcz, B.; Fiser, B. Formation and Growth Mechanisms of Polycyclic Aromatic Hydrocarbons: A Mini-Review. *Chemosphere* **2022**, 291, 132793.
<https://doi.org/10.1016/j.chemosphere.2021.132793>.
- [339] Hansen, N.; Cool, T. A.; Westmoreland, P. R.; Kohse-Höinghaus, K. Recent Contributions of Flame-Sampling Molecular-Beam Mass Spectrometry to a Fundamental Understanding of Combustion Chemistry. *Progress in Energy and Combustion Science* **2009**, 35 (2), 168–191.
<https://doi.org/10.1016/j.pecs.2008.10.001>.
- [340] Miller, J. A.; Pilling, M. J.; Troe, J. Unravelling Combustion Mechanisms through a Quantitative Understanding of Elementary Reactions. *Proceedings of the Combustion Institute* **2005**, 30 (1), 43–88. <https://doi.org/10.1016/j.proci.2004.08.281>.
- [341] Weilmünster, P.; Keller, A.; Homann, K.-H. Large Molecules, Radicals, Ions, and Small Soot Particles in Fuel-Rich Hydrocarbon Flames: Part I: Positive Ions of Polycyclic Aromatic Hydrocarbons(PAH) in Low-Pressure Premixed Flames of Acetylene and Oxygen. *Combustion and Flame* **1999**, 116 (1), 62–83.
[https://doi.org/10.1016/S0010-2180\(98\)00049-2](https://doi.org/10.1016/S0010-2180(98)00049-2).
- [342] Tokmachev, A. M.; Boggio-Pasqua, M.; Mendive-Tapia, D.; Bearpark, M. J.; Robb, M. A. Fluorescence of the Perylene Radical Cation and an Inaccessible D0/D1 Conical Intersection: An MMVB, RASSCF, and TD-DFT Computational Study. *J. Chem. Phys.* **2010**, 132 (4), 044306. <https://doi.org/10.1063/1.3278545>.
- [343] Hirata, S.; Lee, T. J.; Head-Gordon, M. Time-Dependent Density Functional Study on the Electronic Excitation Energies of Polycyclic Aromatic Hydrocarbon Radical Cations of Naphthalene, Anthracene, Pyrene, and Perylene. *J. Chem. Phys.* **1999**, 111 (19), 8904–8912. <https://doi.org/10.1063/1.480235>.
- [344] Vala, M.; Szczepanski, J.; Pauzat, F.; Parisel, O.; Talbi, D.; Ellinger, Y. Electronic and Vibrational Spectra Of Matrix-Isolated Pyrene Radical Cations: Theoretical and Experimental Aspects. *J. Phys. Chem.* **1994**, 98 (37), 9187–9196.
<https://doi.org/10.1021/j100088a017>.
- [345] Snow, T. P.; Le Page, V.; Keheyan, Y.; Bierbaum, V. M. The Interstellar Chemistry of PAH Cations. *Nature* **1998**, 391 (6664), 259–260. <https://doi.org/10.1038/34602>.
- [346] Reddy, S. N.; Mahapatra, S. Theoretical Study on Molecules of Interstellar Interest. I. Radical Cation of Noncompact Polycyclic Aromatic Hydrocarbons. *J. Phys. Chem. A* **2013**, 117 (36), 8737–8749. <https://doi.org/10.1021/jp4033645>.
- [347] Reddy, S. N.; Mahapatra, S. Theoretical Study on Molecules of Interstellar Interest. II. Radical Cation of Compact Polycyclic Aromatic Hydrocarbons. *J. Phys. Chem. B* **2015**, 119 (34), 11391–11402. <https://doi.org/10.1021/acs.jpcc.5b03614>.
- [348] Menon, A.; Martin, J. W.; Leon, G.; Hou, D.; Pascazio, L.; You, X.; Kraft, M. Reactive Localized π -Radicals on Rim-Based Pentagonal Rings: Properties and Concentration in Flames. *Proceedings of the Combustion Institute* **2021**, 38 (1), 565–573. <https://doi.org/10.1016/j.proci.2020.07.042>.
- [349] Richter, H.; Benish, T. G.; Mazyar, O. A.; Green, W. H.; Howard, J. B. Formation of Polycyclic Aromatic Hydrocarbons and Their Radicals in a Nearly Sooting Premixed Benzene Flame. *Proceedings of the Combustion Institute* **2000**, 28 (2), 2609–2618.
[https://doi.org/10.1016/S0082-0784\(00\)80679-7](https://doi.org/10.1016/S0082-0784(00)80679-7).

- [350] McEnally, C. S.; Pfefferle, L. D.; Atakan, B.; Kohse-Höinghaus, K. Studies of Aromatic Hydrocarbon Formation Mechanisms in Flames: Progress towards Closing the Fuel Gap. *Progress in Energy and Combustion Science* **2006**, *32* (3), 247–294. <https://doi.org/10.1016/j.pecs.2005.11.003>.
- [351] Miller, J. A.; Melius, C. F. Kinetic and Thermodynamic Issues in the Formation of Aromatic Compounds in Flames of Aliphatic Fuels. *Combustion and Flame* **1992**, *91* (1), 21–39. [https://doi.org/10.1016/0010-2180\(92\)90124-8](https://doi.org/10.1016/0010-2180(92)90124-8).
- [352] Howard, J. B. Carbon Addition and Oxidation Reactions in Heterogeneous Combustion and Soot Formation. *Symposium (International) on Combustion* **1991**, *23* (1), 1107–1127. [https://doi.org/10.1016/S0082-0784\(06\)80371-1](https://doi.org/10.1016/S0082-0784(06)80371-1).
- [353] Johansson, K. O.; Head-Gordon, M. P.; Schrader, P. E.; Wilson, K. R.; Michelsen, H. A. Resonance-Stabilized Hydrocarbon-Radical Chain Reactions May Explain Soot Inception and Growth. *Science* **2018**, *361* (6406), 997–1000. <https://doi.org/10.1126/science.aat3417>.
- [354] Nobili, A.; Pratali Maffei, L.; Baggioli, A.; Pelucchi, M.; Cuoci, A.; Cavallotti, C.; Faravelli, T. On the Radical Behavior of Large Polycyclic Aromatic Hydrocarbons in Soot Formation and Oxidation. *Combustion and Flame* **2022**, *235*, 111692. <https://doi.org/10.1016/j.combustflame.2021.111692>.
- [355] Mao, Q.; Hou, D.; Luo, K. H.; You, X. Dimerization of Polycyclic Aromatic Hydrocarbon Molecules and Radicals under Flame Conditions. *J. Phys. Chem. A* **2018**, *122* (44), 8701–8708. <https://doi.org/10.1021/acs.jpca.8b07102>.

Résumé

Ce manuscrit présente les résultats d'une étude expérimentale et théorique de deux systèmes moléculaires d'intérêt environnemental : la 2',3-dihydroxyflavone (2'3HF) et les hydrocarbures aromatiques polycycliques (HAP). Ces systèmes ont été étudiés par une combinaison de techniques de spectroscopies électroniques (absorption et fluorescence) et de calculs de chimie quantique (DFT et TD-DFT). Dans une première partie de cette thèse, il est montré que la 2'3HF présente des propriétés acido-basiques singulières par rapport aux autres flavonols. La diminution de plusieurs unités de la valeur du pK_a est attribuée à la présence d'un réseau de liaisons hydrogènes. A l'état-excité, un transfert de proton intramolécule est à l'origine d'une fluorescence duale. Une bande d'émission supplémentaire, semblant provenir d'une forme tautomère perturbée par interaction avec le solvant, a été mise en évidence. Enfin, une étude exhaustive des complexes de Ca(II), Mn(II) et Zn(II) a montré la formation de chélates avec la fonction α -hydroxycétone. Dans la deuxième partie, trois hypothèses structurales pour expliquer l'observation expérimentale de fluorescence induite par laser (LIF) dans le visible ont été explorées. Une étude sur les dimères de van der Waals (vdW) des HAPs a permis de mieux comprendre la nature de l'interaction entre monomères et de mettre en évidence la difficulté de modéliser ces systèmes, cependant, les transitions électroniques calculées suggèrent que ces espèces ne peuvent pas être responsables des signaux de LIF. Ensuite, une étude identique de HAP liés par ponts aliphatiques a montré des résultats très similaires aux dimères de vdW, excluant leur implication dans la fluorescence observée. Enfin, l'hypothèse de l'émission provenant de radicaux de HAPs a été explorée. Cette dernière est très prometteuse et ouvre la voie à des études expérimentales et théoriques ultérieures.

Mots-Clés : 2',3-dihydroxyflavone, DFT, fluorescence, dimères d'HAPs, spectroscopie électronique, complexes métalliques

Abstract

This manuscript reports the results of an experimental and theoretical study of two molecular systems of environmental interest: 2',3-dihydroxyflavone (2'3HF) and polycyclic aromatic hydrocarbons (PAH). These systems were studied by a combination of electronic spectroscopic techniques (absorption and fluorescence) and quantum chemical calculations (DFT and TD-DFT). In the first part of this thesis, it is shown that 2'3HF has singular acid-base properties compared to other flavonols. The decrease of the pK_a by several units is attributed to the presence of a hydrogen-bond network. In the excited state, an intramolecular proton transfer causes a dual fluorescence. An additional emission band, seemingly originating from a tautomeric form perturbed by interaction with the solvent, was revealed. Finally, an exhaustive study of the Ca(II), Mn(II) and Zn(II) complexes showed the formation of chelates with the α -hydroxyketone function. In the second part, three structural hypotheses to explain the experimental observation of visible-range laser-induced fluorescence (LIF) were explored. A study of van der Waals (vdW) dimers of PAHs provided insights into the nature of the monomer interaction and highlighted the difficulty of modelling these systems. However, the calculated electronic transitions suggest that these species cannot be responsible for the LIF signals. Secondly, an identical study of aliphatically bridged PAHs showed very similar results to vdW dimers, ruling out their involvement in the observed fluorescence. Finally, the hypothesis of emission from PAH radicals was explored. The latter is very promising and opens the way for further experimental and theoretical studies.

Keywords: 2',3-dihydroxyflavone, DFT, fluorescence, PAH dimers, electronic spectroscopy, metal-complexes